TUDelft

Delft University of Technology

Shedding light on dynamic processes in the intestinal epithelium

Spoelstra, Willem Kasper

DOI
10.4233/uuid:2325fb02-b43a-455e-9e03-16a5fbccb5a3

Publication date
2025

Document Version
Final published version

Important note
To cite this publication, please use the final published version (if applicable).
Please check the document version above.

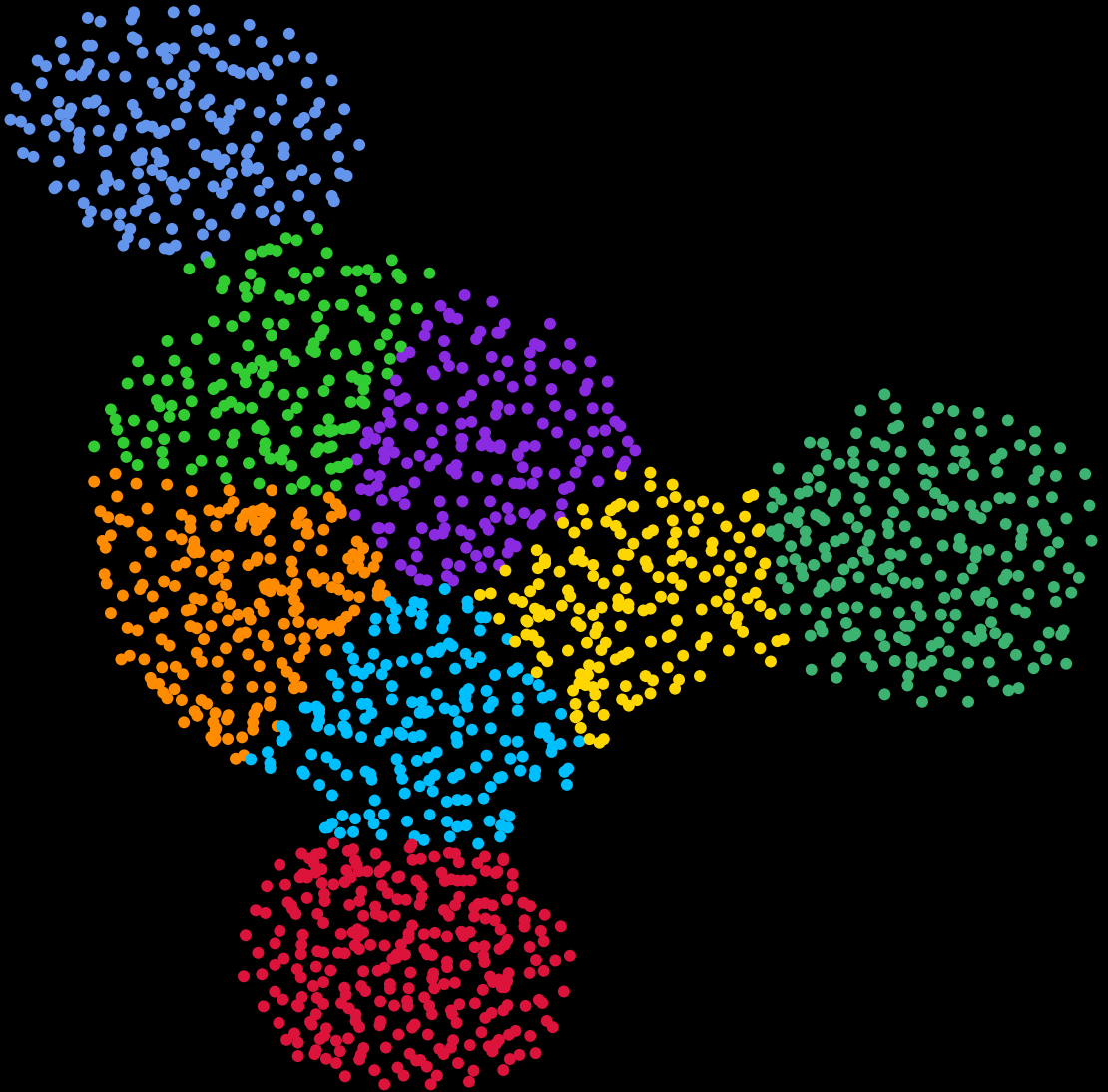# Shedding light on dynamic processes in the intestinal epithelium

Willem Kasper Spoelstra

Shedding light on dynamic processes in the intestinal epithelium

Shedding light on dynamic processes in the intestinal epithelium

Dissertation

for the purpose of obtaining the degree of doctor
at Delft University of Technology,
by the authority of the Rector Magnificus Prof. Dr. Ir. H. Bijl,
chair of the Board for Doctorates,
to be defended publicly
on January 23, 2026 at 10:00 o'clock.

by

Willem Kasper SPOELSTRA

Master of Science Nanobiology,
Delft University of Technology, Netherlands,
born in Voorburg, Netherlands.

This dissertation has been approved by the promotors.

Composition of the doctoral committee:

Rector Magnificus,	Chairperson
Prof. Dr. Ir. S. J. Tans,	TU Delft / AMOLF, Promotor
Prof. Dr. P. R. Ten Wolde,	VU Amsterdam / AMOLF, Promotor
Prof. Dr. J. S. van Zon	Leiden University / AMOLF, Promotor

Independent members:

Prof. Dr. A.M. Dogterom,	TU Delft
Dr. M. Gloerich,	Utrecht University
Prof. Dr. G.C. Hansson,	University of Gothenburg, Sweden
Prof. Dr. X. Trepat,	University of Barcelona, Spain
Prof. Dr. M.E. Tanenbaum	TU Delft / Hubrecht Institute, Reserve member

And time goes by so slowly,
and time can do so much.

Unchained melody

Contents

Summary

The intestine is the primary site for the absorption of nutrients, minerals, and water from the food that we eat. This vital function is performed by the intestinal epithelium—a single layer of specialized cells lining the inner surface of the intestine. In addition to facilitating absorption, the intestinal epithelium acts as a protective barrier that protects the underlying tissue from the potentially harmful contents of the intestinal lumen. In essence, this thesis is about two things: the intestinal epithelium and time. Specifically, it investigates how the intestinal epithelium preserves its structural and functional integrity over time and it focuses on the dynamic processes that enable the epithelium to sustain its barrier function. **Chapter 1** provides an overview of the structure, cell types, and core functions of the intestinal epithelium, along with the state-of-the-art methodologies used to study it. This chapter also introduces intestinal organoids, which are small, in vitro models of the intestinal epithelium, and serve as the central experimental system throughout this thesis.

Part I presents novel experimental insights into the dynamic mechanisms that regulate epithelial homeostasis and barrier function. A key feature of the intestinal epithelium is its ability to maintain constant cell density and integrity through continuous stem cell proliferation and extrusion of cells. In **Chapter 2**, we propose a new model for epithelial cell extrusion. Our findings reveal that epithelial cells engage in a constant mechanical "tug-of-war", exerting dynamic pulling forces on their neighbors. This mechanical competition allows cells to assess the tension they generate relative to adjacent cells. Those that produce insufficient tension are more likely to be extruded. This mechanism selectively retains mechanically robust cells, thereby enhancing epithelial integrity and preserving barrier function. **Chapter 3** explores how differentiation is regulated within the intestinal epithelium. We demonstrate that once stem cells lose access to Wnt ligands, they initiate a differentiation timer. If Wnt signaling is restored before the timer elapses, cells can reset the process and retain their stem cell identity. If not, they commit to a differentiated fate. These findings suggest that differentiation is a spatially dependent, reversible process rather than a strictly linear one. In **Chapter 4**, we investigate the differentiation of the rare and only recently identified BEST4/CA7$^+$ cells. While absent in mouse intestinal epithelium, these cells were originally discovered in humans and have since been found in other animals. Using human intestinal organoids and transcriptional fluorescent reporters, we tracked the differentiation of this cell type. Our data show that BEST4/CA7$^+$ cells and mucus-producing (goblet) cells are mutually dependent: Goblet cells direct the differentiation of neighboring cells toward the BEST4/CA7$^+$ lineage. In turn, BEST4/CA7$^+$ cells are critical for the long-term survival of goblet cells.

Part II introduces new tools and protocols for studying dynamic processes in the intestinal epithelium. **Chapter 5** presents a machine learning-based algorithm for the in

silico labeling of nuclei and membranes in 3D organoids. This approach conserves fluorescent channels for other reporters and enables high-resolution, single cell tracking with minimal phototoxicity. Finally, **Chapter 6** details protocols for long-term live-cell imaging combined with in-situ fixation. These methods allow for the real-time tracking of organoid development with experimental perturbations and identification of cell types at the endpoint.

Samenvatting

In de darmen worden de voedingsstoffen, mineralen en water uit ons eten in ons lichaam opgenomen. Deze functie wordt vervuld door het darmepitheel – een enkele laag van gespecialiseerde cellen aan de binnenkant van de darm. Naast het faciliteren van absorptie heeft het darmepitheel ook de belangrijke functie om een barrière te vormen die het onderliggend darmweefsel beschermt tegen de deels vijandige inhoud van de darm. In essentie gaat deze dissertatie over twee zaken: het darmepitheel, en tijd. Specifiek wordt onderzocht hoe het darmepitheel haar structurele en functionele integriteit behoudt over de tijd. Dit werk focust op de dynamische processen die het darmepitheel in staat stellen haar barrièrefunctie uit te voeren. **Hoofdstuk 1** biedt een overzicht van de structuur, cel types en belangrijkste functies van het darmepitheel. Daarnaast wordt moderne methodologie besproken om het darmepitheel te bestuderen. Dit hoofdstuk introduceert ook darmorganoïden – mini-versies van het darmepitheel die in het lab gekweekt kunnen worden. Darmorganoïden vormen het centrale experimentele modelsysteem in deze dissertatie.

Deel I presenteert nieuwe experimentele inzichten in de dynamische mechanismen die de homeostase en barrièrefunctie van het darmepitheel reguleren. Een belangrijke eigenschap van het darmepitheel is het behouden van constante celdichtheid en integriteit door continue stamcelproliferatie en celextrusie. In **Hoofdstuk 2** poneren wij een nieuw model voor celextrusie in het darmepitheel. Onze bevindingen laten zien dat cellen in het darmepitheel verwikkeld zijn in een constante "touwtrekwedstrijd", waarin zij dynamische trekkrachten uitoefenen op hun buurcellen. Deze vorm van mechanische competitie stelt cellen in staat om hun mechanische integriteit te testen tegen hun directe buren. Cellen die onvoldoende trekkrachten kunnen genereren hebben een hogere kans om door celextrusie uit het epitheel verwijderd te worden. Hiermee zorgt dit mechanisme dat robuste cellen behouden blijven, waardoor de integriteit en de barrièrefunctie van het darmepitheel behouden blijven. **Hoofdstuk 3** onderzoekt hoe differentiatie wordt gereguleerd in het darmepitheel. We laten zien dat stamcellen een differentiatie-timer starten wanneer zij toegang verliezen tot een bron van Wnt liganden. Als Wnt signalering wordt herstart voordat de timer volledig afloopt kunnen cellen het proces herstarten en opnieuw een volwaardige stamcel worden. Zo niet, dan commiteren cellen zich aan differentiatie. Deze bevindingen suggereren dat differentiatie geen lineair proces is, maar herhaaldelijk kan worden herstart. In **Hoofdstuk 4** onderzoeken wij de differentiatie van zeldzame, en pas recent ontdekte BEST4/CA7$^+$ cellen. Deze cellen komen niet voor in de muis, maar zijn sinds hun ontdekking in de mens ook gevonden in enkele andere dieren. Door middel van menselijke darmorganoïden met fluorescente labels hebben we de differentiatie van dit celtype over de tijd gevolgd. Onze data laten zien dat BEST4/CA7$^+$ cellen en slijmproducerende (goblet) cellen onderling afhankelijk zijn: goblet cellen geven hun directe buren de instructie om zich te differentiëren als BEST4/CA7$^+$ cel, en BEST4/CA7$^+$ cellen zijn op hun

beurt essentieel voor het overleven van goblet cellen op de langere termijn.

Deel 2 introduceert nieuwe technieken en gedetailleerde protocollen voor het bestuderen van dynamische processen in het darmepitheel. **Hoofdstuk 5** presenteert een op machine-learning gebaseerd algoritme voor het in silico markeren van celkernen en membranen in 3D darmorganoïden. Dit algoritme stelt onderzoekers in staat om meer fluorescente kanalen vrij te houden voor andere signalen en maakt het mogelijk met hoge resolutie en minimale phototoxiciteit individuele cellen te volgen over de tijd. Als laatste bevat **Hoofdstuk 6** gedetailleerde protocollen om levende cellen in darmorganoïden te volgen voor lange tijd, met de mogelijkheid om organoiden op hun plaats te fixeren en verder te kleuren met antilichamen. Deze methode maakt het mogelijk om de ontwikkeling van organoïden te volgen, in combinatie met experimentele vestoringen en het bepalen van celtypes aan het eind.

1

INTRODUCTION

"Whatever you do in life will be insignificant,
but it is very important that you do it."

Mahatma Gandhi

As you are reading this, over 3 billion cells[1] in your intestine are working very hard to absorb nutrients from the food that you have eaten in the previous hours. The intestine is part of the gastrointestinal tract and consists of two anatomically distinct regions: the small intestine and the colon (Fig. 1.1). The small intestine is approximately 6 meters long, and consists of three separate regions, namely the duodenum, jejunum and ileum. After passing through the stomach, food first enters the duodenum, which mainly releases digestive enzymes. Subsequently, it enters the jejunum, which absorbs most nutrients, and to the ileum, which absorbs remaining nutrients, vitamins and bile salts. The remaining luminal content is passed onto the colon, which is approximately 1.5 meters long and specialized in water and mineral (re)uptake. The intestinal lumen is an exceptionally hostile environment, due to its high acidity, pathogenic load and microbiome. In contrast, the intestine itself consists of delicate muscle tissue, blood vessels and immune cells. These two environments are separated by only one layer of cells, which is called the intestinal epithelium. This thesis is a contribution to our understanding of the composition and functions of the intestinal epithelium. The main aim of this chapter to introduce the structure and composition of the intestinal epithelium and discuss the modern scientific approaches for studying it.
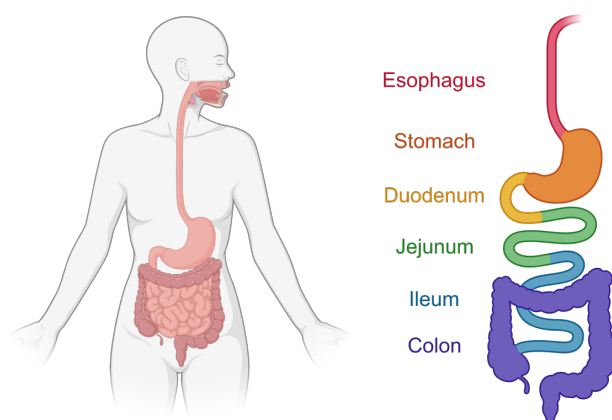
Figure 1.1: The gastrointestinal tract. The esophagus leads food to the stomach, where it is pre-processed and passed to the intestine. Nutrients, water and minerals are then absorbed by the duodenum, jejunum, ileum and colon. Figure made using Biorender.

---

[1]This number is calculated under the assumption that the inner surface area of the intestine 32 μm^2 long, covered with cells that occupy an area on the order of 100 μm^2. As will be discussed below, the structure of the inner lining of the intestine is such that it is not straightforward to compute its surface area, and the literature contains estimates that run from a few to several hundreds of square meters. As far as I can tell, the debate was settled in 2014 by a careful analysis that resulted in a paper concluding "The total area of the human adult gut mucosa is not in the order of tennis lawn (*sic*), rather is that of half a badminton court" [106].

1

1.1 Structure and composition of the intestinal epithelium

The small intestinal epithelium is organized into crypts and villi (Fig. 1.2a). Crypts are protrusions into the intestinal tissue, and contain mostly undifferentiated, proliferative cells. Villi are protrusions into the intestinal lumen and contain the differentiated, post-mitotic cells that fulfil the primary functions of the intestinal epithelium. In contrast to the small intestine, colonic epithelium contains crypts with proliferative cells and inter-crypt regions, but no villi (Fig. 1.2b). Stem cells at the bottom of the crypt proliferate, occasionally lose stemness and differentiate into the different mature cell types [14]. Cell division in the crypt ("mitotic pressure") pushes cells up to the crypt neck and into the villus, from where cells continue to migrate from the villus shaft to the tip using active migration [149]. At the end of their lifetime – which is typically, but not always, at villus tip [36] – cells extrude into the lumen and die as a result of the lack of attachment and molecular signals (anoikis). The birth of cells in the crypts, and their extrusion in the villus means that the intestinal epithelium is generally understood as a conveyor-belt.

The intestinal epithelium has a spectacularly high turnover rate: Cells in the crypt proliferate approximately once per day to compensate for the cells that are shed into the lumen [14]. The intestinal epithelium consists of two types of proliferative cells, namely $Lgr5^+$ stem cells and transit-amplifying (TA) cells, from which all seven differentiated cell types descend. The differentiated cell types are Paneth cells, enterocytes, goblet cells, enteroendocrine cells, tuft cells, M cells and $BEST4/CA7^+$ cells (Fig. 1.2c & Table 1.1). For the intestinal epithelium to function smoothly, cells of all types need to perform their function(s), and all cells depend on other cell types as well. Understanding how the intestinal epithelium works therefore requires understanding the primary function(s) of each cell type individually, but also how cell types affect other cell types.

The stem cell zone
At the bottom of the crypt, we find the stem cell niche, which is the motor driving the fast turnover of the intestinal epithelium. Stem cells in the stem cell niche are characterized by the expression of Leucine-rich repeat-containing G-protein coupled receptor 5 (LGR5) and active Wnt signalling [14]. The stem cell niche in mice typically consists of 12-24 highly proliferative $Lgr5^+$ stem cells [9, 248]. In the small intestine Paneth cells are interspersed between the $Lgr5^+$ stem cells (Fig. 1.3a), where they protect their stem cell neighbours by secreting antimicrobial peptides (cryptidins) and enzymes (lysozyme), and supply the $Lgr5^+$ stem cells with essential ligands to maintain Wnt signalling [71–73, 88, 233]. Colonic crypts lack Paneth cells, but rely on the mesenchyme [88] and deep-crypt secretory (DCS) cells [232] for the maintenance of the stem cell niche. When $Lgr5^+$ stem cells exit the stem cell niche, they lose their supply of Wnt ligands and therefore Wnt signalling. This loss of Wnt signalling turns stem cells into proliferative transit-amplifying (TA) cells that ultimately give rise to the differentiated cell types [71]. However, the precise mechanism that regulates the onset of differentiation remains unresolved.
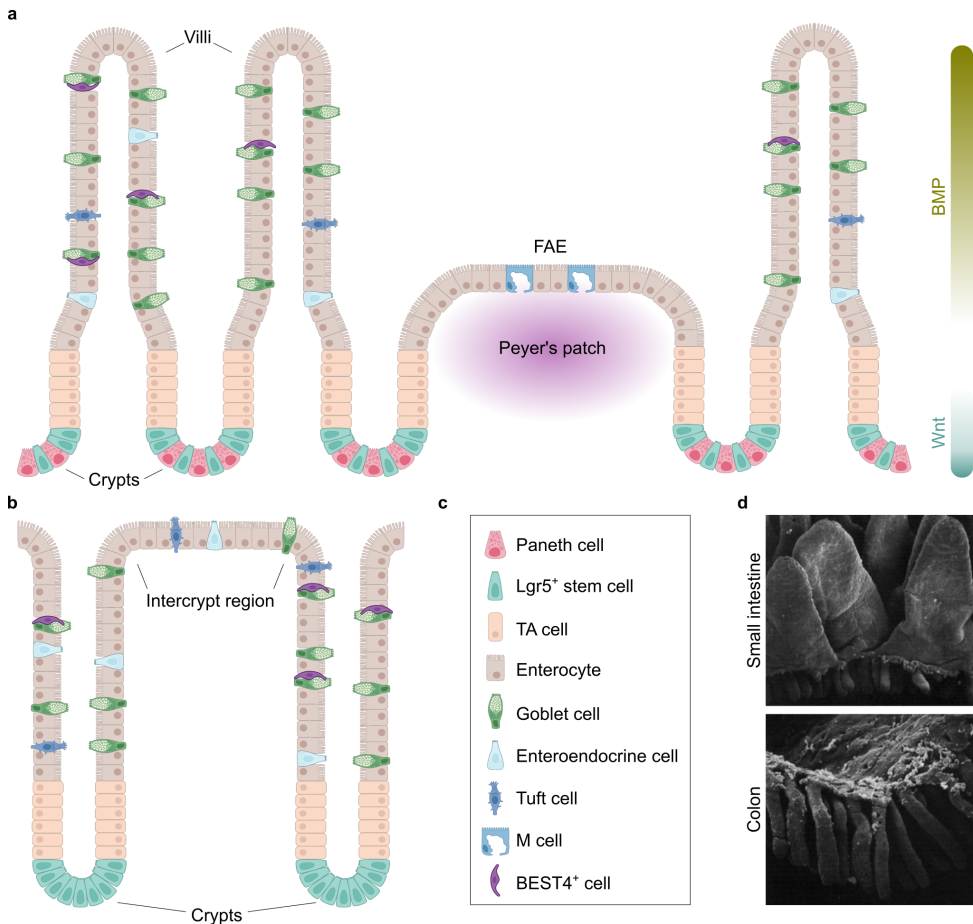
Figure 1.2: Structure and composition of the (human) intestinal epithelium. (a, b) Schematic depictions of the intestinal epithelium in the small intestine (a) and the colon (b). The small intestinal and colonic epithelia differ in three important ways. The small intestine contains distinct protrusions (villi), whereas the colon does not. Additionally, the small intestinal epithelium contains follicle-associated epithelium (FAE) that overlay Peyer's patches. Finally, small intestinal crypts contain Paneth cells which are absent in the colonic crypts. Of note, colonic crypts in the middle and distal colon contain Reg4$^+$ deep-crypt secretory cells (DCS), which perform similar functions as Paneth cells. Because these cells are almost completely absent from the proximal colon [232], they are ommitted from this schematic. (c) Legend showing the cell type composition of the intestinal epithelium. For our purposes we distinguish between two types of proliferative cells, being Lgr5$^+$ stem cells and transit-amplifying (TA) cells, and seven differentiated cell types, being enterocytes, goblet cells, Paneth cells, enteroendocrine cells, tuft cells, M cells and BEST4/CA7$^+$ cells. (d) Scanning Electron Microscopy (SEM) images of duodenal (top) and colonic epithelium (bottom). Images modified from ref. [166]. Panels a-c made with Biorender.

ENTEROCYTES: ABSORPTIVE WORKHORSES OF NUTRIENT UPTAKE

By far the most abundant cell type in the intestinal epithelium is the enterocyte, making up approximately 90% of the intestinal epithelium [14]. Enterocytes are responsible for the absorption of nutrients from the lumen. This capability is enhanced by microvilli, which are small protrusions of the apical membrane that increase the surface area exposed

1

to the lumen. Enterocytes have the shortest turnover time[2] of all the differentiated cells in the intestinal epithelium, of roughly 3-5 days [52]. Interestingly, enterocytes undergo continuous transitions during their lifetime (Fig. 1.3b) [186]: At the bottom of the villus, they protect the crypt by expressing anti-microbial peptides. In the mid-villus, they gradually start expressing nutrient transporters for (in chronological order) amino acids, carbohydrates, peptides and apolipoproteins. At the villus tip, they express machinery for the conversion of luminal ATP to adenosine, likely to inhibit an immune response to the intestinal microbiome. This zone-specific expression of proteins ("zonation") of enterocytes along the villus is regulated by the supply of BMP [25], which increases gradually as cells move up to the villus tip (Fig. 1.2a) [99].

Goblet cells and the maintenance of the mucus layer
The second most abundant cell type in the intestinal villus is the goblet cell, named after its goblet-like morphology. Like enterocytes, goblet cells in the small intestine are zonated along the villus by the BMP-gradient [25]. While the main goblet cell marker expression does not change along the villus axis, they increasingly express antimicrobial proteins as they get closer to the villus tip. The primary function of goblet cells is to produce and secrete mucins, which constitute the mucus layer that protects the intestinal epithelium from pathogens and the commensal microbiome. Goblet cells contain a comparatively large reservoir of mucin, which is packaged into mucin granules (Fig. 1.3c) [160]. In recent years, colonic goblet cells have been shown to be a heterogenous cell type. Initially two functionally distinct goblet cell subtypes were distinguished in the gut, being intercrypt goblet cells that secrete continuously secrete mucus [122], and sentinel goblet cells (senGCs) at the crypt entrance that protect the crypt by secreting a thick mucus [26]. Detailed mapping of intestinal goblet cells later showed at least four distinct subpopulations of goblet cells, differing (among other things) in the composition and viscoelastic properties of their secreted mucus [201].

Hormone production: enteroendocrine cells
Enteroendocrine cells (EECs) are cells in the intestinal epithelium that produce and secrete hormones. Although EECs can express multiple hormones [95], they were originally thought to express only one at any given time. For this reason, they are commonly subdivided into subtypes defined by whether they express serotonin (EC subtype), cholecystokinin (CCK; I subtype), gastric inhibitory peptide (Gip; K subtype), glucagon-like peptide 1 (GLP-1; L subtype), ghrelin (X subtype), secretin (S subtype) or neurotensin (N subtype) [24]. EECs have longer turnover times than enterocytes, suggesting that they do not participate in the conveyor-belt [256, 260]. Similar to enterocytes and goblet cells, EECs switch their hormone expression profile while migrating along the crypt-villus axis, again depending on the BMP gradient [22]. EEC differentiation starts with the expression of a pulse of the master regulator Neurogenin-3 (Neurog3; Fig. 1.3d), which (in humans) was recently shown to be under the control of the repressor ZNF800 [159]. At the moment, the molecular mechanisms that regulate commitment to the different EEC subtypes is still very poorly understood.

---

[2]The turnover time is the time between their last cell division and their extrusion.
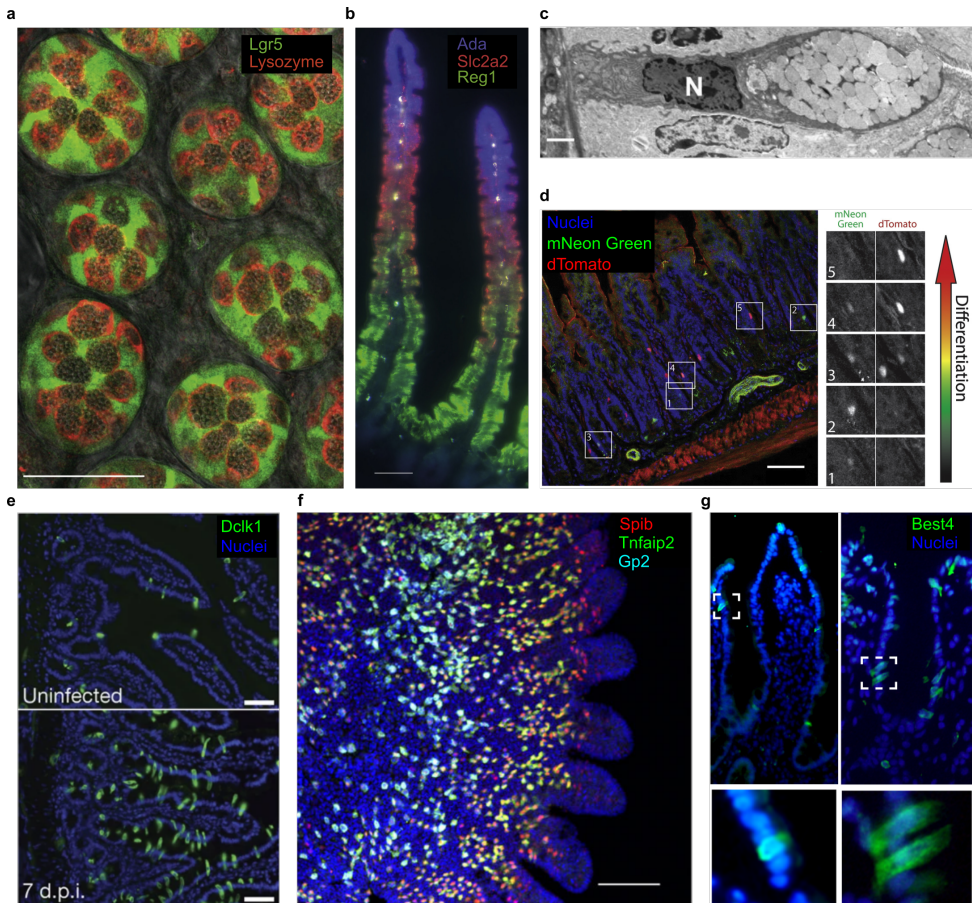
Figure 1.3: Microscopy images of the intestinal cell types. (a) Stem cell zone with Paneth cells and Lgr5$^+$ stem cells labelled. Paneth cells express lysozyme (red) and contain granules. From ref. [248]. (b) Enterocytes stained for zonation markers using fluorescent mRNA in situ hybridization. From ref. [186]. (c) Transmission Electron Microscopy (TEM) image of a goblet cell. Note the mucus reservoir on the right-hand side of the nucleus (N). From ref. [160]. (d) Micrographs from Neurog3Chrono mice, where enteroendocrine precursor cells go from green to yellow to red as they differentiate. From ref. [81]. (e) Tuft cells (green) in uninfected conditions (top) and after 7 days of infection with the parasitic worm *N. brasiliensis*. From ref. [275]. (f) Follicle-associated epithelium and associated crypts stained for early M cells (Spib$^+$; red), late M cells (Tnfaip2$^+$; green) and mature M cells (Gp2$^+$; cyan). From ref. [134]. (g) BEST4/CA7$^+$ cells in the human small intestine (left) and colon (right). From ref. [118]. Scale bars in panels a, b, d, e represent 50 µm; scale bar in panel d represents 2 µm; scale bar in panel f represents 100 µm.

1

Tuft cells

Tuft cells are very rare intestinal cell types that owe their name to the morphology of their apical membrane, which contains long protrusions (tufts) reminiscent of tufts of grass. While tuft cells represent approximately 1% of the healthy intestine, their abundance increases to over 10% during infections of parasitic worms (Fig. 1.3e) [112, 275]. During these infections, tuft cells release interleukin-25 (IL-25), which prompts tissue-resident group 2 innate lymphoid cells (ILC2s) to secrete interleukin-13 (IL-13), which in turn leads to more tuft and goblet cells. Therefore, tuft cells initiate a positive-feedback loop that leads to more tuft cells, while simultaneously increasing the number of goblet cells to secrete the mucus necessary to clear out the worm infection [112, 275]. In addition to their role in the type II immune response against pathogenic worms, tuft cells also express taste receptors and can respond to the luminal content [95]. Mounting evidence suggests that tuft cells are also a heterogeneous and zonated cell type [35, 95], potentially including proliferative subtype(s) [114].

M cells: bridges between the lumen and the immune system

The rarest cell type in the intestinal epithelium is the M cell. M cells transcytose luminal antigens such as bacteria, viruses and small particles, and present them to immune cells on their basal surface. Mature and functional M cells localize exclusively to the follicle-associated epithelium (FAE) overlaying Peyer's patches (Fig. 1.3f). Peyer's patches are only found in the small intestine, and number 50-250 in human [48] and 8-10 in mouse [129]. The FAE consists of 5-10% fully mature M cells [47, 135] and the rest enterocytes; secretory cells are absent from the FAE [202]. The lack of goblet cells in the FAE makes it directly accessible for bacteria, so that M cells can transcytose them to dendritic cells in their basal pocket. M cells use glycoprotein-2 (Gp2) to bind and endocytose luminal antigens [100], and therefore Gp2 is regarded as a marker for fully mature and functional M cells. In contrast to the other epithelial cell types, M cell differentiation strictly depends on the cytokine Receptor-Activator for NF-κB Ligand (RankL) [139], which is supplied to the epithelium by direct physical contact with fibroblasts in the Peyer's patch [192, 212]. Directly after receiving RankL, cells that commit to the M cell fate start expressing Spib [127] and Sox8 [134], which leads to the expression of the M cell-specific markers TRAF6 [128], RelB [128], Opg [135], Ccl9 [255], Tnfaip2 [101] and finally Gp2 [100] within approximately 4 days.

BEST4/CA7^{+} cells

BEST4/CA7^{+} cells are the most recent addition to the catalogue of cell types in the intestinal epithelium (Fig. 1.3g). BEST4/CA7^{+} cells are differentiated and typically found in the villus and intercrypt regions of the small intestine and colon, respectively [37, 70]. After being first discovered in the human intestinal epithelium [118], BEST4/CA7^{+} cells were also identified in other animal species such as pig [158], rhesus macaque [158], rabbit [170], rat [65], Burmese python [280] and zebrafish [284]. Notably, however, they are absent from the mouse intestine. Many functions of BEST4/CA7^{+} cells remain to be discovered, but recent work has demonstrated that BEST4/CA7^{+} cells play an important role in the electrolyte homeostasis of the mucus layer. For example, BEST4/CA7^{+} cells in the small intestine (but not in the colon) were shown to regulate the efflux of water in response to bacterial toxins (colloquially known as watery diarrhea) [278]. On the basis of their gene expression

profile, BEST4/CA7^{+} cells are furthermore predicted to sense and regulate luminal pH [205], modulate electrolyte secretion by regulating cGMP signalling in neighbouring cells [170] and absorption of heavy metals [37], but direct experimental evidence for these BEST4/CA7^{+} cell functions is still lacking.

Table 1.1: Summary of intestinal epithelial cell types, their lineages, locations, abundances, markers, and turnover times (in mouse) models. *Based on Notch signalling. [†]BEST4/CA7^{+} cells exist in human, but not the mouse intestine. [‡]Abundances of all cell types can differ strongly during infections; values shown here assume normal healthy conditions. Abbreviations: LI, large intestine; SI, small intestine; FAE, follicle-associated epithelium.

Cell type	Lineage*	Location	Abundance[‡]	Markers	Turnover time (mouse)
Lgr5^{+} stem cells	-	Crypt bottom	12–26 per crypt [9, 248]	Lgr5 [14], Olfm4 [266]	12–24 h [14, 115]
Paneth cells	Secretory	Crypt bottom	4–6% [14, 95]	Lyz, Defa5	57 days [117]
Enterocyte	Absorptive	SI villus, FAE and LI	90% [14]	Aldob, Fabp1	3–5 days [52]
Goblet cells	Secretory	SI villus, LI	4–12% [41, 83]	Muc2	3 days [41]
EECs	Secretory	SI and LI	4% [95]	Neurog3, Pax4, ChgA	10–23 days [256, 260]
Tuft cells	Secretory	SI villus and LI	0.4–2% [83, 95, 112, 275]	Dclk1 [82], Chat	7 days [83]
M cells	Absorptive	FAE	5–10% of FAE [47, 135]	Gp2 [100], Tnfaip2 [102]	5 days [140]
BEST4/CA7^{+} cells	Absorptive	SI villus and LI	1% [247]	BEST4, CA7, OTOP2 [37, 69, 70]	N/A[†]

1.2 Classification of the intestinal cell types

Traditionally, the cell types in the intestinal epithelium have been classified as either absorptive or secretory, based on whether their primary function involves the absorption of nutrients (enterocytes), or the secretion of mucus (goblet cells), antimicrobial peptides and growth factors (Paneth cells) or hormones (enteroendocrine cells) [23]. Active Notch signalling is commonly used as a marker to separate absorptive from secretory cells, since enterocytes have active Notch signalling, whereas goblet, Paneth and enteroendocrine cells do not [78]. Arguably, however, it generalizes poorly to the rare intestinal cell types (tuft cells, M cells and BEST4/CA7^{+} cells). While these cell types can be attributed to either lineage based on their Notch signalling state (Table 1.1), their function is neither clearly absorptive nor secretory. Tuft cells, for example, are Notch-negative and commonly

1

included in the secretory lineage, but their primary functions include both the secretion (of IL-25), as well as chemoreception. M cells are Notch-positive and commonly included in the absorptive lineage, but their primary function is to absorb luminal antigens at the apical side and secrete them on the basal side. Furthermore, M cells are also known to secrete Gp2 on the apical side [100]. BEST4/CA7$^+$ cells are also Notch-positive and included in the absorptive lineage. While their function is not well understood, their expression profile differs too much from that of enterocytes to justify the assumption that their primary function is the absorption of nutrients [37, 38, 69, 70, 205, 247]. For these reasons, I propose a slightly modified classification that distinguishes cells on the basis of their Notch-signalling state, as well as the expression of the transcription factor Spib (Table 1.3).

Table 1.3: Proposed classification of intestinal cell types on the basis of both Notch signalling and Spib expression.

	Notch$^+$	Notch$^-$
Spib$^+$	M cells BEST4/CA7$^+$ cells	Tuft cells
Spib$^-$	Enterocytes	Goblet cells EECs Paneth cells

1.3 Modern approaches for studying the intestinal epithelium

Approaches to understand the intestinal epithelium can be divided into two complementary approaches. First, there are approaches focusing on the internal molecular state of cells, colloquially known as "Omics" approaches. These include analysis of the genome (genomics), epigenome (epigenomics), gene expression (transcriptomics), protein levels (proteomics), small molecule content (metabolomics), lipid content (lipidomics), glycan content (glycomics), and the microbiome (microbiomics), and combinations thereof within a single pipeline (multi-omics). The last decades have seen a spectacular improvement in techniques that can be used to gather information on the internal molecular state of entire organs and organisms with single-cell resolution. Especially single-cell RNA sequencing has proven very powerful in mapping the diversity of cell types in the intestinal epithelium, allowing the generation of multiple large databases ("atlases") of transcriptomes [24, 37, 69, 70, 95, 201]. Clustering cells based on their transcriptomic profile has in large part confirmed the existence of distinct cell types [69, 70, 95, 205, 247], as well as regional differences and variation between cells of the same type [22, 24, 47, 186, 201] (Fig. 1.4). Because Omics-approaches inherently require cell lysis, they only yield a snapshot of cells at a given point in time and preclude analysis of dynamics within a cell. Despite ongoing efforts to obtain temporal information from Omics-approaches such as RNA velocity [152], trajectory inference [230] and Chrono-reporters [81], a persistent main disadvantage of Omics-approaches remains the lack of dynamics.

1

To study the intestinal epithelium in space and time, omics-approaches need to be complemented with imaging. Brightfield microscopy, fluorescence microscopy, scanning and transmission electron microscopy are routinely employed to study the intestinal epithelium in space, but to study the intestinal epithelium over time is still highly complex. Live-imaging approaches are ill-suited for studying the intestinal epithelium in vivo, because intravital microscopy is only possible in model organisms and at low time resolution [223]. For this reason, studying the intestinal epithelium over time requires in vitro culture systems: enter intestinal organoids.
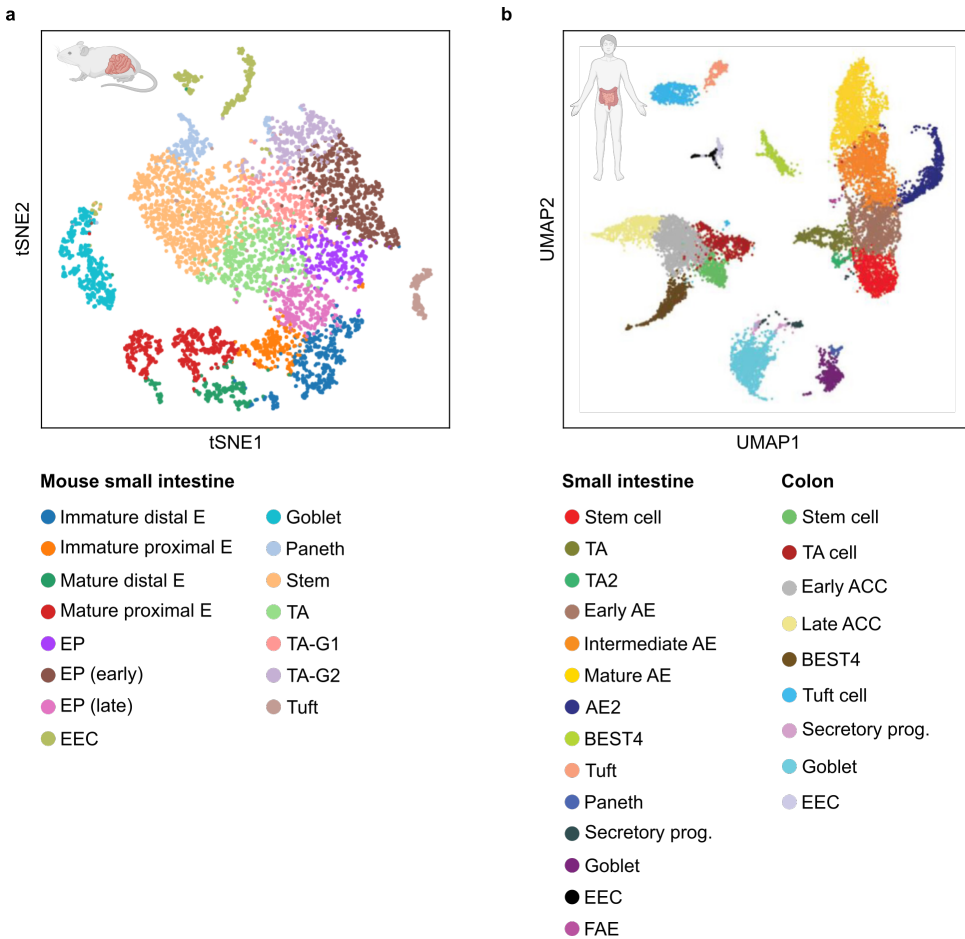
Figure 1.4: Uniform manifold projection (UMAP) of murine and human gut epithelium. (a) UMAP plot of scRNA sequencing of the mouse small intestinal epithelium, adapted from ref. [95]. (b) tSNE plot of scRNA sequencing of the human intestinal epithelium, adapted from ref. [37]. ACC, absorptive colonocyte; AE, absorptive enterocyte; E, enterocyte; EP, enterocyte progenitor; EEC, enteroendocrine cell; FAE, follicle-associated epithelium; TA, transit-amplifying cell (G1 and G2 indicate the cell-cycle phase).

1

1.4 The organoid revolution

In 2009, researchers in the group of Hans Clevers made a discovery that changed the course of intestinal biology. When they embedded mouse small intestinal Lgr5$^+$ stem cells in extracellular matrix, a very small fraction would grow into structures that were similar to the in vivo intestinal epithelium [235]. These structures, which they coined "intestinal organoids", started out as little spherical clumps of stem cells, but grew crypt-like protrusions within days (Fig. 1.5a, b). The only four requirements to grow and culture intestinal organoids, were a laminin-rich gel (e.g., Matrigel or Basement Membrane Extract) and external supply of epidermal growth factor (EGF), Noggin and Wnt agonist R-spondin. It was furthermore found that if small intestinal Lgr5$^+$ stem cells were still attached to Paneth cells, the organoid formation efficiency was strongly increased [234]. Like crypts in vivo, organoid crypts were shown to contain Lgr5$^+$ stem cells and Paneth cells at the bottom, regions with undifferentiated TA-like cells, and villus-like regions with enterocytes, goblet cells, enteroendocrine cells [235] and sporadically also tuft cells [112] (Fig. 1.5c-g). Intestinal organoids were later shown to contain M cells upon stimulation with the cytokine RankL (Fig. 1.5h) [57]. Within years after the initial discovery of small intestinal organoids, organoid culturing systems were developed for many other organs [45], albeit that for many organoid systems the medium needs to be supplemented with additional components. For example, mouse colon organoids could similarly be generated from (colonic) Lgr5$^+$ stem cells, but only if Wnt3A was supplied to the medium [233]. It was shown that human intestinal organoids can be generated using similar procedures (Fig. 1.5i) [104, 233].

For the purpose of this thesis, I wish to draw a distinction between *homeostatic* organoid models, and *synchronous* organoid models. Homeostatic organoids recapitulate the in vivo crypt architecture and have the feature that a cell's position in space correlates strongly with the cell's state along the differentiation trajectory (Fig. 1.6a). The most obvious and widely used example of a homeostatic organoid system is the mouse small intestinal organoid, in which crypts, TA-like and villus domains and almost all cell types differentiate spontaneously in a single "ENR" medium^3 [235]. For human and rat intestinal organoids, medium was developed that supported the long-term co-culturing of stem cells and all cell types [80, 210], but this medium typically does not consistently produce 3D organoids with clearly distinct crypt and villus domains. For this reason, substrates and microfluidic chips with multiple channels have recently been developed to generate homeostatic human organoids with the same 3D architecture as the in vivo intestine [31, 86, 161, 162, 184, 196]. One constraint on homeostatic organoid models is that the environment (cell culture medium) around the cells is homogeneous and they lack a clear "time-zero" for when differentiation starts. Synchronous organoid models are models where cells are first expanded in an "expansion medium" that keeps all cells in a proliferative and undifferentiated state, before the medium is replaced with a "differentiation medium" that biases cells towards differentiation (Fig. 1.6b) [114, 278]. For this reason, synchronous organoids have a well-defined start of the differentiation process that is suited to determine the temporal order of events during the differentiation process. Synchronous organoid models can also have multiple medium changes, for example to induce Paneth cell differentiation and

---

^{3}This medium is referred to as ENR medium because it contains the proteins <u>E</u>GF, <u>N</u>oggin and <u>R</u>-spondin. However, the medium is typically also supplemented with N-Acetyl-L-Cysteine (NAC), and supplements N2 and B27.

crypt-formation [104], or mimic different regions along the villus by changing BMP and Noggin concentrations [22, 25].
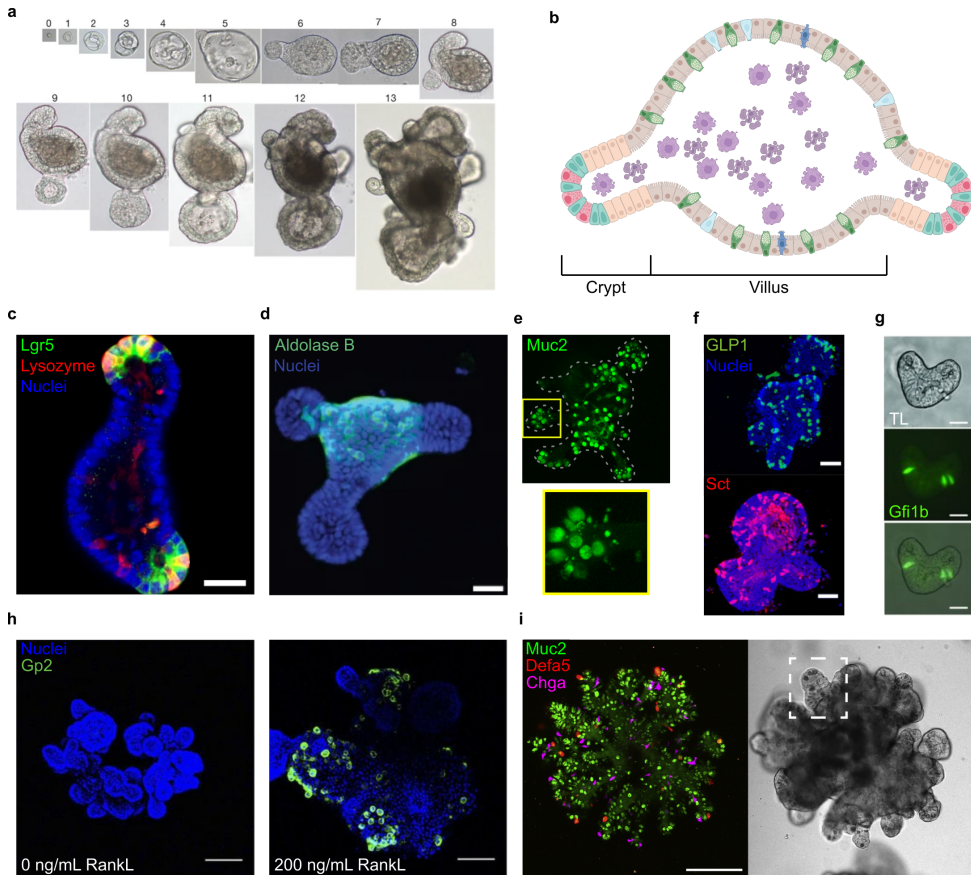

Figure 1.5: Intestinal organoids are accurate, accessible in vitro models of the intestinal epithelium. (a) Transmitted light images of the development of mouse small intestinal organoid from a single Lgr5$^+$ stem cell. From ref. [235]. (b) Schematic of intestinal organoid, made using Biorender. (c) Paneth and Lgr5$^+$ stem cells in an organoid crypt. From ref. [242]. (d) Enterocytes, marked by Aldolase B, in the organoid villus. From ref. [242]. (e) Goblet cells, marked by Muc2. From ref. [64]. (f) Organoids in top panel were grown in EEC enrichment medium (ENR with Wnt, MAPK and Notch inhibitors), which enriches for EECs subtypes typically found in the crypt, such as the L cells that secrete Glp1. Organoids in bottom panel were cultured in medium where Noggin was replaced with BMP-4 to enrich for the secretin (Sct) secreting "S" subtype typically found in the villus. From ref. [22]. (g) Tuft cells in organoids from mice with fluorescently tagged Gfi1b. From ref. [112]. (h) Addition of RankL to the culture medium induces M cell differentiation in mouse intestinal organoids. From ref. [134]. (i) Human intestinal organoids with fluorescent reporters for Muc2, Defa5 and Chga. Paneth cell differentiation was induced by adding IL-22. From ref. [104]. Scale bars in panel c represents 40 µm; scale bar in panels d, g represents 25 µm; scale bars in panel f and i represent 50 µm; scale bars in panel h represent 100 µm.

Organoids are revolutionary for three important reasons. The first and most obvious advantage of organoids is that they allow to study the donor's intestinal biology while the donor remains alive. Many experiments that previously required sacrifice of lab animals

1

have been replaced by assays of intestinal organoids. The second is that they are accessible for long-term high-resolution live-cell imaging with perturbations. The third is that they can be genetically manipulated, for example using CRISPR-Cas [6, 239] or lentiviral transduction. This makes it possible to study the effect of knocking out proteins of interest, or to make fluorescent reporter proteins. These advantages now allow investigation of the (human) intestinal biology in ways that were previously impossible.

In the past decades, organoids have contributed to a large number of discoveries on how the intestine works, specifically because they allow long-term live-cell microscopy of intestinal epithelial cells in real time. For example, it was shown that the crypt-villus symmetry breaking is a spontaneous process that starts after the first Paneth cell differentiates [242]. The subsequent mechanical crypt folding was also mapped, by mapping the distribution and dynamics of forces generated by cells on each other and on the hydrogel [208, 287]. Long-term tracking of intestinal organoids led to the discovery that sister cells either both differentiate, or both remain proliferative [115], likely to minimize fluctuations [144]. Furthermore, sister pairs that both differentiate typically do so into the same cell type [291]. These two examples of 'sister-symmetries' imply that the proliferative state of cells and cell fate decisions are controlled by cells one or more generations earlier. In conclusion, the organoid revolution has made it possible to directly visualize dynamic processes in the intestinal epithelium, such as proliferation, differentiation and protein expression, in real time.
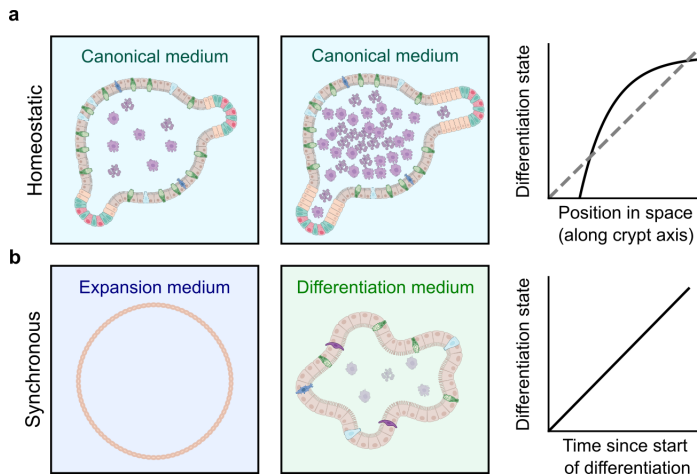
Figure 1.6: Homeostatic versus synchronous organoid models. (a) Homeostatic organoid models are organoid models in which the spatial crypt-villus axis is modeled in vitro. The defining feature of these organoid models is that the differentiation state of cells in homeostatic organoid models correlates with their position in space, but that there is no absolute "time zero". (b) Synchronous organoid models are organoid models where cells are kept in multipotent, proliferative state (expansion phase) until differentiation is induced in all cells simultaneously. Synchronous organoid models therefore have a well-defined "time zero" for when differentiation starts.

1.5 THIS THESIS

Thesis is fundamentally concerned with how the intestinal epithelium maintains its barrier function over time. **Part I** of this thesis contains several chapters that yield new insights into this key question. In **Chapter 2**, we propose a new model for how the intestinal epithelium manages to retain a homeostatic physical barrier between the hostile lumen and delicate underlying tissue during cell extrusion events. In **Chapter 3**, we use live-cell imaging of organoids with a reporter for Wnt signalling to show that loss of Paneth cell contact starts a timer by which Lgr5$^+$ stem cells differentiate. In **Chapter 4**, we look at the differentiation and function of BEST4/CA7$^+$ cells in a synchronous human colon organoid model with live-cell reporters for goblet and BEST4/CA7$^+$ cells. Herein, we reveal that BEST4/CA7$^+$ cells and goblet cells have an inter-dependent relationship in the human intestinal epithelium. In **Part II**, we focus on methodology, presenting a new in silico labelling approach for 3D organoids in **Chapter 5**. Finally, in **Chapter 6**, we share protocols for long-term live-cell imaging of intestinal organoids with experimental perturbations and endpoint analysis.

PART I

THE INTESTINAL BARRIER IN SPACE AND TIME

2

Epithelial tension controls intestinal cell extrusion

> You got to know when to hold 'm,
> know when to fold them.
> Know when to walk away,
> know when to run.

The Gambler

Cell extrusion is essential for homeostatic self-renewal of the intestinal epithelium. Extrusion is thought to be triggered by crowding-induced compression of cells at the intestinal villus tip. Here we found instead that a local "tug-of-war" competition between contractile cells regulated extrusion in the intestinal epithelium. We combined quantitative live microscopy, optogenetic induction of tissue tension, genetic perturbation of Myosin-II activity, and local disruption of the basal cortex in mouse intestines and intestinal organoids. These approaches revealed that a dynamic actomyosin network generates tension throughout the intestinal villi, including the villus tip region. Mechanically weak cells unable to maintain this tension underwent extrusion. Thus, epithelial barrier integrity depends on intercellular mechanics.

2.1 Introduction

The intestinal epithelium is a defensive barrier protecting the underlying tissue from micro-biota, pathogens, and acidity. The turnover of cells within the intestinal epithelium is rapid, and most cells are replaced within a few days [13, 52]. Stem cells are generated in the crypt, and then migrate upwards to the tissue protrusions called villi [149] as they differentiate and acquire specialized function [14, 236]. After several days, mature cells are extruded in a controlled manner into the gut lumen [86, 233, 235]. The mechanisms regulating cell extrusion in the intestine are not well understood [50], and current models are largely inferred from non-mammalian model organisms and systems. Apoptotic cell extrusion has been demonstrated to regulate cell numbers in cell lines, Drosophila [2], and the zebrafish epidermis [67, 90]. However, mouse intestines with genetic knockouts of key apoptotic pathway components such as Bcl-2, Bax, Bcl-w, and Caspase-3/7/8 display normal villus morphology, indicating a normal regulation of homeostatic cell extrusion [85, 92, 213, 214]. In Madin-Darby canine kidney (MDCK) monolayers [68], zebrafish epidermis [68] and the Drosophila notum [156, 171], extrusion is driven by increased cell density. These findings have inspired a model for the mammalian intestinal epithelium, in which the flow of cells to the villus causes cell crowding. In that model, compression forces at the villus tip would trigger extrusion (see refs. [209] and [111] for recent reviews). However, cell extrusion is enriched at - but not limited to - the villus tip: the frequency of cell extrusion gradually increases along the villus shaft, and peaks at the villus tip [36, 283]. However, cell density is high in the crypt and at the villus base, lower along the villus shaft, and returns to villus-base levels at the villus tip [149]. Thus, crowding alone seems insufficient to explain the extrusion pattern.

Previous work suggests that active cell migration along the villus leads to cell crowding at the villus tip, while leaving the villus bottom under tension, as indicated by laser ablation experiments [149]. Cell contractility and mechanical forces have been implicated in the regulation of cell extrusion or delamination in other epithelial systems. For example, induction of Rho kinase - an upstream regulator of Myosin II - reduces extrusion in the Drosophila notum and zebrafish epidermis [7, 51, 293]. In the Drosophila abdominal epidermis, extrusion is associated with pulsatile actomyosin contractions, and extrusion frequency increases under conditions of elevated tensile stress [183]. In contrast, elevated cortical tension inhibits the apical extrusion of oncogenic H-RasV12 cells in liver epithelial monolayers [254]. Thus, the role of mechanical force is important for cell extrusion and depends on the tissue context but has remained largely unaddressed in the intestinal villi.

2.2 Results

Cells extrude from regions under tension in a crowding-independent manner

Mouse intestinal organoids faithfully recapitulate the self-renewal processes of the gut epithelium [235]. At the tips of organoid buds (the equivalents of the Crypts of Lieberkühn), Lgr5^{+} stem cells are interspersed between Paneth cells, the latter serving as a source of niche signals. Daughter cells rapidly proliferate and move away from the buds towards a central villus domain. As they reach the villus domain, the cells differentiate into one

of the mature intestinal epithelial cell types, the most abundant being the enterocyte. To establish an experimental platform for mechanistic studies of cell extrusion process, we developed a method to quantify the localization of the cell extrusion events. We imaged mouse intestinal organoids expressing an H2B-mCherry nuclear marker over multiple days. Using a neural network approach [143], we tracked single cells and identified hundreds of extruding cells (Fig. 2.1a, b). We observed two distinct extrusion modes: one showed fragmented nuclei prior to extrusion, indicative of extrusion driven by apoptosis; the other showed extrusion with intact nuclei, indicating a live-cell process (Fig. 2.1c, d & Fig. 2.8a). Apoptotic cell extrusion was the predominant form in the stem cell-containing crypt region, where, under physiological in vivo conditions, cell extrusion is typically rare. However, the vast majority (92%) of extrusions in the villus-like region were live-cell extrusions (Fig. 2.1e & Fig. 2.8b). Next, we tested if cell extrusion was determined by an intrinsic timer set before the last division [115]. The lifetime of cells - defined as the period between the last division and extrusion - showed major differences for apoptotic and live-cell extrusion. The median lifetime of apoptotic cells was short (6 h) and similar between sister cells: cells had an 82% chance of extruding in apoptotic manner if their sister also did so (Fig. 2.8c). Thus, apoptotic cell extrusion appears to result from fatal errors in the mother's cell cycle or during mitosis [157]. The lifetimes of cells undergoing live-cell extrusion were broadly distributed, with a median of 27 hours (Fig. 2.1f & Fig. 2.8d, e). The lifetime of one sister cell undergoing live-cell extrusion poorly predicted the lifetime of the second sister (Fig. 2.8f). Conclusively, live cell extrusion is not controlled by a timer set prior to the cell's birth.

To test whether tissue crowding triggers live-cell extrusion in the intestinal epithelium, we analyzed the positions of extrusion events and the local cell density by tracking nuclei. Nuclei of neighbors of extruding cells initially moved away from the extruding cell and returned directly after extrusion so that the local cell density recovered to pre-extrusion levels within approximately 45 minutes (Fig. 2.8g, h). Furthermore, cell extrusion events were spatially and temporally correlated; cells tended to extrude close to each other and shortly after a nearby cell had extruded, typically when cells from different crypts came into contact (Fig. 2.8i-l). Notably, extrusions were not concentrated in regions of high cell density. Instead, cells showed a tendency to extrude from areas of average - or low - cell density within the villus-like domain (Fig. 2.1g, h). Thus, cell extrusion in intestinal organoids is not primarily driven by tissue crowding.
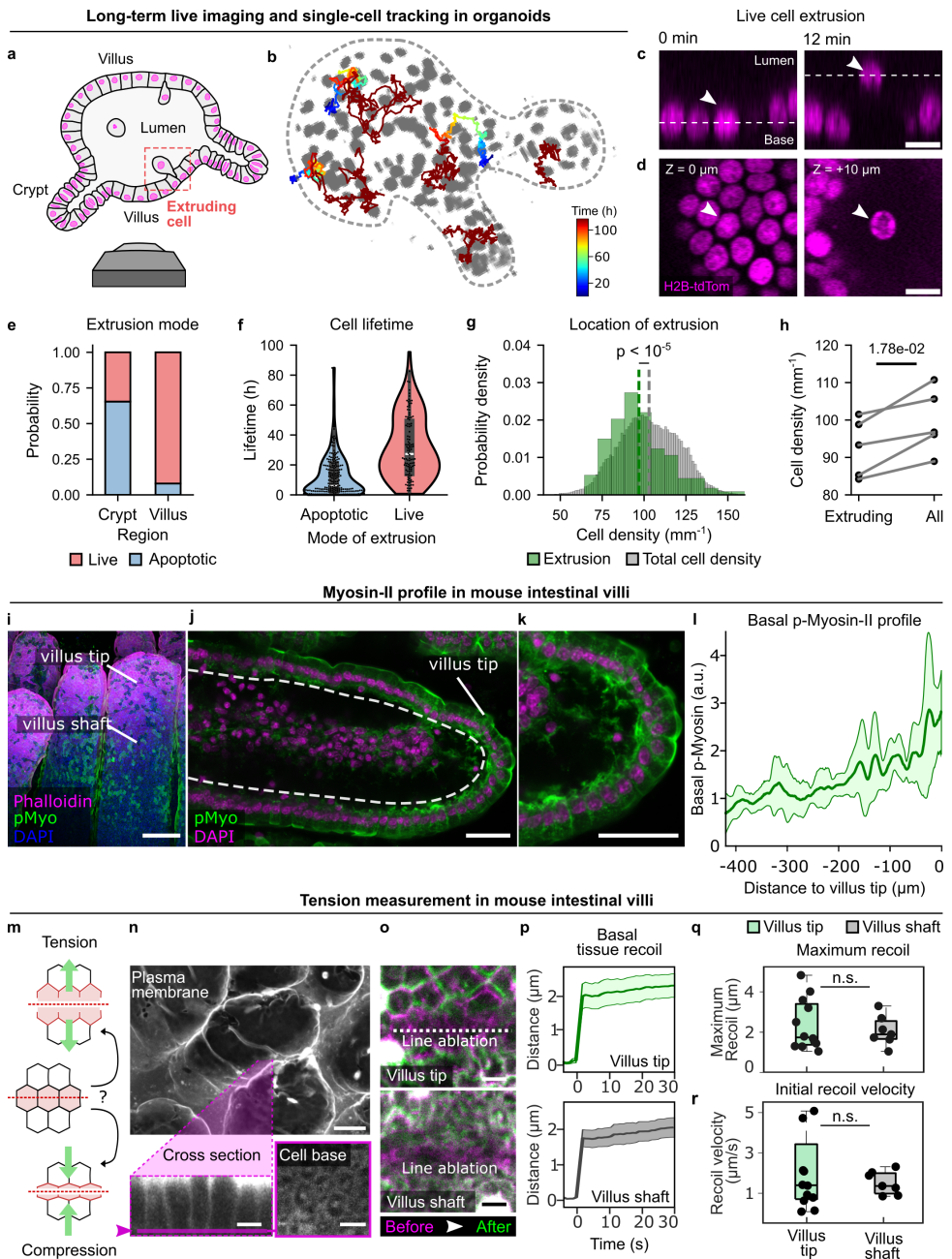
Figure 2.1: Intestinal live-cell extrusion occurs predominantly from regions under tension. (a) Live imaging and single-cell tracking of nuclear-labeled intestinal organoids. (b) Time-colored tracks overlaid on a tracked organoid. (c, d) Cross-section (c) and top-view (d) of a live-cell extrusion, defined by the presence of an unfragmented nucleus at its final timepoint in the epithelium. Arrow heads indicate the extruding cell. Scale bars: 10 μm. (e) Proportions of apoptotic and live-cell extrusions in villus and crypt. (f) Lifetime distribution of 217 apoptotically and 114 live extruding cells.

Figure 2.1: (continued) (g) Cell density around 142 extruding cells (green) and non-extruding cells from N = 5 organoids (Mann-Whitney U test on individual densities). Cell density was defined as the reciprocal of the average distance to the six nearest neighbors. Binning is for visualization only. (h) Average cell density of extruding and non-extruding per organoid (N = 5 organoids; two-sided one-sample Student's t-test). (i-k) Whole-mount stain of mouse intestinal villi. (i) Overview showing F-actin (phalloidin, magenta), active Myosin-II (pMyo, green) and nuclei (DAPI, blue). Scale bar: 100 µm. (j) Cross-section of an intestinal villus stained for pMyo (green) and nuclei (magenta). Dashed line marks the basal surface. (k) Zoom of villus tip in (j). (l) Basal Myosin-II profile along the villus (mean ± SD; N = 6 villi). (j, k) Scale bar: 25 µm. (m) Schematic: line cut reveals tension by recoil, compression by condensation. (n) Dissected mouse intestine stained with membrane marker (CellMask-Orange). Top: overview of villi. Bottom left: villus cross-section with magenta line marking the basal plane, shown in the bottom right. Line ablation was performed at this basal section. Scale bars: 50 µm (top), 10 µm (bottom). (o) Line ablation (dashed line) at the villus tip (top) and shaft (bottom). Magenta shows the basal surface before, green after ablation. Scale bars: 10 µm. (p) Orthogonal recoil after basal line ablation at the villus tip (left) and shaft (right). Bold lines: mean; shaded areas: S.E.M. (q, r) Maximum recoil (q) and initial velocity (r) after basal ablation at villus tip and shaft (two-sided Student's t-test). (p-r) Data from 12 villus tips, 7 villus shafts (N = 3 mice).

These findings prompted us to investigate whether alternative mechanisms involving mechanical forces underlie cell extrusion. We examined the actomyosin network along the intestinal villus by staining whole-mount mouse intestines for active (phosphorylated) Myosin-II, the primary force-generating motor protein. We observed a pronounced accumulation of Myosin-II at the basal surface of villus cells, which increased from the base to the tip (Fig. 2.1i-l & Fig. 2.9a-d). This Myosin-II accumulation suggested the generation of tensile forces, prompting us to question whether compression forces prevail at the villus tip.

To test if the intestinal epithelium at the villus tip was under tension or compression in vivo, we dissected small intestines from wild-type mice and immediately afterwards applied line-shaped laser ablations at different regions of the villus: If the tissue were under tension, one would expect an outward retraction orthogonal to the cut line, whereas a compressed tissue would shrink or remain static (Fig. 2.1m). In one set of experiments, we ablated the basal surface of a lateral group of 6-10 adjacent cells using a line cut spanning ~60 µm (Fig. 2.9e, f) - sizeable enough to integrate the response of multiple cells, yet within the geometric constraints imposed by the villus curvature [28]. These cuts were performed both at the villus shaft and at the villus tip region. Upon ablation at the basal surface, we observed a rapid outward tissue recoil orthogonal to the ablation line in both regions (Fig. 2.1n-p, Fig. 2.9f) with a similar maximum recoil and initial recoil velocity of approximately 1.4 µm/s (Fig. 2.1q, r). In another setup, we ablated entire single cells along their apical-basal axis at the villus tip, rather than cutting only their basal surface. Here too, neighboring cells consistently retracted away from the ablated cell (Fig. 2.9g-j). Thus, the mouse villus tip, the main region of cell extrusion, is under tension rather than compression.

A HIGHLY DYNAMIC ACTOMYOSIN NETWORK UNDERLIES BASAL TISSUE TENSION.

Given the above findings and the known cytoskeletal remodeling required for cell extrusion, we hypothesized that local tensile tissue forces could play a role in its regulation. We generated intestinal organoid reporter lines for Myosin-II by integrating a fluorescent tag (mNeonGreen) in the endogenous locus of different subunits of the Myosin-II multiprotein complex (Fig. 2.2a, b & Fig. 2.10a-d). The reporter targeting myosin regulatory light

chain (*Myl12a*) co-localized strongly with antibodies for active (phosphorylated) Myosin-II (Fig. 2.10e, f). It was also enriched at sites of actomyosin contraction, for example at the cytokinetic furrow during cell division (Fig. 2.10g). During cell extrusion, Myosin-II rapidly increased at the cell base and redistributed in a zipper-like pattern along the lateral surface towards the apex, before the cell was expelled apically into the organoid lumen (Fig. 2.2c, Fig. 2.10h). This suggests that Myosin-II-mediated contraction exerts the force necessary to extrude a cell into the lumen.
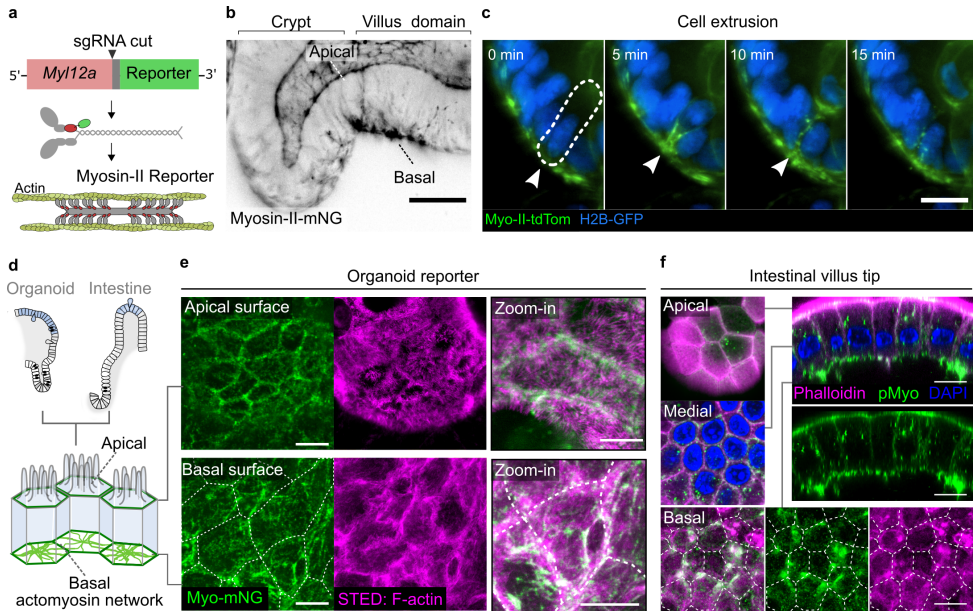
Figure 2.2: A basal actomyosin network connects intestinal epithelial cells. (a) Generation of fluorescent reporter organoid line for Myosin-II activity. The endogenous myosin regulatory light chain gene *Myl12a* was tagged with a fluorescent fusion protein (mNeonGreen). (b) Myosin-II-mNeonGreen reporter organoid showing Myosin-II enrichment at the basal surface in the villus-like domain. (c) Time-lapse of an extruding cell in an organoid co-expressing Myosin-II-tdTomato (green) and H2B-GFP (blue). Dashed line marks the cell just before extrusion. Scale bar: 20 μm; imaged using light-sheet microscopy. (d) Schematic of cells in the villus region of intestinal organoids and in vivo villus tips (light blue). The apical surface facing the lumen features actin-rich microvilli and a cortical cytoskeleton lining the plasma membrane. (e, f) The basal actomyosin network (green) connects cells through junctions. (e) Super-resolution STED microscopy images of the apical (top row) and basal (bottom row) actomyosin network stained for F-actin (phalloidin, magenta, middle), in an organoid expressing Myosin-II-mNeonGreen (green, left). The right images show a zoom-in of a single cell with superimposed actin and myosin signals. Scale bars: 10 μm (left); 5 μm (zoom-ins). (f) High-resolution confocal images of cells of the mouse intestinal villus tip with top views of the apical (top), medial (middle) and basal (bottom) section and cross-sections of the entire cell (right) stained for F-actin (phalloidin, magenta), phosphorylated myosin (green) and nuclei (DAPI, blue). Scale bars: 5 μm. Dashed lines in (e, f) indicate the cell boundaries.

The Myosin-II intensity profile along the organoid's crypt-villus axis showed a strong apical signal in the crypt region, diminishing towards the villus domain [208, 287] (Fig. 2.10i, j). Conversely, basal Myosin-II exhibited its highest intensity in the villus region, both in organoids and in tissue (Fig. 2.1l & Fig. 2.10i, j). Stimulated emission depletion (STED) super-resolution microscopy identified two distinct Myosin-II localization patterns: a junctional pool, which lined the cell boundaries and predominated the apical surface; and a medial pool where Myosin-II coalesced in the cell center and extended radially to cell-cell junctions, predominantly found at the basal cell surface in the villus domain (Fig. 2.2d, e). The overlap of medial and junctional Myosin-II at the basal surface creates an interconnected actomyosin network, similar to those facilitating coordinated cell movements in other epithelial tissues [18, 211]. We confirmed that this organization was also prevalent in vivo throughout the intestinal villi, both in the shaft region and at the villus tip (Fig. 2.2f & Fig. 2.10k). The prominent basal enrichment of both medial and junctional Myosin-II suggests a network capable of generating tissue tension through coordinated contractions [173, 253].

To reconstruct the force-transmission between cells in an in vivo-like fashion, we grew Myosin-II reporter organoids on 3D hydrogel substrates that closely mimic the tissue architecture of the intestine (Fig. 2.3a & Fig. 2.10l) [86]. Live-cell imaging of the synthetic villus tip showed dynamic basal myosin-II remodeling, revealing a pulsatile reorganization of the actomyosin network on the basal surface of the intestinal epithelium (Fig. 2.3b-f, Fig. 2.11a-e). With our earlier data, this suggested that while the tissue is permanently under tension, individual cells' contractility dynamically changes. This is reflected in transient Myosin-II accumulation that was accompanied by a concomitant decrease of basal cell area presumably owing to the Myosin-II-mediated pulling forces (Fig. 2.3c-f & Fig. 2.11a-e). Conversely, basal expansion was accompanied by decreasing Myosin-II levels, and Myosin-II minima coincided with an increase of basal area. (Fig. 2.3c-f & Fig. 2.11a-e). Pulsatile actomyosin networks have been described in other epithelia to coordinate cellular rearrangements such as the inward folding of a tissue [173, 253] or delamination of individual cells [4]. These dynamics allow cells to continuously interact with their neighbors, probe the environment, and enable tissue-level coordination [40, 253]. Such tissue-level coordination was evident in the inverse relationship between the cell areas of neighboring cells: when a central cell constricted, its neighbors expanded (Fig. 2.11f, h). Thus, cells in the villus region dynamically regulate Myosin-II, driving pulsatile basal area changes. Through mechanical coupling via cell junctions, Myosin-II-generated forces appear to propagate to adjacent cells, orchestrating a tissue-wide tug-of-war.
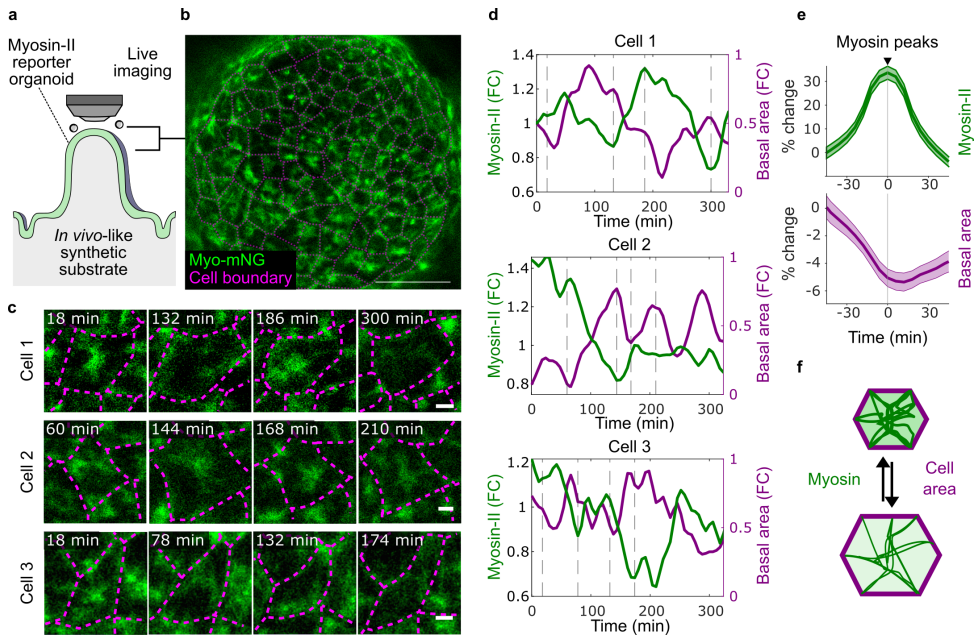
2

Figure 2.3: Intestinal epithelial cells use their basal cytoskeleton to exert highly dynamic pulling forces on their neighbors. (a) Experimental setup to analyze basal cell dynamics at the villus domain using crypt-villus substrates mimicking the in vivo tissue architecture. (b, c) The myosin reporter line co-expressing a membrane-bound mCherry fluorescent marker was grown on crypt-villus substrates and the tip region was imaged using confocal microscopy. Segmented membranes (magenta) were overlaid with the myosin signal (green). (b) Synthetic villus tip. Scale bar: 50 µm. (c) Time-lapse showing the accumulation and dissipation of Myosin-II in cells causing basal cell area pulsations. Scale bar: 5 µm. (d) Mean Myosin-II signal (green, left axis) and corresponding basal cell area (magenta, right axis) of three cells indicated in panel (c). Gray vertical lines indicate the respective timepoints of the micrographs in panel (c). (e) Time-aligned mean traces of Myosin-II peaks (top) reveals a concurrent decrease in basal cell area (bottom). Solid lines indicate mean fold change and shaded area the S.E.M. (f) Schematic illustrating the observed anticorrelation between basal Myosin-II and basal area.

Cell extrusion is regulated by a cell's ability to exert tissue tension

To determine whether tissue tension generated by basal actomyosin contractions has a role in regulating cell extrusion, we established an optogenetic method to control Myosin-II-mediated contractility, and thereby tissue tension, in intestinal organoids. We integrated a doxycycline-inducible optogenetic system called opto-Arhgef11 [263] into intestinal organoids. Opto-Arhgef11 is based on the light-dependent heterodimerization of the photosensor CRY2, fused to the small RhoGTPase Arhgef11, and its interaction partner CIBN, which is anchored at the plasma membrane (Fig. 2.4a). Arhgef11-CRY2 remained cytoplasmic and inactive in the dark, but rapidly translocated to the plasma membrane upon blue light excitation (Fig. 2.4b). On the membrane it initiated the endogenous Rho signaling cascade, which triggers Myosin-II-induced cell contractility and increases tissue tension. Indeed, local photoactivation caused a focused contraction of the organoid, which relaxed

again owing to the dissociation of CRY2-CIBN in the absence of blue light (Fig. 2.4c). Staining uniformly photoactivated opto-Arhgef11 organoids for phosphorylated Myosin-II revealed a ~1.7-fold overall increase in active Myosin-II levels, with minimal impact on its subcellular distribution (Fig. 2.12a-c).

To test the impact of Myosin-II activity on cell extrusion systematically, we grew opto-Arhgef11 organoid cells on synthetic 3D hydrogel substrates and measured the rate of extrusion at the villus tip (Fig. 2.4d & Fig. 2.11c). Continuous global photoactivation led to increased tissue tension compared to non-activated villi (Fig. 2.12d-f) and resulted in a 5-fold increase in the average extrusion rate (Fig. 2.4e & Fig. 2.12g-j). The increase of extrusion rates upon photoactivation was dependent on the addition of doxycycline, confirming that it was not caused by phototoxicity (Fig. 2.12g). The extrusion rate increased readily upon photoactivation, directly following the overall increase of tissue tension. This suggested a link between the tension exerted by cells on their neighbors and extrusion. To test the effect of contractility differences between neighboring cells, we photoactivated one half of the optogenetic villus tip, creating an artificial boundary between Myosin-induced and non-induced cells (Fig. 2.4f, g). Cell extrusion was increased locally along the boundary of photoactivation (Fig. 2.4h-k). Cells most frequently extruded in the non-activated area facing the boundary with the photoactivated area, while cells adjacent to the boundary in the photoactivated region extruded less frequently in comparison (Fig. 2.4j). Extrusion events were evenly distributed along the photoactivation boundary, indicating that the effect was specific to the illumination pattern (Fig. 2.4k). Thus, individual cells with lower contractile capabilities compared to the surrounding tissue appear to be more prone to extrusion.
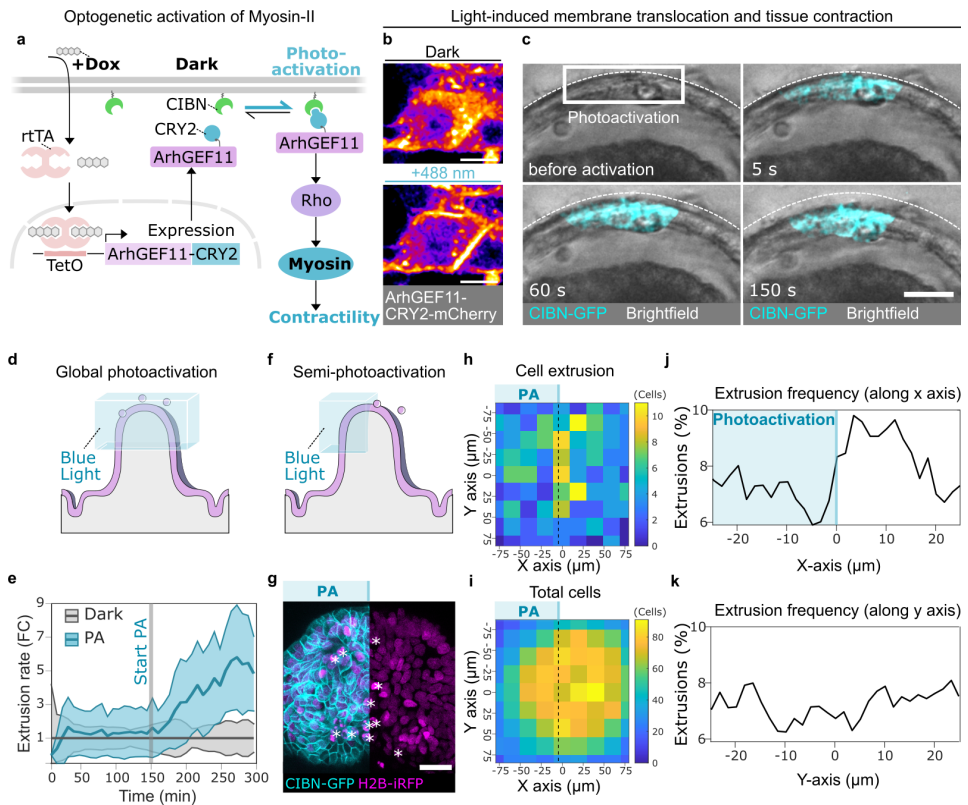
Figure 2.4: Differences in intercellular tension influence cell extrusion at the villus tip. (a) Schematic of the Arhgef11-CRY2 optogenetic system. Doxycycline (Dox) induces Arhgef11-CRY2 expression via rtTA (TetON). Blue light triggers its dimerization with membrane-bound CIBN, causing Arhgef11 translocation to the membrane, activation of Rho signaling, and increased myosin-driven contractility. (b) Arhgef11-CRY2-mCherry was recruited to the membrane upon photoactivation with 488 nm light. Scale bar: 10 μm. (c) A group of cells in an opto-Arhgef11 organoid was photoactivated with 488 nm light, inducing contraction. Membrane-anchored CIBN-GFP visible in the photoactivated region (blue). Scale bar: 50 μm. (d) Setup to assess acute, global myosin activation: opto-Arhgef11 organoids on crypt-villus substrates were photoactivated at the tip (488 nm). Extrusion was tracked via H2B-iRFP. (e) Cell extrusion rates over time in non-photoactivated (gray) and photoactivated (blue) synthetic villi. Villi were imaged with 640 nm before 488 nm photoactivation (vertical line), which triggered up to a 5-fold increase. Rates are shown as fold change (FC) relative to dark control (mean ± standard deviation; 19 dark, 13 photoactivated villi). (f-k) Patterned activation of myosin-mediated tension: one half of synthetic villus tips was photoactivated (PA, blue) to create an artificial boundary between myosin-activated and non-activated cells (N = 24 villi). (f) Schematic illustrating the setup. (g) Confocal image of a villus tip with cells co-expressing opto-Arhgef11 (CIBN-GFP, cyan) and H2B-iRFP (magenta). Asterisks mark extrusion events detected within 45 min. (h, i) Heatmap showing the location of extrusion events detected within 2.5 h in 24 villi (h) and total cell density (i). The dashed lines indicate the boundary of the photoactivated region (left). (j, k) Density of extrusion events averaged along the x-axis, with photoactivation creating a boundary between photoactivated (left, x < 0) and non-activated (right, x > 0) regions (j), and along the y-dimension (k). Cells near the pattern boundary extruded less in the photoactivated region and more in the adjacent non-activated region.

To test this hypothesis, we generated mosaic organoids containing varying ratios of wild-type (WT) cells (tagged with H2B-iRFP or H2B-mCherry nuclear markers) and opto-Arhgef11 organoid cells (Fig. 2.5a). Upon photoactivation, WT cells were significantly overrepresented among extruded cells, particularly in mosaics where WT cells were present as a minority. To quantify this effect, we compared the fraction of WT cells in the extruded population to their overall presence in the organoid, referred to as extrusion enrichment. In organoids where WT cells represented the majority, their extrusion occurred approximately at a rate proportional to their abundance (Fig. 2.5b). However, as the proportion of opto-Arhgef11 cells increased, WT cells were extruded at a disproportionately higher rate resulting in a 4-fold extrusion enrichment (Fig. 2.5b). This imbalance was not observed in control organoids that were not induced with doxycycline or not exposed to blue light - in these cases WT cell extrusion rates remained proportional to their overall presence in the organoid (Fig. 2.5c). When examining mosaic organoids with a WT cell majority (> 50%), the probability of WT cell extrusion increased with their local proximity to opto-Arhgef11 cells (Fig. 2.5d). Thus, when optogenetic cells form the majority, the increased tissue-level tension enhances mechanical competition and drives the preferential extrusion of less contractile WT cells. This effect is further reinforced at the local level, because WT cells are more likely to extrude when close to highly contractile optogenetic cells.

To further substantiate these findings, we created a *Myh9* heterozygous knockout ($Myh9^{+/-}$) organoid line, which has genetically impaired Myosin heavy chain function [167, 176, 238, 287, 290] (Fig. 2.5e & Fig. 2.12k, l). When $Myh9^{+/-}$ were combined with wild-type cells in 3D mosaic organoids, WT cells were consistently underrepresented among extruded cells, while $Myh9^{+/-}$ cells were overrepresented (Fig. 2.5f-i). The observation that $Myh9^{+/-}$ extrusion enrichment progressively increased with higher WT cell content argued that higher organoid-level tension promotes the preferential removal of less contractile cells (Fig. 2.5i). Indeed, when two $Myh9^{+/-}$ populations labeled with different nuclear markers (H2B-mCherry and H2B-GFP) were combined - hence eliminating contractility differences - no extrusion bias was observed (Fig. 2.5j, k). Thus, cells appear to assess their neighbors' ability to generate tension continuously, resembling a tug-of-war competition for extrusion of weaker cells.
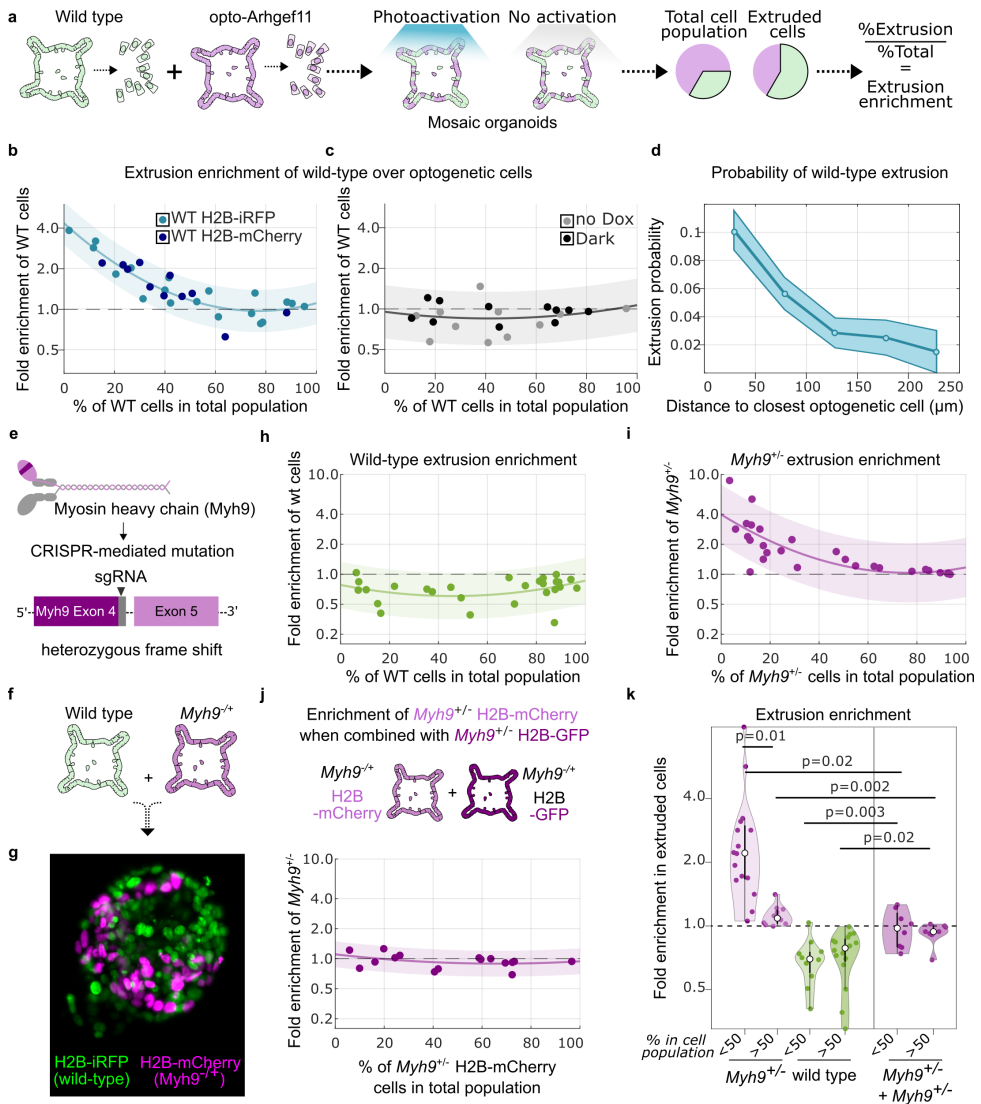
Figure 2.5: Contractility differences drive competitive extrusion of Myosin-II-compromised cells in mosaic organoids. (a) Schematic of the setup: wild-type (green) and opto-Arhgef11 (purple) cells were mixed in mosaic organoids. Photoactivation increased contractility of optogenetic cells. Extrusion enrichment was defined as the ratio of a cell type's fraction in extruded cells to its fraction in the organoid. (b, c) Wild-type extrusion enrichment in mosaic organoids with varying wild-type fractions. Each dot: one organoid; solid line: exponential fit with 95% CI (shaded). Y-axis: log scale. Sample sizes: 31 (b), 22 (c) organoids. (b) Wild-type cells tagged with H2B-iRFP (light blue) or H2B-mCherry (dark blue) showed increased extrusion enrichment when in the minority. (c) Control conditions without doxycycline induction (no Dox) or without photoactivation (Dark) show no significant extrusion enrichment. (d) Wild-type cell extrusion probability increases near opto-Arhgef11 cells. Solid line: mean; shaded area: S.E.M. (82 extrusions from N = 6 organoids). (e) CRISPR-Cas9 strategy to generate a heterozygous loss-of-function mutant organoid line for *Myh9*, encoding non-muscle myosin heavy chain IIA.

Figure 2.5: (continued) (f) *Myh9*$^{+/-}$ cells (H2B-mCherry) and wild-type cells (H2B-iRFP) were mixed as single cells to form mosaic organoids. (g) Light-sheet image of a mosaic organoid showing wild-type (green) and *Myh9*$^{+/-}$ (magenta) nuclei. Scale bar: 50 μm. (h, i) Extrusion enrichment of wild-type (h) and *Myh9*$^{+/-}$ (i) cells. Wild-type cells are underrepresented, while *Myh9*$^{+/-}$ cells are enriched among extruded cells, especially when in the minority (27 organoids). Y-axes: log scale. (j) Control mosaic organoids with two differentially labeled *Myh9*$^{+/-}$ populations (H2B-mCherry and H2B-GFP) show no extrusion bias (16 organoids). (k) Violin plot summarizing fold enrichment of *Myh9*$^{+/-}$ and wild-type cells in extruded populations, grouped by whether the genotype was in the minority (<50%) or majority (>50%) in the mosaic organoid. Each dot: one organoid. P-values: two-sided one-sample Student's t-test. Dashed line: equal extrusion probability.

DISRUPTION OF THE BASAL CORTEX INTEGRITY CAUSES CELL EXTRUSION

To test this "tug-of-war" hypothesis at the cellular level, we used infrared (IR) laser microsurgery [218, 287] to destabilize the basal cell cortex of individual cells in the villus region (Fig. 2.6a, b). Disrupting the basal cytoskeleton consistently led to the extrusion of the targeted cell within one hour (Fig. 2.6c-g), whereas applying the same laser stimulus directly to the nucleus had no such effect (Fig. 2.6e-g). In line with our finding that villus cells are under tension, basally targeted cells expanded within 15 seconds of ablation, indicating a rapid release of basal tension, while expansion was absent when ablation was instead targeted to the nucleus (Fig. 2.6i). The magnitude of the basal area expansion correlated with the probability of subsequent cell extrusion (Fig. 2.6j), but not with the extrusion time (Fig. 2.6k). The reliable induction of cell extrusion following basal expansion further supported the notion that a critical loss of tension-generating capacity owing to cytoskeleton disruption is necessary to trigger extrusion.

Directly after basal microsurgery, basal Myosin-II levels accumulated at the lateral cell boundaries accompanied by a contraction of the basal surface that brought together the membranes of neighboring cells (Fig. 2.6l, m). When Myosin-II activity was inhibited pharmacologically with blebbistatin, the probability that cells extruded at all within one hour decreased from 83% in control organoids to 51% in blebbistatin-treated organoids (Fig. 2.6n), while the duration of the extrusion process after basal microsurgery increased ~2-fold (Fig. 2.6o, p). Thus, Myosin-II activity is required for executing cell extrusion and for the timely removal of mechanically weakened cells.

Next, we examined the cellular response when applying the laser stimulus to tension-bearing bi- or tri-cellular basolateral junctions (Fig. 2.6q). This procedure reliably induced the simultaneous extrusion of a duplet or triplet of cells, respectively, showing that the mechanical destabilization of multicellular junctions led to the simultaneous extrusion of the affected cells (Fig. 2.6r, Fig. 2.13a-f). Again, when we inhibited Myosin-II activity with blebbistatin and destabilized the bases through microsurgery, only 51% of the cells extruded within 1 hour, compared to 83% without inhibition (Fig. 2.13g-i). The stimulated multi-cell extrusion was driven by the contraction of a common actomyosin accumulation that enclosed all extruding cells (Fig. 2.13j). E-cadherin junctions in neighboring cells were maintained (Fig. 2.13k) and the overall extrusion rate at the organoid level did not significantly increase (Fig. 2.14a-c), indicating that the epithelial barrier and tissue integrity was

maintained. Thus, the epithelium appears to eliminate groups of neighboring cells when they become mechanically compromised and lose the ability to maintain junctional tension.

This prompted us to investigate whether extrusion is driven by cell-autonomous contraction or the coordinated contraction of adjacent cells. We generated mosaic organoids composed of Myosin-II reporter cells and cells expressing only a nuclear marker and analyzed reporter cells surrounded by non-labelled neighbors (Fig. 2.6s), as well as non-labelled cells surrounded by reporter neighbors (Fig. 2.6t). Myosin-II levels increased drastically in spontaneously (i.e. non-ablated) extruding cells, but also in the cell neighbors (Fig. 2.6u). Thus, the extruding cell appears to trigger an endogenous response to drive its own extrusion through Myosin-II upregulation supported by the coordinated Myosin-II upregulation in adjacent cells. Together these processes reflect a coordinated tissue behavior to achieve proper contraction, extrusion, and maintenance of epithelial integrity. Thus, intestinal cell extrusion is a coordinated tissue behavior.

Epcam loss distorts tissue tension and epithelial homeostasis in tufting enteropathy

Dysregulation of contractility-based tissue coordination can profoundly impact tissue homeostasis. For example, congenital tufting enteropathy (CTE) is a rare genetic disorder characterized by severe, intractable diarrhea in infants, often leading to intestinal failure. It is caused by mutations in *Epcam* [188, 243], which encodes a negative regulator of Myosin-II: its loss leads to Myosin-II hyperactivation [165, 203]. The disease phenotype includes impaired intestinal barrier function, epithelial defects, and disrupted tissue organization, such as villous atrophy, crypt hyperplasia, and focal epithelial tufts (Fig. 2.7a) [55]. These tufts are distinct histological features characterized by the disorganization and crowding of surface enterocytes into tuft-like structures.

To investigate the potential role of our proposed extrusion regulation mechanism in CTE, we introduced *Epcam* loss-of-function mutations in intestinal organoids using CRISPR/Cas9, generating three independent *Epcam*$^{-/-}$ lines (Fig. 2.7b, c & Fig. 2.15a). Mutant organoids displayed distorted morphology: the well-structured morphology of wild-type organoids, characterized by distinct budding protrusions and a cystic center, was largely lost in *Epcam*$^{-/-}$ organoids (Fig. 2.7c, d & Fig. 2.15b, c). Time-lapse imaging of *Epcam*$^{-/-}$ organoids growing from small cystic organoids over several days revealed repeated cycles of inflation and deflation. Compared to wild-type organoids, *Epcam*$^{-/-}$ organoids exhibited delayed budding, initiating bud formation after three rather than two days. Additionally, they grew into noticeably larger structures than WT organoids (Fig. 2.15c). Using qPCR and immunofluorescence, we confirmed that *Epcam*$^{-/-}$ organoids differentiated into all major intestinal lineages but exhibited some marked differences (Fig. 2.15d, e): Consistent with CTE's crypt hyperplasia, *Epcam*$^{-/-}$ organoids showed increased expression of markers for stem cells and immature enterocytes, and a reduction in markers of mature cell types in comparison to WT organoids (Fig. 2.15d, e). These findings align with reports of delayed differentiation and persistent differentiation defects in CTE [53, 54].
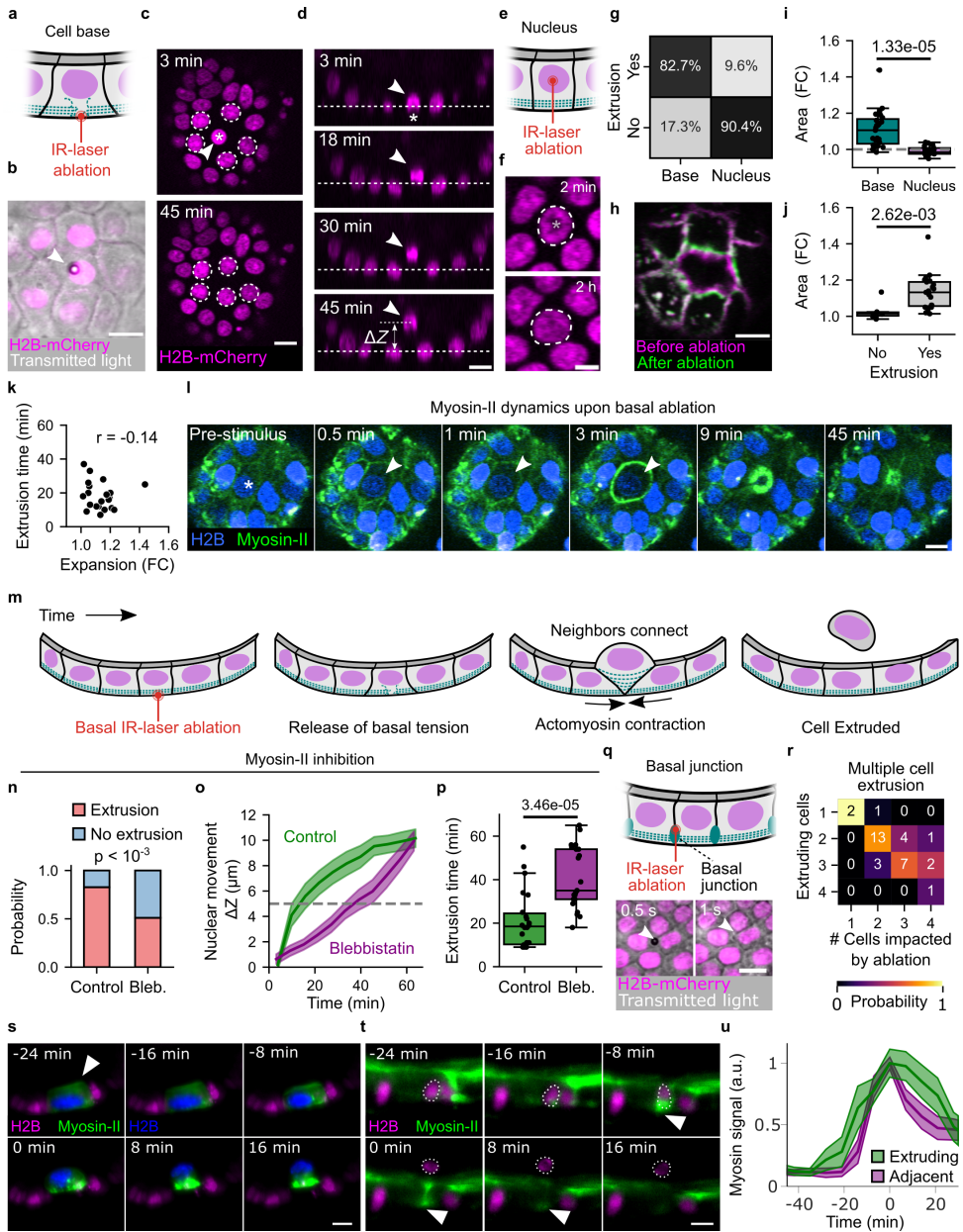
Figure 2.6: Release of tissue tension triggers cell extrusion. (a-d) Point ablation of a single cell's basal surface. (b) Brightfield with H2B-mCherry (magenta); (c, d) Confocal top view (c) and cross-section (d) after basal ablation. Arrowhead indicates targeted cell; dashed circles indicate neighbors. ΔZ: vertical shift of the extruding cell relative to neighbor Z-levels. Scale bars: 10 μm. (e, f) Schematic (e) and confocal images (f) of point ablation in the nucleus. Timestamps in c, d, f indicate time since ablation. Asterisk indicates location of the stimulus.

Figure 2.6: (continued) (g) Basal ablation triggered extrusion, unlike nuclear stimulation (Data from 81 basal and 94 nuclear stimulations; $p < 10^{-23}$, Fisher's exact test). (h) Point ablation causes cell base expansion. (magenta: before, green: after). (i) Cell area expanded after basal but not nuclear ablation (Student's t-test; Data from 27 basal and 18 nuclear stimulations). (j) Basal expansion predicted extrusion (Mann-Whitney U test; 21 extrusions, 6 non-extrusions). (k) Basal expansion after ablation did not correlate with extrusion time (Pearson r: 0.14). (l) Confocal images of Myosin-II (green) dynamics after basal point ablation. Asterisk indicates the location of the stimulus; arrowhead indicates the extruding cell. (m) Response to acute basal tension loss by laser-induced cytoskeletal ablation. (n) Blebbistatin reduced extrusion probability within 1 h after basal ablation (Fisher's exact test; 81 control, 49 blebbistatin-treated organoids). (o) Vertical shift (ΔZ) over time (mean ± S.E.M. of stimulated cells). (p) Extrusion time (Mann-Whitney U test; 22 extrusions per condition in o, p). (q) Multicellular junction ablation. Arrowheads: ablation site. (f, h, l, q) Scale bar: 5 μm. (r) Ablation of multicellular junctions triggered extrusion of nearby cells (within 9 μm; N = 34 organoids). (s, t) Mosaic organoids with Myosin-II reporter (green) and H2B-iRFP-only cells (magenta). Time relative to spontaneous extrusion. Scale bars: 10 μm. (s) Extruding myosin reporter cell autonomous upregulation of myosin. (t) Non-reporter cell extrusion induced myosin in neighbors. (u) Myosin-II levels over time in extruding cells (green) and their neighbors (magenta), aligned to extrusion. Data from 10 extruding and 15 adjacent cells.

The reduced presence of mature cell types could be attributed to increased cellular turnover. To investigate this, we measured cell extrusion rates using a transwell assay and flow cytometry. $Epcam^{-/-}$ organoids exhibited a ~1.5-fold increase in extrusion rate compared to WT (Fig. 2.7f) and immunostaining for phospho-Myosin-II confirmed myosin hyperactivation (Fig. 2.7g & Fig. 2.15f, g). Our findings that excessive contractility and elevated tissue-level tension accelerated cell extrusion (Fig. 2.4d, e) suggested that $Epcam$ loss may contribute to epithelial dysregulation by increasing mechanical tension, which could promote premature cell removal and thereby manifest the disease phenotype.

To examine the effects of contractility differences in this disease-relevant context, we generated mosaic organoids containing WT and $Epcam^{-/-}$ cells and analyzed cell extrusion. Live imaging and quantification of extrusion enrichment revealed that hypercontractile $Epcam^{-/-}$ cells extruded less frequently, while WT cells were overrepresented among extruded cells. This effect became stronger with increasing abundance of $Epcam^{-/-}$ cells (Fig. 2.7h, i). This mirrored our earlier finding with WT and opto-Arhgef11 cells, where the less contractile minority population was preferentially extruded (Fig. 2.5b). Combining two WT lines with different nuclear markers did not show such biased extrusion (Fig. 2.7j), confirming that contractility differences rather than genetic labels drive extrusion. To determine whether Myosin-II hyperactivation directly drives competitive extrusion, we inhibited Rho signaling pharmacologically using Y16 (Rho-GEF inhibitor) and Y-27632 (ROCK inhibitor) in mosaic $Epcam^{-/-}$/WT organoids with a majority $Epcam^{-/-}$ cells. Both inhibitors significantly reduced WT extrusion enrichment, demonstrating that suppressing Myosin-II activity alleviates the extrusion bias against WT cells (Fig. 2.7k). Thus, tension heterogeneity within the epithelium drives cell extrusion and differences in Myosin-II-mediated contractility create mechanical competition that determines which cells are extruded. This process, when dysregulated, may contribute to epithelial pathologies such as congenital tufting enteropathy.
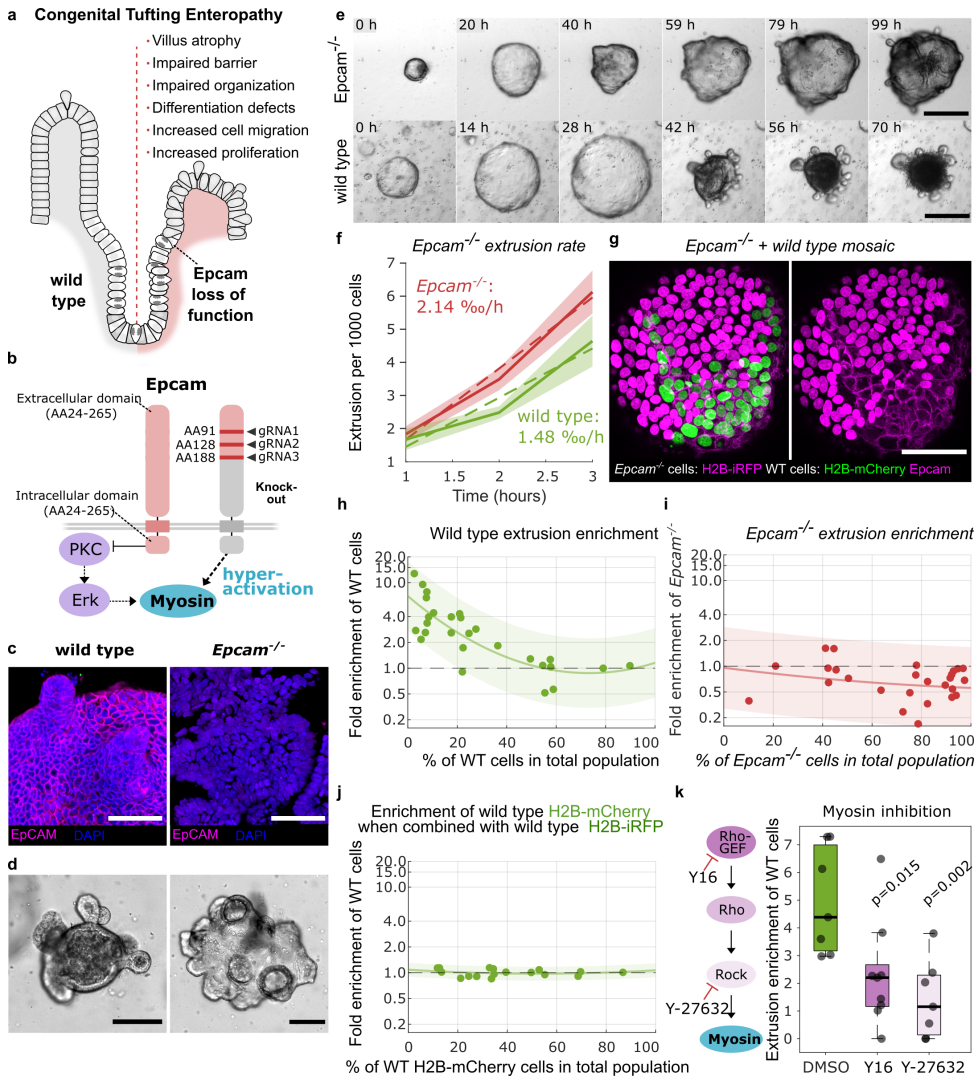
Figure 2.7: Hyperactivation of Myosin-II in *Epcam*$^{-/-}$ cells disrupts epithelial homeostasis and drives competitive cell extrusion. (a) Hallmarks of congenital tufting enteropathy (CTE), a disease caused by loss-of-function mutations in *Epcam*. (b) Schematic of *Epcam* function and its role in Myosin-II inhibition. Right: CRISPR/Cas9 strategy to generate *Epcam*$^{-/-}$ organoids (guide sites shown). *Epcam* loss leads to Myosin-II hyperactivation. (c, d) Immunofluorescence staining (*Epcam* (magenta) and DAPI (blue)) and brightfield images of wild-type and *Epcam*$^{-/-}$ mutant organoids. Scale bars: 50 µm (c) and 100 µm (d). (e) Brightfield images showing growth and morphological changes of wild-type (bottom) and *Epcam*$^{-/-}$ (top) organoids over time. Scale bar: 100 µm. (f) Quantification of cell extrusion rates using a transwell assay and flow cytometry; *Epcam*$^{-/-}$ organoids (red) show a significantly higher extrusion rate compared to wild-type (green). Solid line shows mean and semi-transparent region the S.E.M. Data: 5 WT, 12 *Epcam*$^{-/-}$ (5 of g1 and g2; and 2 of g3) transwells. (g) Immunofluorescence for *Epcam* (magenta) in a mosaic organoid with H2B-iRFP-labeled *Epcam* cells (also magenta) and H2B-mCherry-labeled wild-type cells (green). Scale bar: 50 µm.

Figure 2.7: (continued) (h, i) Extrusion enrichment in mosaic organoids composed of H2B-iRFP-labeled *Epcam*$^{-/-}$ cells and H2B-mCherry-labeled wild-type cells. Extrusion enrichment of wild-type (h) or *Epcam*$^{-/-}$ (i) cells is shown at varying fractions of the respective cell population in the mosaic organoid. Wild-type cells become increasingly enriched among extruded cells as the proportion of *Epcam*$^{-/-}$ neighbors rises, while *Epcam*$^{-/-}$ cells are underrepresented (27 organoids). (j) Extrusion enrichment in control mosaics with wild-type cells labeled by different nuclear markers showed no bias. (h-j) Each dot: one organoid; exponential fit ± 95% CI (shaded). Y-axis: log scale. (k) Pharmacological inhibition of Rho signaling upstream of Myosin-II activity with Y16 or Y-27632 (scheme on left) reduces extrusion enrichment of WT cells in WT/*Epcam*$^{-/-}$ mosaics. Data from 7 DMSO-treated, 9 Y16-treated and 7 Y27632-treated organoids; two-sided Student's t-test.

2.3 Discussion

The self-renewal of the intestinal epithelium is commonly described using the analogy of a conveyor belt: cells are continuously produced in intestinal crypts, move into the villus domain as they differentiate, and finally extrude into the lumen from the villus tip. In line with this model, it has been suggested that cells extrude in response to tissue crowding as they ultimately accumulate at the villus tip, where owing to the limited space, the tissue is compressed [111, 209]. Our findings challenge this model: instead of tissue compression, we find that the basal surface of intestinal villi, including the tip region, is under tension. This tension is mediated by Myosin-II pulsations in the basal cytoskeleton, and cell extrusion rates are directly coupled to this tissue-level tension. Laser ablation of the cell base, causing local weakening, or genetic impairment of contractility both induce extrusion, suggesting that cells unable to sustain tension are eliminated. In contrast, (opto-)genetic activation of Myosin-II increases tissue-wide tension and amplifies the mechanical competition between cells, promoting the preferential extrusion of weaker cells (Fig. 2.16). These complementary approaches reveal a shared principle: A cell extrudes when it can no longer sustain or reciprocate the tension exerted by neighboring cells - whether due to a local impairment of contractility or increased tension exerted by its neighbors.

In the intestine, an interconnected basal actomyosin network facilitates the transmission of physical forces throughout the villus epithelium, coordinating tissue-level behaviors such as cell extrusion, as shown here, but potentially also cell migration [149] and proliferation [10, 181]. Indeed, a cell's extrusion triggers cell contractility in its neighbors and impacts tissue-level tension. We propose a revision of the roles of cell extrusion and proliferation in tissue homeostasis. Cells at the villus tip are not pushed into crowding and compression but instead pull on their neighbors driving a mechanical competition, leading to the preferential extrusion of less contractile ("weak") cells. Hence, the intestinal epithelium acts as a self-renewing network of cells that autonomously replaces its weakest links. Indeed, cell extrusion thus not only serves to maintain cell number homeostasis, but also serves to maintain "mechanical homeostasis" - the need to maintain and restore the optimal mechanical tissue state. Mechanochemical signaling dynamics driven by Myosin-II-mediated tissue tension thus complements biochemical signaling gradients in the organization and maintenance of intestinal homeostasis. This tissue-level tension caused by the extrusion of weak cells could, in turn, promote cell proliferation and thus proliferation may respond to extrusion to maintain cell number homeostasis, rather than driving extrusion. This would invert the conventional view of cause and effect in intestinal homeostasis. Indeed, increased tissue tension in intestinal organoids [10, 181], MDCK

monolayers [91], mouse colon [76] or the pig intestine [249] can stimulate cell proliferation.

While the role of tensile basal actomyosin has been recognized in morphogenesis [182, 215, 252], we show its importance for intestinal barrier maintenance during tissue homeostasis. This has implications for pathologies in which the epithelial barrier function is impaired, beyond the tufting enteropathy studied here. For example, mutations in cytoskeletal components such as Myosin IIA heavy chain [194], RAC1 [174], Myosin IXB [264], Keratin 8 [12] and cytoskeletal crosslinking protein ACF7 [164] are associated with increased epithelial permeability and are implicated in diseases characterized by excessive cell extrusion such as inflammatory bowel disease (Crohn's disease and Ulcerative Colitis). On the other hand, cancerous epithelial cells evade homeostatic cell extrusion and initiate primary tumors by distorting extrusion mechanisms and extruding through the basal rather than the apical surface [172, 246]. Mutation of RAS oncogenes - prime drivers of small intestinal adenocarcinomas [97] - interfere with Myosin-II activity and alter tissue mechanics (see ref. [200] for review). Based on our findings, we propose tissue tension as a potential therapeutic target that could be influenced through pharmacological modulation [33] to alleviate excessive shedding in the context of inflammatory bowel disease (IBD) or to accelerate the extrusion of cells that threaten intestinal integrity, e.g. during pathogen infections [74, 132, 189].

2.4 Materials & Methods

Organoid culture

Organoids were grown in basement membrane extract (BME; Biotechne R&D Systems; cat. #3533-010-02) and ENR growth medium. ENR growth medium was prepared with murine recombinant Noggin (100 ng/mL; ThermoFisher, cat. #250-38-100UG) and human recombinant R-spondin 1 (500 ng/mL; ThermoFisher, cat. #120-38-5UG), 1 mM n-acetylcysteine (Merck, cat. #A9165-5G), 50 ng/mL epidermal growth factor (EGF; ThermoFisher cat. #315-09-500UG), N2 and B27 supplement (1×; ThermoFisher, cat. #17502048 and #17504044, respectively), Glutamax (2 mM; ThermoFisher cat. #35050061), HEPES (10 mM; ThermoFisher, cat. #15630080), 100 U/mL Penicillin, 100 µg/mL Streptomycin (Penicillin-Streptomycin, Gibco Thermo Fisher Scientific, cat. #11548876) in Advanced DMEM/F12 (ThermoFisher, cat. #12634010). Passaging was done once and the medium change two times per week on non-consecutive days. During passaging, BME was dissolved in cold base medium (2 mM Glutamax, 10 mM HEPES in Advanced DMEM/F12) and organoids were mechanically disrupted, before embedding in new BME and plating onto a culturing plate. BME was left to solidify for 20-30 minutes before new growth medium was added. For expansion and outgrowth of single cells, organoids were cultured in Wnt-conditioned medium (ENR, 10 mM Nicotinamide (Sigma-Aldrich, cat. #98-92-0), home-made Wnt3A conditioned medium 50% (v/v) [210]). Organoids expressing the optogenetic module were kept in the dark in an aluminum vessel. To inspect optogenetic organoids, culture plates and dishes were placed in containers wrapped in Deep Amber lighting filter foil (Cabledelight) to filter blue light.

Cloning

Gibson Assembly (NEBuilder HiFi DNA Assembly, NEB, cat. # E2621) was used for the cloning of all constructs. Transgenic constructs were cloned into p2T vectors that flank

2

the inserts with 3' and 5' tol2 sequences. These transposable elements mediate the mT2TP transposase-dependent random integration of the expression constructs into the cell genome. For p2T-CIBN-GFP-PuroR, a new p2T vector was assembled by combining fragments containing an empty p2T backbone, the CAG promoter, CIBN-GFP (from ref. [119]) and IRES-PuroR. To express Arhgef11-CRY2 under Dox-inducible promoter, in a p2T backbone, the Tet-ON 3G transcription factor driven by a CMV promoter (from ref. [24]) was combined with a P2T-T2T tandem and a HygromycinR. In opposite direction, a TRE3GS promoter (from ref. [24]) was cloned to drive the PHR-CRY2 domain fused to Arhgef11 (from Addgene plasmid #89481) and followed by a SV40 polyA tail. A second construct containing Argef11-mCherry-CRY2 was generated based on the p2T-TetON-Hygro-Arhgef11-CRY2 construct. For H2B-iRFP-BlastR and H2B-mCherry-BlastR nuclear markers, the p2T-CIBN-GFP-PuroR construct was cut with XhoI and BsrGI (both New England Biolabs, cat. #R0146S, #R3575S) and fragments containing H2B, iRFP670 or mCherry and IRES-BlasticidinR were combined. H2B-GFP-HygroR was assembled to contain the p2T backbone, a CMV promoter driving H2B-mEGFP and a SV40 promoter driving a HygromycinR. Two new CRISPR-HOT donor plasmids were generated. Based on pCRISPaint-mNeon (Addgene plasmid #174092), new donors containing pCRISPR-HOT_mNeon-P2A-T2A-mCherry-CAAX (to generate mNeonGreen fusion protein that co-translates a red-fluorescent plasma membrane marker), pCRISPR-HOT_mNeon-Stop-PGK-mCherry-CAAX (to generate mNeonGreen fusion protein and expresses a red-fluorescent plasma membrane marker independently under the PGK promoter) were generated using Gibson assembly.

CRISPR-mediated reporter and knockout generation

Knock-in reporter organoids were generated using CRISPaint technology [239] and the CRISPR-HOT method [6]. A gene-specific sgRNA-containing plasmid (Table 2.1) was co-transfected [79] with a donor plasmid containing the fluorescent tag and the frame-selector plasmid containing an sgRNA to linearize the donor plasmid and the Cas9 into mouse intestinal organoids (each 5 µg sgRNA plasmid) using a NEPA electroporation system (NEPAGENE). Myosin knock-in reporter organoids were generated using both pCRISPR-HOT_mNeon-P2A-T2A-mCherry-CAAX and pCRISPR-HOT_mNeon-Stop-PGK-mCherry-CAAX donor vectors. The Comparison of the target-specific co-expression and independent expression of the mCherry plasma membrane marker allowed an estimation of signal strength and localization across gene targets. *Myl12a*-mNeonGreen-P2A-T2A-mCherry-CAAX was selected to characterize myosin activity and dynamics in organoid tissue. In addition, pCRISPR-HOT_tdTomato (Addgene plasmid #138567) was used to generate a *Myl12a*-tdTomato line and pCRISPaint-mNeon in combination with a *Cdh1*-specific sgRNA was used to generate a live reporter for E-cadherin. Three days before and two weeks after electroporation organoids were split and cultured in Wnt-conditioned medium. Expression of fluorescent reporters in individual organoids was monitored daily. To generate stable organoid lines, fluorescent organoids were picked, dissociated to single cells using TrypLE Express Enzyme (Thermo Fisher Scientific, cat. #12605010) and expanded for two weeks in Wnt-conditioned medium. Stable lines were cultured in ENR medium. For gene-specific knockout generation, a sgRNA vector conferring a transient Hygromycin and a Cas9 vector conferring a transient Puromycin resistance were co-transfected. After electroporation organoids were cultured in Wnt-conditioned medium. One day after

electroporation the organoids were exposed to Puromycin (2 µg/ml; InvivoGen, cat. #ant-pr) and Hygromycin B Gold (100 µg/ml; InvivoGen, cat. #ant-hg) for 24 h. Two weeks after electroporation outgrown organoid clones were picked, dissociated to single cells, DNA was extracted using Quick-DNA Microprep Kit (Zymo Research Corporation, cat. #D3021) and genotyped using gene-specific primer pairs (Sanger sequencing performed by Macrogen Europe BV). Clonal organoid lines were cultured in ENR medium.

GENERATION OF TRANSGENIC ORGANOIDS

Organoid lines expressing H2B nuclear marker [115, 291], Dox-inducible optogenetic modules and the optogenetic anchor CIBN-GFP were generated by co-electroporation of 5 µg of the respective expression construct and 5 µg of a vector containing the mT2TP transposase driven by the CAG promoter for the transient expression of mT2TP mediating the tol2-dependent genome integration of expression constructs. One week after electroporation organoids were exposed to the expression construct-conferred resistance. The culture was propagated and maintained in ENR medium containing the expression construct-conferred resistance.

SAMPLE PREPARATION OF SYNTHETIC HYDROGELS WITH CRYPT-VILLUS TOPOLOGY

ECM-based hydrogel substrates were generated as described previously [86]. Before organoid seeding, the substrates attached to 35 mm culture dishes were sterilized using UV illumination and repeated washes using PBS solution containing Primocin (1:500; InvivoGen, cat. #ant-pm) and incubated in Wnt-conditioned medium overnight. Cells were incubated in Wnt-conditioned medium three days before seeding. For cell seeding, BME was enzymatically digested using Dispase (Stemcell Technologies cat. #07913) and washed away using cold base medium. Cells were dissociated to single cells using Accutase Cell Detachment Solution (Innovative Cell Technologies, cat. #AT104-500), pelleted by centrifugation at 250xg for 5 min and resuspended in 15 µl of Wnt-conditioned medium. Medium was aspirated from substrates and the cell suspension was seeded evenly onto the surface. Cells were allowed to attach for 5 min at 37°C before more Wnt-conditioned medium containing 10 µM Y-27632 (Abmole, cat. #M1817) was added to fill the culture dish. The cells were kept in Wnt-conditioned medium for four days, in Wnt-conditioned medium diluted 1:2 in ENR for three days and eventually kept in ENR medium. Organoids expressing the optogenetic modules were kept in medium containing Puromycin (1 µg/ml) and Hygromycin B Gold (100 µg/ml) and incubated in a dark aluminum chamber and inspected through blue-light filtering foil.

GENERATION OF MOSAIC ORGANOIDS

Two organoid lines were dissociated to single cells as described for seeding on hydrogel substrates, resuspended in Wnt-conditioned medium and combined at desired ratios. The cell suspension containing 300k cells in 20 µl medium was mixed well by repeated pipetting and 20 µl were seeded per well onto a 48-well-plate. The plate was spun at 200xg for 5 min and incubated for 30 min at 37°C before Wnt-conditioned medium (with 10 µM Y-27632) was added. After 24 h the cell layer was mechanically detached by scaping of the cell layer using a pipette tip and repeated flushes with base medium. Without extra mechanical

sheering, the cells were collected by centrifugation and seeded directly into microscope sample carriers. Organoids were cultured in ENR medium. Mosaic organoids were imaged for 12-20 h using a Leica Stellaris confocal microscope or Viventis Light sheet microscope.

Extrusion measurement of $Epcam^{-/-}$ and wild type cells

Transwell inserts with 0.1 μm pore size (Corning, cat. #CLS3396) were coated with 5% BME for 30 minutes. Organoid cells were dissociated into single cells as described above, resuspended in Wnt-conditioned medium supplemented with 10 μM Y-27632, and seeded onto the transwell surface at a density of 200,000 cells per insert. The cells were cultured for four days in Wnt-conditioned medium to achieve full confluency, followed by two days in transition medium (1:1 mix of ENR and Wnt-conditioned medium). To promote differentiation, monolayers were then maintained for 10 days in ENR medium. Only transwells with complete and confluent monolayer coverage were included in downstream analysis. Flow cytometry was used to count extruded cells in the medium covering the monolayer. To this end, the medium covering the monolayer was refreshed and collected after 1, 2, and 3 hours. The cells were stained with DAPI (1 μg/ml) and the number of extruded cells was measured by FACS using a CytoFLEX (Beckman Coulter). To normalize extrusion rates to the number of cells in the monolayer, the transwell membranes were fixed in 4% paraformaldehyde for 30 minutes at room temperature, washed with PBS, and stained with DAPI (1 μg/ml). Whole-membrane tile scans were acquired using a Leica Thunder widefield microscope with a 5× air objective. Cell nuclei were segmented using StarDist in Fiji, and total cell numbers were quantified. The extrusion rate was calculated as the number of extruded cells (by FACS) divided by the total number of monolayer cells (by image segmentation), normalized to the time of sample collection.

Long-term live-cell imaging and image analysis

For long-term live imaging of nuclear reporter organoids, organoids were seeded onto an imaging chamber (CellVis 4 Chambered Coverglass System cat. #C4-1.5H-N) and imaged on a A1R MP (Nikon) scanning confocal microscope outfitted with a 1.30 NA 40× magnification oil immersion objective, incubation chamber set to (37 ºC, 5% CO2) [115]. Images were taken every 12 minutes, and at each timepoint, 31 Z-slices were imaged with 2 μm intervals. For live imaging of organoids grown on synthetic crypt-villus substrates, the chips were placed into a μ-Dish 35 mm glass bottom dish (Ibidi, cat. #81218-200) onto a circular holder made of PDMS material with a width of ~2 mm. The samples were imaged using a Leica SP8 confocal microscope using a HC PL APO CS2 20x/0.75 air objective at 37 °C and 5% CO2. Z-Stacks of 40 μm were collected with 1 μm Z-interval and with a time interval of 6 min. $Epcam^{-/-}$ and wild type organoids were seeded on a 96-well glass bottom plate and imaged over a period of 1 week using a Leica Thunder widefield microscope using a 5X air objective and brightfield illumination.

Cell tracking

Semi-automated tracking of single cells and their extrusion from organoids was done by tracking the cell nuclei using the OrganoidTracker [143] software. Tracks and lineage trees were analyzed in Python. Cells were censored when they moved out of view or were still alive when the image acquisition was stopped. We measured the cell density around a cell

as the inverse of the average distance to its six closest neighbors (in millimeters), using the cell_density_calculator in OrganoidTracker [143].

Optogenetic experiments

Photoactivation of opto-Arhgef11 organoids was done using a Leica SP8 confocal microscope using a HC PL APO CS2 40x/1.10 water objective. 3D organoids expressing the system were imaged first using only 640 nm excitation to collect transmitted light and the H2B-iRFP nuclear marker signal (pre-activation). For regional photoactivation a region of interest (ROI) was designed, which was set to be illuminated with low intensity of 488 nm light (0.5-1%). A time course with a time interval of 1 seconds was started with simultaneous illumination of the entire organoid with 640 nm excitation (to collect transmitted light and the H2B-iRFP nuclear marker signal) and 488 nm-photoactivation specific to the ROI. In this region, the GFP signal of the labelled optogenetic anchor was recorded. To stop photoactivation, the laser power of the 488 nm laser was set to zero. To record the translocation of Arhgef11-CRY2-mCherry to the plasma membrane, a Zeiss LSM780 was used with a C-Apochromat 40x/1.20 W Korr M27 water objective (Zeiss). First, the mCherry signal was collected using 564 nm excitation, then a region was illuminated within a ROI using 488 nm illumination and the mCherry signal was collected again after 5 seconds. For the photoactivation of optogenetic organoids grown on synthetic hydrogels, a Leica SP8 confocal microscope using a HCX IRAPO L 25x/0.95 water objective was used. A water pump was attached to the water immersion objective that compensated for water evaporation during the experiments. As a control, we first imaged optogenetic organoids on hydrogel substrates that were not induced by doxycyclin before for 2.5 h at a time interval of 4 min with both 640 nm light to record the H2B-iRFP nuclear signal and 488 nm blue light. The positions of the imaged villi were saved. Afterwards the organoids were incubated for 12 h to let them recover, induced with 1 μg/mL doxycyclin (Thermo Fisher Scientific, cat. #10592-13-9) for 24 hours and the same villi were imaged for 2.5 h only with 640 nm light without 488 nm. Again, the organoids were incubated for 12 h and the villi were imaged for 2.5 h with both 640 nm and photoactivated using 488 nm light. Extrusions were counted and the extrusion rates were calculated for each villus. In another setup, the samples were first imaged for 2.5 h exclusively with 640 nm light (non-activation), followed by 2.5 h with simultaneous photoactivation using 488 nm light in time intervals of 4 min. Similar to the localized photoactivation in 3D organoid cultures, for the patterned photoactivation of only one half of the villus tip, the villus tip was centered and imaged in the full field of view using 640 nm light, while only the left half of the tip was illuminated with 488 nm for 2.5 h. Mosaic organoids were imaged using a Leica Stellaris Confocal microscope using a 20X air objective (20x/0.75 Air, Leica) or using a Viventis Light sheet microscope, as described below, and photoactivated every 5 min. For all optogenetic experiments: To be able to position the optogenetic samples at confocal microscopes a deep Amber lighting filter foil (Cabledelight) was placed on top of the condenser to block blue light from brightfield illumination.

Light sheet imaging

Live imaging of Myo-mNG reporter organoids and mosaic organoids was performed using a LS1 Live light sheet microscope (Viventis Microscopy) using a Nikon 25X NA 1.1 water

immersion objective at a magnification of 18x. Organoids were mounted on a single-chamber sample holder one day before the start of imaging. Organoids were imaged at 37°C and 5% CO2. A position-specific alignment of the light sheets with a thickness of 2.2 μm was done. Organoids were imaged every 8 minutes using appropriate laser lines depending on the fluorophores expressed. Myo-mNG reporter organoids were imaged with 488 nm and 561 nm illumination. Mosaic organoids expressing combinations of H2B-mCherry, H2B-iRFP, H2B-GFP, or CIBN-GFP were imaged using 561 nm, 638 nm, and 488 nm illumination, respectively. Organoids co-expressing Myo-mNG with H2B-iRFP, or Myo-tdTomato with H2B-GFP and H2B-iRFP, were imaged using 488 nm and 638 nm, or 488 nm, 561 nm, and 638 nm illumination, respectively. Post-acquisition analysis was performed using Fiji.

Image analysis of short-term movies

Image processing and analysis was done using Fiji [237]/ImageJ2 [228]. To measure the basal expansion after laser-ablation of the basal cytoskeleton, organoids expressing H2B-mCherry and E-cadherin-mNeonGreen were plated onto an imaging plate (day 0) and ablated at the base on day 2. The time-lapse video of the stimulation was taken from 5 seconds before stimulation until 15 seconds after stimulation, and the basal area of the ablated cells was measured on the average E-cadherin-mNeonGreen signal before (-5 s < t < 0 s) and after (10 s < t < 15 s) ablation. 3D renderings were generated by exporting nuclei positions from OrganoidTracker and rendering in ParaView (v. 5.11.0).

The basal surface of reporter organoids grown on synthetic crypt-villus substrates was extracted using the Fiji plugin LocalZProjector [108]. Basal cell membranes were segmented and tracked manually using Napari (napari.org) and analyzed in Matlab (2021b, MathWorks). Myosin levels were quantified using Matlab by creating binary masks for individual cells and timepoints to calculate the cell area and mean fluorescent signal. Graphs were visualized using the plot function and smoothened with a factor of 3. To identify myosin peaks, a trend curve was calculated and subtracted from the raw signal before maxima were identified using the findpeaks function. To calculate the trend, a polynomial function of 4th degree was fitted to single cell myosin curves (signal over time) using the fit function. To estimate the pulsation period, only cell traces with more than four identified peaks were analyzed and the time interval between two peaks was measured. The myosin activity-curves and corresponding cell area data around identified peaks were superimposed. An average curve for these peaks was calculated over a 120-minute time interval centered on the peaks. 3D rendering of organoids growing on hydrogels with crypt-villus topology was done using Imaris 10.0 (Oxford Instruments). To quantify apical and basal myosin levels, crypts recorded in the cross-section were selected and using FIJI a line was drawn following the shape of the epithelium with ~150 μm length. The epithelium was virtually transformed into a straight line using the straighten function. A line was drawn on the apical and basal surface respectively and the signal measured with a line width of 4 μm to obtain the respective line profiles. Line profiles centered around multiple crypts were averaged and depicted in the final graph. The same approach was used to measure the apical and basal myosin profile for a single developing crypt over time. To this end, for each time point the shape of the epithelial line was adjusted and the measured

distances scaled to match the length of the final crypt-villus region.

To analyze extrusion of cells upon optogenetic activation of myosin, the acquired H2B-iRFP nuclear marker signal was used to monitor cell dynamics. The detection of cell extrusion events and total cell counts were done using the FIJI plugin Cell Counter and the position and time were registered. Counting was done in a blinded fashion without information about the photoactivation pattern by a person, who was not the experimenter. Using Matlab, the positional and temporal data was analyzed. To analyze the extrusion rate over time, it was calculated as the average number of extrusions per total cells within a 25-minute time window. To analyze the position of extruding cells, the position data of extrusion events and total cells were binned equally using the hist3 and visualized using the imagesc function. The x- and y-profile for cell extrusions and total cells was generated by calculating the mean density along the respective axis within a 9 μm window. The raw extrusion profile was then normalized by the total cell profile to obtain the final extrusion profile. For the quantification of mosaic organoids, the respective cell population was measured as fraction of the total and extruded cell population (extrusion enrichment), extrusions and total cells were manually counted based on the co-expressed fluorescent markers using Napari and Fiji Cell counter. Counting was done in a blinded fashion.

IMMUNOFLUORESCENT STAINING OF WHOLE-MOUNT INTESTINAL TISSUE

Mice were sacrificed and the small intestine was dissected. The lumen was flushed several times with cold PBS. The tissue was cut as a tube and opened along the longitudinal axis. The tissue was fixed in 4% paraformaldehyde solution at 4°C overnight and washed with PBS. The cells were permeabilized using 2% PBST (2% Triton X-100 in PBS) for 2 days at room temperature and washed with PBS. The sample was incubated in blocking buffer (10% normal goat serum, 1% Triton-X 100, 2.5% DMSO in PBS) for 2 days at 4 °C. The sample was incubated in primary antibody solution (1% normal goat serum, 0.2% Triton-X 100, 2.5% DMSO, and 0.2% sodium azide in PBS; rabbit anti-Myosin light chain (phospho S20) antibody (Abcam, cat. #ab2480) diluted 1:200), incubated for 5 days at 4°C and washed with PBS at room temperature. The sample was incubated in secondary antibody solution (1:500 goat-Alexa-488-anti rabbit (Thermo Fisher Scientific, cat #A-11008) and 1:1000 phalloidin-atto647N (Sigma-Aldrich, cat. #65906)) for 2 days at 4°C and washed in PBS. The sample was stained with DAPI (1 μg/ml) diluted in PBST 4°C overnight. The sample was cleared with RapiClear 1.47 Solution (SunJin Lab, cat. #RC147001) overnight at 4°C. The sample was placed on a glass-well plate and imaged using a Leica Stellaris confocal microscope using a HC PL APO CS2 20x/0.75 air objective (Leica) for overview images (voxel size: $0.28x0.28x0.69$ μm^3) and a HC PL APO CS2 63x/1.40 oil objective (Leica) for high-resolution image stacks (voxel size: $0.0586x0.0586x0.2985$ μm^3). For the quantification of basal myosin level along the villus, villi that were located longitudinally to the objectives were imaged and stacks were recorded. Using Fiji, a Z-profile was generated using the reslice function and a line was drawn below the nuclei at the basal surface. The line profiles of several villi were overlayed relative to the distance to the villus tip.

Whole-mount organoid staining.
Organoids were fixed in 4% paraformaldehyde for 30 min at room temperature, washed in PBS, blocked in blocking solution (PBS; 0.5% Tween, 5% normal goat serum) for 1 h at room temperature and stained overnight with primary antibodies in antibody solution (PBS; 0.1% Tween, 1% normal goat serum). Primary antibody used for phosphor-Myosin-II staining: Rabbit anti-mouse phospho-myosin light chain 2 (Thr18/Ser19) (Cell Signaling Technology, cat. #3674). Primary antibody used for *Epcam* staining: Rat Anti-mouse CD326-APC (Clone G8.8) (eBioscience, cat. #17-5791-80). After washing in PBS, organoids were stained with secondary antibody (Goat anti-Rabbit IgG Alexa-488, Invitrogen, cat. #A-11008) in antibody solution for 1.5 h at room temperature. After washing in PBS, organoids were stained with DAPI (1 μg/ml) in PBS for 15 min and mounted on glass slides.

STED super-resolution microscopy.
Organoids were fixed in 4% paraformaldehyde for 30 min at room temperature, washed in PBS, blocked in blocking solution (PBS; 0.5% Tween, 5% normal goat serum) for 1 h at room temperature and stained overnight for phalloidin conjugated to the STED fluorophore atto647-N. The organoids were washed and incubated for 10 min at room temperature in PBS containing DAPI (1 μg/ml). Organoids were mounted in ProLong Gold Antifade Mountant (Molecular Probes/Thermo Fisher Scientific, cat. # P10144) medium on a glass carrier. A 0.16-0.19-mm-thick (thickness 1.5) cover glass (Glaswarenfabrik Karl Hecht GmbH & Co KG, cat. #41014) was placed on top, and excessive mounting medium was removed using tissue paper, dried, and sealed using nail polish. 2D-STED image stacks were collected using a Leica Stellaris 8 STED microscope with a HC PL APO CS2 100x/1.40 oil objective and type F immersion liquid. The phalloidin-atto647N-stained sample was imaged combining 650-nm excitation with the 775-nm STED depletion laser. The image was scanned with a voxel size of $0.0199x0.0199x0.1826 \ \mu m^3$, a line accumulation of 16, a dwell time of 0.75 μs. Sequentially the myosin-mNeonGreen reporter and DAPI signal was collected in the classical confocal mode.

Animal work
Mice were maintained by professional caretaker according to procedures approved by the Central Committee Animal Experimentation (CCD) of the Dutch government and approved by the KNAW/Hubrecht Institute Animal Welfare Body (IvD). Mouse strain (Mus Musculus): C57BL6/J, male and female of age 7-12 wks without genetic modifications (RRID:IMSR_JAX:000664) was used.

Laser ablation in the living mouse intestine.
Mice were sacrificed and immediately afterwards the intestine was dissected in ice-cold PBS-Orange containing CellMask Orange Plasma Membrane Stain (Invitrogen/Thermo Fisher Scientific, cat. #C10045) diluted 1:1000 and Primocin (InvivoGen; 1:500) in PBS. The lumen was flushed several times with ice-cold PBS-Orange. The musculature and connective tissue outside the intestinal tube was removed as much as possible. The intestine was cut open, inverted, and placed onto a glass-bottom well with a cover glass on top to bring the sample closer to the objective. The well was filled with ENR medium containing CellMask Orange (1:1000) and Primocin (1:500). A Leica SP8 confocal microscope equipped

with a tunable Chameleon multiphoton laser with a HC PL IRAPO 40x/1.10 water objective (Leica) was used at room temperature and 5% CO2. The objective was positioned at villus regions, and the cell base identified. Laser ablation using a wavelength of 800 nm of the Chameleon laser was done with a 1-pixel wide and 15 μm long line with 80 % laser intensity for 3 iterations. Before laser ablation 10 and after ablation 30 frames were collected with a time interval of 1 s. Per mouse sample multiple positions at the villus tip and villus shaft were processed. The procedure from dissection to laser ablation was optimized to not exceed a duration of 1.5 h. To analyze tissue recoil, the Euclidean distance from the initial position was manually tracked for at least 10 cell interfaces on both sides of the ablation line. The mean recoil for each ablation experiment was calculated, and the average across multiple experiments was presented in the final graph. The initial recoil velocity was calculated by fitting a sigmoidal curve (with A: amplitude, k: steepness, t_0: inflection point, y_0: vertical offset) to each experiment and the slope of the curve at the inflection point (vinitial) was calculated:

$$f(t) = \frac{A}{1 + e^{-k(t-t_0)}} + y_0 \tag{2.1}$$

$$v_{initial} = f'(t_0) = \frac{A \cdot k}{4} \tag{2.2}$$

To ablate individual cells along their apical-basal axis, villus tip regions were selected where tissue orientation allowed a ~30 μm line cut through the full length of a single cell, using the same laser settings as described above. The boundaries of the targeted cell were segmented, and all experiments were aligned by normalizing cell dimensions prior to ablation. Average cell shapes before and after ablation were calculated, and boundary displacement vectors were computed based on these contours.

Laser point ablation

For the laser point ablation experiments, organoids were seeded onto an imaging chamber (CellVis) and imaged on a Nikon A1R MP scanning confocal microscope using a 1.30 NA 40× magnification oil immersion objective, and the incubation chamber was set to (37 ᵒC, 5% CO2) [115]. For each timepoint, 31 Z-slices were imaged with 2 μm intervals. We only selected organoids that contained at least one crypt and a villus domain. An 8 ms laser stimulus of 800 nm wavelength was applied (MaiTai DeepSee, 100% laser power), which was optimized such that epithelial barrier integrity was maintained while still triggering cell extrusion. Time lapse videos for laser stimulation were acquired at more than 2 frames-per-second. Only one ablation was done per organoid and organoids were subsequently imaged for at least one hour to determine if a stimulated cell extruded. Ablated organoids were excluded from analysis if (i) the stimulus missed the organoid (i.e., if no visible bleaching of the nucleus occurred and/or no cavitation bubble was observed when stimulating the cytoskeleton), (ii) imaging failed within one hour after stimulation, (iii) ablated cells extruded to the basal side in response to the ablation. Determination of the region (base/nucleus/junction) in which cells were ablated was determined as follows: If a cavitation bubble was observed below the nucleus, a cell was classified as ablated at the base. If no cavitation bubble was observed, but the nucleus was partially bleached, the cell was classified as ablated in the nucleus. If a cavitation bubble was observed in the

same xy-plane as the nucleus but a cavitation bubble was observed outside the nucleus, the stimulation was classified as a stimulation of a multicellular junction. Whether cells extruded (within 1 hour) in response to point ablation was determined by visual inspection. To determine the extrusion time of cells that extruded in response to the point ablation, we tracked the nuclei of the extruding cells and their immediate neighbors for 1 hour. For single-cellular extrusions, we computed the relative vertical displacement of the extruding cells from their non-extruding neighbors (ΔZ) as follows:

$$\Delta Z = Z_i - \frac{1}{|\Omega_i|} \sum_{j \in \Omega_i} Z_j \tag{2.3}$$

Where Ω_i is the set of neighbors of extruding cell i. For multicellular extrusions, we computed ΔZ as:

$$\Delta Z = \bar{Z}_{ext} - \frac{1}{|\Omega|} \sum_{j \in \Omega} Z_j \tag{2.4}$$

Where $\bar{Z}_{ext}$ is the average Z-level of all the co-extruding cells, and Ω is the set of all non-extruding neighbors of all extruding cells. Extrusion time was defined as the time until $\Delta Z > 5$ μm.

Real-Time quantitative PCR

Total RNA was extracted from control and *Epcam*$^{-/-}$ organoids using the RNeasy Mini Kit (Quiagen), following the manufacturer's protocol. RNA concentration was determined spectrophotometrically and diluted to a uniform concentration. cDNA was synthesized from 540 ng total RNA using the High-Capacity RNA-to-cDNA™ Kit (Applied Biosystems, cat. #4388950). Quantitative PCR was performed using SYBR Green Supermix (Bio-Rad, cat. #1725121) in 384-well format with gene-specific primers (Table 2.3) and 4 ng of cDNA per reaction. The cycling protocol consisted of an initial denaturation at 95 °C for 3 min, followed by 40 cycles of 95 °C for 10 s, 60 °C for 30 s, and 72 °C for 30 s. Fluorescence was recorded after each cycle. Average CT values were calculated from technical duplicates and normalized to the geometric mean of Actb and Gapdh. Relative gene expression levels were determined using the $\Delta\Delta$CT method and normalized to control organoids.

Pharmacological treatments

For the laser ablation of blebbistatin-treated organoids, the organoids were incubated overnight in ENR medium supplemented with 100 μM (±)-blebbistatin (Abcam, cat. #120425). For measuring extrusions in mosaic *Epcam*$^{-/-}$ organoids, organoids were pre-incubated for 5 h in 50 μM Y-16 (MedChemExpress, cat. #HY-12649) and 10 μM Y27632 (AbMole, cat. #M1817) and imaged for 16 h.

Statistical analysis

Statistical tests were done using the scipy.stats library [274] and the Matlab Statistics and Machine Learning Toolbox (Mathworks).
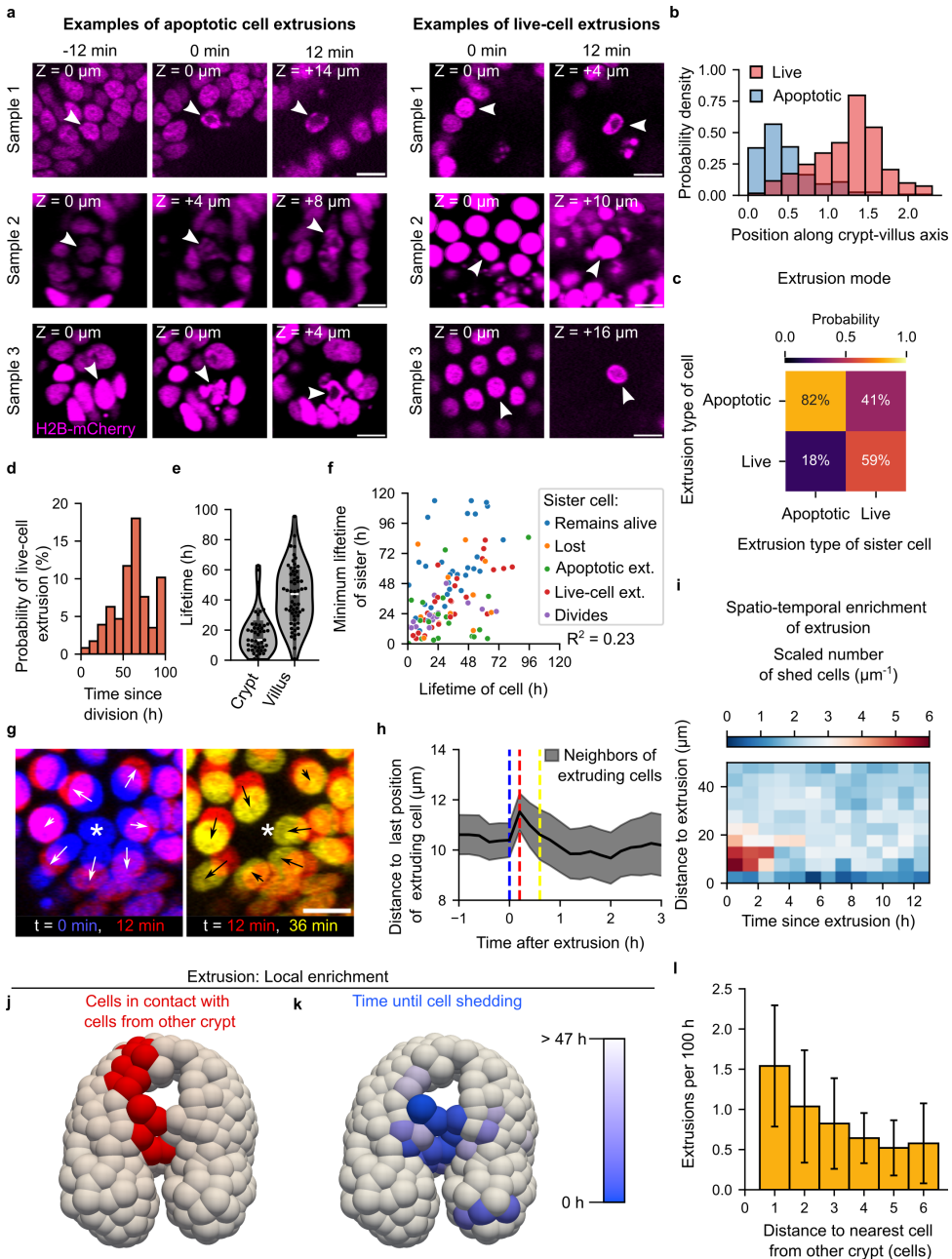
2.5 SUPPLEMENTARY INFORMATION

Figure 2.8: Quantitative analysis of apoptotic and live-cell extrusions in space and time.

Figure 2.8: (continued) (a) Confocal timelapse images of an organoid expressing H2B-mCherry nuclear marker showing a representative example of an apoptotic and live-cell extrusions. Note that the extruding cell's nucleus fragmented while the cell was still in the epithelium. (b) Probability distributions of apoptotic and live cell extrusion events along the normalized crypt-villus axis (368 live and 211 apoptotic extrusions). (c) Probabilities of a cell to undergo apoptotic or live-cell extrusion given that its sister either live-extruded (51 cases) or extruded apoptotically (119 cases). (d) Probability of a cell undergoing live-cell extrusion in the next 10 h plotted against the cell age (time since division). (e) Lifetime distribution for cells that undergo live-cell extrusion plotted separately for cells extruding in the crypt and the villus region. (f) Scatterplot showing the minimum sister cell lifetime of live-extruding cells. Colors indicate the fate of the sister cell at the last trackable time point. "Lost" indicates cells that were lost from imaging (e.g. because they moved out of view). (g) Movement of nuclei directly before and after cell extrusion. Scale bar: 10 μm. (h) Distance of neighbor cells to the last position of an extruding cell over time during an extrusion (mean ± S.E.M.; N = 15 extrusion events with 87 neighbors tracked in total). (i) Spatiotemporal enrichment of cell extrusion events. (j-l) Cells most frequently extruded in the villus domain, and most abundantly in a region where cells from neighboring crypts converged.
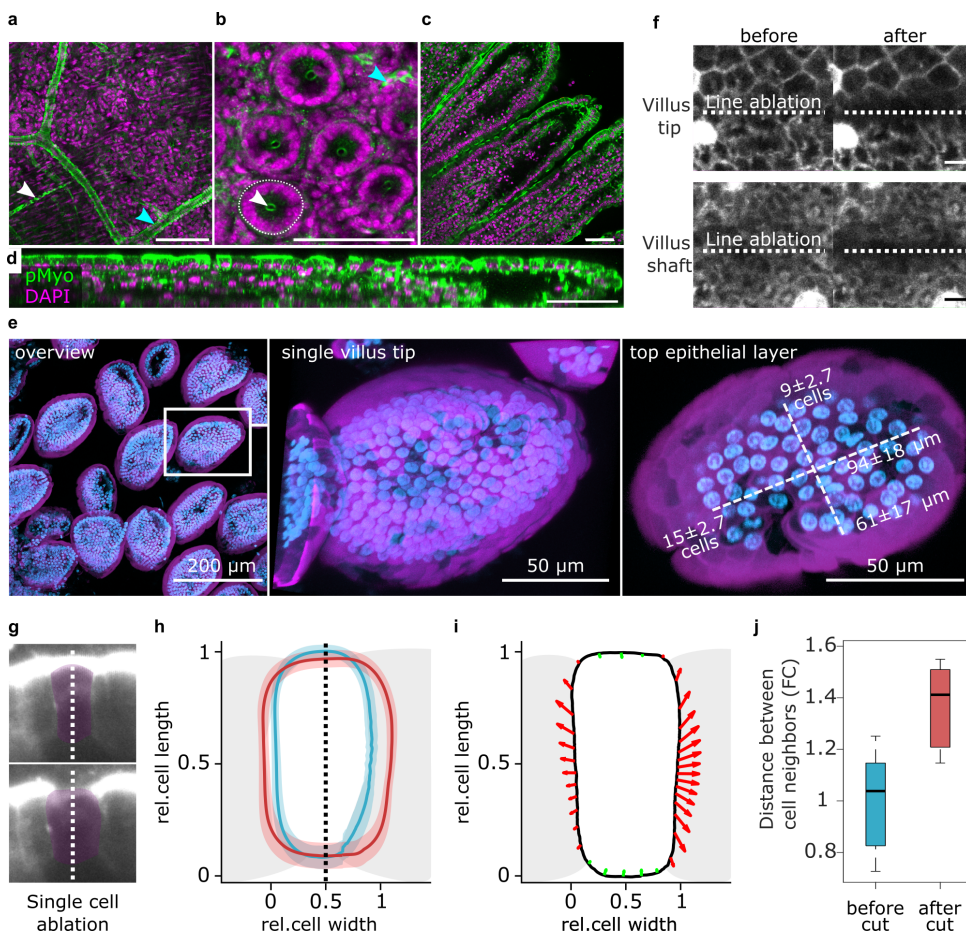
Figure 2.9: Laser ablation reveals tensile forces at the villus tip. (a-d) Whole mount tissue stain of the mouse intestine showing phosphorylated Myosin-II (pMyo) and nuclei (DAPI). Scale bars: 50 μm. (a) Tissue below the intestinal crypts showing muscle (white arrowhead) and endothelia (cyan arrowhead) enriched for active myosin. (b) Intestinal crypts showing apical myosin enrichment (white arrowhead) and myosin signal in migratory immune cells (cyan arrowhead). The dashed line indicates the basal surface of a crypt. (c) Intestinal villi. (d) Intestinal villus positioned longitudinal to the imaging plane was imaged and quantified to obtain basal pMyo profiles. (e) Whole mount stain of mouse intestinal villus tips for DAPI (blue) and phalloidin (magenta) at different magnifications showing the geometry and dimensions of the villus tip. On the right: the epithelium at the villus tip. Quantification of cell numbers and dimensions based on n = 15 villus tips. (f) Confocal section of the cell base of the villus tip (top) and villus shaft (bottom) stained with the live plasma membrane marker CellMaskOrange before (left) and after (right) line ablation (dashed line). Scale bars: 10 μm. (g) Still images before and after ablation of a single epithelial cell along its apical-basal axis (magenta overlay) at the villus tip. The white dashed line marks the ablation plane. Scale bar, 5 μm. (h) Average cell outlines before (blue) and after (red) cell ablation. Cell shapes were normalized and aligned; shaded regions indicate standard deviation across all experiments. An orthogonal recoil is observed post-ablation. (i) Recoil vectors (red arrows: outward retraction; green arrows: inward retraction) plotted from segmented cell outlines. Recoil occurs orthogonally to the ablation axis, consistent with the presence of tensile forces. (j) Quantification of the distance between neighboring cell boundaries before and after ablation shows an increase upon cutting. (h-j) Data from 8 ablations from N = 2 mice.
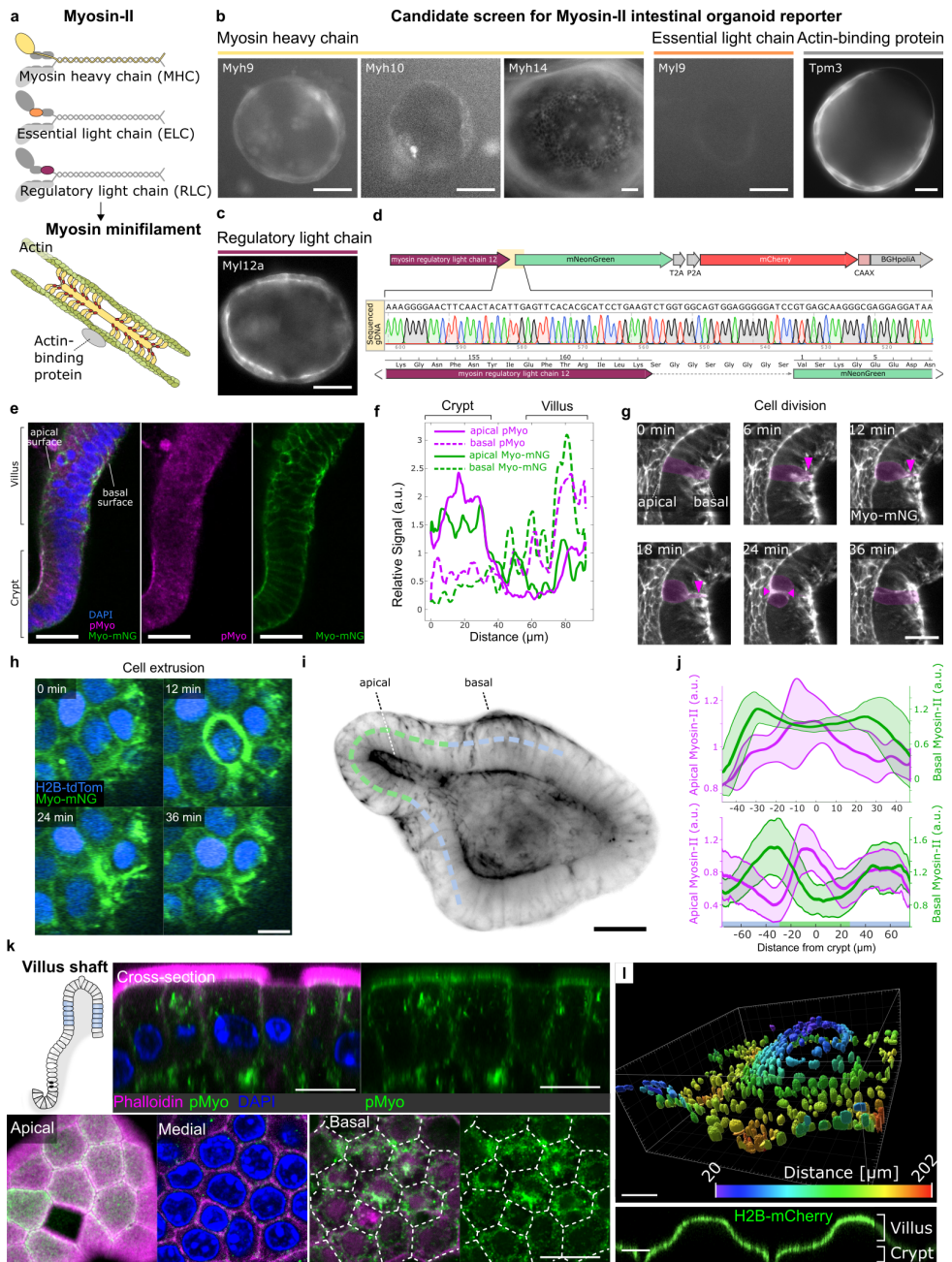
Figure 2.10: Generation and characterization of myosin regulatory light chain reporter organoid lines.
(a) Scheme of the Myosin-II multiprotein complex constituting myosin minifilaments. (b, c) CRISPR-HOT was used to tag components of the myosin complex with fluorescent reporters, including heavy chains (*Myh9*, *Myh10*, *Myh14*), light chains (*Myl9*, *Myl12a*), and the actin-binding protein *Tpm3*. Only *Myl12a* (c) was expressed at sufficiently high level to visualize the protein and showed expected localization pattern.

Figure 2.10: (continued) (d) Sanger sequencing confirming in-frame insertion of mNeonGreen into the *Myl12a* locus (Myosin-mNG). A membrane-anchored mCherry (CAAX) was co-expressed via a T2A-P2A linker. (e, f) Micrographs (e) and quantification (f) of the relative signal of phospho-Myosin light chain 2 staining, Myosin-mNG. Scale bar: 50 µm. (g) Timelapse of Myosin mNG reporter organoid during cell division (magenta). Arrowheads show myosin enrichments as the cell body shifting apically and during the formation of the cytokinetic furrow. Scale bar: 25 µm. (h) Timelapse of Myosin-mNG reporter organoid during cell extrusion. Scale bar: 5 µm. (i) Light-sheet section of a Myosin-mNG reporter organoid (inverted grayscale). Dashed line (crypt green, villus domain blue) indicates the profile quantified in (j). Scale bar: 25 µm. (j) Quantification of apical and basal myosin along the crypt-villus axes of 11 organoids (top) and of a single developing crypt over multiple time points (bottom; 50 time points with interval of 7 min); lines show mean ± SD of organoid average (top) or temporal average (bottom). (k) Confocal images of cells from the mouse intestinal villus shaft (blue region in schematic), showing cross-sections (top) and top views of apical, medial, and basal planes (bottom), stained for F-actin (phalloidin), phospho-myosin, and nuclei (DAPI). Dashed lines mark cell boundaries. Scale bars: 5 µm. (l) Z-colored 3D rendering (top) and side-view (bottom) of organoids expressing a nuclear marker (bottom) grown on synthetic substrate mimicking the in vivo architecture of the intestinal epithelium. Scale bars: 100 µm (top), 50 µm (bottom).
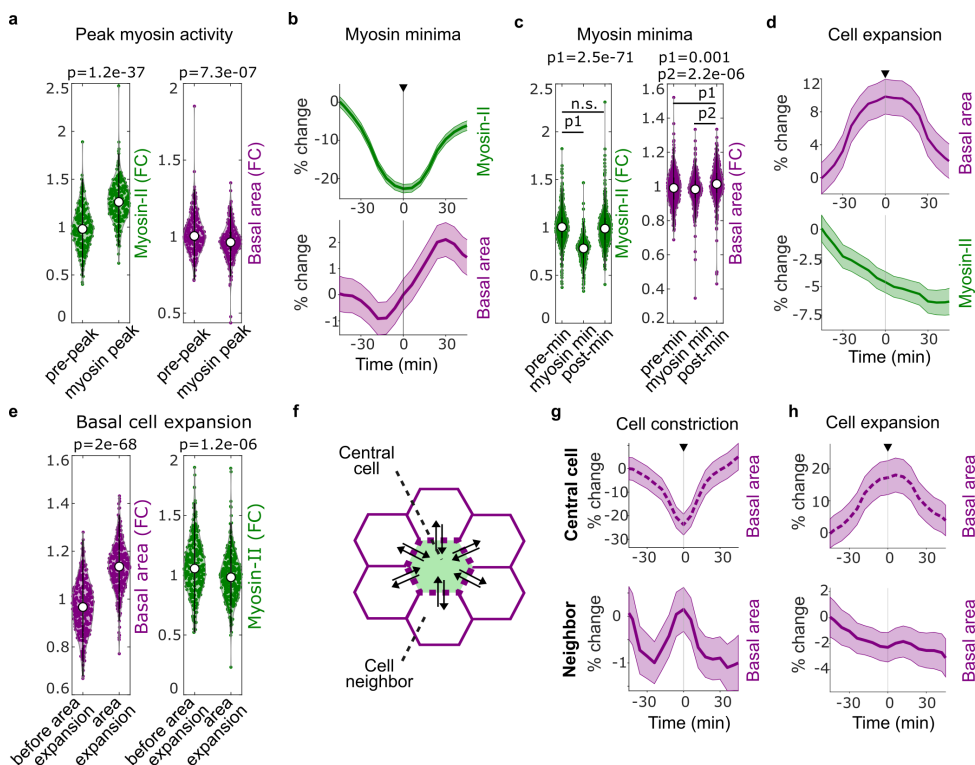
2

Figure 2.11: Dynamic Myosin-II remodeling regulates basal area fluctuations and mechanical coupling between neighboring cells. (a) Violin plots showing fold change (FC) in Myosin-II intensity and basal cell area before and during Myosin-II peaks (left), and before and during basal expansion (right). (b) Time-aligned mean traces of Myosin-II minima (top) and the concurrent average change basal area (bottom) showing a concomitant area increase (mean ± S.E.M.). (c) Violin plots showing fold change (FC) in Myosin-II intensity (left) and basal cell area (right) before, and during and after Myosin-II minima. (d) Time-aligned mean traces of basal cell area expansions (top) coincide with decreasing Myosin-II levels (bottom), indicating that expansion is associated with reduced contractile activity (mean ± S.E.M.). (e) Violin plots showing fold change (FC) in basal area (left) and Myosin-II (right) during basal cell expansion. (a, c, e) White dots indicate medians; Paired comparisons: p-values from two-sided one-sample Student's t-test. (f) Schematic illustrating the reciprocal relationship between basal cell area (magenta) and Myosin-II intensity (green) in one cell and the physical interaction of a central cell and its neighbors. (g) Time-aligned mean traces of basal area for constricting cells (top; dashed line) and their neighbors (bottom; solid line). (h) Time-aligned mean traces of basal area for expanding cells (top; dashed line) and their neighbors (bottom; solid line). Neighboring cells contract when a central cell expands, and vice versa. Data in (g, h) shows mean ± S.E.M. Number of cells analyzed: 309 (a), 408 (b, c), 379 (d, e), 115 (g), 77 (h).
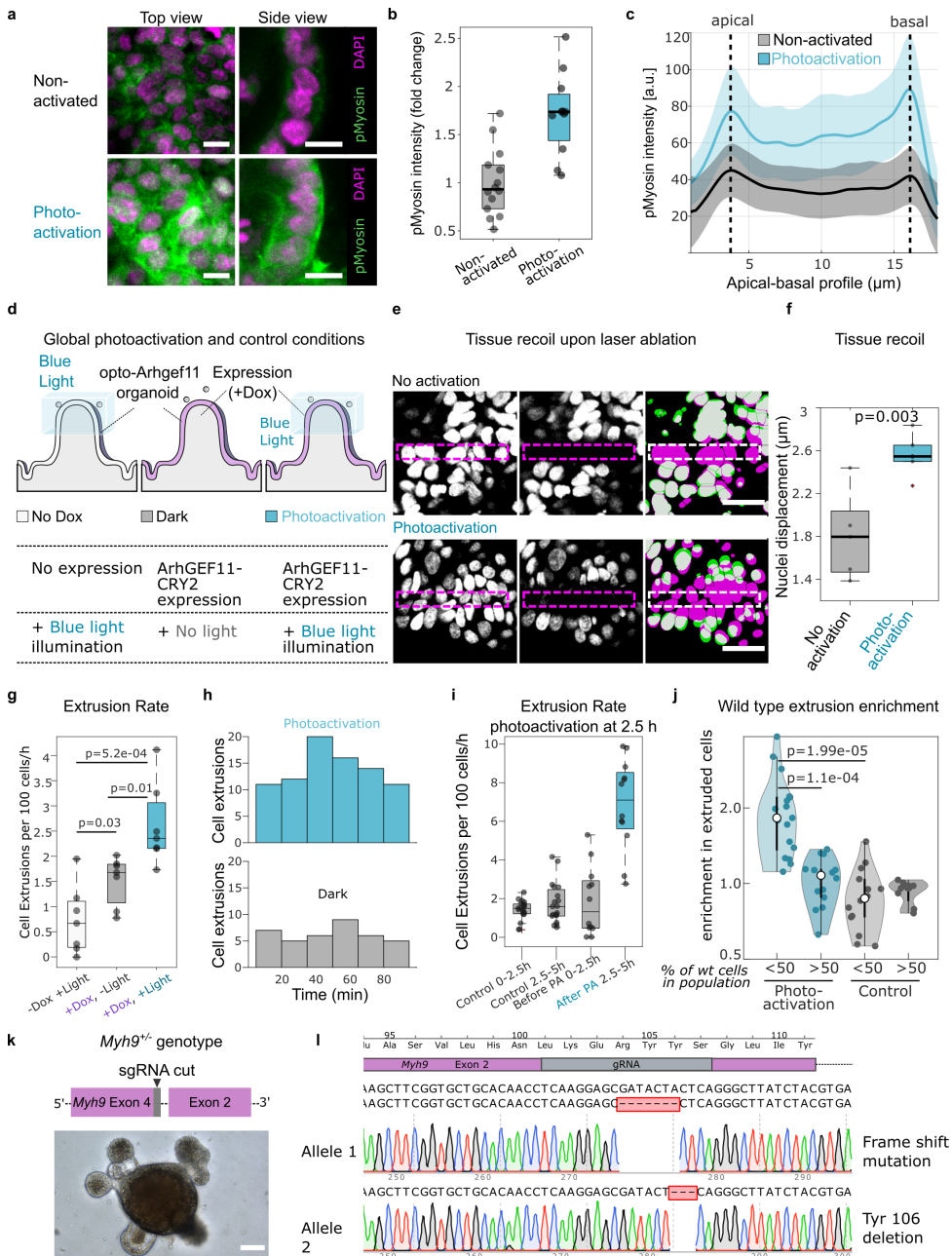
Figure 2.12: Overall increase of tissue tension increases the extrusion rate at the villus tip. (a) Confocal images of opto-Arhgef11 organoids stained for phospho-Myosin-II (green) and nuclei (magenta) under non-activated (top) and globally photoactivated (bottom) conditions. Scale bars: 10 µm. (b) Quantification of phospho-Myosin-II intensity in 14 control and 11 photoactivated organoids. (c) Apical-basal phospho-Myosin-II intensity profiles in non- and photoactivated organoids (mean ± S.E.M.; data from 7 control and 6 photoactivated organoids). Despite increased overall signal (b), subcellular distribution remains unchanged (c).

Figure 2.12: (continued) (d) Setup: Opto-Arhgef11 organoids on crypt-villus hydrogels were photoactivated at the villus tip with (right; +Dox +Light) or without (left; -Dox +Light) prior Dox induction or imaged without blue light (middle; +Dox -Light). (e) Line ablation at the synthetic villus tip in non-activated or photoactivated samples. Confocal images show nuclei before (left) and after (middle) laser ablation, and as a composite (right). Scale bars: 20 μm. (f) Quantification of recoil based on nuclear displacement (Mann-Whitney U test, 5 villi per condition). (g) Extrusion rates in conditions described in (d), from 7 villi per condition. (h) Histogram of cumulative extrusions: photo-activated (top) and non-activated villi (bottom), 7 villi per condition. (i) Quantification of extrusion rates in non- (dark) and photoactivated (PA) villi. PA samples were first imaged with 640 nm light, as in controls. Data from 19 dark and 13 photoactivated villi. (j) Violin plot showing fold enrichment of wild-type cells in extruded populations from mosaic opto-Arhgef11 organoids, grouped by minority (<50%) or majority (>50%) presence. Data: 31 organoids; dots represent organoids; two-sided one-sample Student's t-test. (k) Schematic of sgRNA targeting exon 2 of *Myh9* and brightfield image of an intestinal organoid with a heterozygous knockout. Scale bar: 25 μm. (l) Sanger sequencing confirmed a heterozygous knockout: one allele had a frameshift causing premature truncation, the other a 3-base deletion removing Tyr106.
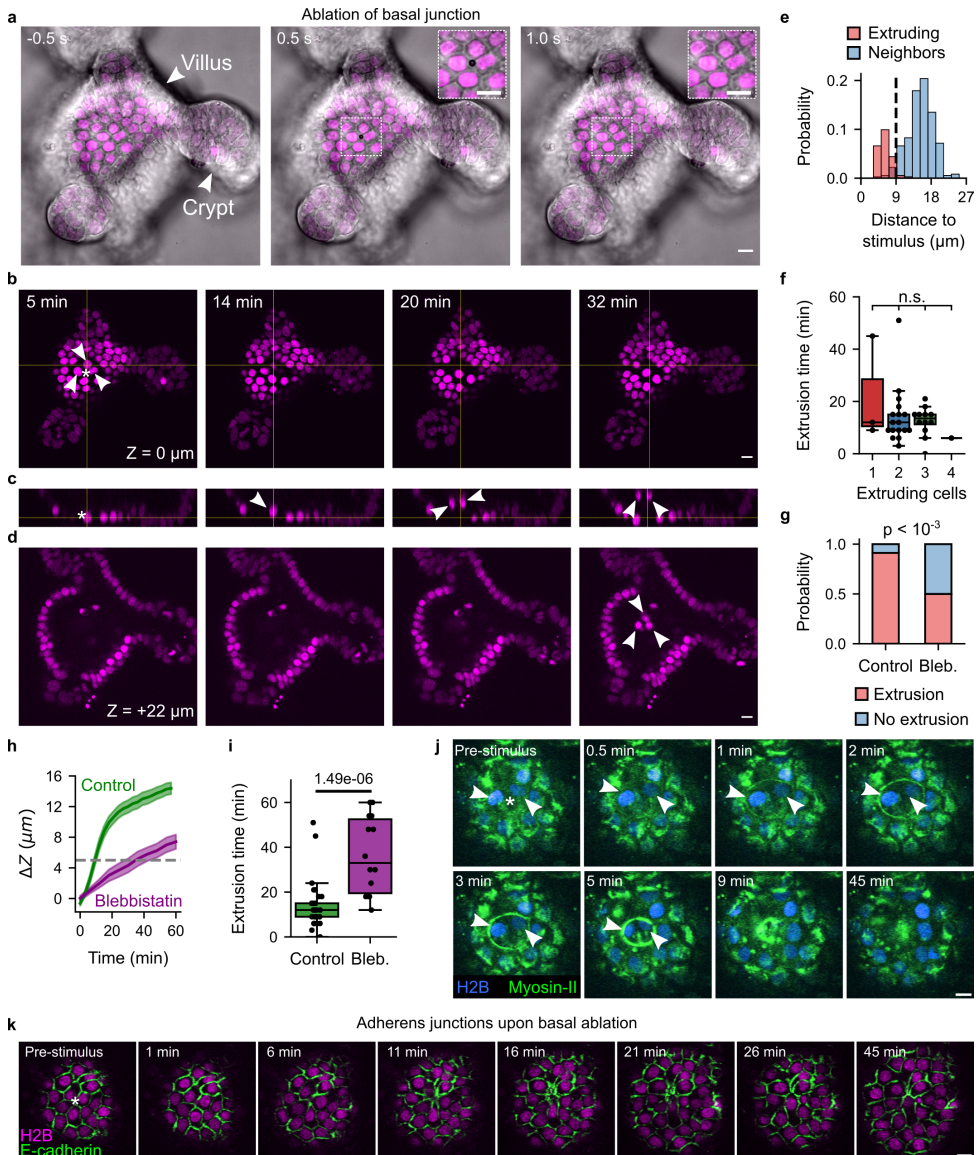
Figure 2.13: Local ablation of intercellular junctions triggers multicellular extrusion. (a) Local ablation of a tri-cellular junction. Confocal images show transmitted brightfield overlaid with H2B-tdTomato nuclear marker (magenta). Dashed rectangle shows region enlarged in the zoom-in (top right). (b-d) Timelapse confocal images showing the extrusion of three cells induced by the ablation of a tri-cellular junction (H2B-tdTomato nuclear marker, magenta). Top view showing cells at the level of the epithelium (b) and shifted 22 μm towards the lumen (d). The cross-section is shown in (c). Arrowheads indicate the extruding cells. All scale bars in panels a-d indicate 10 μm. (e) Upon ablation of basal junctions, cells within a range of 9 μm (measured from the nucleus center) from the ablation point extruded. (f) Extrusion time for cells responding to point-ablation of multicellular junction for given numbers of extruding cells. Extrusion time was independent of the number of extruding cells (n.s.: p > 0.05; two-sided Student's t-test; $n_1 = 3$, $n_2 = 18$, $n_3 = 12$, $n_4 = 1$).

Figure 2.13: (continued) (g) Fraction of cases in which extrusion was observed within 1 hour after point-ablation at cell junctions, for both untreated and blebbistatin treated organoids (Fisher's exact test; 68 control and 42 blebbistatin-treated organoids). (h) Z position of extruding cells relative to the epithelium (ΔZ) for blebbistatin-treated and untreated controls (mean ± S.E.M.). (i) Extrusion time of blebbistatin-treated and untreated control organoids (two-sided Student's t test). (h, i) Data from 34 control organoids and 20 blebbistatin-treated organoids. (j) Myosin dynamics upon ablation of basal bicellular junction. Myosin accumulated around the two affected cells (arrows), constricted and the cells extruded. Scale bar: 5 μm. (k) Organoid expressing a live reporter for E-cadherin (*Cdh1*-mNeonGreen) together with a nuclear marker (H2B-mCherry) was ablated at basal multicellular junction. The E-cadherin signal in the ablated point (asterisk) disappeared but remained present in untargeted cell boundaries suggesting that epithelial continuity was maintained during the process of multicellular extrusion. Scale bar: 10 μm.
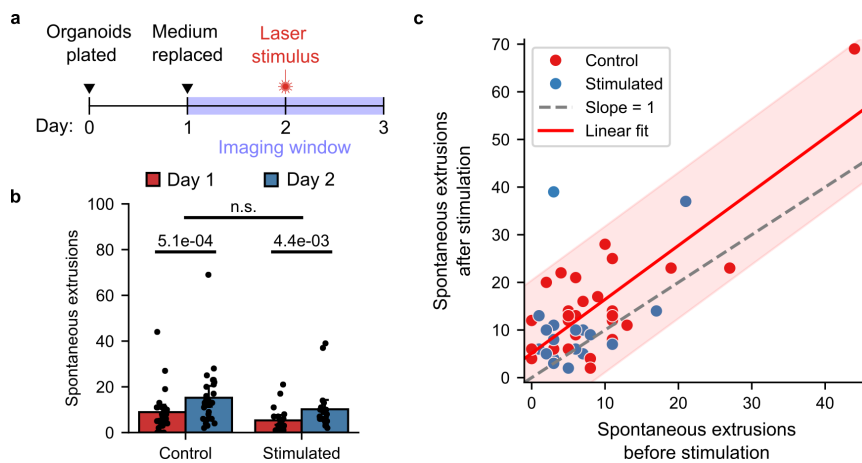
Figure 2.14: Multicellular extrusion in response to basal junction ablation did not lead to an increase of overall cell death. (a) Timeline of the experiment: Organoids were plated on day 0 and organoids were imaged for exactly 24 hours, starting on day 1. After this first timelapse, some organoids were ablated at a multicellular junction in the villus (22 organoids), and the rest left as a control (28 organoids). (b, c) Number of spontaneous extrusions before and after stimulation. There was a significant increase in the number of spontaneous extrusions between the timelapse started on day 1 and the one started on day 2 because the organoids were older ($p < 0.01$; Wilcoxon signed rank test), but the difference in the number of extruding cells was not significantly different between control and ablated organoids (Mann-Whitney U test). Shown is the data from N = 3 independent timelapse experiments.
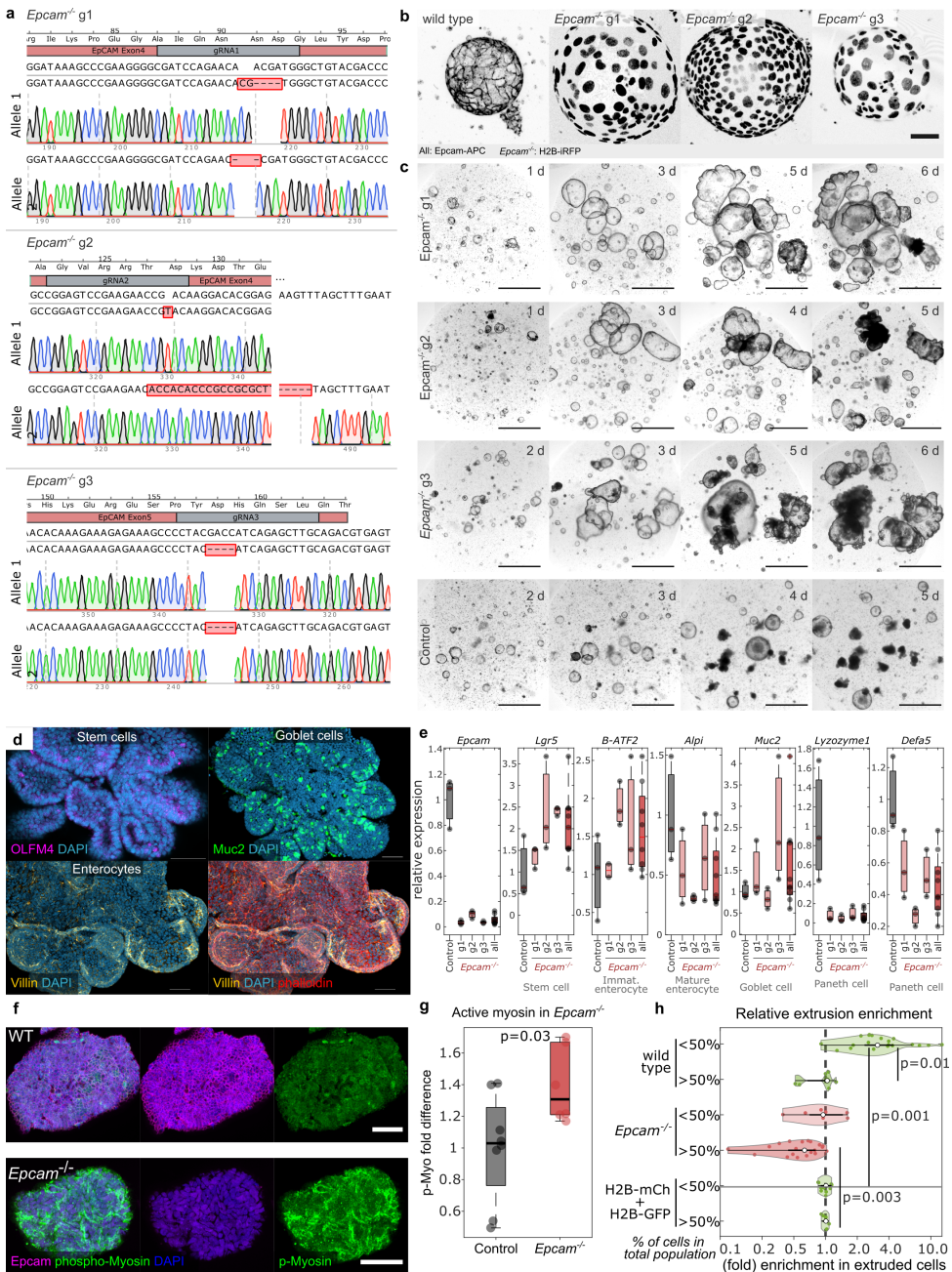
Figure 2.15: Characterization of *Epcam*^−/− organoid lines reveals impaired morphology, altered differentiation, and upregulated Myosin-II activity. (a) CRISPR/Cas9 gene editing of *Epcam*. Sanger traces of both alleles in three knockout clones (g1-g3) show frameshift mutations in exon 4 or 5. (b) Confocal images of wild-type and *Epcam*^−/− organoids (g1-g3) expressing H2B-iRFP and both stained for *Epcam*-APC (both inverted greyscale), showing loss of *Epcam* protein. Scale bar: 25 μm.

Figure 2.15: (continued) (c) Brightfield time course showing morphological changes in *Epcam*$^{-/-}$ organoids (g1-g3) versus wild type over 6 days. Scale bar: 250 μm. (d) Immunofluorescence images of *Epcam*$^{-/-}$ organoids stained for lineage markers: Olfm4 (stem cells), Muc2 (goblet cells), Villin and phalloidin (enterocytes). Scale bar: 50 μm. (e) qPCR analysis showing reduced expression of cell-type markers in *Epcam*$^{-/-}$ organoids. Boxplots show expression levels relative to wild type. *Epcam*$^{-/-}$ organoids expressed markers of all major intestinal lineages, indicating that differentiation still occurred. However, relative expression levels differed from control: stem cell (Lgr5) and immature enterocytes (B-ATF2) markers were elevated, goblet cell (Muc2) were unchanged, and mature enterocyte (Alpi) and Paneth cell (Lysozyme1, Defa5) markers were reduced in all three *Epcam*$^{-/-}$ lines, suggesting impaired differentiation. (f) Immunofluorescence staining of WT and *Epcam*$^{-/-}$ organoids for phospho-Myosin-II (green), *Epcam* (magenta), and nuclei (blue). Scale bar: 50 μm. (g) Quantification of phospho-Myosin intensity in 6 *Epcam*$^{-/-}$ and 8 wild type organoids (P-values from paired two-tailed Student's t-tests. (h) Violin plot showing the fold enrichment of *Epcam*$^{-/-}$ and wild-type cells in extruded populations, grouped by minority (<50%) or majority (>50%) genotype in mosaic organoids (27 organoids). The same analysis for the control (mosaic organoid with wild type H2B-mCherry and H2B-iRFP) shows no enrichment bias between differently labeled wild type cells (17 organoids). Each dot represents one organoid; p-values calculated based on two-sided one-sample Student's t-test. Dashed line indicates equal extrusion probability.
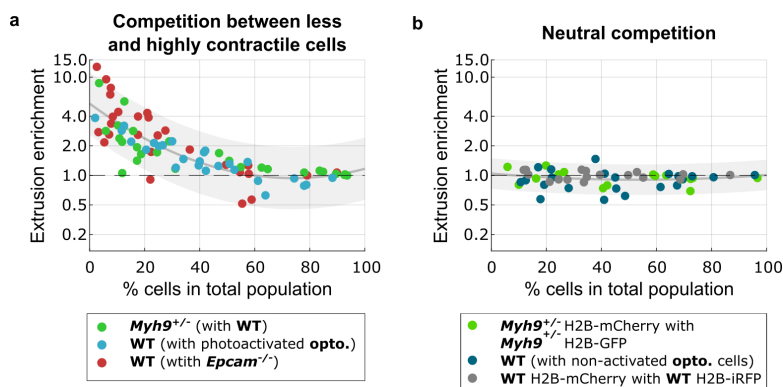
Figure 2.16: Cells with lower capability to exert tension than their direct neighbors preferentially extrude across a broad range of experimental manipulations. Note that the "Enrichment" on the y-axis refers to the ratio between the fraction of cells of a type extruding and the fraction of those cells in the organoid. (a) Extrusion enrichment is > 1 for a cell type that is less contractile ("weaker") than the other in mosaic organoids. These are *Myh9*$^{+/-}$ cells in mosaics with wild type (WT) cells, WT cells in mosaics with photo-activated opto-Arhgef11 (opto.) cells, and WT cells in mosaics with *Epcam*$^{-/-}$ cells. Data from 28 WT/*Myh9*$^{+/-}$, 31 WT/opto. and 34 WT/*Epcam*$^{-/-}$ organoids. (b) Extrusion enrichment is approximately 1 (balanced) in all neutral competition conditions. These conditions are mosaic organoids consisting of *Myh9*$^{+/-}$ cells (with different nuclear markers), mosaic organoids consisting of WT and opto. cells but without photo-activation, and WT organoids from two different WT organoid lines with different nuclear markers. Data from 16 *Myh9*$^{+/-}$/ *Myh9*$^{+/-}$, 22 WT/nonactivated opto. and 17 WT/WT mosaic organoids.

Table 2.1: CRISPR-Cas9 guide RNAs.

Gene	sgRNA	Application
Myh9	CGATGCCAAGGCAGCTGAAT	knock-in
Myh10	ACAGCCACCCCAATCAGAAT	knock-in
Myh14	TCTAGGACAGACTGGATCAT	knock-in
Myl9	CAAACACGGCGCCAAGGACA	knock-in
Myl12a	TTCACACGCATCCTGAAGCA	knock-in
Tpm3	GGGAGGTCTACATCTCGTTC	knock-in
Cdh1	GCGGTGGTGAGGACGACTAG	knock-in
Myh9	TCAAGGAGCGATACTACTCA	knock-out
Epcam g1	GGGCGATCCAGAACAACGAT	knock-out
Epcam g2	CGGAGTCCGAAGAACCGACA	knock-out
Epcam g3	GCAAGCTCTGATGGTCGTAG	knock-out

Table 2.3: RT-qPCR primers.

Gene	Forward primer (5'-3')	Reverse primer (5'-3')
Actb	GGCTGTATTCCCCTCCATCG	CCAGTTGGTAACAATGCCATGT
Gapdh	GATTTGGTCGTATTGGGCGC	TTCCCGTTCTCAGCCTTGAC
Lgr5	CCTACTCGAAGACTTACCCAGT	GCATTGGGGTGAATGATAGCA
Batf2	GCCCAGCGCAGCCGGCAGAA	CCAGCTCAGTCTGCAAGGCCT
Alpi	GGCTACACACTTAGGGGGACCTCCA	AGCTTCGGTGACATTGGGCCGGTT
Muc2	GAAGCCAGATCCCGAAACCA	CCAGCTTGTGGGTGAGGTAG
Lyz1	GGTGGTGAGAGATCCCCAAG	CAGACTCCGCAGTTCCGAAT
Defa5	TCAAAAAAGCTGATATGCTATTG	AGCTGCAGCAGAATACGAAAG
Epcam	GAGTCCGAAGAACCGACAAGGA	GATGTGAACGCCTCTTGAAGCG

3

3

Loss of Paneth cell contact starts a WNT differentiation timer in intestinal crypts

"You may delay but time will not,
and lost time is never found again."

Benjamin Franklin

WNT signaling is pivotal to the renewal of many organs including the intestine. WNT gradients are thought to provide a spatial differentiation cue, and hence control the required spatial patterning of cell types. Testing this mechanism is difficult, however, as current methods are static while the underlying processes are highly dynamic. Here, we show that a 'timer' mechanism rather than spatial cues controls the WNT signaling decreases that drive cell differentiation. Using live-cell imaging and single-cell tracking of intestinal organoids, we find that WNT signaling in stem cells decreases immediately after loss of Paneth cell contact. This WNT signaling decrease does not depend on cell growth and division, and precedes differentiation, as shown by subsequent antibody staining and cell type propagation along lineage trees. Cells frequently regain Paneth cell contact, which in turn increases WNT signaling again, showing that differentiation is not progressive but rather repeatedly reset. Our WNT timer mechanism overturns existing spatial gradient models, explains differentiation within the intestinal crypt, and may well be more broadly relevant to WNT-mediated tissue renewal.

3.1 Introduction

Only a handful of mechanisms have been identified that spatially organize cells in development. This includes lateral inhibition that coordinates cell fate decisions between adjacent cells [244], reaction-diffusion systems that generate self-organized patterns [145], and spatial morphogen gradients that regulate cell proliferation, differentiation, and migration [224]. WNT (Wingless-related integration site) signaling is considered a prototypical spatial gradient mechanism to achieve cellular patterning throughout the metazoan kingdom [16, 281]. In mammals, WNT morphogen gradients have been shown to control diverse processes such as anteroposterior patterning [5, 131], somitogenesis [180] and neural patterning [198] in the embryo, and tissue homeostasis and regeneration in adults [199].

In the vigorously renewing adult intestine, a WNT gradient along the crypt-villus axis is thought to control the underlying continuous cell reorganization [44, 250], with Notch, BMP and mesenchymal WNT playing additional roles [77, 78, 250]. Proliferation drives stem cells from the high-WNT crypt to the lower-WNT transit amplifying (TA) compartment, where differentiation is triggered, and further onwards to the villus region, where most differentiated cells reside. This WNT-driven conveyor-belt model is appealing because, by providing a spatial cue, the WNT gradient can simultaneously explain the progression of differentiation and the spatial arrangement of the different cell types along the crypt-villus axis. Testing it is challenging, however. Techniques such as lineage tracing, single-cell sequencing, and antibody staining have reported that WNT target genes including key stemness markers like Ascl2 are differentially expressed along the crypt-villus axis [190, 240, 267], that cell division is important to shaping the short-range WNT gradient [71, 179], and that differentiation is triggered stochastically following neutral competition between stem cells [148, 231, 248, 259]. However, the employed methods are static in nature while the underlying cell movements, WNT signaling activity, and differentiation are highly dynamic. Hence, how WNT signaling controls cell organization in the intestine remains incompletely understood.

Here, we developed an organoid-based method to study the spatio-temporal dynamics of WNT signaling, differentiation, and cellular reorganization. We followed intestinal organoid cells in time by cell tracking, quantified expression of the established WNT target gene Axin2 [120, 163] as a measure of WNT signaling activity, and performed subsequent multiplexed antibody staining on the same cells to link WNT signaling dynamics to differentiation. Loss of Paneth cell contact, either due to spontaneous cell rearrangements or Paneth cell ablation, was found to induce an immediate decrease of WNT signaling activity. These decreases occurred independently of cell growth and division, and for cells remaining close to or even moving towards Paneth cells. The WNT signaling decrease was followed by the differentiation of stem cells into TA-like cells, and subsequently to enterocyte and secretory types. WNT signaling increased soon after regaining Paneth cell contact, even after extended excursions. These findings indicate a novel patterning mechanism that differs fundamentally from the spatial gradient model, with the WNT signaling decrease representing a cell-intrinsic temporal cue rather than an external spatial cue. Importantly, WNT signaling thus does not directly provide positional information to stem and TA cells, but instead generates spatial patterns by coupling a timer with cell

movement, suggesting that additional processes such as cell sorting must be involved. Our WNT timer model explains recent observations of cell differentiation within the crypt and indicates that differentiation is not progressive but instead is characterized by frequent resets.

3.2 Results

WNT signaling decreases directly upon loss of Paneth cell contact

To study WNT signaling dynamics in intestinal crypts, we measured expression of Axin2, a WNT target gene and well-established reporter of active WNT signaling [163, 187] in Axin2P2A rtTA3 TA2 3xNLS-SGFP2; Rosa26mTmG intestinal organoids (Fig. 3.1a). In this Axin2 reporter line, the endogenous Axin2 promoter controlled the expression of a nuclear SGFP2 using a multi-cistronic targeting cassette, while cell membranes were labelled with tdTomato. In intestinal organoids, the only source of WNT are Paneth cells [66, 133, 233, 271], which we identified as crypt-based cells with low Axin2-reporter levels (Fig. 3.1a) [187]. We acquired a large long-term live-cell imaging dataset of Axin2-reporter organoids (N = 4 crypts), tracked individual cells with visible nuclear SGFP2 fluorescence and used the membrane marker to assess cell-cell contact (Methods). We quantified Axin2-reporter levels up to the moment of division, noting that the fluorophores are then distributed over both daughter cells without reflecting WNT signaling changes. The average Axin2-reporter level decreased with increasing distance to the nearest Paneth cell (Fig. 3.1b), as seen previously for other WNT target genes [14]. We found that Axin2-reporter levels typically increased if cells contacted a Paneth cell. After loss of contact, however, the reporter signal typically decreased within 1-2 hours, and well before the cell cycle ended, indicating a WNT signaling decrease independent of cell division (Fig. 3.1c, d) [71].

To test if this behavior was general, we analyzed all 4-hour intervals in which the monitored cell was not dividing and considered intervals where the cell was either in continuous Paneth cell contact or was not in contact. We determined the slope of the Axin2-reporter in time for each interval, and its mean absolute level (Fig. 3.1e). Cells in Paneth cell contact had a positive slope (79% of intervals) and higher absolute Axin2-reporter level than cells not in contact. The latter typically showed a negative slope (61% of intervals), especially when their absolute Axin2-reporter level was high (74% of intervals, Fig. 3.1e). Consistently, the average Axin2-reporter slope was positive only for cells adjacent to Paneth cells, while the slope was close to zero or negative for more distant cells (Fig. 3.1f). Using fluorescence-recovery after photobleaching (FRAP), we estimated Axin2 expression rates from Axin2-reporter slopes, obtaining a similar decrease with Paneth cell distance (Supplementary Note 3.5.1 and Fig. 3.5). Overall, these results indicated that direct Paneth cell contact is required to maintain active WNT signaling, with loss of Paneth cell contact directly triggering a decrease of WNT signaling in time in stem cells.
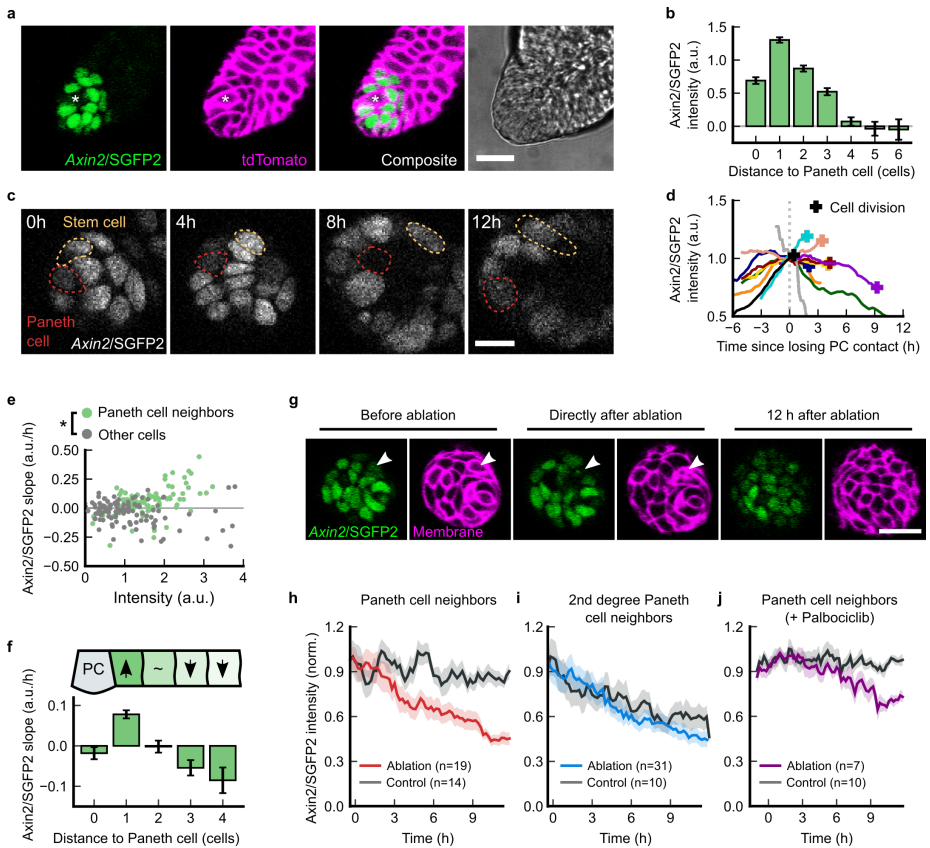
3

Figure 3.1: WNT signaling decreases directly upon loss of Paneth cell contact. (a) Axin2/SGFP2 fluorescent reporter organoids. Asterisk indicates Paneth cell; scale bar: 20 μm. (b) Axin2/SGFP2 intensity for cells in stem cell niche (median ± SEM; n > 65 cells from N = 3 organoids). (c) Time-lapse images of a stem cell (yellow line) losing contact with a Paneth cell (red line). Time is hours since loss of Paneth cell contact. Scale bar: 10 μm. (d) Normalized Axin2/SGFP2 intensity of cells that lost Paneth cell (PC) contact for more than 2 hours. Fluorescence intensity is normalized by value at time of contact loss. Crosses indicate trajectories that end with cell division. (e) Axin2/SGFP2 intensities averaged over individual trajectories versus each trajectory's slope (*p < 0.05; two-sided Student's t-test; n = 75 Paneth cell neighbors and n = 52 other cells, from N = 3 organoids). (f) Slope of Axin2/SGFP2 trajectories versus distance to the closest Paneth cell (mean ± S.E.M. of n > 37 cells per distance from N = 3 organoids) (g) Targeted photoablation of a Paneth cell (white arrow). Scale bar: 20 μm. (h, i) Normalized Axin2/SGFP2 intensity of first-degree (h) and second-degree (i) neighbors of Paneth cells following Paneth cell ablation in the crypt. (j) Normalized Axin2/SGFP2 intensity of first-degree neighbors of an ablated Paneth cell in organoids treated with cell-cycle inhibitor Palbociclib. Dark-grey curves in (h-j) are control crypts where no Paneth cell was ablated. Curves in (h-j) show the average (± SEM) of the normalized Axin2/SGFP2 time-averaged over a 2-hour window (N > 2 organoids per curve).

WNT SIGNALING DECREASES INDEPENDENTLY OF CELL GROWTH

Next, we asked whether the WNT signaling decrease resulted from dilution of surface-associated WNT by cell growth and division, or rather by growth-independent mechanisms such as WNT receptor degradation [121]. To this end, we laser-ablated individual Paneth cells and examined subsequent Axin2-reporter levels of surrounding cells (Fig. 3.1g). We

selected crypts with 1-2 Paneth cells, so that almost all cells contacted at most a single Paneth cell. Upon Paneth cell ablation, Axin2-reporter levels in directly neighboring cells declined within hours, leading to a ~50% decrease in 12 hours (Fig. 3.1h). Consistently, Paneth cell ablation did not impact second-degree neighbors, as Axin2-reporter levels showed a similar decrease whether Paneth cells were ablated or not (Fig. 3.1i). These results confirmed our observation of highly dynamic and short-ranged WNT signaling, with direct Paneth cell contact increasing and maintaining WNT signaling, and loss of contact causing an WNT signaling decrease. We found that the cell cycle inhibitor Palbociclib [241] not only arrested cell division but also cell volume growth, as observed by reconstructing 3D volumes of single cells using the membrane marker (Fig. 3.6a, b). Yet, following Palbociclib exposure, Axin2-reporter levels in Paneth cell neighbors still decreased substantially (35%) upon Paneth cell ablation (Fig. 3.1j). Control organoids with intact Paneth cells exposed to Palbociclib showed no such decrease, consistent with Paneth cell contact stimulating WNT signaling activity. Overall, this indicates that the gradual WNT signaling decrease in stem cells upon loss of Paneth cell contact is independent of cell growth and division.

WNT SIGNALING DECREASE PRECEDES DIFFERENTIATION

To elucidate how the dynamic changes in WNT signaling activity linked to differentiation [240], we employed the TypeTracker approach [291] we developed recently (Fig. 3.2a, b). After long-term live-cell imaging and single-cell tracking of Axin2-reporter organoids, we fixed organoids and performed multiple rounds of antibody staining to identify the main intestinal cell types (Paneth, stem, TA, enterocyte, goblet, and enteroendocrine, with the latter two categorized jointly as secretory). These end-point cell types were propagated backwards in time along the reconstructed cell lineages [291], to determine cell type at each point within the lineage. The highest average Axin2-reporter levels were found in stem cells, followed by Paneth cells, TA-like cells, secretory cells and enterocytes, respectively (Fig. 3.2c). The lower WNT signaling level for Paneth cells is consistent with previous work [187]. This ordering of cell types by WNT signaling also agrees with single-cell RNA sequencing data of the mouse intestinal epithelium [95] (Fig. 3.7), both for Axin2 and other WNT target genes linked to differentiation (Lgr5, Sox9, Myc and Ascl2) [14, 21, 27, 240]. Finally, we observed the expected spatial distribution of cell types, with stem cells bordering Paneth cells or separated by one cell distance, and secretory cells and especially enterocytes located further away (Fig. 3.2d).

Cells in contact with a Paneth cell at the start of imaging were either stem or TA cells at the time of fixation. Both groups showed high Axin2-reporter levels at the start of imaging, and were maintained at high levels in stem cells, but in TA cells decreased after 10 hours to 50% of the initial value (Fig. 3.2e, left). The TA cells started to lose contact with the Paneth cells 5 hours before the Axin2-reporter level decreased, whereas stem cells remained in Paneth cell contact (Fig. 3.2e, left). Cells without Paneth cell contact at the start of imaging either were TA cells at the time of fixation or had by then differentiated into enterocytes or secretory cells (Fig. 3.2e, right). While in both cases cells showed low Axin2-reporter levels at time of fixation, for TA cells this followed a steady decrease in Axin2-reporter levels over the course of the experiment, while enterocytes and secretory cells exhibited constant low Axin2-reporter levels throughout. This agrees with our previous observation
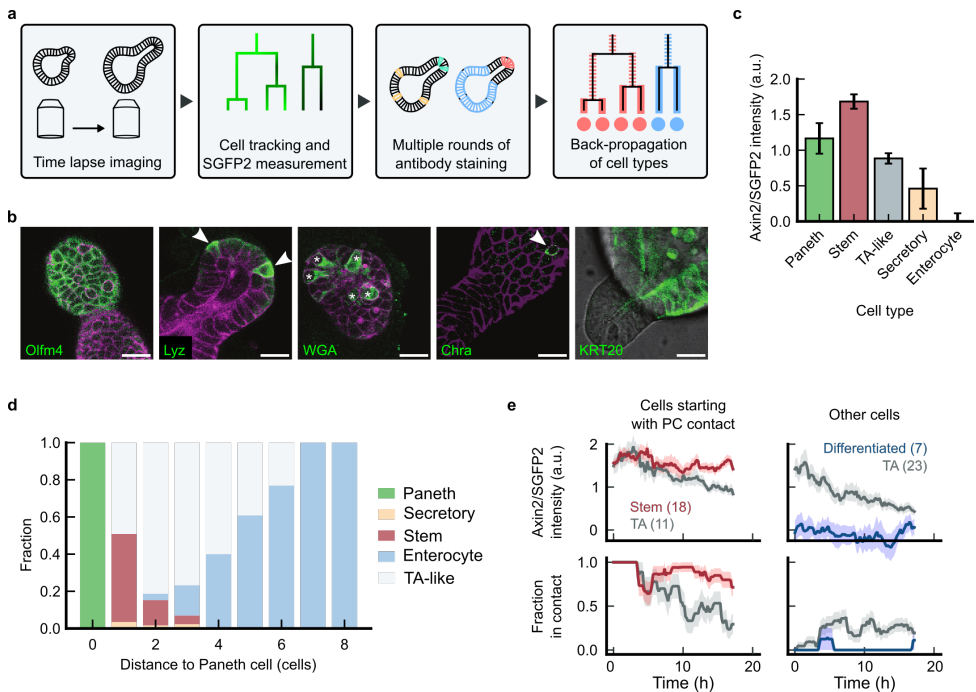
Figure 3.2: Temporal WNT signaling decline drives differentiation. (a) TypeTracker approach for linking Axin2-expression levels to differentiation. (b) Antibody staining used for cell type annotation. (c) Axin2/SGFP2 intensity for different intestinal cell types (mean ± S.E.M. across all time points, for n = 26 Paneth cells, n = 62 stem cells, n = 183 TA-like cells, n = 10 secretory cells and n = 15 enterocytes). (d) Position of different cell types relative to the closest Paneth cells, as observed at the time-lapse imaging end point (n > 3 cells per distance). (e) Axin2/SGFP intensities and corresponding contact fractions with Paneth cells (PCs) for stem cells (red), TA-like cells (gray) and differentiated cells (blue). Lines and shaded area indicate mean ± S.E.M. of 2-hour time-averaged intensities (top) and fractions in contact (bottom). Number in parenthesis indicates the number of cells used to compute the curves.

that expression of differentiation markers requires at least one cell cycle [291] and hence is detectable only after WNT signaling has been low for that time. Consistent with the low or decreasing WNT signal, both groups showed reduced levels of Paneth cell contact (Fig. 3.2e). Overall, these experiments indicate a specific sequence of events underlying differentiation: First, stem cells lose Paneth cell contact (5-hour timescale). Then, they decrease in WNT signaling, lose stem cell markers and assume TA cell fate (10-hour timescale). Finally, differentiation markers are expressed after low WNT signaling for over 10 hours.

A timer model of WNT-mediated differentiation.

Together, our observations indicated a 'timer' model. In this model, WNT signaling decreases cell-intrinsically and gradually in time for stem cells that no longer contact Paneth cells, which in turn triggers differentiation to TA and subsequently to terminally differentiated cell types. Maintenance of WNT signaling requires continued Paneth cell contact. Our timer model contrasts with spatial gradient models [71], where WNT signaling depends

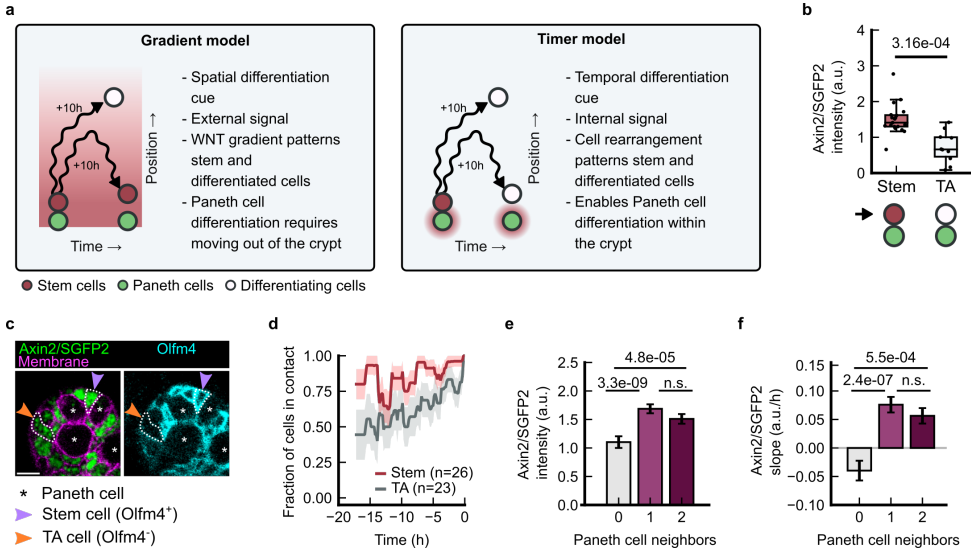strictly on the distance to Paneth cells, and hence provides a spatial differentiation cue (Fig. 3.3a).

Figure 3.3: A timer model of WNT-mediated differentiation. (a) Gradient and Timer model for differentiation in the intestinal crypts. (b) Axin2/SGFP2 intensity for stem and TA cells found in contact with Paneth cells (n = 10 stem cells and n = 15 TA-cells identified based on Olfm4 staining, p < 0.001; Mann-Whitney U test). (c) Micrographs of crypt with Axin2/SGFP2 and membrane signal (left) and Olfm4 staining (right). Arrows indicate a representative stem cell (violet arrows) and TA cell (orange arrows). Asterisks indicate Paneth cells, which are identified by low Axin2/SGFP2 signal and granules. Images were rescaled and Axin2/SGFP2 signal was smoothed for optimal visibility. Scale bar: 10 μm. (d) History of Paneth cell contact for stem (red) and TA cells (gray). Line and area indicate mean ± S.E.M. of n = 49 cells from N = 3 organoids. (e, f) Axin2/SGFP2 intensity and slope for cells with 0, 1 or 2 Paneth cell neighbors (n > 30 cells from N = 3 organoids; value above bar indicates p-value for Mann-Whitney U test).

A key functional implication of our timer model is that it explains terminal differentiation within the crypt, as recently observed for Paneth cells [30, 291]. In the timer model, stem cells can decrease WNT signaling and lose stemness already when still close to Paneth cells, in contrast to spatial gradient models (Fig. 3.3a). To verify this prediction, we tested for the presence of differentiating cells in close vicinity of Paneth cells. Indeed, we identified a small subgroup of TA cells that were in direct Paneth cell contact at time of fixation. Paneth cell-contacting TA cells had lower Axin2-reporter levels than Paneth cell-contacting stem cells (Fig. 3.3b, c), implying that their WNT signaling activities were distinct despite their similar position. Importantly, when examining cell trajectories prior to fixation, these TA cells showed a history of reduced Paneth cell contact compared to Paneth cell-contacting stem cells (Fig. 3.3d). This indicated that they gained contact recently, while the stem cells had been in prolonged contact. We excluded that differences in Axin2-reporter level reflected the number of direct Paneth cell neighbors (Fig. 3.3e, f). Together, these data were consistent with the timer model and contrasted with spatial gradient models.

DIFFERENTIATION AS A REPEATED TRIAL PROCESS

Many cells switched multiple times between positions in and out of contact with a Paneth cell, on a timescale of multiple hours (Fig. 3.4a), including cells that regained Paneth cell contact after 5-10h without contact. Cells that regained Paneth cell contact did so by moving in from up to 4 cell distances away (Fig. 3.4b). This inward movement was accompanied by a strong decrease in Axin2-reporter level (Fig. 3.4c, d). We note that this observed loss of WNT signaling activity in cells moving towards the WNT source is inconsistent with the spatial gradient model but readily explained by the timer model (Fig. 3.3a). Moreover, cells that regained Paneth cell contact generally exhibited an immediate (0-5 h) increase in Axin2-reporter levels (Fig. 3.4e, f), with a slope comparable to that of cells already in prolonged Paneth cell contact (> 5h). Overall, these results show that WNT signaling activity depends crucially on each cell's unique history of Paneth cell contact, as driven by cell rearrangements within the crypt. It also reveals that differentiation is an inherently random repeated trial process, driven by a WNT-decrease timer that counts down upon loss of Paneth cell contact but is repeatedly reset when contact is randomly regained.
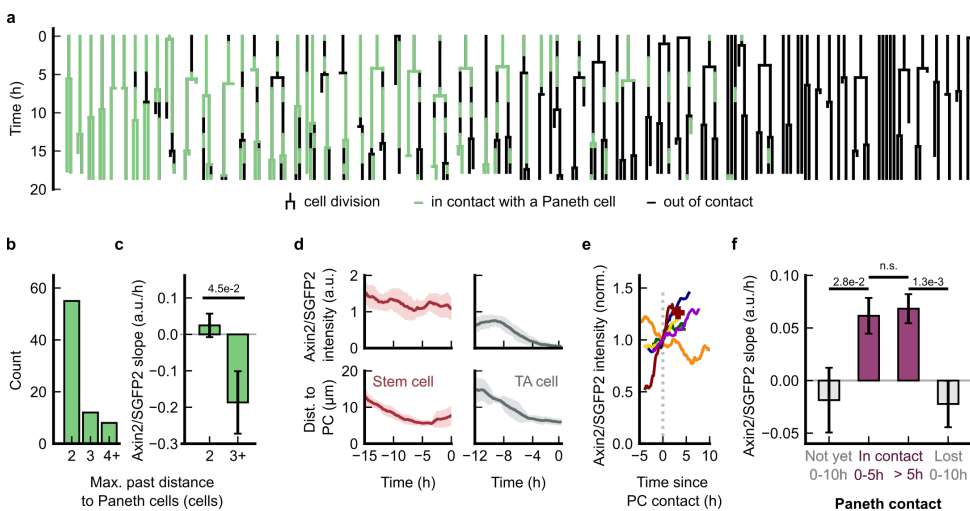
Figure 3.4: WNT signaling activation depends on Paneth cell contact history. (a) Lineage tree gallery of cells; color-coded by whether cells are in contact with a Paneth cell (green) or not (black). (b) Histogram showing the distribution of maximum separation from Paneth cells, prior to regaining Paneth cell contact. (c) Axin2/SGFP2 slope for cells with different maximum separation from Paneth cells, prior to regaining contact (n > 7 tracked cells). (d) Axin2/SGFP2 intensity and distance to Paneth cell for an example stem cell (top) and TA cell (bottom) that regain Paneth cell contact. (e) Normalized Axin2/SGFP2 intensity for cells regaining Paneth cell (PC) contact. (f) Axin2/SGFP2 slopes for cells before, during and after Paneth cell contact (n > 83 tracks; Mann-Whitney U test; n.s. indicates p > 0.05).

3.3 DISCUSSION

We studied the dynamic basis of WNT signaling in intestinal organoids by tracking cells in space and time, quantifying WNT signaling activity, and identifying resulting cell type

changes using antibody labeling. Cells that directly contacted Paneth cells showed increasing WNT signaling, while loss of Paneth cell contact caused an almost immediate decrease in WNT signaling that continued gradually in time, independently of growth and division (Fig. 3.1). The decreases occurred within 2 hours of losing contact – well before significant movement along the crypt-villus axis or cell cycle completion and was followed by cell differentiation (Fig. 3.2). Stem and TA cells frequently regained Paneth cell contact by moving towards the crypt, with WNT signaling activity decreasing rather than increasing during this movement (Figs. 3.3 and 3.4).

These data indicated a timer model for intestinal differentiation, in which time elapsed since loss of Paneth cell contact is recorded by a cell-intrinsic decrease in WNT signaling activity, and differentiation is triggered when it decreases below a critical value. Mechanistically, it is well known that WNT signaling activity is attenuated by the endocytosis and subsequent degradation of WNT receptors, possibly including their bound WNT ligands [32]. This is induced by the E3 ubiquitin ligases Rnf43 and Znrf3 that are WNT target genes themselves, thus forming a negative regulatory feedback loop [58]. We speculate that such a WNT-dependent removal of WNT ligand-receptor complexes drives the steady decrease in WNT signaling activity upon loss of Paneth cell contact, as we observed this also in growth-arrested cells (Fig. 3.1), where dilution of surface-bound WNT by growth cannot occur. Our timer model has conceptual similarities to proposed hourglass clock mechanisms in embryonic development [63, 206, 219], and differs fundamentally from spatial gradient models (Fig. 3.3): the WNT signaling activity here provides temporal rather than positional information to cells, and reflects a cell-intrinsic property rather than the read-out of an external spatial cue. The underlying dynamics inherent to the timer model are obscured in static snapshots or cell-averaged profiles of WNT target gene expression [14, 240] (Fig. 3.1).

Our WNT timer model has major implications. First, it provides a mechanism for Paneth cell differentiation within the crypt (Fig. 3.2), which has been observed recently [30, 291]. Similarly, the earliest moment of commitment to other cell types, including enterocytes and secretory cells, was also shown recently to occur within the stem-cell niche [30, 291]. Such observations are readily explained by the timer model, where differentiation can occur directly in the crypt, provided cells remain out of Paneth cell contact. In contrast, spatial gradient models require stem cells to first move up to low-WNT regions to differentiate into Paneth cells, and then move back to the crypt to function [23]. We speculate that mesenchymal WNTs [73, 126], which might interact with cells beyond the Paneth cell-defined niche, would reduce the rate of WNT signaling decrease, thereby modulating the spatial range over which differentiation occurs, while differentiation will be impacted also by other factors including Notch [78, 197] and BMP [99]. Second, the timer model implies a novel spatial cell patterning mechanism. As our findings show that WNT signaling cannot instruct where cells should differentiate, they indicate that other mechanisms must be responsible for spatially organizing differentiated and non-differentiated cells along the crypt-villus axis. We surmise that cell sorting plays a key role in this process. Cell sorting, which is driven by mechanisms ranging from cadherin-based differential adhesion, ephrin-mediated cell repulsion, and surface tension, is an important driver of

spatial patterning in development [147] and might here be important for ensuring, for example, that stem cells remain within the crypt, while differentiating enterocytes are routed towards the villus. Third, in the timer model differentiation can be reset repeatedly, as consequence of random cell movement and rearrangements within the crypt. We found that cells at the crypt bottom frequently lost and regained Paneth cell contact, with the latter causing WNT signaling activity to increase again (Fig. 3.4). Indeed, some stem and TA cells regained Paneth cell contact by moving in from up to 4 cell distances away (Fig. 3.4), consistent with recently reported retrograde movement of intestinal stem cells in vivo [9]. In conclusion, given the ubiquity of WNT signaling across animal development and the increasing recognition that epithelia are more mobile and dynamic [153, 155] than previously appreciated, a timer-based WNT control may be generally relevant.

Acknowledgements

3.4 Methods

Organoid culturing

Axin2P2A-rtTA3-T2A-3xNLS-SGFP2 HOM; Rosa26mTmG murine intestinal organoids were established by the Van Amerongen lab (Universiteit van Amsterdam, The Netherlands) and are described in ref. (Moosdijk2020). Organoids were cultured in 24-well cell culturing plates, which were placed in an incubator at 37 °C and 5% CO2. Each well contained the organoids in 40 μL gel consisting of basement membrane extract (BME, Trevingen) mixed with Advanced DMEM/F-12 in a 2:1 to 3:1 volume ratio. The gel was overlaid with 0.4 mL growth medium. This medium consisted of Advanced DMEM/F-12 (Life Technologies) with murine recombinant epidermal growth factor (EGF 50 ng/mL, Life Technologies), murine recombinant Noggin (100 ng/mL, Peprotech), human recombinant R-spondin 1 (500 ng/mL, Peprotech), n-Acetylcystein (1 mM, Sigma-Aldrich), N2 supplement (1x, Life Technologies), B27 supplement (1x, Life Technologies), Glutamax (2 mM, Life Technologies), HEPES (10 mM, Life Technologies) and Penicillin/Streptomycin (100 U/mL 100 μg/mL, Life Technologies). The organoids were passaged every week, after which they were refed twice during the next seven days: once 2 to 3 days after passaging and once 4 to 5 days after passaging. During refeeding, the growth medium was replaced. During passaging, the organoids were mechanically broken up into smaller organoids, to prevent the organoids from growing too large and therefore dying. The passaging was carried out as follows: The organoids from two wells were collected into a 5 mL Eppendorf tube using 2 mL of Advanced DMEM/F-12 medium. The organoids were broken up by pipetting up and down with a glass pipette, of which the opening was narrowed using a flame. An additional 2 mL of Advanced DMEM/F-12 was added and the tube was centrifuged for 5 minutes at 800 rpm (320 rcf). Afterwards, the supernatant was aspirated. A second centrifugation round was carried out: 4 mL new Advanced DMEM/F-12 medium was added, and the tube was centrifuged for an additional 5 minutes at the same speed. The supernatant was again

removed, after which the organoids were seeded in gel on wells of a new culturing plate. After leaving the plates in an incubator for 20 to 30 minutes, the growth medium was added.

Organoid time lapse microscopy

To perform a time lapse experiment, we first seeded mechanically dissociated organoids in 40 μL gel in four-well chambered cover glass (Cellvis). This was performed one day before the start of the time lapse experiment. To prevent the gel from solidifying immediately, seeding was performed on a cold block. The imaging well was put in a fridge until the organoids had sedimented down, as observed using light microscopy. Typically, this sedimentation process took about five to ten minutes. Afterwards, the chambered cover glass was put in the incubator. After leaving the plates in an incubator for 20 to 30 minutes, the growth medium was added. A Leica confocal microscope was used for time lapse imaging. In this setup, a controlled closed environment was used to maintain the temperature at 37 ℃, CO2 at 9% and high humidity. The CO2 concentration was kept at 9% instead of 5% due to leakiness of the system. A 40x water immersion objective (Leica) was used for image acquisition. Organoids were imaged every 12 minutes for up to 20 h. Z-stacks were made at 2 μm intervals, with a field of view of 233 by 233 μm. Z-ranges were specified for each organoid, with a maximum range of 70 μm. The following excitation wavelengths and laser intensities were used: 488 nm (3% or 1% intensity), 552 nm (1% intensity), 638 nm (1% intensity). Detection was done at 493-547 nm and 582-633 nm. An imaging well typically contains over 50 organoids, of which we only imaged a small number. We selected for small organoids, with only one to three crypts, that we close to the bottom of the imaging plate. The nuclei were made visible using SirDNA. This allowed us to track Axin2-negative cells more easily, as otherwise we would need to rely only on the membrane-located tdTomato signal. When organoids in the imaging plate had generated buds (early crypt structures), the growth medium was removed and replaced by new growth medium supplemented with 1 μM SirDNA (Spirochrome) and 10 μM Verapamil (Spirochrome). This was then left to incubate for 3 hours before starting imaging.

Antibody staining

After time lapse imaging, organoids were immediately fixed using 4% formaldehyde in PBS. After fixation, the organoids were permeabilized using 0.2% Triton-X. Then the organoids were sequentially stained with several rounds of primary and secondary antibody and dyes (Table 3.1). Before antibody staining, organoids were blocked in 5% skim milk for 1 h. Primary antibodies were diluted in 5% skim milk and were incubated on the organoids for 48 h. The organoids were then washed with PBS, and incubated with secondary antibodies diluted in TBS, for 1 h. If applicable, the organoids were then incubated with Wheat Germ Agglutamin (WGA) in PBS for 2 h. The organoids were washed of excess secondary antibody and/or dye before imaging. Imaging was done using the same Leica confocal microscope setup as for time lapse imaging. Using these combinations of antibodies and dyes mentioned before, different cell types can be identified within the intestinal organoid (Table 3.3).

Backtracking of cell types

First, for cells that were visible at the end of the time-lapse, the cell types were assigned for the entire lifetime of that cell using antibody staining, as described in Table 3.3. Then, all remaining cell types were assigned as follows: If two sister cells were assigned to the same type, the mother cell will also be assigned to that type. Furthermore, if at least one sister cell was assigned to a stem cell, the mother cell will be assigned as a stem cell. Finally, if at least one sister was assigned as a transit-amplifying cell, and the other sister was not a stem cell, the mother cell will be assigned as a transit-amplifying cell. These rules match our assumptions about cell differentiation in mouse small intestinal organoids [291].

Ablation of Paneth cells

Imaging for the was performed on a different microscope (Nikon A1R MP) with a 40x oil immersion objective (NA = 1.30). 30 z-slices with 2 μm step size were taken per organoid every 12 minutes. Experiments were performed at 37 ℃ and 5-8% CO2, achieved by using a stage-top incubator (Okolab). Ablation was carried out using an 800 nm laser (tunable Ti:Sapphire laser, Mai Tai High Performance DeepSee, Spectra Physics; 100% power) for 40 to 60 ms, on a single point set at the center of the nucleus. Paneth cells were identified by their bright membrane-localized tdTomato signal and their low Axin2/SGFP2 signal amidst neighbor cells that have a high Axin2/SGFP2 signal. No antibody staining was performed after the time lapse.

Fluorescence recovery after photobleaching

The experiment was performed on the same microscope as the ablation experiment. No antibody staining or SirDNA was used. SGFP2 in three cells per crypt cells was partially bleached for 5 seconds at 20% laser power (Nikon LU-N4 laser unit, 488 nm laser). The remaining cells served as controls. Bleached and control cells were manually tracked for up to 12 hours and fluorescence intensity levels of GFP signal were measured until cell division, death or moving out of frame. For each individual recovery curve, we normalized the fluorescence intensity by the average intensity of the four images taken before bleaching, and we fitted the function

$$S(t) = 1 - Be^{-\delta t} \tag{3.1}$$

to the individual recovery curves using scipy.optimization.curve_fit in Python with the fraction of bleached molecules (B) and the degradation rate of GFP (δ) as free fitting parameters. Bleached cells were excluded from analysis if (i) if the cell could only be tracked for less than five hours, (ii) their average GFP-fluorescence intensity in first hour was more than 65% (insufficient bleaching), (iii) if their maximum measured intensity was higher than 35% above their intensity prior to bleaching (indicating that the cell was not in homeostasis at the moment of bleaching) or (iv) if the measured recovery time (1/b) was more than 21 hours, indicating that Axin2 was either not produced or immeasurably low on the timescale of the cell cycle.

Automatic extraction of fluorescence values

For extracting fluorescence curves outside the FRAP experiment, a different, less labor-intensive method was used compared to drawing ellipses. In addition, instead of measuring

the fluorescent concentration, this method measures the total fluorescence of a nucleus. The centers of the nuclei in the crypt were manually tracked from the start to the end of the time lapses in OrganoidTracker [143]. (The automated tracking module of OrganoidTracker could not be used, as the cells do not contain a nuclear reporter.) Every pixel in the (3D) image was then assigned to the nearest nuclear center position, with a maximum distance of 7 μm. The sum of the intensities of all pixels belonging to a cell is regarded as the total fluorescence of the cell. When a trace of a single cell is shown in this paper, the measured values are averaged over the two hours before and the two hours after. When multiple cells are shown together, the Axin2/SGFP2 values of the cells are averaged, but no time averaging is performed. To be able to compare signals from multiple organoids, we needed to set a consistent scale for each organoid. We wanted to have a scale where 1 represents the Axin2/SGFP2-level of a typical cell where WNT signaling is on, and 0 for a cell that displays only background signal. Since we mostly track cells in the crypt, we defined the median SGFP2 signal of a cell as 1, with the idea that this value represents a typical cell in the crypt. For defining 0, we noticed that starting from the 4th-degree-neighbor of Paneth cells, in general no SGFP2 fluorescence was observed, and that the average measured signal was minimal. Therefore, we defined this average as 0. Since the background is not uniform across the organoid and across time, this caused some cells to have an intensity below zero. We did not cap these negative values to zero, as this would artificially increase the average signals.

Determining neighbors of cells

Neighbors of cells were manually annotated every 10 time points, which corresponds to every two hours. To do this, connections were established between all cells for which the membranes touched, as observed in the tdTomato channel.

Measuring Axin2 slope as a function of distance to the nearest Paneth cell

We measured the Axin2 slope as follows: we iterated over all time lapses, and for every time point for which we had annotated each cell's neighbors (which was done every two hours), we iterated over every cell present in that time point. For every cell, we either measured the distance to the nearest Paneth cell, or the number of Paneth cells the cell was currently in contact with. We then looked at a 4-hour time window of the Axin2/SGFP2 intensities and measured the mean intensity and the slope. If we could not obtain a 4-hour time window for that cell, because the cell divided or we could not track it for that long, we discarded the cell. Note that this method measures the same cell multiple times.

We tracked the cells that were a neighbor at the start of the experiment. If a cell divided, the daughters were regarded as two new cells for the analysis. For all cells that we could track for at least 4 hours, we calculated the mean Axin2/SGFP2 intensity and intensity slope. Note that we now obtain only a single Axin2 production rate for each cell.

RNA sequencing data analysis

Single-cell RNA sequencing data [95] of the murine intestinal epithelium was retrieved from the GEO database (GSE92332). Analysis was performed in Python using the scanpy

library and the recipe based on Wu et al. (2022) [285]. Briefly, cells with more than 5% mitochondrial genes were filtered out, and counts per cell were normalized and log1p transformed. Dimensionality reduction was performed by finding the 4000 most highly expressed genes (excluding mitochondrial and ribosomal), scaling and principal component analysis (50 components) and computing of the neighborhood graph (knn = 15).

3.5 SUPPLEMENTARY INFORMATION

Table 3.1: Used antibodies and dyes.

Antibody/Dye	Concentration	Manufacturer reference	Research Resource Identifier
rabbit anti-OLFM4	1:500 dilution	Bioke D6Y5A	RRID:AB_2650511
rabbit anti-human lysozyme	1:800 dilution	Dako #A0099	RRID:AB_2341230
mouse anti-human Krt20	190 ng/mL	Dako M701929-2	RRID:AB_2133718
mouse anti-human ChrA	2.5 µg/mL	Santa Cruz #sc-393941	RRID:AB_2801371
donkey anti-rabbit	2 µg/mL	Abcam #ab175649	RRID:AB_2715515
donkey anti-mouse	4 µg/mL	Thermofisher #A31571	RRID:AB_162542
Wheat Germ Agglutamin (WGA)	2.5 µg/mL	Biotium #29028-1	N/A

Table 3.3: Mapping from antibody staining to cell type [291]. IMPC is an immature mucus-producing cell, which does not stain positive yet for lysozyme or Krt20. TA represents the transit-amplifying cells, which did not stain positive for any of our markers.

	Stem cell	Paneth cell	IMPC	Goblet cell	Enterocyte	EEC	TA
OLFM4	+						
Lysozyme		+					
WGA		+	+	+			
Krt20				+	+		
ChrA						+	

3.5.1 Supplementary Note - Modelling SGFP2 production and degradation

In this section, we use a Fluorescence Recovery After Photobleaching (FRAP) experiment of SGFP2 and mathematical modelling to demonstrate that our measured SGFP2-data is consistent with a simple production/degradation model, and that cells with active WNT signaling can still show a negative slope in SGFP2 signal.

Changes in WNT signaling likely manifest themselves in concomitant changes in Axin2 production rate. Given that, in our experiments, Axin2 and SGFP2 are transcribed as a single polycistronic mRNA molecule, the production rate of SGFP2 is like that of Axin2 by design. Therefore, assuming simple, linear transcription and translation dynamics, the WNT-dependent Axin2 production rate $r(t)$ is equal to the production rate of the measured SGFP2 signal, can thus be inferred from the observed SGFP2 fluorescence signal $S(t)$ as $r(t) = \frac{dS(t)}{dt} + S(t) \cdot \delta$. Here, $\frac{dS(t)}{dt}$ is the slope of the SGFP2 signal and δ is the degradation rate of the SGFP2 signal. We assume that this degradation rate is constant across all cells in all our experiments. This constant allows direct calculation of the Axin2 production rate $r(t)$, given only the current value and slope of the SGFP2 signal.

Fluorescence recovery after photobleaching

To measure the degradation rate δ, we set up a FRAP experiment and use the following simple production-degradation model to describe how the GFP signal evolves over time:

$$\varnothing \rightleftarrows S \tag{3.2}$$

Here, S is the measured concentration of GFP, which can be produced at rate p and degraded at rate δ. This reaction equation results in the following differential equation:

$$\frac{dS}{dt} = p - \delta \cdot G(t) \tag{3.3}$$

Note that while we assume that the SGFP2 degradation rate d is equal in all cases, we allow the production rate p to vary over time for each cell. For the FRAP experiment, we bleached several cells in the bottom of the crypt (Fig. 3.5a). We measured recovery of SGFP2 fluorescence over time, with the observed recovery over ~8 hours (Methods, Fig. 3.5b). Cells at the bottom of the crypt show a constant amount of SGFP2. Therefore, for these cells $\frac{dS}{dt} = 0$. Substituting this result in Equation 1 shows that the recovery of the bleached cells can then be fit to $\frac{S(t)}{S_0} = 1 - Be^{-\delta t}$ to obtain the degradation rate δ. Here, S_0 is the measured concentration of SGFP2 before bleaching and B the fraction of bleached GFP. By fitting this exponential to the measured SGFP2 values over time, we obtained a degradation rate of $\delta = 0.14 \text{ h}^{-1}$.

Production values for cells

Using the measured SGFP2 degradation rate, we then estimated the Axin2 production rate r based on the SGFP2 intensity and its slope, averaged over 4 hours. As expected, r was highest in direct Paneth cell neighbors, and decreased for second-degree neighbors. For more distant cells, the inferred Axin2 production rate becomes zero (Fig. 3.5c). When we

next inferred the production rate for the ablation experiments, we found that upon Paneth cell ablation r was reduced to a level comparable with the production rate in the second-degree neighbors. Palbociclib-treated organoids showed similar r as control organoids, indicating that Axin2 production rate, and hence WNT signaling, did not depend strongly on cell growth and division (Fig. 3.6c).

3
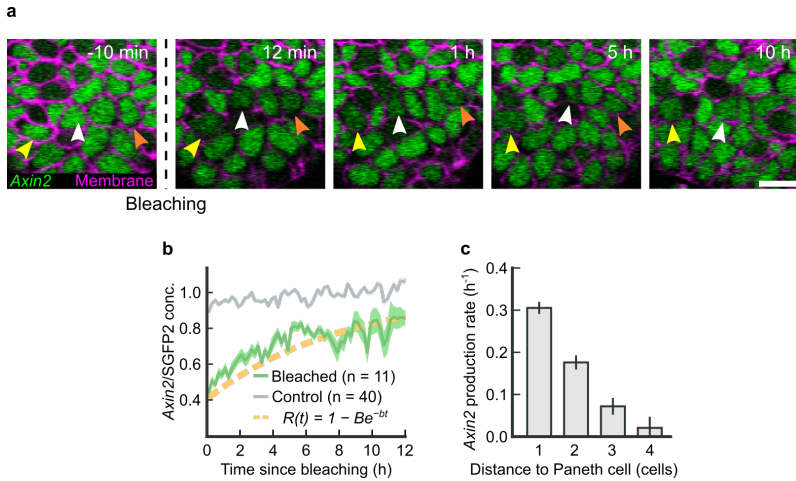
Figure 3.5: Fluorescence recovery after photobleaching experiment. (a) Targeted bleaching of several Axin2-postive cells in the crypt. Scale bar: 10 μm. (b) Fluorescence recovery curve for bleached cells, with fit, and with fluorescence intensities control cells that were not bleached. The shaded area is the standard error across the cells. (c) Axin2 production rate for cells at various distances of Paneth cells, with distance 1 representing the direct neighbors.
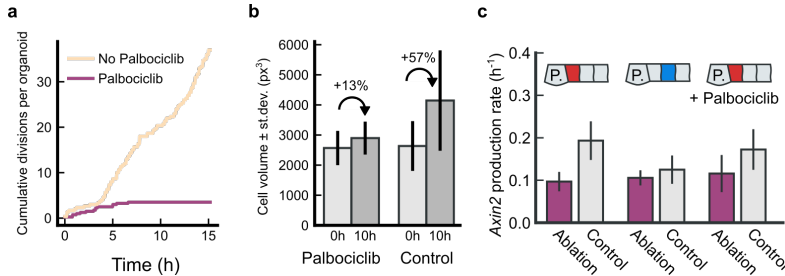
Figure 3.6: Palbociclib effectively halts proliferation and cell growth. (a) Cumulative number of cell divisions for control organoids and for organoids where Palbociclib was added to the medium several hours before imaging. (b) Effect of Palbociclib on cell growth. If a cell divides (which happens in the control only), the volume of the two daughter cells is summed. (c) Axin2 production rate inferred for first-degree Paneth cell neighbors (left), second-degree neighbors (middle) and for first-degree neighbors in Palbociclib-treated organoids, both in Paneth cell-ablated and mock-ablated organoids. Paneth cell ablation reduced Axin2 production rate to levels comparable with second to third-degree neighbors of Paneth cells, independent of cell growth and division.
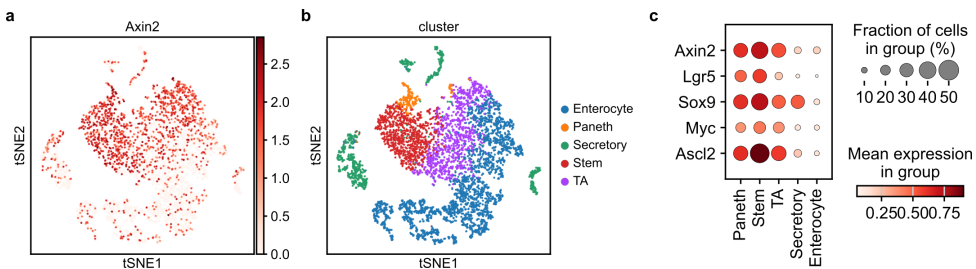
Figure 3.7: Expression of WNT target genes in intestinal cell types. (a) tSNE plot of Axin2 expression in single-cell RNA sequencing dataset from ref. [95] (data accessible at NCBI GEO database [15], accession GSE92332). (b) Reference for panel a. Clusters were combined such that the same cell types were present as distinguished using TypeTracker in this work. (c) Dotplot of WNT target genes, showing that all common WNT target genes are highest in stem cells, followed by Paneth and TA cells, and then by secretory cells and enterocytes.

4

4

BEST4/CA7$^+$ AND GOBLET CELLS ARE INTERDEPENDENT REGULATORS OF INTESTINAL MUCUS HOMEOSTASIS

"Nothing in biology makes sense, except in the light of evolution."

Theodosius Dobzhansky

The intestinal mucus layer is essential for the integrity of the intestinal barrier. It is produced by goblet cells, whose depletion is common in colonic inflammation but remains poorly understood. Here, we show that goblet cell survival relies on a reciprocal dependence with newly discovered BEST4/CA7$^+$ cells. We developed a method to follow BEST4/CA7$^+$ and goblet cells in time from birth to death in human colon organoids. Notably, goblet cells induce BEST4/CA7$^+$ fates in sister cells and other neighbors, using DLL1-mediated lateral activation of Notch-signaling. BEST4/CA7$^+$ cells in turn promote goblet survival, with the latter depleting rapidly after differentiation in absence of BEST4/CA7$^+$ cells. This apoptosis inhibition does not require direct cell-cell contact and instead depends on their shared lumen. Such differentiation and survival interdependencies may be relevant beyond the maintenance of mucosal homeostasis.

4.1 INTRODUCTION

The intestinal lumen is a hostile environment that contains diverse pathogens, which must be effectively separated from the delicate underlying tissue. A mucus layer covering the intestinal epithelium is central to this barrier function. It consists mostly of the O-glycosylated mucin 2 (MUC2), which expands up to 1000-fold to form a hydrated gel after its secretion by goblet cells [94, 125, 272]. Emerging evidence also indicates a role for BEST4/CA7$^+$ cells; a rare cell type discovered only recently in the human intestine [118] and notably absent in the mouse [95]. Specifically, the key markers BEST4 and CA7 both regulate bicarbonate levels. BEST4/CA7$^+$ cells also express proton channels OTOP2 and OTOP3 [37, 69, 70, 75, 205, 247], secrete guanylin and uroguanylin [205], and activate CFTR channels upon bacterial infection [278]. These findings indicate that BEST4/CA7$^+$ cells regulate mucus viscoelasticity and secretion by controlling luminal pH, calcium and bicarbonate concentrations, as well as water efflux [3, 64, 93] (see ref. [170] for a recent review).

Goblet and BEST4/CA7$^+$ cell abundance is therefore important to mucosal defense. Indeed, goblet cell depletion is a known hallmark of ulcerative colitis [84], and more generally observed in chronic inflammatory disorders [98, 123, 124, 268]. However, the processes that control goblet and BEST4/CA7$^+$ cell abundance in the rapidly renewing intestinal tissue are poorly understood. Goblet cells arise from secretory progenitors, but whether their survival is controlled is less clear. BEST4/CA7$^+$ cells are thought to branch from absorptive progenitors [205] and are absent in organoid cultures treated with Notch signaling inhibitors [276, 278]. However, when and in which lineages they are generated is unknown. Curiously, BEST4/CA7$^+$ and goblet cells are often found in close proximity [69, 118], but the causes are unclear. Addressing these questions requires approaches to follow the renewal process of intestinal cells in time and space. Owing to the absence of BEST4/CA7$^+$ cells in the mouse, studying their differentiation and function over time requires the use of human organoid models [276, 278].

Here, we developed a method to track goblet and BEST4/CA7$^+$ cells in a human colon organoid model. The data reveal an unexpected interdependence between these cell types in terms of both differentiation and survival. Notably, we find that BEST4/CA7$^+$ cells emerge often, but not exclusively, as direct sisters of goblet cells. Fate commitment occurs early, with goblet cells arising from cells that are still proliferative, and their sister or other neighboring cells adopting the BEST4/CA7$^+$ fate shortly after. We find that goblet cells laterally activate Notch-signaling through DLL1 to induce BEST4/CA7$^+$ cell differentiation. Finally, we show that goblet cell survival depends on BEST4/CA7$^+$ cells in a contact-independent manner, with the goblet cell pool being dramatically depleted in absence of BEST4/CA7$^+$ cells. This reciprocal relation between goblet and BEST4/CA7$^+$ cells provides a mechanism for homeostasis of the ratio between BEST4/CA7$^+$ and goblet cells. Our findings raise questions on the prevalence of reciprocal dependencies between cell types and their role in regulating cell type proportions across epithelia and during infection, inflammation, and proliferative perturbations.

4.2 Results

BEST4/CA7$^+$ cells differentiate after goblet cells

To study the dynamics of goblet and BEST4/CA7$^+$ cell differentiation, we performed long-term live-cell imaging of human colon organoids [233] carrying reporters for differentiation of goblet cells (labelled by a MUC2-mNeonGreen knock-in allele) [6] and BEST4/CA7$^+$ cells (labelled by a CA7-P2A-tdTomato knock-in allele) [278], with a histone 2B (H2B)-iRFP670 nuclear reporter integrated to enable real-time tracking of individual cells. We grew human colon organoids as undifferentiated stem cells in expansion medium and then shifted to differentiation medium (Fig. 4.1a). Multi-day time-lapses were acquired during these growth processes at 12-min resolution using confocal microscopy and individual nuclei were tracked through time using OrganoidTracker [143]. We classified cells as goblet cells, BEST4/CA7$^+$ cells or unmarked cells based on morphology and fluorescence, and extracted cell positions, fluorescence levels of mNeonGreen and tdTomato (which indicate expression levels of MUC2 and CA7, respectively) and lineage relations (Methods, Fig. 4.1a-d, Fig. 4.5 & Fig. 4.6). Together, this yielded an expansive single cell tracking dataset combining positional information, lineage history, gene expression dynamics and cell types.

Lineage trees showed that cells in expansion medium remained proliferative for at least five days with cell cycle durations varying between 15 and 53 hours, and a median of 27.6 hours (Fig. 4.5a-e). Cell cycle durations were strongly correlated between sister cells (Fig. 4.5f), in line with our previous finding in mouse intestinal organoids that cell cycle durations are controlled by mother cells and transmitted to their daughters [115]. After shifting to differentiation medium, most cell divisions occurred within 24 hours and proliferation virtually stopped within 48 hours (Fig. 4.5g). After 24 hours, a subset of cells started to show MUC2 and CA7 expression (Fig. 4.1e). Notably, we observed a distinct temporal order between goblet and BEST4/CA7$^+$ cell emergence, with MUC2$^+$ goblet cells appearing after a median time of 49 hours, and BEST4/CA7$^+$ cells after 69 hours (Fig. 4.1e, f). Measurements of MUC2 and CA7 mRNA levels by quantitative polymerase chain reaction (qPCR) analysis yielded a similar delay in timing (Fig. 4.1g). This temporal separation can explain previous immunostaining [273] and transcriptomics data [70, 205], which show BEST4/CA7$^+$ cells higher along the crypt/crypt-villus axis than goblet cells, as the former will have moved further towards the villus before their BEST4/CA7 marker is expressed.
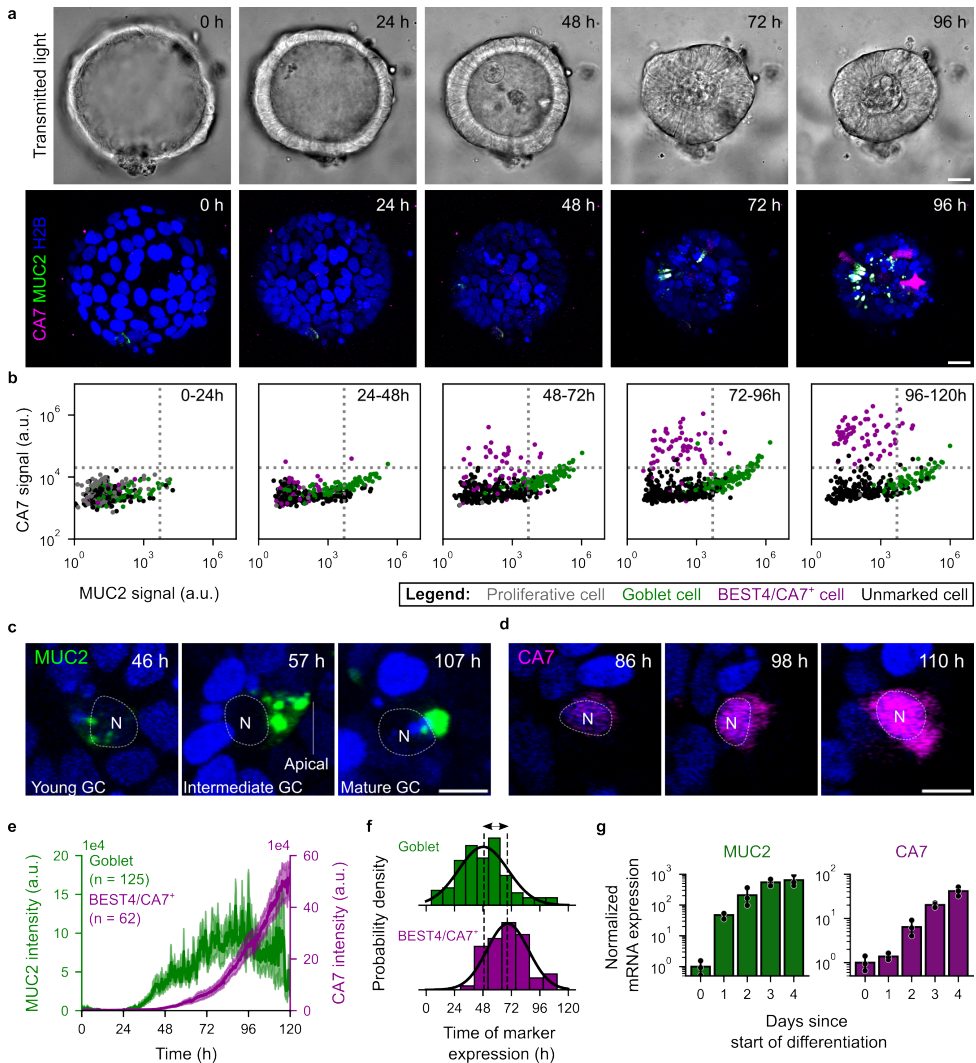
Figure 4.1: Goblet cells emerge before BEST4/CA7^{+} cells. (a) Transmitted light (top) and fluorescence micrographs of a differentiating CA7-MUC2-H2B triple-reporter organoid. Time is hours after shift to differentiation medium. Scale bars: 20 μm. (b) MUC2 (x-axis) and CA7 (y-axis) reporter fluorescence averaged over subsequent time windows. (c, d) Maturation of a goblet cell (GC, c) and BEST4/CA7^{+} cell (d). Scale bars: 10 μm. (e) Average of MUC2 intensity for all goblet cells (green, left y-axis) and average CA7 expression of BEST4/CA7^{+} cells (magenta, right y-axis). 17 organoids derived from three independent experiments are analyzed. n indicates the number of analyzed cells; shaded area indicates the S.E.M. (f) Distribution of times at which MUC2 (top) and CA7 (bottom) is first expressed. Vertical dashed lines indicate the median expression times. Solid line indicates a normal distribution fit to the histogram. (g) Expression of MUC2 (green, left) and CA7 (magenta, right) mRNA quantified using qPCR, at different days after shifting to differentiation medium. Vertical axis indicates the expression relative to GAPDH, normalized by the average expression at day 0 (data from three biological replicates).

Contact with goblet cells predicts BEST4/CA7$^+$ cell fate commitment

BEST4/CA7$^+$ cells often appear to be positioned nearby goblet cells both in vivo and in vitro [69, 118, 278]. Rigorously identifying cell-cell contact in 3D tissue architectures is challenging, however. To address this issue quantitatively, we grew organoids in 2D monolayer cultures [216], to ensure that cell interfaces are clearly visible in bright-field images (Fig. 4.2a, b). On day 3 of differentiation, 90% of BEST4/CA7$^+$ cells were in direct contact with goblet cells. In contrast, only 44% of goblet cells and 42% of unmarked cells were in contact with another goblet cell (Fig. 4.2c, d). Furthermore, sister cells remained close together after division in both expansion and differentiation medium (Fig. 4.7). These findings excluded the possibility that goblet and BEST4/CA7$^+$ cells differentiate independently and subsequently co-localize by spatial rearrangement. Instead, lineage relations or cell-cell signaling could play a role.

To study this issue directly, we analyzed goblet and BEST4/CA7$^+$ lineages in time, as well as their relations. We excluded lineages with cells whose type could not be classified as BEST4/CA7$^+$, goblet, or not expressing either marker (termed unmarked), for example due to cell death or the cell moving out of view (Supplementary Note 4.5.1 and Fig. 4.8). Strikingly, we observed cells dividing into two sister cells of which one adopted the goblet, and the other the BEST4/CA7$^+$ cell fate (Fig. 4.2e). Expression of the goblet cell marker MUC2 typically turned on before the BEST4/CA7$^+$ marker CA7, and never after (Fig. 4.2e-h), consistent with the population-level findings (Fig. 4.1e-g). Hence, these data show that goblet and BEST4/CA7$^+$ lineages can emerge from the same progenitor (mother) cell. Overall, we observed sister cells displaying all five possible combinations that include BEST4/CA7$^+$ and/or goblet type (Fig. 4.2i and Fig. 4.6c). Analysis showed that the goblet-BEST4/CA7$^+$ combination appeared more often than expected for a model where cells choose their fate in an autonomous and neighbor-independent manner (Fig. 4.2i and Supplementary Note 4.5.2).

The data further revealed a key role for spatial relations. Specifically, we considered cases when BEST4/CA7$^+$ cells did not emerge as a goblet cell sister, but rather as a sister of an unmarked cell. We previously established that almost all unmarked cells in these organoids are enterocytes [278], which are also dominant among differentiated cells in the colon. In unmarked-BEST4/CA7$^+$ sister pairs, the BEST4/CA7$^+$ cell typically had more contact with goblet cells than its unmarked sister cell (Fig. 4.2j, k). In the only observed sister pair with two BEST4/CA7$^+$ cells, both BEST4/CA7$^+$ sisters contacted goblet cells continuously until they expressed CA7 (Fig. 4.2l). Together, these results suggested a mechanism in which direct goblet cell contact instructs the BEST4/CA7$^+$ cell fate. This model is consistent with all the above observations: the high frequency of goblet- BEST4/CA7$^+$ sister pairs which contact each other after birth, the temporal order of their differentiation markers, and the induction of the BEST4/CA7$^+$ fate in cells that contact goblet cells of a different lineage.

The data indicated another notable feature, namely the emergence of the goblet fate in each of the two sisters after a division. Indeed, goblet-goblet sister pairs were ~3-fold overrepresented compared to expectation (Fig. 4.2i). In addition, the onset of MUC2 expression relative to the last division was highly correlated for these goblet cell sisters

(Fig. 4.9a), suggesting that the mother cell had already committed to the goblet fate and then divided once more to produce two daughters in which MUC2 became detectable. Indeed, we occasionally observed the onset of MUC2 expression already before this last division (Fig. 4.9b). These observations are consistent with our previous study in mouse small intestinal organoids that showed secretory cells emerging as sisters [291] with the same type, and oppose the view that secretory fate commitment occurs exclusively after cell cycle exit.

BEST4/CA7$^+$ CELL FATE COMMITMENT DEPENDS ON DLL1 FROM GOB-LET CELLS

The data thus far suggested goblet cells instruct the BEST4/CA7$^+$ fate in direct neighbors. We surmised it could be mediated by Notch-signaling; a contact-dependent signaling pathway that regulates fate specification in the intestinal epithelium [78, 270]. RNA-sequencing has shown that BEST4/CA7$^+$ cells highly express the NOTCH2 receptor [69, 70, 205, 247, 278], while inhibition of Notch-signaling using the γ-secretase inhibitor DAPT blocked all differentiation of BEST4/CA7$^+$ cells [276, 278]. However, as DAPT uniformly blocks γ-secretase activity along all lineages, the role of Notch signaling in BEST4/CA7$^+$ specification, including the involvement of goblet cells, remains unclear. Therefore, we aimed to test directly whether goblet cells instruct the BEST4/CA7$^+$ cell fate via lateral Notch-signaling.

In human tissue, five Notch-ligands are expressed, namely Delta-like ligands DLL1, DLL3 and DLL4 and Serrate-like ligands JAG1 and JAG2 [292]. To identify candidate Notch-ligands for activation of Notch signaling in BEST4/CA7$^+$ cells, we analyzed single-cell RNA sequencing data of healthy human colon epithelium from the GutCellAtlas [69]. We found that DLL3 and JAG2 were lowly expressed and DLL1 and DLL4 were highly expressed by colonic goblet cells (Fig. 4.10). JAG1 was previously found to be expressed only in crypt top colonocytes [146], and was therefore unlikely to contribute to Notch signaling in the differentiation process of BEST4/CA7$^+$ cells. Although DLL4 shows overall higher expression than DLL1 (Fig. 4.10), the latter was previously found to have higher affinity for NOTCH2 than DLL4 [261], suggesting distinct but not redundant role of Notch ligands in signaling activation. Hence, we hypothesized that any Notch signaling that instructs BEST4/CA7$^+$ cell fate commitment is activated by DLL1, DLL4 or both.
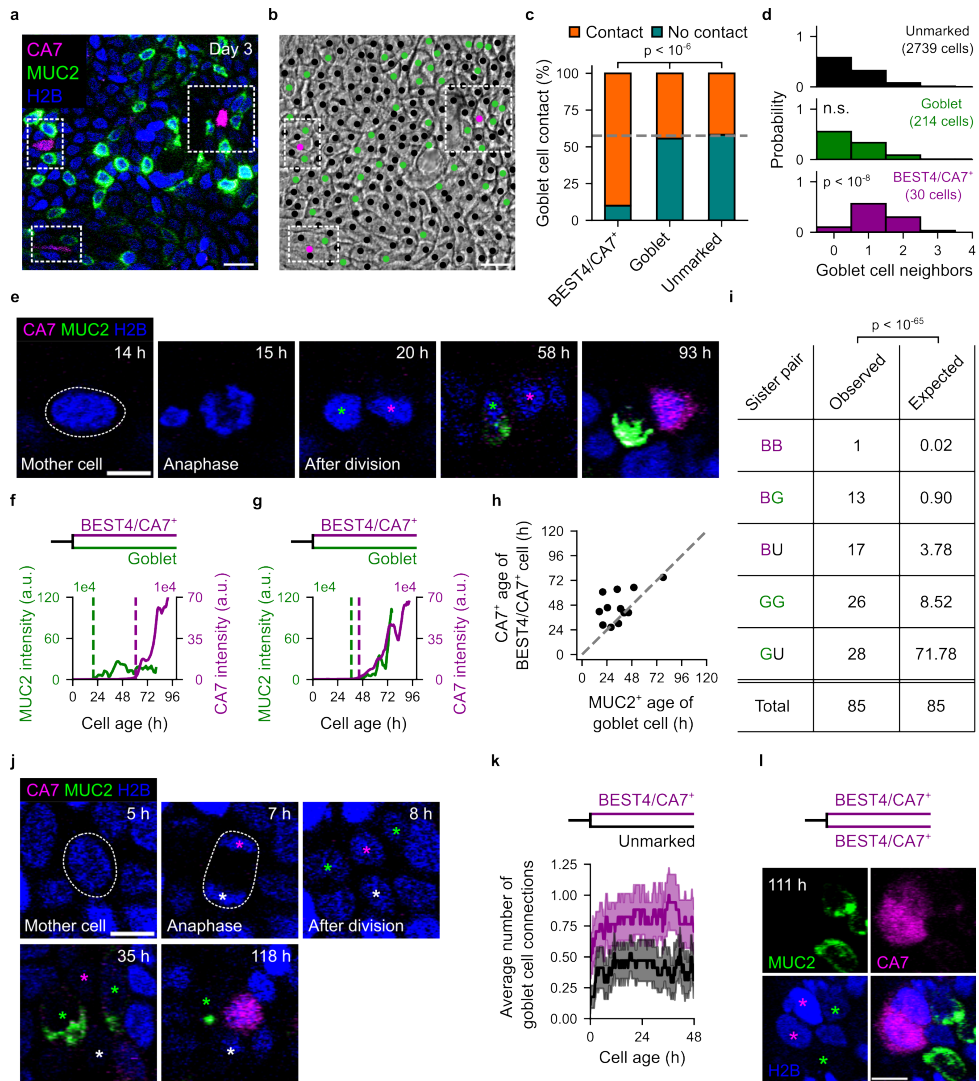
Figure 4.2: Contact with goblet cells predicts BEST4/CA7+ cell fate. (a, b) Fluorescence (a) and bright-field (b) micrograph showing goblet-BEST4/CA7+ cell co-localization in 2D organoids. Dashed white boxes highlight BEST4/CA7+ cells. Scale bars: 20 μm. (c) Fraction of cells in contact with a goblet cell. Pearson χ^2-test is used for comparisons. n = 17 patches from three independent experiments. (d) Distribution of the number of goblet cell neighbors per cell type. Mann-Whitney U test is used for comparisons. n.s. not significant. n = 17 patches from three independent experiments. (e) Example of a dividing cell of which one daughter becomes a goblet cell (green asterisk) and the other a BEST4/CA7+ cell (magenta asterisk). Time is hours after shift to differentiation medium. Scale bar, 10 μm. (f, g) Two representative examples for MUC2 expression of goblet cells (green) and CA7 expression of their BEST4/CA7+ sister. Age indicates time since the last division. Vertical dashed lines indicate the time at which the cells became MUC2-positive (green) or CA7-positive (magenta). Both lines show the 4-hour moving average of the MUC2-mNeonGreen and CA7-P2A-tdTomato fluorescence. (h) Age at which goblet and BEST4/CA7+ cells showed detectable levels of marker expression in goblet-BEST4/CA7+ sister pairs. (i) Observed and expected frequencies of the sister pairs. Expected frequencies were computed using the population-level abundances of goblet and BEST4/CA7+ cells and tested using a Pearson χ^2-test. B, BEST4/CA7+ cell; G, goblet cell; U, unmarked cell.

Figure 4.2: (continued) (j) Example of a mother cell dividing into a BEST4/CA7$^+$ and unmarked cell, indicated by a magenta and white asterisk, respectively. Green asterisks indicate MUC2$^+$ cells adjacent to the BEST4/CA7$^+$ cell. Scale bar: 10 μm. (k) Average number of goblet cell connections for BEST4/CA7$^+$ cells and unmarked BEST4/CA7$^+$ cell sisters. A goblet cell connection is defined as an instance where the nucleus of a cell is within 15 μm of the nucleus of a goblet cell. Shaded area indicates the S.E.M. (l) Micrograph images of the only BEST4/CA7$^+$-BEST4/CA7$^+$ sister pair, showing that both BEST4/CA7$^+$ sisters (magenta asterisks) are in contact with a goblet cell (green asterisks). Scale bar: 10 μm.

To test this, we generated organoid lines where either DLL1, DLL4 or both DLL1 and DLL4 were genetically knocked out on both alleles in the CA7 P2A-tdTomato reporter organoids (DLL1-KO, DLL4-KO and DLL1/4-dKO, respectively; Fig. 4.11a). After organoid differentiation, we measured the percentage of BEST4/CA7$^+$ cells by FACS analysis (Fig. 4.11b). DLL1-KO and DLL1/4-dKO organoids had virtually no BEST4/CA7$^+$ cells, while the percentage of BEST4/CA7$^+$ cells was only mildly decreased in DLL4-KO organoids (Fig. 4.3a, b). Hence, expression of DLL1, but not DLL4, is necessary for instructing BEST4/CA7$^+$ cell fate.

Next, we labeled DLL1-expressing cells by knock-in of a P2A-Clover cassette at the C-terminus of the DLL1 gene (DLL1-P2A-Clover) in the CA7-P2A-tdTomato; H2B-iRFP670 reporter organoids and tracked cells during differentiation (Fig. 4.3c and Fig. 4.11c, d). The resulting lineages of DLL1$^+$ cells showed DLL1 expression after a median time of 35 hours (Fig. 4.3d-f), thus even earlier than MUC2 expression after 49 hours, as shown above (Fig. 4.1f, g). This agrees with findings that DLL1 expression starts low in the crypt and precedes functional marker expression of secretory cells [269]. Notably, out of 25 cells that were tracked from birth and adopted the BEST4/CA7$^+$ fate, 13 had a DLL1$^+$ sister, each of which expressed DLL1 before CA7 emerged in the BEST4/CA7$^+$ cell (Fig. 4.3g and Fig. 4.12). Moreover, at 60 hours after the shift to differentiation medium, all present and future BEST4/CA7$^+$ cells were in direct contact with DLL1$^+$ cells (Fig. 4.3h, i). This suggested that contact with a DLL1$^+$ lineage around 60 hours is necessary for committing to BEST4/CA7$^+$ fate. Overall, these results show that DLL1$^+$ cells, of which the majority is a goblet cell or it's precursor, instruct commitment to the BEST4/CA7$^+$ cell fate by lateral Notch-signaling.
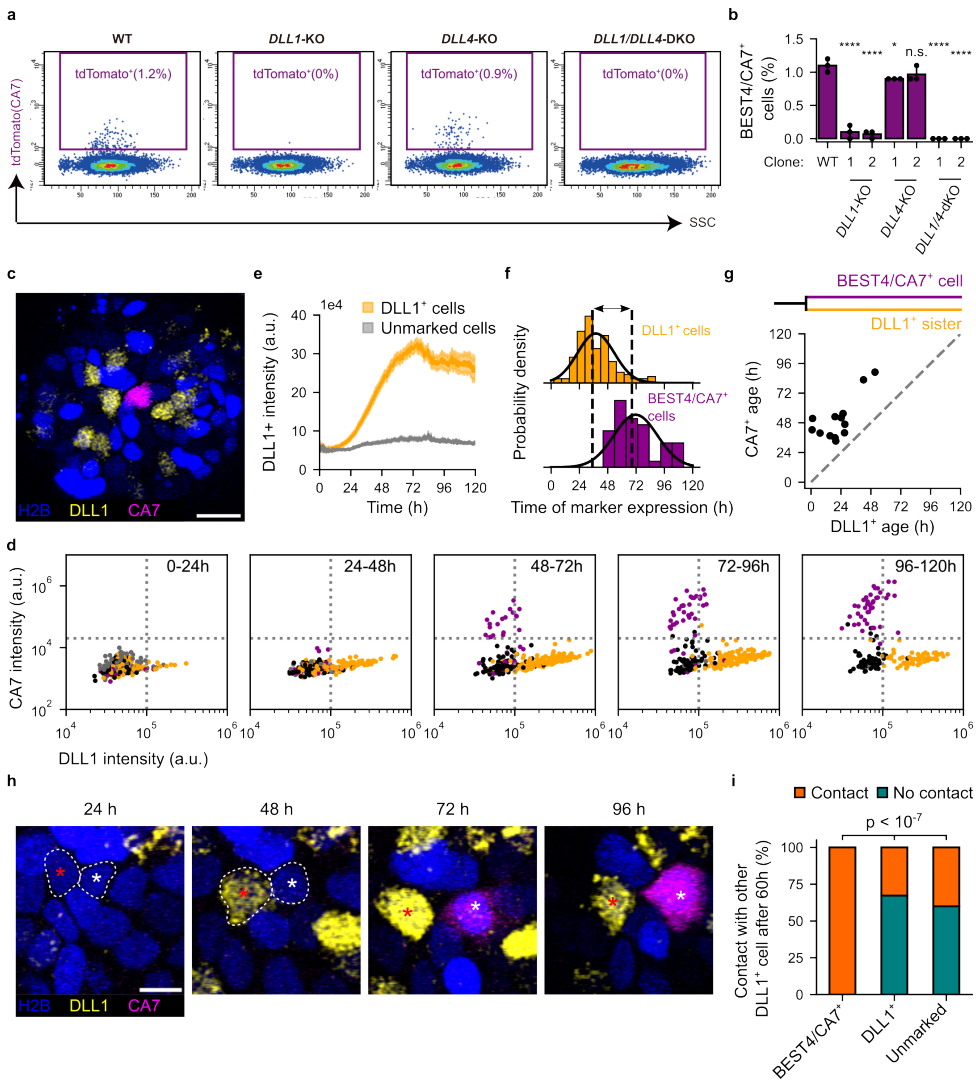
Figure 4.3: DLL1-mediated activation of Notch-signaling instructs BEST4/CA7$^+$ cell fate. (a, b) Representative FACS plot (a) and quantification of BEST4/CA7$^+$ cell percentages (b) in differentiated WT, DLL1-KO, DLL4-KO and DLL1/4-dKO organoids. One-way ANOVA with Dunnett's test is used for multiple comparisons between the DLL-KO groups and the WT (control) group. **** $p < 0.0001$, * $p < 0.05$, n.s.: not significant. SSC, side scatter measurement. Data from n = 3 technical replicates per condition, from N = 2 clones per knock-out line derived from the same donor. Error bars indicate 95% confidence interval. (c) Representative confocal image of a DLL1-CA7-H2B reporter organoid, after 84 hours of differentiation. Scale bar: 20 μm. (d) DLL1 (x-axis) and CA7 (y-axis) reporter fluorescence averaged over time for different time windows after shifting to differentiation medium. (e) DLL1 reporter fluorescence over time for DLL1$^+$ cells and unmarked cells. Shaded area indicates S.E.M. (f) Distribution of times at which DLL1 (top) and CA7 (bottom) is first expressed. Vertical dashed lines indicate the median expression times. Solid line indicates a normal distribution fit to the histogram. (g) Age at which BEST4/CA7$^+$ and DLL1$^+$ cells in BEST4/CA7$^+$-DLL1$^+$ sister pairs showed marker expression.

Figure 4.3: (continued) (h) Time-lapse images of two neighboring cells of which one expresses DLL1 (red asterisk) and the other CA7 (white asterisks). Note that these cells are not sister cells. Dashed white lines indicate the pair of cells at before clear marker expression. Scale bar: 10 μm. (i) Neighbors of present and future DLL1$^+$ cells were evaluated 60 hours after shift to differentiation medium. Null hypothesis that all three cell types (BEST4/CA7$^+$, DLL1$^+$ and unmarked) had equal probability to have a DLL1$^+$ neighbor was tested using Pearson χ^2-test.

BEST4/CA7$^+$ CELLS SUPPORT THE SURVIVAL OF GOBLET CELLS

Having established that Notch ligand-presenting goblet cells instruct differentiation of BEST4/CA7$^+$ fate in neighboring cells, we wondered if there was a functional relevance for this interaction. We and others previously established that the transcription factor SPIB is essential for BEST4/CA7$^+$ cell differentiation by showing that genetic knock-out of SPIB leads to a complete lack of BEST4/CA7$^+$ cells [276, 278]. Here, we then examined whether BEST4/CA7$^+$ cells impacted goblet cell abundance, by comparing goblet cell numbers in both SPIB-KO and wild-type (WT) organoids using FACS analysis. Strikingly, goblet cell fractions in SPIB-KO and WT organoids were similar up until day 4 of differentiation but rapidly decreased in SPIB-KO organoids on day 5 and 6 (Fig. 4.4a, b). To study the survival of goblet cells more directly, we used live-cell imaging and tracking. Tracking showed that goblet cells were significantly more likely to undergo apoptosis in SPIB-KO organoids (compared to WT organoids), as evidenced by fragmentation of the nucleus and the mucus granules (Fig. 4.4c, d and Fig. 4.13a, b). These observations thus revealed a novel function for BEST4/CA7$^+$ cells, namely, to increase goblet cell survival.

To understand how goblet cell survival is supported by BEST4/CA7$^+$ cells, we tested whether it depended on direct cell-cell contact or was instead mediated indirectly – either via the lumen (apically) or the medium (basally). In WT organoids, survival of goblet cells beyond day 6 did not depend on BEST4/CA7$^+$ cell contact (Fig. 4.4e, f and Fig. 4.13c). The difference in goblet survival observed above between WT and SPIB-KO organoids was not decreased by co-culturing these organoids in a 1:1 ratio (Fig. 4.4g and Fig. 4.13d), arguing against signals secreted basally into the shared medium. To determine whether goblet cell survival required a shared lumen between the goblet and BEST4/CA7$^+$ cells, we assessed goblet cell survival in mosaic organoids consisting of SPIB-KO and WT cells (with WT cells labeled by H2B-iRFP670, Fig. 4.4h, i). Notably, the survival of SPIB-KO goblet cells was much closer to that of the WT goblet cells in the same mosaic organoid (Fig. 4.4j, k), as compared to the previous two conditions (Fig. 4.4g-i). Together, these results show that goblet cell survival beyond day 4 of differentiation does not rely on direct cell-cell contact but instead depends on the shared lumen.
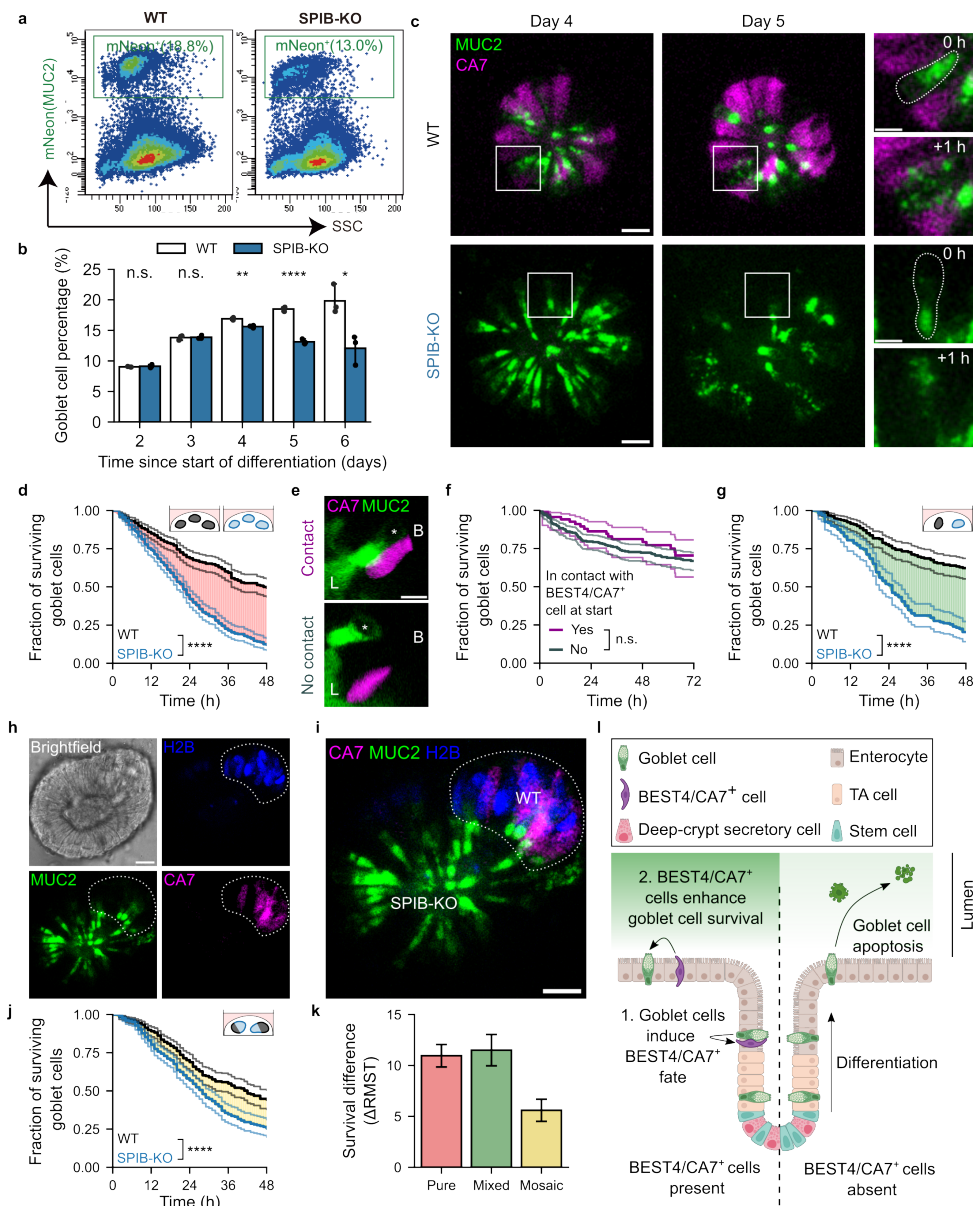
Figure 4.4: BEST4/CA7$^+$ cells enhance goblet cell survival via the lumen. (a) Representative FACS plots of goblet cell percentages in WT and SPIB-KO organoids after 6 days of differentiation. (b) Goblet cell percentage on day 2 to day 6 since shift to differentiation medium, as quantified by FACS analysis. n = 3 biological replicates. Student's t-test is used for comparisons. **** p < 0.0001, ** p < 0.01, * p < 0.05, n.s.: not significant. Error bars indicate 95% confidence interval. (c) Examples of goblet cell apoptosis in WT (top) and SPIB-KO (bottom) organoids. SPIB-KO lack BEST4/CA7$^+$ cells. Insets show time point of goblet cell death. Scale bars, 20 μm in the large images and 10 μm in the insets. (d) Goblet cell survival in differentiated organoids. Data are derived from 365 WT goblet cells and 393 SPIB-KO goblet cells. N = 16 organoids derived from three independent imaging experiments are analyzed per condition. Logrank test at 48 hours is used for comparison. **** p < 0.0001.

Figure 4.4: (continued) (e) Micrographs showing goblet cells in contact (top) and one not in contact (bottom) with a BEST4/CA7$^+$ cell. Asterisk indicates the nucleus of goblet cells. L and B indicate the luminal and basal side of the organoids, respectively. Scale bar: 10 μm. (f) Survival curves for goblet cells with and without contact with a BEST4/CA7$^+$ cell at the start of imaging. Imaging was started after day 6 of differentiation. Data are derived from 69 goblet cells with and 290 goblet cells without contact with a BEST4/CA7$^+$ cell. N = 28 organoids derived from three independent imaging experiments are analyzed. Logrank test at 72 hours is used for comparison, n.s.: not significant. (g) Survival curves for goblet cells in co-cultures of WT and SPIB-KO organoids. Data are derived from 210 WT goblet cells and 162 SPIB-KO goblet cells in mixed cultures. N = 15 organoids derived from two independent imaging experiments are analyzed. Logrank test at 48 hours is used for comparison. **** p < 0.0001. (h, i) Micrographs of a WT/SPIB-KO mosaic organoid. White dotted lines indicate the part of the organoid containing WT cells (with nuclear H2B-iRFP670 fluorescence). The rest of the organoid consists of SPIB-KO (H2B-iRFP670$^-$) cells. Scale bars: 20 μm. (j) Survival curves of SPIB-KO and WT goblet cells in mosaic organoids. Data are derived from 363 WT goblet cells and 412 SPIB-KO goblet cells. N = 23 organoids derived from three independent experiments are analyzed. Logrank test at 48 hours is used for comparison. **** p < 0.0001. Confidence interval for survival curves in panels (d), (f), (g) and (j) are computed using Greenwood's exponential formula. (k) Difference in survival between WT and SPIB-KO goblet cells in pure cultures, mixed cultures and mosaic cultures, measured as the difference in Restricted Mean Survival Times (ΔRMST) up to t = 48 hours. ΔRMST corresponds to the area between the survival curves, as shown with red, green and yellow shaded areas in panels (d), (g) and (j). Error bars indicate the standard error (SE) of the ΔRMST. (l) Proposed model for interdependence of goblet and BEST4/CA7$^+$ cells in the human intestinal epithelium.

4.3 Discussion

By quantifying spatial-temporal differentiation dynamics using live-cell imaging, we uncovered a cell abundance-control mechanism based on an interdependence between BEST4/CA7$^+$ and goblet cells (Fig. 4.4l). Goblet cells – as the primary source of Notch-activating DLL1 –laterally activate Notch signaling in their sister cells, as well as in other direct neighbors, thereby instructing BEST4/CA7$^+$ cell fate commitment in these neighbors [78, 270]. In turn, the long-term survival of goblet cells requires the presence of BEST4/CA7$^+$ cells. The latter interaction does not depend on direct contact and is mediated by their shared lumen. Thus, goblet cells induce BEST4/CA7$^+$ cells that in turn support their long-term survival.

The existence of reciprocal relations between intestinal epithelial cells that control not only differentiation but also survival is notable. Interactions between different cell types in the intestinal epithelium are well-known to drive differentiation and thereby contribute to proper homeostasis. Paneth cells are known to provide EGF, Wnt and Notch ligands that help to maintain stemness [234]. Tuft cells were shown to increase goblet and tuft cell numbers during helminth infections [112, 275], though this interaction was not strictly intra-epithelial, depending on secretion of cytokines by innate lymphoid cells. M cells were shown to inhibit further M cell differentiation by lateral inhibition [113] and expression of RANKL decoy receptors [135]. Yet, cell abundance is in principle equally dependent on cell survival, which we show here is regulated by intra-epithelial cellular interactions. Such reciprocal cooperation between cells may occur more generally and be important to maintaining and adapting the intestinal barrier during normal and inflammatory conditions.

The observed reciprocal interactions may impact medical intervention as well. Pharmacological blocking of Notch-ligands DLL1 and DLL4 has been explored as a strategy for reducing tumor growth [109]. This is based partly on insights from the mouse intestinal

epithelium, where BEST4/CA7$^+$ cells are absent [170], and blocking Dll1 moderately increases goblet abundance without the complete loss of any cell type [193, 207]. However, here we show that in the human intestinal epithelium, abrogated DLL1 expression leads to an almost complete loss of BEST4/CA7$^+$ cells, which in turns causes strongly enhanced goblet cell death. Targeting DLL1 in the human intestine will therefore likely generate responses that differ strongly from those in the mouse. Our findings thus highlight the important differences between human and mouse intestinal epithelia.

The interdependence between BEST4/CA7$^+$ and goblet cells may be particularly relevant for conditions such as Crohn's disease and ulcerative colitis, which are associated with goblet cell depletion [84, 98, 123, 124, 268]. Interestingly, the expression of mature BEST4/CA7$^+$ marker genes in the colon are then also substantially decreased [118, 175, 205] (Fig. 4.14). Decreasing abundance of BEST4/CA7$^+$ cells may thus limit goblet cell survival in these diseases, while goblet cell depletion may conversely also cause BEST4/CA7$^+$ cell number decline. This model is consistent with earlier reports showing that goblet cells are specifically depleted in the upper part of the crypt regions of patients with active ulcerative colitis [84]. The results provide new perspectives on identifying the upstream causes of goblet and BEST4/CA7$^+$ cell depletion, dependence on signals detected by goblet and BEST4/CA7$^+$ cells, downstream effects on epithelial integrity, and the design of alternative therapeutic interventions.

4.4 Methods

Human intestinal organoid lines

Human colon organoids were established previously in our lab [265]. The colon tissue (Donor No: P11N) was obtained from the Diakonessen Hospital Utrecht, with informed consent. The study was approved by the ethical committee and was conducted in accordance with the Declaration of Helsinki and Dutch law. This study complied with all relevant ethical regulations regarding research involving human participants.

Organoid culture

Organoids were cultured as previously described [210, 278]. Briefly, organoids were embedded in small 5-10 µL droplets of Cultrex Basement Membrane Extract, growth factor reduced type 2 (BME2; R&D Systems; cat. #3536-005-02) and kept in expansion medium. Expansion medium consists of adDMEM/F12 (Gibco; cat. #12634028) supplemented with 100 U/ml Penicillin/Streptomycin (P/S; Gibco; cat. #15140122), 10 mM HEPES (Gibco; cat. #15630056), 1× Glutamax (Gibco; cat. #35050038), 1× B-27 supplement (Thermo Fisher; cat. #12587010), 1.25 mM N-acetyl-L-cysteine (NAC; Sigma-Aldrich; cat. #A9165), 1% (v/v) recombinant Noggin in conditioned medium (U-Protein Express BV; custom order), 0.5 nM WNT surrogate (U-Protein Express BV; Custom order), 50 ng/ml human Epidermal Growth Factor (EGF; Peprotech; cat. #AF-100-15), 0.5 µM A83-01 (Tocris; cat. #2939), 1 µM SB202190 (Sigma-Aldrich; cat. #S7067), 1 µM Prostaglandin E2 (PGE2; Tocris; cat. #2296), 10 mM Nicotinaminde (NIC; Sigma-Aldrich; cat. #N0636) and 20% (v/v) recombinant R-spondin 1 in conditioned medium (U-Protein Express BV; custom order).

To differentiate organoids, expansion medium was removed, and cells were incubated for 2 hours in adDMEM/F12 supplemented with 100 U/ml P/S, 10 mM HEPES and 1× Glutamax (wash medium) for 2 hours. Then, differentiation medium was added, which had the same composition as expansion medium except that EGF, Noggin, SB202190, A83-01, WNT surrogate, PGE2 and NIC.

Generation of genetically modified organoids

Generation of CA7-P2A-tdTomato and MUC2-mNeonGreen reporter organoids, by CRISPR-HOT approach, has been described in our previous study [278]. DLL1-P2A-Clover knock-in reporter organoids were similarly generated using CRISPR-HOT [6, 107]. Three plasmids were used: (1) the frame-selector plasmid containing an sgRNA (to linearize the donor-targeting vector), Cas9 and mCherry (for the detection and FACS sorting of the successfully transfected cells) was obtained from Addgene (plasmid# 66941); (2) The P2A-Clover donor-targeting vector was obtained from Addgene (plasmid# 138568) and (3) the sgRNA vector (Addgene, plasmid# 47108) containing sequence targeting 3' end of DLL1 gene. The sgRNA sequence is 5'-TGAGTGCGTCATAGCAACTG-3'. 5 µg sgRNA vector, 5 µg frame-selector plasmid and 5 µg donor-targeting vector were co-transfected into organoid cells using the NEPA electroporation system (NEPAGENE). After FACS sorting, based on the mCherry fluorescence, subclones were picked and expanded in expansion medium. Successful insertions were first identified by direct visualization of the fluorescence marker in the differentiated organoids and then confirmed by targeted genotyping via Sanger sequencing. The

H2B-iRFP670 sequence was integrated into the genome using mT2TP transposase system. 5 µg transposase plasmid and 5 µg donor plasmid with terminal inverted repeats (TIRs) bearing H2B-iRFP670 sequence were co-transfected into organoid cells by electroporation. Generation of SPIB knock-out organoids has been described in our previous study [278]. DLL1 and DLL4 knock-out organoids were similarly generated by introducing an early stop codon) using CRISPR C-to-T base-editing: 7.5 µg spCas9-CBE6b plasmid (Addgene, plasmid# 215820), 2.5 µg sgRNA plasmid and a two-plasmid transposon system (5 µg PiggyBac transposase plasmid + 5 µg donor plasmid with terminal inverted repeats (TIRs) bearing hygromycin resistance for organoid selection) were co-transfected into organoid cells through electroporation. After FACS sorting of DAPI- live single cells followed by hygromycin selection, subclones were picked and expanded in expansion medium. Successful homozygous knock-out organoids were confirmed by targeted genotyping via Sanger sequencing. The sgRNA sequence for DLL1-KO and DLL4-KO are: 5'-TCCCAGGACCTGCACAGCAG-3' and 5'-CATCCAGGGCTCCCTAGCTG-3', respectively. Genotyping primers used for knock-in and knock-out validation were listed in Table 4.1.

Sample preparation and flow cytometry

Organoids were released from BME using ice-cold Corning Cell Recovery Solution (Sigma-Aldrich; cat. #CLS354253) and dissociated with 1 ml TrypLETM Express Enzyme (TrypLE; Thermo Fisher; cat. #12605010) at 37 °C for 6-8 mins, followed by gently pipetting 20 times. After TrypLE dissociation, the cell suspension was filtered through a 40 µm cell strainer and stained with DAPI (Sigma-Aldrich; cat. #10236276001) for FACS analysis or cell sorting. Samples were analyzed on a BD LSR Fortessa X20 equipped with 4 lasers (BD Bioscience). At least 5,000 DAPI$^-$ live cells were recorded for each analyzed sample.

RNA extraction and quantitative PCR

Organoids were subjected to RNA isolation using a NucleoSpin RNA kit (Macherey-Nagel; cat. #740955.50) following the manufacturer's protocol. Reverse transcription reactions were performed using GoScriptTM reverse transcriptase kit (Promega; cat. #A5000). cDNA was subjected to qPCR analysis using iQTM SYBR Green Supermix (BioRad; cat. #1708887) on a CFX Connect Real-Time PCR machine (BioRad). For gene expression analysis, qPCR was performed with gene-specific qPCR primers. Ct value of each gene was normalized to GAPDH (as the ΔCt), and fold change between experimental groups was calculated with the 2-ΔΔCt method. All qPCR primers used in this study are listed in Table 4.1.

Long-term live-cell imaging

For tracking experiments of differentiating and expanding organoids, organoids were dissociated(pleguezuelos-manzano2020) and plated onto an imaging chamber (CellVis) and expanded for 2-3 days. Organoids were then washed with wash medium for 2 hours before differentiation medium added. Cells were imaged using a A1R MP (Nikon) scanning confocal microscope with a 1.30 NA 40× magnification oil immersion objective. Images were taken every 12 minutes, and at each time point, 31 Z-slices were imaged with 2 µm intervals. For tracking goblet cell survival, differentiated live reporter organoids were staged on the Leica SP8 confocal detection system fitted on a Leica DMi8 microscope or a Leica TCS SP8 to capture time series images every 15 – 60 mins for 18 – 48 hours. All

tracking experiments were performed at 37 °C and 5% CO2.

Cell tracking

Tracking of expansion and differentiation of human colon organoids was done manually using our custom tracking software OrganoidTracker [143]. For tracking the organoids in expansion medium, we selected three organoids and tracked the nuclei from the bottom 10 μm of the organoid at the start, and continued tracking until cells extruded, moved out of view, or were no longer trackable with high fidelity. For tracking the remaining differentiating organoids, we tracked We reconstructed the full lineage tree of all observable CA7$^+$, MUC2$^+$ and DLL1$^+$ cells. Organoids were excluded from this analysis if they moved out of view, collapsed, contained CA7$^+$, MUC2$^+$ or DLL1$^+$ cells already at the start of imaging, or contained no cells expressing CA7, MUC2 or DLL1 throughout the entire time-lapse.

Single-cell RNA sequencing analysis

Single-cell RNA sequencing data of the human colon epithelium was retrieved from the GutCellAtlas [69, 70]. The .h5ad file was loaded as an AnnData object and processed using the scanpy library. Only cells with less than 20% mitochondrial gene expression, derived from primary healthy pediatric and adult human colon epithelium were included. Furthermore, only genes expressed in at least three cells were included in the analysis. Cell types with less than 20 cells were excluded from this analysis. Data was normalized (target sum 10.000), log10 transformed, and the top 2,000 highly variable genes were found. Data was then scaled, and 20 principal components (PCs) coordinates were found, and the nearest neighbor distance matrix and neighborhood graph was computed (knn = 15) using all 20 principal components. Then, dimension reduction was performed using t-distributed stochastic neighborhood embedding (tSNE) using 20 components.

Mosaic organoids

To generate the mosaic organoids, WT (labeled with H2B-iRFP670) and SPIB-KO double reporter organoids were dissociated into single cells (as described above), mixed at a 1:1 ratio, and plated into a BME-coated transwell insert or culturing well for 2D attachment for 2 days in the expansion medium. Then, the monolayer of mixed cells was dissociated, seeded as BME droplets, and cultured in expansion medium for organoid growth.

Data retrieval from IBD TaMMA database

Expression levels of selected proteins in colon tissue samples of patients with Crohn's Disease (CD), Ulcerative Colitis (UC) and healthy control were retrieved from the IBD Transcriptome and Metatranscriptome Meta-Analysis (IBD TaMMA) database [175]. P-values of statistical tests for proteins of interest were obtained from the IBD TaMMA web-app (`https://ibd-meta-analysis.herokuapp.com/`).

Statistics

Statistical analyses were performed as indicated in the figure legends. Mann-Whitney U test, Student's t-tests, Pearson χ^2-tests were performed using the scipy.stats library in

Python [274], with the following significance: **** $p < 0.0001$, *** $p < 0.001$, ** $p < 0.01$, * $p < 0.05$, and n.s. $p > 0.05$. Logrank test and survival analysis were performed using the lifelines library in Python [56]. Restricted Mean Survival Time (*RMST*) and corresponding variance were computed directly from the Kaplan-Meier estimates for the survival functions. For given survival curve $S(t)$, and time horizon t^*, RMST is computed via

$$RMST \equiv \mu = \int_0^{t^*} S(t)dt \qquad (4.1)$$

Given two survival curves $S_0(t)$ and $S_1(t)$, the RMST difference (Δ) corresponds to the area between survival curves and serves as a measure of the effect size for the difference in survival between two groups even if the proportional hazard assumption is breached [227]. The Restricted Standard Deviation of Survival Time (*RSDST*), which corresponds to the standard deviation of the *RMST*, was computed as [227]:

$$RSDST \equiv \sigma = \sqrt{\int_0^{t^*} 2tS(t)dt - \left(\int_0^{t^*} S(t)dt \right)^2} \qquad (4.2)$$

For each estimated RMST difference ($\hat{\Delta} = \hat{\mu}_1 - \hat{\mu}_0$) between two groups with Kaplan-Meier survival curves $\hat{S}_0(t), \hat{S}_1(t)$, sample sizes n_0, n_1 and *RSDST* estimates $\hat{\sigma}_0, \hat{\sigma}_1$, the standard error was computed as

$$SE(\hat{\Delta}) = \sqrt{\frac{\hat{\sigma}_0^2}{n_0} + \frac{\hat{\sigma}_1^2}{n_1}} \qquad (4.3)$$

SOFTWARE

Image processing was done in Fiji/ImageJ (v1.54g). Tracking was performed in Organoid-Tracker [143]. FACS data was plotted using BD FACS Diva software (v8.0.1), FlowJo (v10). Downstream data analysis and plotting was done in Python 3.9, with the use of the following libraries: numpy (v1.26.0, scipy (v1.12.0), pandas (v2.1.0), seaborn (v0.13.0), matplotlib (v3.6.3), lifelines (v0.27.8), scanpy (v1.9.3). Figures were made in Inkscape (v1.1.1; 3bf5ae0d25, 2021-09-20).

ACKNOWLEDGEMENTS

4.5 SUPPLEMENTARY INFORMATION
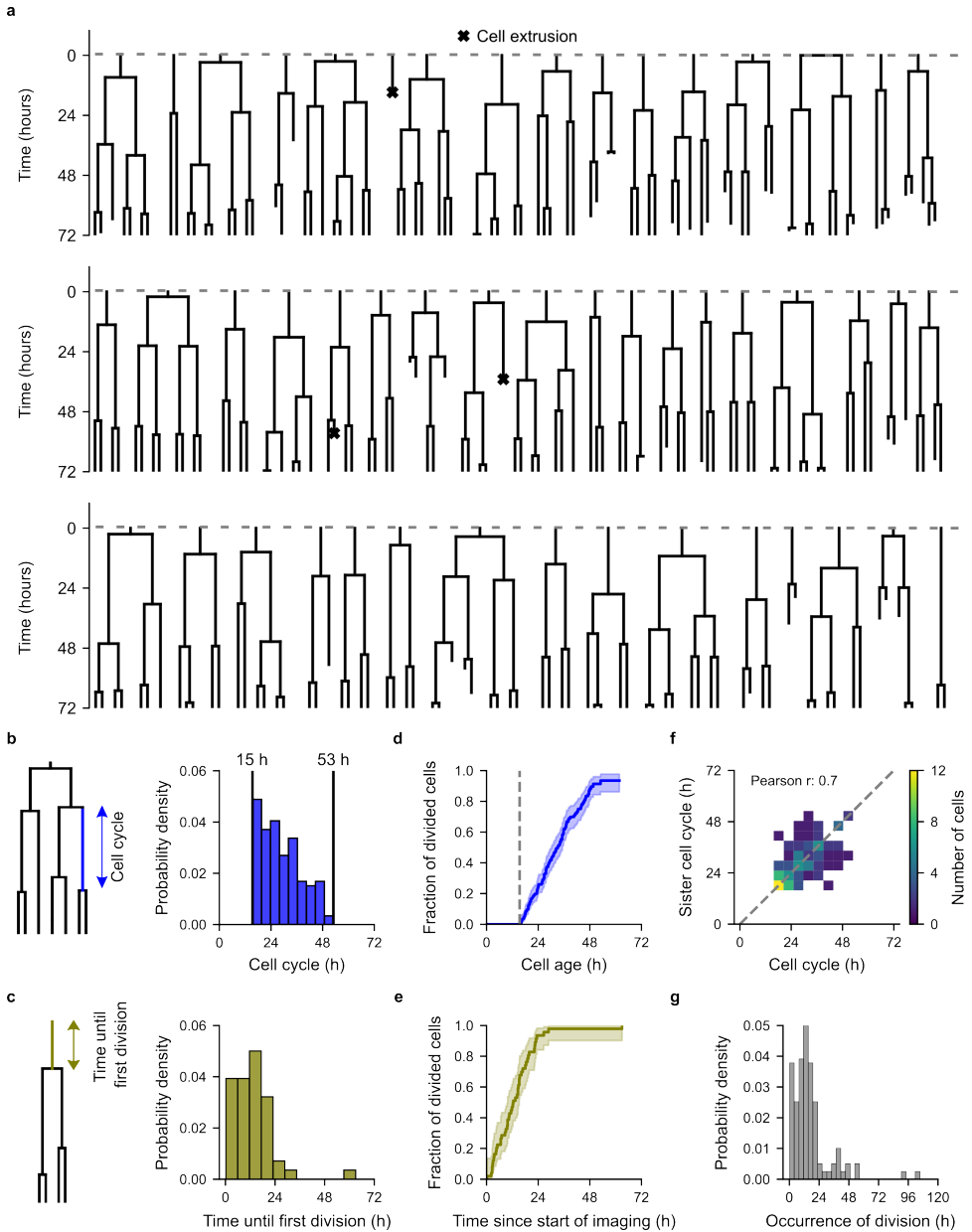
Figure 4.5: Expansion medium keeps cells in a proliferative and undifferentiated state. (a) Lineage tree gallery of three organoids in expansion medium. (b, c) Distribution of cell cycle durations (b) and time until division of cells present at the start of imaging (c).

Figure 4.5: (continued) (d, e) Cumulative distribution of divided cells since their birth (d) and since the start of imaging (e). Error around the distributions due to censoring (e.g. cells moving out of view or extruding) are estimated using a Kaplan-Meier model. Vertical dashed line in (e) indicates the shortest observed cell cycle. (f) Correlation of cell cycle durations between sister cells (n = 118 sister pairs). (g) Divisions virtually stop occurring after approximately 48 hours in differentiation medium.

4
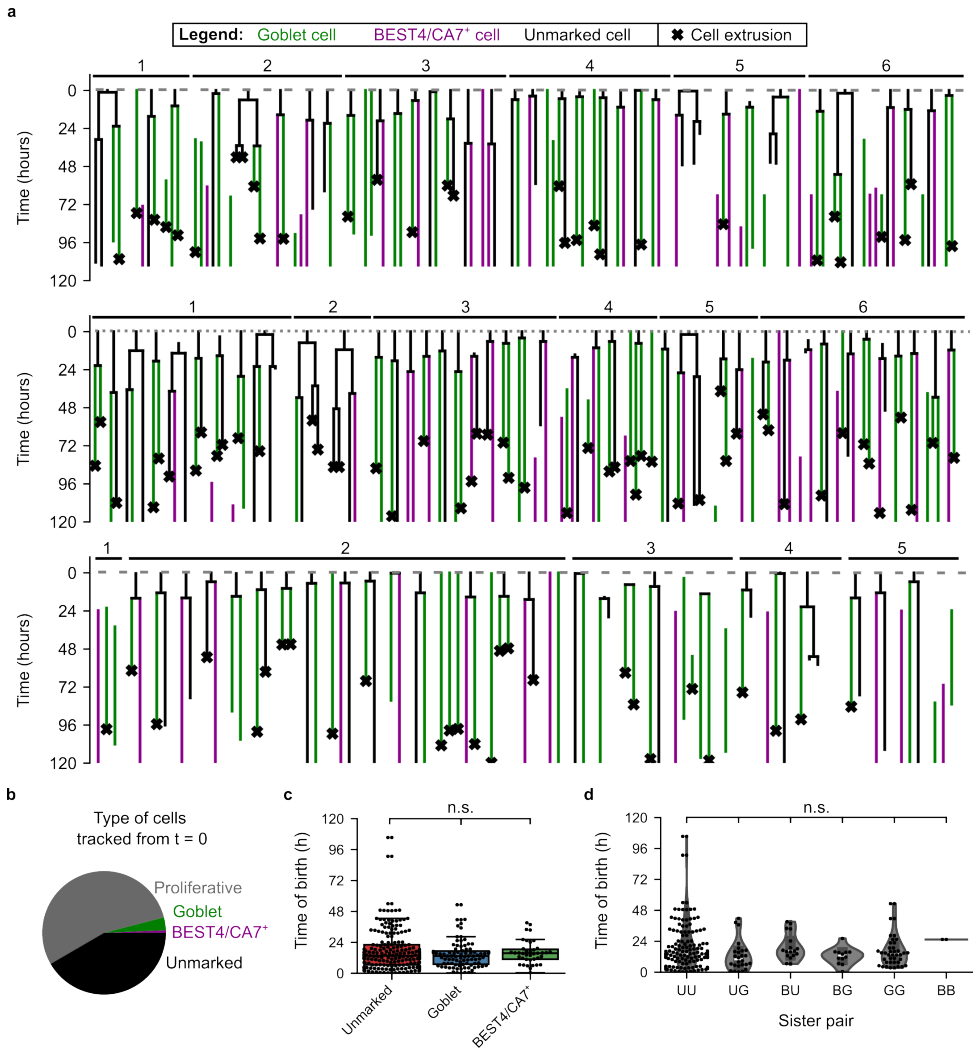
Figure 4.6: Lineage tree reconstruction of goblet and BEST4/CA7⁺ cells in differentiating organoids.
(a) Lineage tree gallery of n = 17 organoids derived from three independent tracking experiments. Shown are only lineage trees that contained at least one BEST4/CA7⁺ or goblet cell. (b) Identity of the cells present already at time zero. (c) Time of birth of unmarked, goblet and BEST4/CA7⁺ cells. Kruskal-Wallis test is used for multiple comparisons, n.s.: not significant. In box plots, the center line shows the median, the box spans the interquartile range (IQR), and the whiskers extend to the most extreme data points within 1.5×IQR from the quartiles. (d) Distribution of birth-times for all sister pairs. Kruskal-Wallis test is used for multiple comparisons, n.s.: not significant. Panels (c) and (d) only included cells that were tracked beyond 63.7 hours after the start of differentiation, see Supplementary Note 4.5.1.
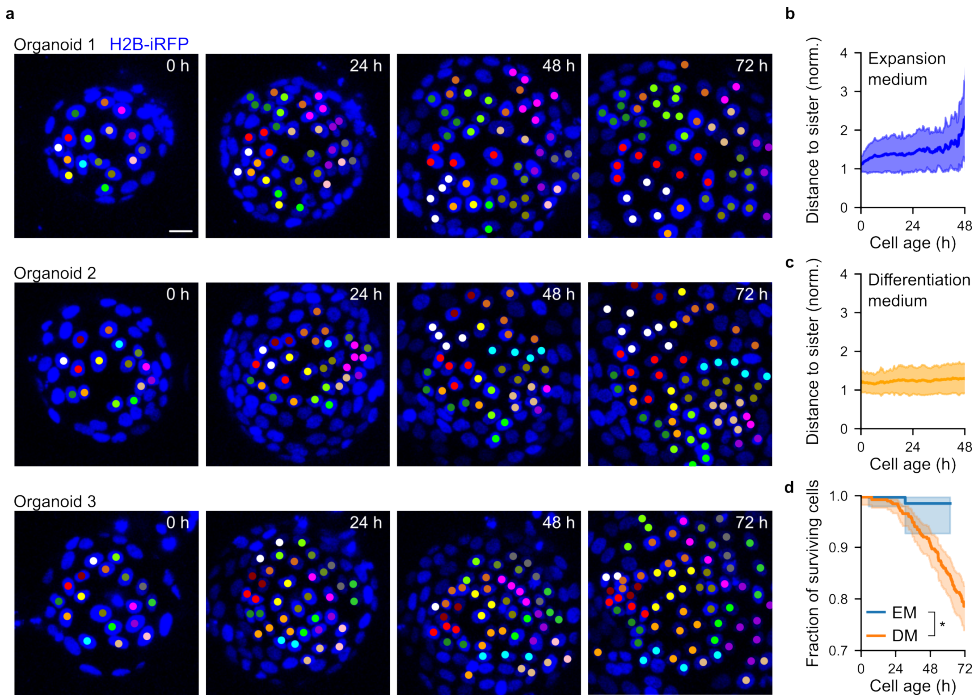
Figure 4.7: Cell-cell rearrangement rate in the organoids is low in both expansion and differentiation.
(a) Spatial distribution of clones for three organoids in expansion medium. The color of the dot in the nuclei indicates from which cell the given cell has descended. (b, c) Distance to sister cell normalized by the distance to the closest cell for organoids in expansion medium (b) and differentiation medium (c). n = 190 sister pairs (b) and n = 104 sister pairs (c) derived from three organoids in each medium. Only fully tracked organoids were included in (c). Shared area in panels indicates the standard deviation. (d) Survival curves of cells in both expansion and differentiation medium estimated from Kaplan-Meier fits. Logrank test is used for comparison at t = 48 h. * $p < 0.05$. Confidence interval for survival curves are computed using Greenwood's exponential formula. EM, expansion medium; DM, differentiation medium.

4.5.1 SUPPLEMENTARY NOTE - INCLUSION CRITERION FOR UNMARKED CELLS

For quantification of the frequencies of sister pairs, every cell type must be assigned either BEST4/CA7$^+$ cell, goblet cell or unmarked cell fate. Cells are, however, frequently lost from the imaging dataset, either due to cell death or because the cell moves out of the imaging window. It is therefore possible that some cells without BEST4/CA7$^+$ or goblet cell marker when they are lost from the dataset would have shown the markers later. To avoid overrepresentation of Unmarked cells in the dataset, we filtered out unmarked cells for which the probability was > 5% that they would have expressed the BEST4/CA7$^+$ or goblet cell marker if they could have been tracked for longer (Fig. 4.8a). This amounts to excluding cells that were lost from the imaging dataset before the point in time, denoted as $t_{0.95}$, when a given cell still has a > 5% probability to express either marker.

Let U_t, G_t and B_t be the events that a cell is an unmarked cell, a goblet cell or a BEST4/CA7$^+$ cell at time t, respectively. The probability that a cell would have remained unmarked (event U_∞), given that it is unmarked at time t, is:

$$P(U_\infty|U_t) = 1 - P(B_\infty|U_t) - P(G_\infty|U_t) \tag{4.4}$$

Using Bayes' theorem, this can be rewritten as:

$$P(U_\infty|U_t) = 1 - P_B \cdot P(U_t|B_\infty) - P_G \cdot P(U_t|G_\infty) \tag{4.5}$$

Here P_B and P_G are the a priori probabilities (base-rates) of cells committing to goblet or BEST4/CA7$^+$ cell fate, which we previously found to be $P_B \approx 1.4\%$ and $P_G \approx 18.8\%$ using FACS-sorting [278]. The remaining conditional probabilities, which represent the probabilities that an eventual BEST4/CA7$^+$ or goblet cell is still unmarked at time t can be estimated from the probability density functions of the marker expression times (Fig. 4.2e, h & Fig. 4.8b). We approximate these distributions as normal distributions, so that:

$$P(U_t|B_\infty) = \frac{1}{2} \, \text{erfc}\left(\frac{t - \mu_B}{\sigma_B \sqrt{2}}\right)$$

$$P(U_t|G_\infty) = \frac{1}{2} \, \text{erfc}\left(\frac{t - \mu_G}{\sigma_G \sqrt{2}}\right)$$

Here $\text{erfc}(x) = 1 - \text{erf}(x)$ is the complement of the error function, the constants μ_B, σ_B and μ_G, σ_G indicate the mean and standard deviations of marker expression times for BEST4/CA7$^+$ and goblet cells, respectively. Together, this means that the sought probability is given by:

$$P(U_\infty|U_t) = 1 - \frac{P_B}{2} \, \text{erfc}\left(\frac{t - \mu_B}{\sigma_B \sqrt{2}}\right) - \frac{P_G}{2} \, \text{erfc}\left(\frac{t - \mu_G}{\sigma_G \sqrt{2}}\right) \tag{4.6}$$

By equating this probability to 95% and solving for t, we find that $t_{0.95} = 63.7$ hours (Fig. 4.8c).
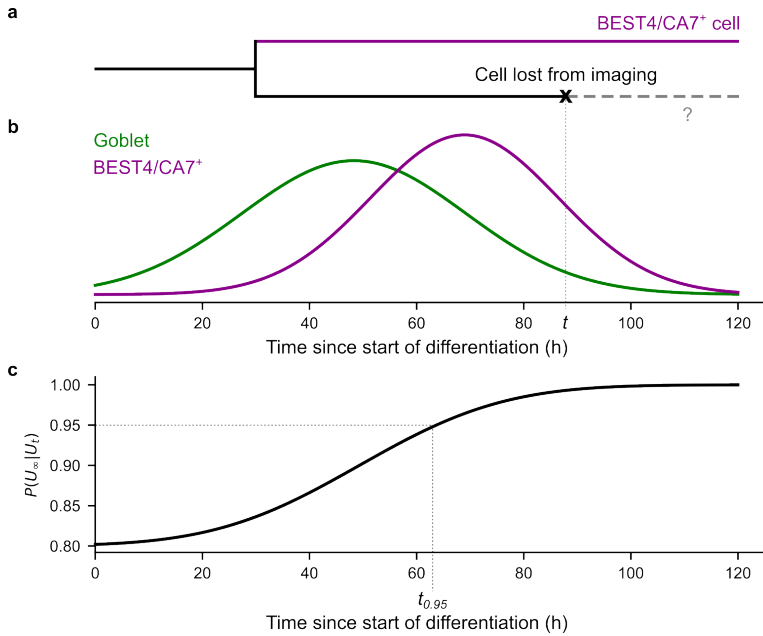
Figure 4.8: Estimation of the probability that unmarked cells at a given time remain unmarked. (a) Hypothetical example of a case where a BEST4/CA7$^+$ was tracked until the end of the time-lapse, but its sister was lost from the tracking dataset (either due to death or after moving out of the imaging field) at time t. (b) Probability density functions for marker expression times. (c) Probability that an unmarked cell would have remained unmarked as a function of time.

4.5.2 SUPPLEMENTARY NOTE – COMPUTING OF BASELINE EXPECTATION OF SISTER PAIRS

Here, we derive the equations used for computing the expected numbers of distinct sister pairs under the baseline assumption that cell fate commitment to either the BEST4/CA7$^+$ (B), goblet (G) or unmarked (U) fate is fully cell-autonomous and independent of lineage history and spatiotemporal cues. In this picture, the three cell types B, G and U are randomly distributed over lineages, with the probability that two cells of particular type are sisters given by the product of the frequencies at which each type occurs within the population.

Let P_B and P_G be the population level probabilities (priors) that a given cell commits to the BEST4/CA7$^+$ and goblet cells. Using FACS-experiments, $P_B \approx 1.4\%$ and $P_G \approx 18.8\%$ in previous work [278] (see also Supplementary Note 4.5.1). In general, the set of possible sister pairs (S) consists of 9 possible sister pairs, namely:

$$S = \{(B,B),(B,G),(B,U),(G,B),(G,G),(G,U),(U,B),(U,G),(U,U)\} \tag{4.7}$$

In our dataset, however, we only tracked lineage trees of lineages containing at least one BEST4/CA7$^+$ or goblet cell and therefore excludes UU sister pairs. Thus, our dataset $D \subset S$ contains the following elements:

$$D = \{(B,B),(B,G),(B,U),(G,B),(G,G),(G,U),(U,B),(U,G)\} \tag{4.8}$$

The probability that a given sister pair in our dataset D is of type (i,j) under the baseline assumption is then given by:

$$P_{(i,j)} = \frac{P_i \cdot P_j}{1 - P_{UU}} \tag{4.9}$$

Here the denominator $1 - P_{UU}$ ensures that the probabilities that a sister pair is of type (i,j) within our dataset D sum up to 1.

$$\sum_{(i,j) \in D} P_{(i,j)} = 1 \tag{4.10}$$

Noting that $P_U = 1 - P_B - P_G$ and therefore $P_{UU} = (1 - P_B - P_G)^2$, we obtain

$$P_{ij} = \frac{P_i \cdot P_j}{1 - (1 - P_B - P_G)^2} \tag{4.11}$$

Since we do not distinguish between the order of the cell types in asymmetric sister pairs, we are interested in the probabilities of each possible sister pair independent of the order. That is, we look at the symmetrized dataset $\bar{D}$, being:

$$\bar{D} = \{BB, BG, BU, GG, GU\} \tag{4.12}$$

We note that we use the convention to abbreviate the types of sister pairs in alphabetical order, as BB, BG, BU, GG and GU. Now, the probability of each possible sister pair $ij \in \bar{D}$ is given by:

$$P_{ij} = \begin{cases} \frac{2P_i \cdot P_j}{1 - (1 - P_B - P_G)^2} & i \neq j \\ \frac{P_i^2}{1 - (1 - P_B - P_G)^2} & i = j \end{cases} \tag{4.13}$$

The expected numbers of sister pairs is then calculated using:

$$E[n_{ij}|ij \in \bar{D}] = N \cdot P_{ij} \tag{4.14}$$

4
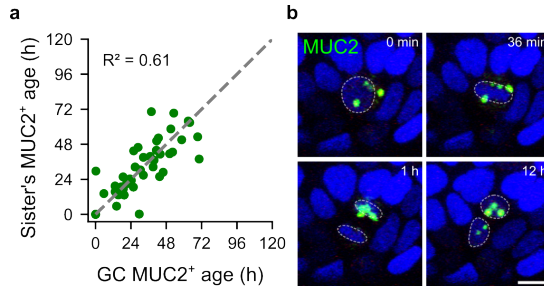
Figure 4.9: Goblet-goblet sister pairs can be explained by commitment in the mother cell. (a) Correlation between age of MUC2 expression for goblet-goblet cell sisters. R^2 indicates the coefficient of determination. (b) MUC2^{+} proliferative cell dividing into two goblet cells. Scale bar, 10 μm.

4
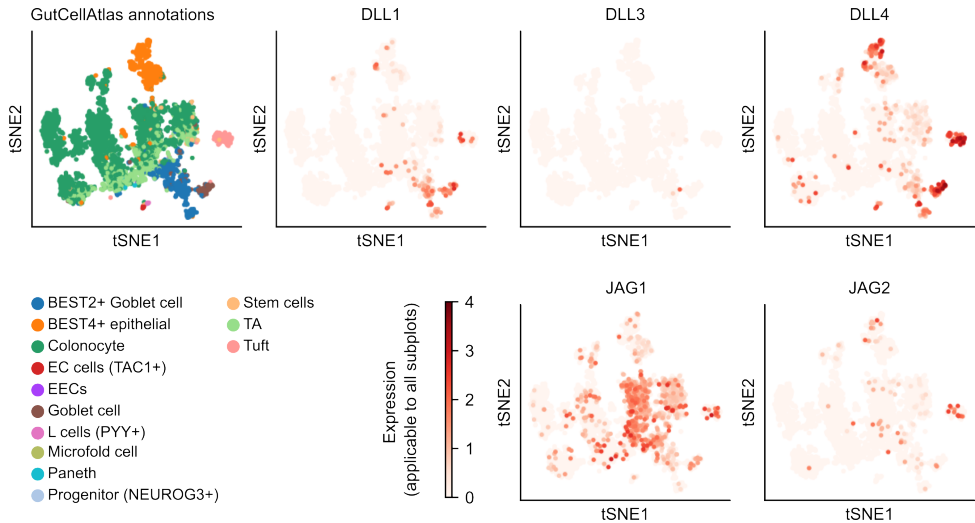
Figure 4.10: Expression of Notch-ligands in primary human colon epithelial cells. Data and cell type annotations was retrieved from the GutCellAtlas [69].
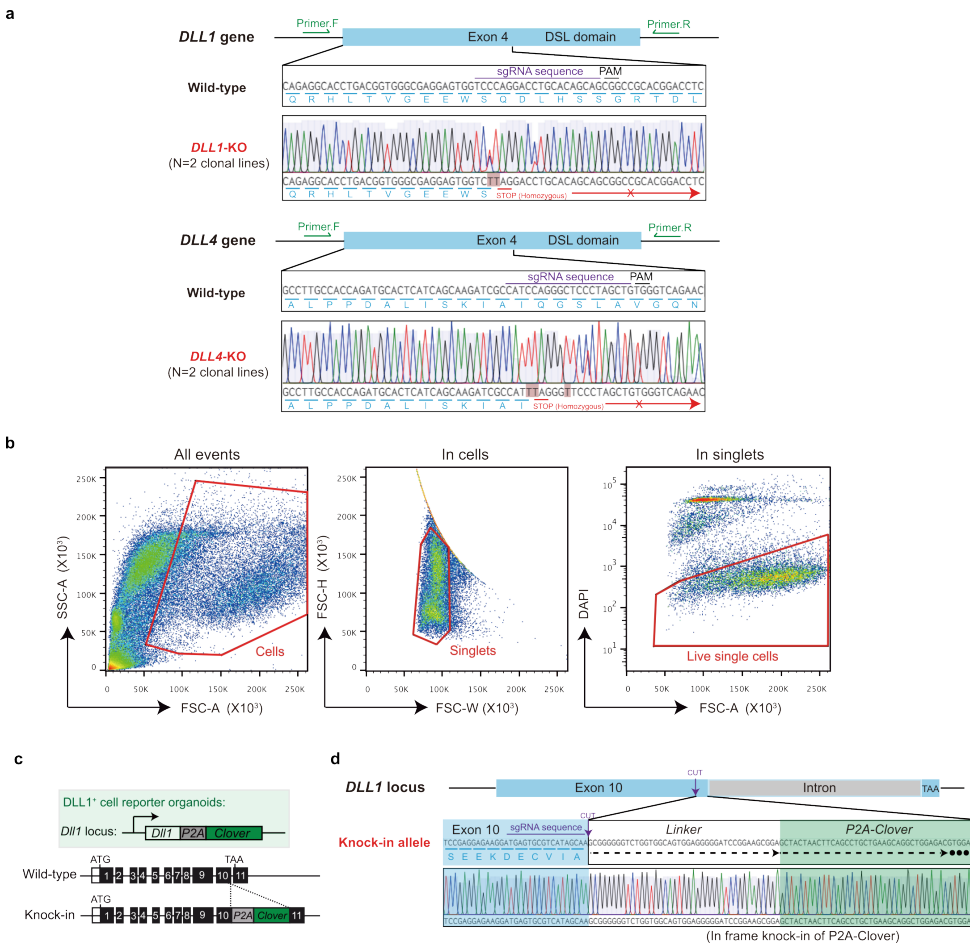
Figure 4.11: Genotyping and FACS gating strategy of knock-in and knock-out DLL reporter organoid lines. (a) Validation of DLL1 and DLL4 knock-out (KO) organoids by targeted genotyping. For each targeted gene, n = 2 different homozygous clonal lines are generated. The gene locus, sgRNA targeting sites, locations of genotyping primers, and amino acid sequence (including the CRISPR-generated early STOP codon) are indicated. (b) Gating strategy for FACS analysis of organoid cells. All detected events are gated based on their sizes to enrich the cell fraction (left). Doublets are then gated out (middle). Live singlets are gated based on the negative staining of DAPI (right). Additional analysis of cell percentage is based on the fluorescence expression of the knock-in (KI) reporter organoids. (c) Illustration of the knock-in reporter organoids containing a P2A-Clover cassette inserted at the C-terminus, before the stop codon, of the DLL1 gene. (d) Targeted genotyping of DLL1-P2A-Clover reporter organoids.
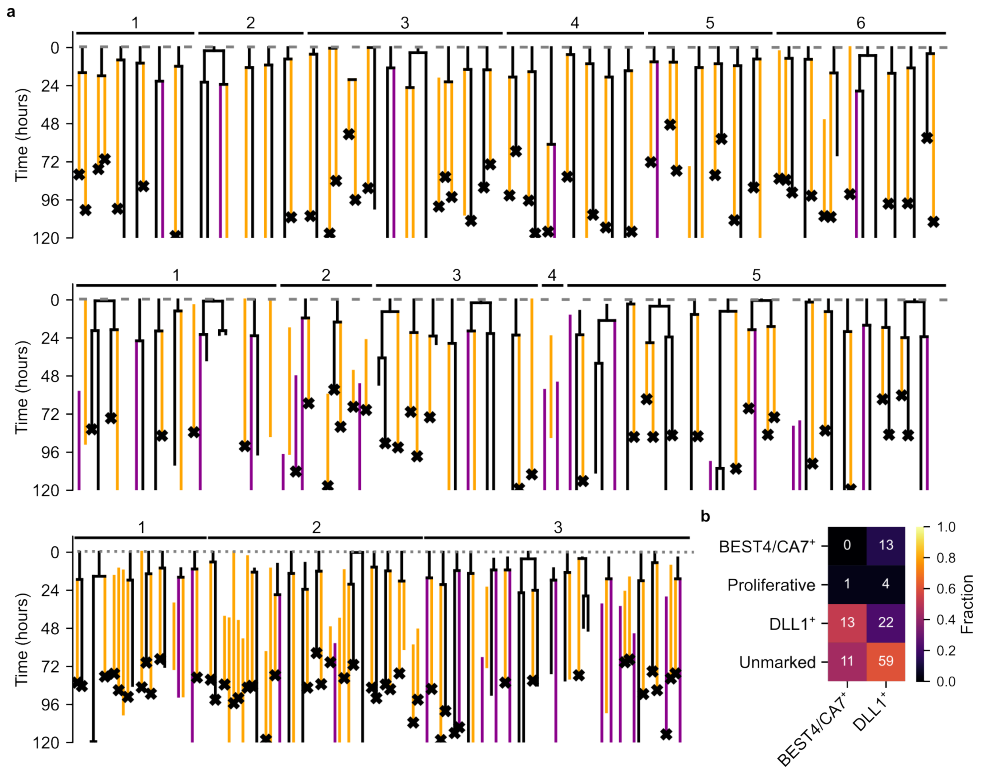
Figure 4.12: Tracking and lineage tree reconstruction of DLL1^{+} and CA7^{+} cells. (a) Lineage tree gallery of CA7-DLL1-H2B reporter organoids. (b) Table showing frequencies of sister pairs for the lineages in panel (a).
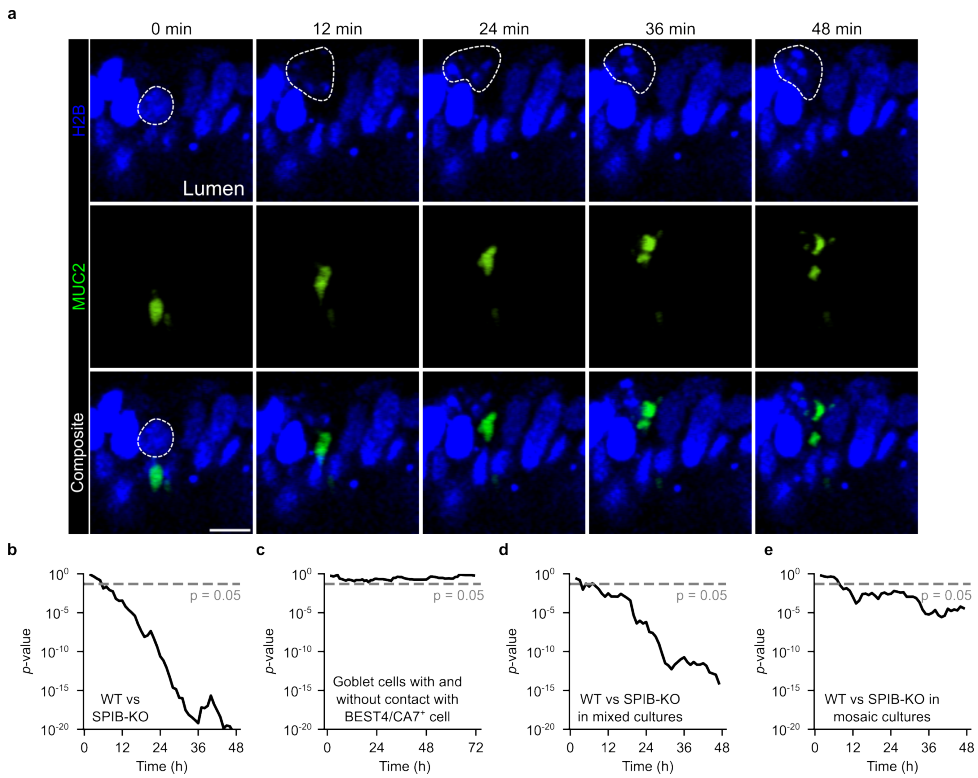
Figure 4.13: Goblet cell apoptosis. (a) Representative example of a goblet cell undergoing apoptosis. Note that the nucleus and the mucus reservoir fragment simultaneously. Scale bar, 10 μm. (b-e) Significance (p-value) of the comparisons between WT and SPIB-KO goblet cells (b), goblet cells with and without contact with a BEST4/CA7$^+$ cell at the start of imaging (c), WT and SPIB-KO goblet cells in mixed cultures (d), WT and SPIB-KO goblet cells in mosaic organoids (e). The p-value was computed using the log-rank test with log($-$log($\cdot$)) transformation to increase statistical power [138].
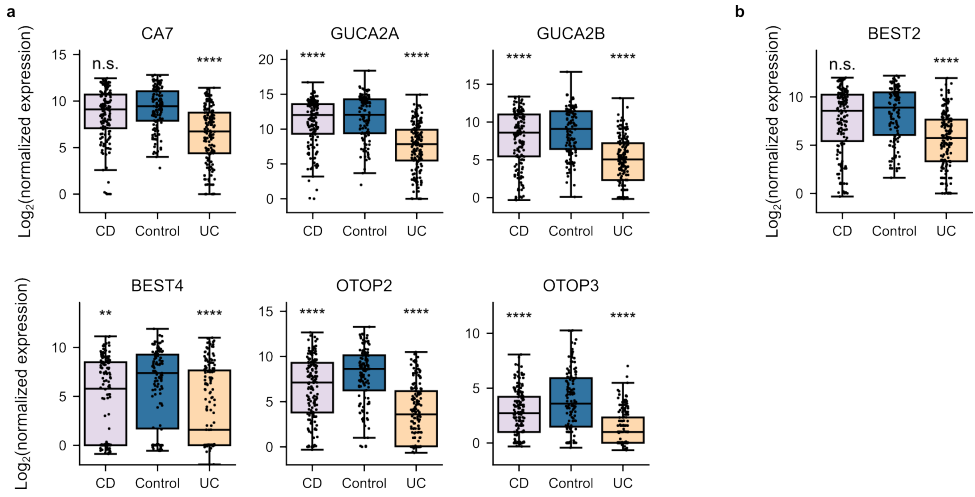
Figure 4.14: Expression of mature BEST4/CA7$^+$ cells and BEST2 is decreased in Ulcerative Colitis and Crohn's Disease patients. (a, b) Expression of mature BEST4/CA7$^+$ marker genes (a) and the colonic goblet cell marker BEST2 (b) as retrieved from the IBD TaMMA database [175]. P-values from Tukey's HSD test were also retrieved from the TaMMA database. **** $p < 0.0001$, *** $p < 0.001$, ** $p < 0.01$, * $p < 0.05$, and n.s.: not significant. In the box plots, center lines show the median, boxes span the interquartile range (IQR), and whiskers extend to the most extreme data points within 1.5×IQR from the quartiles.

Table 4.1: Primers used in this study.

SPIB-knock-out	CAGTCCCACAGGGAGTCTGGGGG

Genotyping PCR primers

Primer Name	Sequence
CA7-knock-in-Forward	TGACTCTCCAACTAGCACCCCACA
P2A-tdTomato-Reverse	ATCTCGAACTCGTGGCCGTT
MUC2-knock-in-Forward	TGCTCCTGCTGCAAAGAGGAG
mNeon-Reverse	GCCATACCCGATATGAGGGACCA
DLL1-knock-in-Forward	GTGTCTTCCTGGAACCACTGCT
P2A-Clover-Reverse	GCTTGCCGGTGGTGCAGATGAA
DLL1-knock-out-Forward	CAGGGCACCTTCTCTCTGATTA
DLL1-knock-out-Reverse	TCCGTGTTCGTGGACGAGTGA
DLL4-knock-out-Forward	GTCCCTCTGGCCTGTTCTTGCT
DLL4-knock-out-Reverse	GCAGGCAGGACAAGTTGCCAT
SPIB-knock-out-Forward	ATGCAAATCCTGGGGTCAGAGA
SPIB-knock-out-Reverse	ACTGTCCCCTTACCACTCACC

qPCR primers

Primer Name	Sequence
Q-CA7-Forward	TGGAGACAGGAGACGAGCA
Q-CA7-Reverse	TCCAGGTGACACTCTCACTGA
Q-MUC2-Forward	AGGATGACACCATCTACCTCAC
Q-MUC2-Reverse	CATCGCTCTTCTCAATGAGCA
Q-GAPDH-Forward	CTGGGCTACACTGAGCACC
Q-GAPDH-Reverse	AAGTGGTCGTTGAGGGCAATG

PART II

NEW METHODS FOR STUDYING DYNAMICS IN INTESTINAL ORGANOIDS

4

5

LABEL-FREE CELL IMAGING AND TRACKING IN 3D ORGANOIDS

"Nothing is worth doing,
except what the world says is impossible."

Oscar Wilde

Fluorescence live-cell microscopy is one of the most frequently used techniques to study dynamic processes in organoids. However, it is often limited by laborious fluorescent reporter engineering, limited numbers of fluorescence channels, and adverse phototoxicity and protein over-expression effects. Label-free imaging is a promising alternative, but not yet established for 3D cultures. Here, we introduce LabelFreeTracker, a label-free machine-learning based method to visualize the nuclei and membranes in brightfield images of 3D mouse intestinal organoids. The approach uses U-Net neural networks trained on the brightfield transmitted light and fluorescence images of mouse intestinal organoids, as obtained by standard confocal microscopy. LabelFreeTracker frees up fluorescence channels to study fluorescent reporters and allows (semi-)automated quantification of cell movement, cell shape and volume changes, proliferation, differentiation, and lineage trees. This method greatly simplifies live-cell imaging of tissue dynamics and will accelerate screening of patient-derived organoids, for which reporter engineering is not feasible.

5.1 Introduction

Organoids are rapidly advancing as a major tool in drug discovery, personalized medicine, and basic research, and offer an alternative to animal testing [45]. The dynamics of cell proliferation [59, 115], migration [217], and differentiation [291] in organoids are critical to understanding normal and pathological development [20]. Furthermore, organoids are rapidly advancing as in vitro model systems to study drug responses. To study dynamics at the single-cell level requires that cells are distinguishable from each other and can be followed in time. This is typically achieved by fluorescent labelling of either the cell nucleus or membrane [59, 115, 143, 217, 251, 262, 291]. However, the required engineering of fluorescent labels is in practice unfeasible for many applications, such as screening in patient-derived organoids. Furthermore, the nuclear and membrane labels needed to identify cells in 3D tissues limits the colors available for functional studies, such as monitoring cell fate markers or FRET sensors in time, while adding to the phototoxicity. Alternatives such as holographic and hyperspectral imaging have been developed [130, 286], but require specialized equipment that is not broadly available. In contrast, bright-field microscopy is broadly available and is extensively used for imaging overall organoid growth and morphology [29, 60, 96, 177, 185]. Besides its general availability, a major advantage of bright-field microscopy is that it has virtually no phototoxic effects on cells in the sample. Machine learning approaches have been used to visualize and track cells in 2D monolayer cultures [42, 49, 204]. Organoids, however, are typically several 10's of micron thick, which causes strong light scattering by the intervening tissue and obscures cellular features such as nuclei and membranes [130] (Fig. 5.1a, left panel).

Here, we present LabelFreeTracker, a label-free imaging method to visualize and track cells in 3D organoids using the 3D bright-field images as obtained from the transmitted light in standard 3D confocal microscopy (Fig. 5.1a). Using a custom machine learning approach and a min-cost flow-solver, it integrates spatial information in 3D from the scattered light to reconstruct cell nuclei and shapes over 50 μm deep, and temporal information to track cells over multiple generations. The method overcomes the substantial tracking challenges in organoids, where cell nuclei are densely packed and move rapidly during division, while tracking cells through cell divisions is prone to errors and even single errors can cause large-scale alterations to lineage trees. LabelFreeTracker works in conjunction with OrganoidTracker [143], our custom-built and freely available software tool for single-cell tracking in organoids, and can be used on data acquired with a standard confocal microscope. Furthermore, LabelFreeTracker can readily be extended to other organoid systems and cellular features. It will enable the analysis of dynamic processes in patient-derived and other organoids when nuclear and membrane labels are not available.
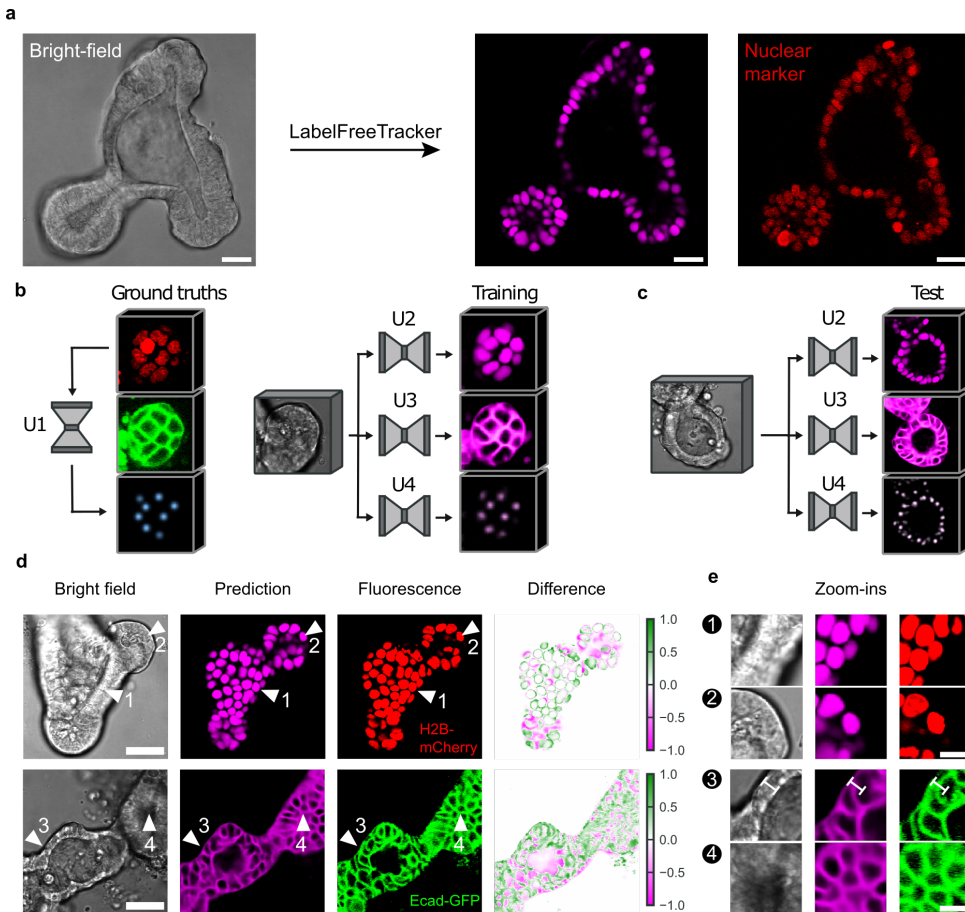
Figure 5.1: LabelFreeTracker predicts cell nuclei and membranes from bright-field images of 3D intestinal organoids. (a) Bright-field image of a mouse intestinal organoid (left image) predicted nuclear fluorescence signal by LabelFreeTracker (middle image) and measured fluorescence signal (right image). Scale bars indicate 20 μm. (b, c) Overview of the training (b) and testing (c) neural networks that constitute LabelFreeTracker. U1 is used to predict nuclear center positions from nuclear fluorescence images, which serves as a ground-truth for U4. U2, U3 and U4 are networks trained to predict the nuclear fluorescence, membrane fluorescence and nuclear center positions from brightfield images, respectively. Micrographs in (b) and (c) are 128 by 128 pixels, equivalent to 40 by 40 μm. (d) 2D slices from organoids with H2B-mCherry nuclear reporter (top) and E-cadherin-GFP reporter (bottom). Difference image shows difference between normalized measured and predicted fluorescence intensities. Green indicates underprediction, magenta indicates overprediction. Scale bars indicate 30 μm. (e) Zoom-ins of regions indicated by arrow-tips in panel (d). Note that LabelFreeTracker shows correct predictions despite: (1) almost no visible nuclear features and edge distortions in villus, (2) some membrane but limited nuclear features in crypt, (3) distortions in the bright-field images suggesting thinner epithelial thickness than found in the measured fluorescence image, (4) limited membrane features. Scale bars in zooms indicate 10 μm.

5.2 Results

The LabelFreeTracker structure

To train LabelFreeTracker, we used a dataset of 3894 paired bright-field/nuclear fluorescence images from 22 organoids, and bright-field/membrane fluorescence images from 25 organoids, which are all obtained using standard 3D confocal microscopy (80%/20% training/validation split; see "Training data for nucleus and membrane predictions" Experimental Procedures for details). With this dataset, we trained four different neural networks, each with a 3D U-Net architecture [43, 225] (Fig. 5.1b). We first trained a U-Net (U1) to predict nuclear center positions from nuclear fluorescence images acquired with a confocal microscope. This allowed us to obtain a complete ground truth dataset with nuclear fluorescence, membrane fluorescence, nuclear center positions, and the corresponding brightfield images. We then used this complete dataset to train three new neural networks that directly predict the nuclear signal (U2), membrane signal (U3) and nuclei center points (U4) from the corresponding bright-field images. By training on crypt and villus domains, we included cell types at all positions along the crypt-villus axis, and cell shape changes during growth, division, and differentiation. After training, U2, U3 and U4 accurately predicted cell nuclei, membranes, and nuclear positions (resp.) from new bright-field movies (Fig. 5.1c). LabelFreeTracker identified nuclei and membranes even when these structures were not recognizable by eye (Fig. 5.1d). Specifically, it correctly predicted the membrane signal in areas where visual inspection of the bright-field images suggested a substantially thinner epithelial layer, and hence epithelial boundaries at the wrong location (Fig. 5.1d, arrow 3). In some areas it appeared superior even to the measured fluorescence in recognizing all parts of the membrane, which is key to reconstructing cell shape (Fig. 5.5).

LabelFreeTracker performance increases with the provided number of Z-slices

The ability of LabelFreeTracker to combine information in 3D from many Z-slices was important to its identification capabilities. In contrast with the human eye, neural networks can combine information from multiple Z-slices in 3D images. To further optimize the prediction process, we assessed the degree to which prediction of fluorescent signals improved with the number of Z-slices given to the neural networks. Importantly, we observed strong local differences: In some regions within the imaged volume, LabelFreeTracker was completely unable to identify nuclei and membranes when using a single bright field Z-slice (Fig. 5.2a, b, yellow circles). These challenging regions could be properly resolved only when making use of multiple Z-slices (Fig. 5.2a, b, yellow circles). To further quantify the performance of the U2 and U3 networks, we computed the Pearson correlation coefficient for each pair of measured and predicted fluorescence images (Equation 5.1):

$$r = \frac{\sum_i (x_i - \overline{x})(y_i - \overline{y})}{\sqrt{\sum_i (x_i - \overline{x})^2 (y_i - \overline{y_i})^2}} \tag{5.1}$$

Here, x is the fluorescent image, y the predicted image, x_i and y_i are the intensities in the image at pixel i, $\overline{x}$ and $\overline{y}$ are the mean intensities of each entire image. For both nuclear and membrane fluorescent signal, we found that the correlation coefficients increased with

increasing number of Z-slices, although the difference between 8 and 16 Z-slices is not statistically significant (Fig. 5.2c-f). We also note that the minimal values of the correlations increased as more Z-slices were used (Fig. 5.2c, e).
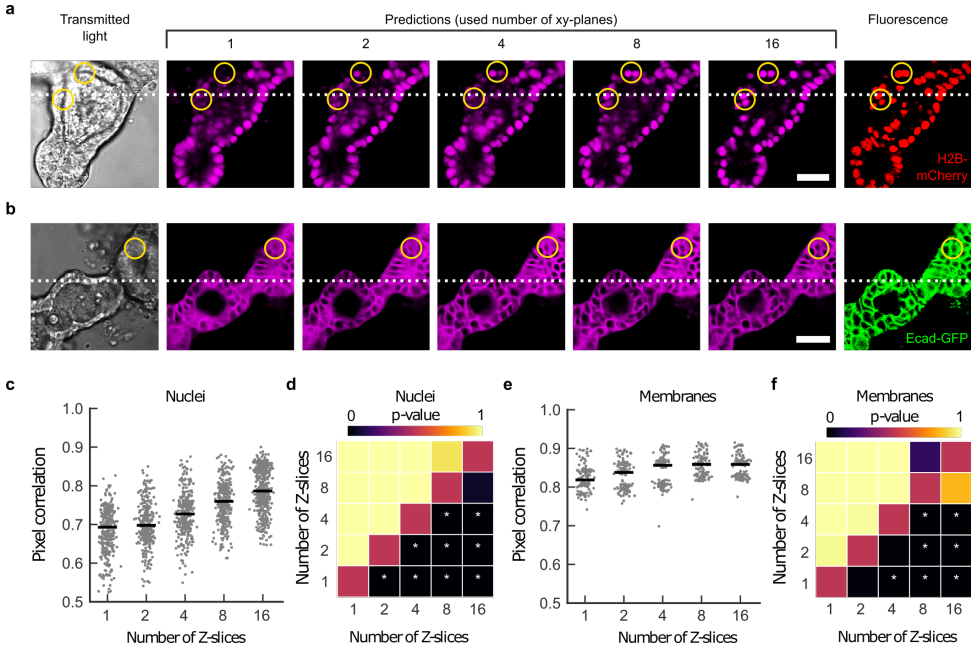
Figure 5.2: LabelFreeTracker prediction accuracy increases by combining information across multiple Z-slices. (a) Predictions based on increasing number of Z-slices supplied as input to the nucleus prediction network (U2). Yellow circles indicate regions in which a single Z-slice predicts poorly, but multiple Z-slices do work well. (b) Predictions based on increasing number of Z-slices supplied as input to the prediction network (U3). Scale bars in (a) and (b) indicate 30 µm. (c) Pixel-wise correlations for variants of the nuclear prediction network (U2) with the given number of Z-slices (U2). Note that improvements in specific areas (yellow circles in a) are poorly represented in this global metric. (d) Statistical significance (p-value) that the number of Z-slices on the horizontal axis results in higher correlations than the number of Z-slices on the vertical axis (* $p < 0.05$; one-tailed Student's t-test). (e) Pixel-wise correlations for variants of the membrane prediction network (U3) with the given number of Z-slices (U3). (f) Like panel d, but for membranes. The horizontal lines in panels c and e indicate the median.

VERIFICATION AND VALIDATION OF LABELFREETRACKER

Overall, LabelFreeTracker identified features over 40 µm into the organoid tissue, enabling full 3D reconstruction of crypt and villus domains (Fig. 5.3a). The percentage of identified nuclei was high up to an imaging depth of 50 µm, after which the performance dropped, with the precision showing a similar trend (Fig. 5.3b & Fig. 5.5). To verify that predicted intensity values match the fluorescence intensity values, we compared the average intensity values in 8-by-8-pixel areas in the predicted and measured fluorescent signals and found close agreement (Fig. 5.3c & Fig. 5.6a, b). Similarly, we computed the Pearson correlation coefficient for the measured and predicted intensity values for individual pixels and found strong correlations for both the nucleus and membranes (0.76 and 0.85 respectively).

Next, we set out to measure how well the predicted foreground (nuclei or membranes) colocalized with the actual foreground. Every pixel reaching at least 10% of the maximum brightness was considered foreground. The Intersection-over-Union ratios were 0.59 and 0.79 for nuclei and cell membranes, respectively, indicating that the approximation was moderate for nuclear shape, and good for cell shape. Within the foreground, the Pearson correlation coefficients were 0.52 and 0.45 for nuclei and membranes, respectively, indicating a moderate correlation between fluorescence intensity and predicted signal. In addition, we analyzed the batch-to-batch variability and found a coefficient of variation of 0.04 and 0.24 for nuclei and membranes, respectively (Fig. 5.6c, d).

We also performed a validation experiment to exclude that the presence of fluorescent markers had any detectable effect on the transmitted light signal. To this end, we acquired bright-field images of completely label-free wild-type (WT) organoids and predicted the nuclear signal. Directly after this initial round of imaging, we added a fluorescent dye marking the cell nucleus (Hoechst) and imaged the same organoids after 20 minutes. In these 20 minutes, changes in the number of cells were negligible (Fig. 5.3d). We compared the predicted number of cells to the number of cells determined by manual annotation after staining, and consistently found strong correlation (Fig. 5.3e). Furthermore, we computed the convex hull volume of the organoids and the distance between cell centers in the predicted images and found close agreement with the fluorescence images (Fig. 5.6c, d).

Neural network retraining

To illustrate network retraining for a different experimental setting, we used fluorescent dyes to stain the nucleus (Hoechst) and cell boundaries (EpCAM). We acquired time-lapse imaging data consisting of 916 Z-stacks images with accompanying Hoechst and EpCAM staining from 91 wild-type organoids and trained neural networks for nuclear and membrane prediction (Fig. 5.3f). The full process of data acquisition and training took less than one day. The resulting network was able to predict nuclei and cell membranes, though as expected the results were not as good due the lower-quality staining (Fig. 5.3f-h). We thus provide a protocol for adapting LabelFreeTracker to other systems and imaging modalities. Note that the training dataset, batch-numbers and training parameters can be adapted to achieve the desired accuracy, depending on the application. This procedure may be further optimized by using more specific and brighter nuclear and membrane dyes and using background correction for images with noticeable background signal.

Applications of LabelFreeTracker

LabelFreeTracker can be used for quantitative analysis of diverse types of single-cell and organoid analyses. Here we demonstrate three applications of LabelFreeTracker to illustrate its utility for intestinal organoids. The first application is counting the number of cells in a developing organoid in time. We used LabelFreeTracker to count the number of nuclei in growing organoids where at a certain time point the cell division inhibitor cyclin-dependent kinase 4 & 6 inhibitor (palbociclib) was added. After addition of palbociclib, the cell count continued to increase for approximately 15 hours, after which cell division was effectively blocked (Fig. 5.4a). In contrast, control organoids continued to contain proliferative cells

in the same timeframe. While methods that quantify the overall organoid size can detect overall changes in organoid growth, they average between cells and hence are less suited to address spatially localized proliferation in a small subset of cells. Overall, this assay illustrates how LabelFreeTracker can assess pharmacological interventions on the single cell level without the need for nuclear fluorescent markers.

A second application of LabelFreeTracker is single cell tracking, which allows lineage tree reconstruction and quantification of fluorescent reporters. Here, we used LabelFree-Tracker to analyze live-cell imaging data of an organoid line with a live nuclear reporter for Axin2 [187]. Axin2 is a Wnt target gene that indicates stemness [88], and is only expressed in stem cells at the bottom of the intestinal crypt. We reconstructed lineage trees of individual cells tracked for over 60 hours (Fig. 5.4b-d). In these tracks we measured the fluorescence intensity of the Axin2/SGFP2 signal for all individual cells. Three types of cells were clearly distinguishable (Fig. 5.4b-d & Fig. 5.7): First, stem cells were identified that remained in the stem cell zone at the bottom of the crypt. They remained proliferative throughout the duration of imaging and kept high levels of Axin2/SGFP2 (red line, Fig. 5.4b-d). The second category were transit-amplifying cells, which remained proliferative but lost their Axin2/SGFP2 marker as they moved away from the stem cell zone (blue line, Fig. 5.4b-d). The third category were the differentiating cells, which stopped proliferating for over 24 hours and had lost all their Axin2/SGFP2 signal (green line, Fig. 5.4b-d). This shows that LabelFreeTracker allows the reconstruction of lineage trees of individual cells with high linking accuracy (Fig. 5.8), while leaving fluorescence channels available to resolve key developmental processes.

A third application of LabelFreeTracker is the quantification of cell volume over time (Fig. 5.4e-g). Importantly, this requires cell membrane reconstruction on all sides for many time points, which is especially challenging in dense epithelia. To measure cell volumes, we segmented the cells using the predicted membrane signal. For each timepoint, we first predicted the membrane signal of each image. Next, we obtained a mask of the entire organoid by thresholding (10% of the maximum intensity) the predicted membrane signal, closing any holes and eroding the final mask by four pixels. Using a watershed algorithm with the predicted nucleus center points as seeds then yields a full 3D reconstruction of individual cells (Fig. 5.4e). Here, we exploited the fact that the predicted signal is smooth, as it lacks imaging noise, thus creating a favorable intensity landscape for the watershed algorithm. While cell volume at individual timepoints was noisy, a six-hour moving average gave consistent predictions of cell volume over time. The 3D reconstructions during one cell cycle showed cells rounding up during cell division, the formation of a narrow apical surface directly after division, and then finally growing again in volume (Fig. 5.4e). Volume growth showed an expected doubling during the cell cycle for dividing lineages, but also a notably sudden arrest directly after the last division (Fig. 5.4f, g), which correlates with cell differentiation [291].
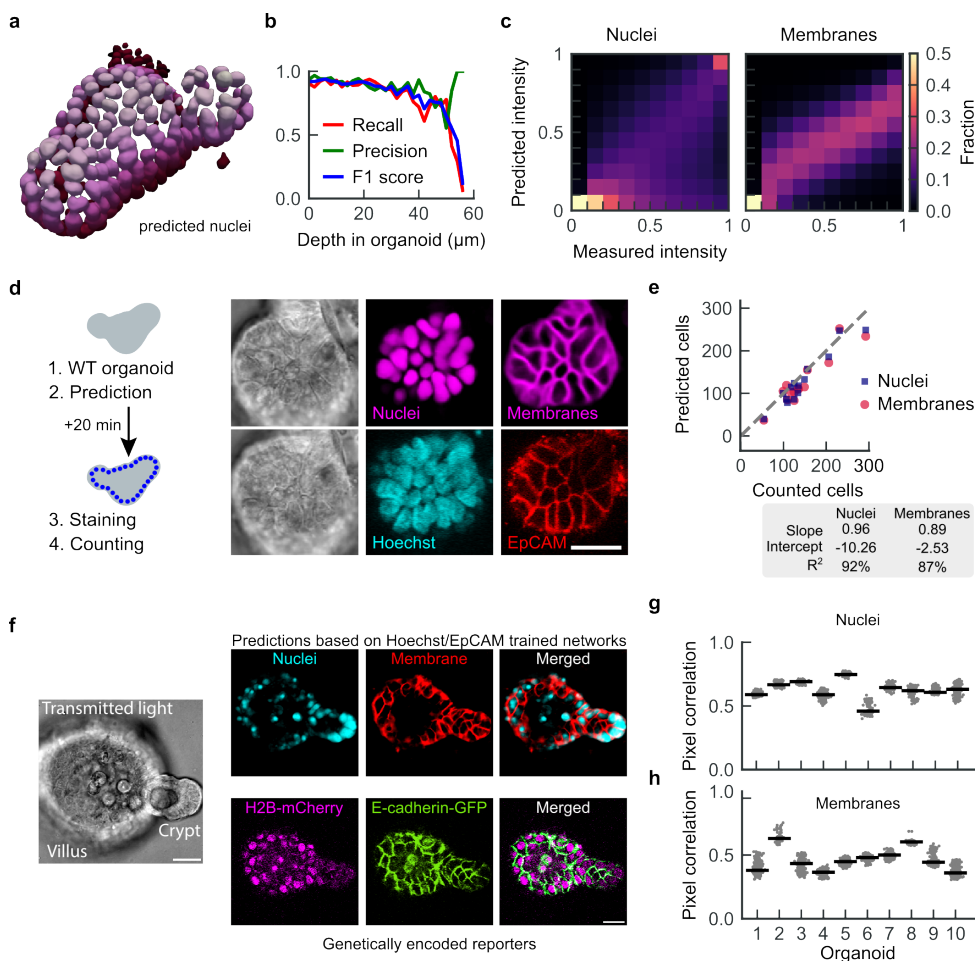
Figure 5.3: Verification and validation of LabelFreeTracker. (a) 3D reconstruction of nuclear predictions up to 50 µm deep into the tissue. (b) Precision, recall and F1 score of nuclear prediction against depth (n = 15 stacks from N = 3 organoids). The precision is the number of correctly predicted nuclei, divided by the total number of predicted nuclei (true- and false-positives together). The recall is the number of correctly predicted nuclei divided by the actual number of nuclei. The F1-score is the harmonic average of the precision and the recall. (c) Predicted versus measured fluorescence intensity for 8-by-8-pixel areas (327 and 136 stacks for nuclei and membranes, respectively, each from N = 3 organoids). Fractions were normalized such that the columns add up to 1. (d) Bright-field image of WT organoid before staining, with nuclear and membrane prediction (top row). Bright-field image of WT organoid after staining with Hoechst and conjugated EpCAM antibody (bottom row). Scale bar indicates 20 µm. (e) Number of cells predicted by nucleus center prediction network (blue squares) and membrane network (red dots) versus number counted after subsequent Hoechst staining (N = 14 organoids). (f-h) LabelFreeTracker retraining for organoids stained for nuclei and membranes with fluorescent dyes (Hoechst and EpCAM, respectively). (f) Bright-field image (left) was used to predict nuclei and membranes using the retrained LabelFreeTracker network (top row). Bottom row shows genetically encoded reporters H2B-mCherry and E-cadherin-GFP for comparison. Scale bars indicate 20 µm. (g, h) Pearson correlation coefficients for predicted and measured nuclear (g) and membrane (h) signals, using the retrained network. Horizontal line indicates the median Pearson correlation.

5.3 Discussion

With the development of organoid models, highly dynamic processes can be directly observed through live-cell imaging in a broad range of tissues. Live-cell microscopy, however, comes with a set of limitations, such as the limited number of fluorescent labels due to spectral overlap, phototoxicity, photobleaching and laborious manual data annotation [245]. To overcome these limitations, label-free imaging approaches present an exciting direction. Previously, label-free or in silico labelling methods were developed [42, 49, 204], but were only used to predict cellular structures in bright-field 3D Z-stacks of flat, 2-dimensional monolayer cell cultures, which are not hampered by light scattering of intervening tissue. Additionally, a recent study presented a method to predict the nuclei of cells in spheroids, inside a microfluidic chip for high-content screening applications [8]. To broaden the scope of label-free imaging to 3D organoid cultures, we developed LabelFreeTracker, a machine-learning based algorithm for the prediction of nuclei, membranes in 3D, as well as their tracking through time. LabelFreeTracker is based on 4 U-Net neural networks, which together predict nuclear and membrane fluorescence and nucleus center positions from bright-field images as obtained from the transmitted light in standard confocal microscopy. Strikingly, LabelFreeTracker accurately predicted the cell nuclei and membranes even in cases where these structures were completely invisible to the human eye (Fig. 5.1a). To some extent, this can be explained by the fact that in contrast to the human eye, LabelFreeTracker is able to simultaneously integrate information from multiple slices of a 3-dimensional stacks. LabelFreeTracker allows reconstruction of nuclear volumes up to 50 μm deep into the tissue, after which recall (that is, the percentage of retrieved nuclear center positions) drops sharply. We demonstrated the applicability of LabelFreeTracker with three use-cases of tracking the dynamics of individual cells over longer periods of time, though it can also be used for the static analysis at a single time point. First, we showed that LabelFreeTracker can perform cell counting in organoids grown under normal conditions, and conditions where cell division was pharmacologically blocked. Second, we demonstrated that it enables cell tracking, and hence allows complete lineage tree reconstructions and quantification of intracellular fluorescent signal from transcriptional reporters. Finally, we showed that our approach allows quantification of the dynamics of single-cell shape and volume.

LabelFreeTracker is especially promising as a tool for quantitative analysis of dynamic processes in patient-derived organoids. For example, our approach allows automated tracking of cells across multiple division, and therefore makes it possible to directly test the effect of drugs and pharmacological treatments that target cell proliferation. While we focused on the prediction of nuclei and membranes of mouse intestinal organoids, LabelFreeTracker can be readily expanded to other organoid systems. Extending LabelFreeTracker to other organoid systems and/or imaging setups requires training datasets of bright-field images paired with nuclear/membrane fluorescence images. Key here are the size of the training dataset, the imaging resolution in space and time, and the laser power. While the desired reconstruction quality can differ between applications, we note these guidelines (see the Methods for specific numbers): (1) The size and diversity of the training dataset should be such that all organoid morphologies are represented and that different batches are included. (2) For tracking cells across multiple generations, the time resolution should be such that

at least two images are taken during each cell division. This ensures that two daughter cells can be connected to the corresponding mother cell. (3) The Z-resolution should be set such that nuclei span multiple (3 or more) Z-slices. In the case of mouse intestinal organoids, we found that this criterium was satisfied for 2-micron intervals between Z-slices. (4) Bright-field images must not be over- or undersaturated, as this dramatically effects the training and performance (Fig. 5.9). Finally, while we have here only shown that LabelFreeTracker works for nuclei and membranes, the approach may be extended to identify other subcellular features, such as mucin in goblet cells, nucleoli, microtubules and mitochondria [204].
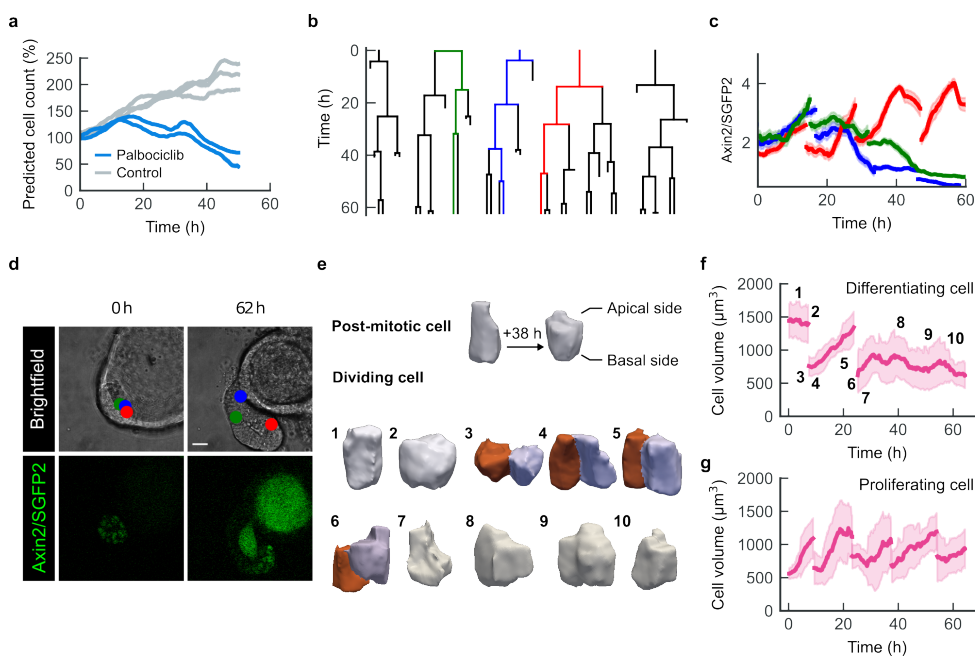
Figure 5.4: Applications of LabelFreeTracker. (a) Predicted cell count in control organoids (gray) and in organoids where cell division is blocked pharmacologically by palbociclib (blue). (b) Lineage trees of cells in Axin2/SGFP2 reporter organoids tracked over 60 hours. Green lineage indicates a cell that eventually differentiates, whereas the blue and red lineages indicate cells that remain proliferative throughout the timelapse. (c) Normalized measurements of Axin2/SGFP2 fluorescent signal for the branches highlighted in panel b (see Methods section for details of normalization). The green, blue and red curves correspond to the cells that are in the villus, transit-amplifying region and crypt (resp.) at the end of the timelapse. Area around the lines represent the standard error of an 8-hour time window. (d) Images corresponding to panel b showing the positions of the highlighted cells along the crypt-villus-axis at the start (0 h) and end (62 h) of the time lapse. Scale bar indicates 20 μm. (e) 3D rendering of predicted volume of post-mitotic cell (top) and dividing cell (bottom). (f) Predicted cell volume over time for the mitotic cell in panel e. (g) Predicted volume for a cell that remains proliferative (same organoid for panels e and f). Area around the curves in panels f and g represent the standard deviation of a 6-hour time window.

5.4 Methods

Organoid culturing

Organoids were cultured under standard conditions in ENR medium [235]. Briefly, organoids were seeded in gel consisting of basement membrane extract (BME2, Trevingen) mixed with Advanced DMEM/F-12 in a 2:1 to 3:1 volume ratio. This medium consisted of Advanced DMEM/F-12 (Life Technologies) with the following added ingredients:

- murine recombinant epidermal growth factor (EGF 50 ng/mL, Life Technologies)

- murine recombinant Noggin (100 ng/mL, Peprotech)

- human recombinant R-spondin 1 (500 ng/mL, Peprotech)

- n-Acetylcystein (1 mM, Sigma-Aldrich)

- N2 supplement (1x, Life Technologies)

- B27 supplement (1x, Life Technologies)

- Glutamax (2 mM, Life Technologies)

- HEPES (10mM, Life Technologies)

- Penicillin/Streptomycin (100 U/mL 100 µg/mL, Life Technologies)

The organoids were passaged every week, after which they were refed twice during the next seven days. The passaging was carried out as follows: The organoids from two wells were collected in Advanced DMEM/F-12 medium, mechanically disrupted broken up by pipetting up and down with a narrowed glass pipette (5 min, 320 rcf). Supernatant was aspirated and a second centrifugation round was carried out. The supernatant was again removed, after which the organoids were seeded in gel on wells of a new culturing plate. After leaving the plates in an incubator for 20 to 30 minutes, the growth medium was added.

Organoid lines

H2B-mCherry / Lgr5-GFP and wild-type murine intestinal organoids were a gift of Norman Sachs and Joep Beumer (Hubrecht Institute, The Netherlands). H2B-mCherry / E-cadherin-GFP organoids were a gift of Daniel Krueger (Hubrecht Institute, The Netherlands). Axin2P2A-rtTA3-T2A-3xNLS-SGFP2; tetO-Cre; Rosa26mTmG murine intestinal organoids were a gift from the Van Amerongen lab (Universiteit van Amsterdam, The Netherlands) [187].

Organoid time lapse microscopy

One or two days before the start of the time lapse experiment, we seeded mechanically dissociated organoids in BME2 gel in four-well chambered cover glass (CellVis), using the same procedure as during passaging. To prevent the gel from solidifying immediately, seeding was performed on a cold block. The imaging well was put in a fridge for ten minutes to allow the organoids to sediment down. Afterwards, the chambered cover glass

was put in the incubator to allow the gel to solidify. After leaving the plates in an incubator for 20 to 30 minutes, the growth medium was added. Imaging was performed on a Nikon A1R MP microscope with a 40x oil immersion objective (NA = 1.30). 31 z-slices with 2 μm step size were taken per organoid every 12 minutes. Experiments were performed at 37 °C and 5-8% CO2, achieved by using a stage-top incubator (Okolab). An imaging well typically contains over 50 organoids, of which we imaged about 20 per experiment. We selected for a diverse set of organoids, as our goal was to obtain a diverse training set. By diverse, we mean that organoids had different sizes, number of crypts, morphologies (cystic, bulged, budded, etc) and degrees of debris present in and around the organoid. We set the imaging settings such that the bright-field was never oversaturated or undersaturated. For the fluorescent channels for imaging H2B and E-cadherin, we aimed to make all cells anywhere in the imaged part of the organoid appear as bright cells, at the cost of oversaturation elsewhere in the organoid.

Imaging and measuring Axin2 reporter organoids

The organoids were passaged one day before the experiment and were imaged over an entire weekend as described above. We performed semi-automatic tracking on these organoids (see above) and corrected the tracks for five larger lineage trees. We then segmented all cells at all time points (see above) and used the obtained masks to measure the total Axin2/SGFP2 signal of every cell. We noticed that a specific type of cell segmentation error was causing issues with the GFP measurement. Sometimes, the membranes between two cells were missing, likely because the neural network could not locate it. This caused the volume of one cell to be assigned to a neighbor of the cell. This error was largely eliminated by averaging the predicted membranes with a distance map, which was 0 at the center of the cell, and then increased linearly up to 1 at a distance of 7 μm. In this average, the membranes had a weight of 75%, and the distance map a weight of 25%. The downside of adding the distance map to the watershed landscape is that for cells that are both large and stretched, it causes them to appear more spherical than they are. For measuring the intensity of a nuclear-localized signal, this is not an issue, but for measuring the volume of the cell it is. Therefore, we only used the distance map for measuring Axin2/SGFP2, and not for measuring the cell volume. The Axin2/SGFP2 signals were then normalized as follows: The lowest measured Axin2/SGFP2 signal in the time lapse was assumed to correspond to the background. This background, measured in intensity per pixel, was then subtracted from every measured Axin2/SGFP2 signal. The intensities where then multiplied by a factor such that the median intensity of the organoid, across all time points, was 1. To reduce noise in the measured Axin2 signal, we applied a moving average with an eight-hour time window.

Inhibition of cell divisions

A 5.6 mM Palbociclib (Sigma-Aldrich) stock solution was prepared by dissolving in endotoxin-free demineralized water. A few hours before the start of a time lapse movie a certain amount of the thawed stock solution was added to the medium, such that the final concentration in the medium was 10 μM.

Training data for nucleus and membrane predictions

For acquiring training data of nuclear fluorescence, we used H2B-mCherry / Lgr5-GFP murine intestinal organoids, which were a gift of Norman Sachs and Joep Beumer (Hubrecht Institute, The Netherlands). For acquiring training data of membrane fluorescence, we used H2B-mCherry / E-cadherin-GFP organoids, which were a gift of Daniel Krueger (Hubrecht Institute, The Netherlands). We did not use this line to create nucleus prediction training data, as the nuclear marker of this line is less bright compared to our other line. We used E-cadherin as a membrane marker, even though it technically only marks cell-cell junctions. In practice, this is not a problem, as the intestinal epithelium is a tightly connected epithelium. As a result, often the entire cell surface is still visible in images of E-cadherin. We used this fluorescence marker because it produced a bright signal in our organoids, making it easy to image. We have collected 3894 pairs of images of bright-field/nuclei of 22 organoids in total. 13 organoids were newly imaged, the rest is from a previous publication [143]. The data consists of four independent experiments. In addition, we have collected 1908 pairs of images of bright-field/membranes of 25 organoids, distributed over two independent experiments. The images we split into a train/validation set using an 80%/20% split at the individual time point level. The same organoid can thus appear in both the train and validation set, although always at different time points. We normalized the time lapse so that at all time points and all depths layers the fluorescent signal is saturated. Different normalizations were sometimes used for different depths and time points. We split the 512 by 512 by 32-pixel images in smaller patches of 128 by 128 by 16 pixels. For many of our images, the organoids do not occupy the entire view, which caused a considerable number of patches to show no fluorescence. To speed up the training process, we removed almost all these patches. A patch was considered black if the brightest pixel found in the patch is lower than half of the highest fluorescence in the entire image. We kept 5% of the black patches in the training set, so that the network still learns to not predict any fluorescence outside the organoid. We first trained the network that predicted the nuclear signal from bright-field, and then the network that predicted the membrane signal. For the network predicting the membrane signal, we used the trained network that predicts nuclei as a starting point, so that the cell membrane network can reuse cell detection knowledge of the nuclear network. We trained the network to minimize the mean squared error loss between the fluorescent signal and the predicted signal.

Testing data for nucleus and membrane predictions

For the testing data in Figs. 5.2 and 5.3a-c, we used an additional 4 organoids (same line) for the nucleus network (544 image pairs). Three organoids were from a previous publication [143]. For testing the membrane predictions, we imaged 2 organoids in two independent experiments (136 image pairs). Microscope, imaging settings/conditions and organoid lines were identical to training data.

Predicting nucleus center positions

For training the nucleus center position network, we used pairs of bright-field images, and images with bright spots at the center of the nuclei. We first used OrganoidTracker [143] to automatically find the nucleus centers in our training set, based on the fluorescent nuclei. Then, we created images with bright Gaussian spots at the location of the nucleus centers

with the standard deviations of the Gaussian function σ_x and σ_y being 4 px (1.28 µm), and σ_z being 1 px (equal to 2 µm in this case, as the resolution is lower in the z-direction). We trained the neural network on the training set for 10 epochs. A large part of the images containing the nucleus centers was black, as there are no nucleus centers within a few pixels. Therefore, the network tended to just predict all pixels as black, and not draw any nucleus centers at all. We solved this issue by reducing the weight of black pixels by a factor of 4. To test the network, we applied the network to three organoids. We first obtained a ground truth for five time points in each of these organoids, by manually annotating all cell centers in these time points. We selected the time points at 0%, 25%, 50%, 75% and 100% of the time lapse duration. To obtain a performance metric, we used the following method to calculate the number of true positives (TP), false positives (FP) and false negatives (FN): Any nucleus center detected by the neural network was assigned to the closest nucleus center from the ground truth, under the condition that the distance was no longer than 5 µm. Every nucleus center cannot have more than one assignment. Each successful assignment was a true positive. Then, any manually tracked nucleus center that was left with no assignments became a false negative. Finally, any nucleus center from the neural network that was left with no assignments was regarded as a false positive. The precision is then calculated "TP"("TP" +"FP") and the recall is calculated as "TP"("TP" +"FN"). The F_1 score is the harmonic average of the precision and recall:

$$F_1 = \frac{2 \cdot Precision \cdot Recall}{Precision + Recall}. \tag{5.2}$$

Prediction neural network
The network architecture follows a U-Net type architecture, with a downwards block, an upwards block and skip connections between the blocks. The input of the network consists of 3D greyscale images of 128×128×16 pixels. The downwards part of the network consists of four repeating units, with each unit consisting of two 3D convolutions, maximum pooling, and batch normalization. The upwards part consists of four repeating units, with each unit consisting of a transposed convolution, followed by two convolutions, followed by batch normalization. At the end of the network, a final convolution is done. The network is optimized using the Adam optimizer [136] with the mean squared error loss function. The intensities of the bright-field images are offset and multiplied such that the average of an entire 3D stack of a single time point is 0, and the standard deviation is 1. For the fluorescent images, the images were normalized from 0 to 1, with the background at zero. Normalization factors were chosen by hand for several slices during the time lapse, at both different times and depths. For other slices, the factors were calculated from the manually set factors by linear interpolation. The only data augmentation that was done was horizontal and vertical flipping. Rotations and scaling data augmentations were omitted on purpose, as to not remove any details provided by individual pixels.

Comparison of human annotated and predicted cell counts in wild-type organoids
To demonstrate that bright-field-based prediction of nuclei works in label-free organoids, wildtype (WT) mouse intestinal organoids were mechanically disrupted and embedded in BME2 gel with growth medium. Two days after passaging, Z-stacks of label-free organoids

were acquired. After the first image acquisition, cells were incubated for 15-25 minutes in live-cell staining medium consisting of growth medium supplemented with Hoechst 34580 and 0.8 μg/mL Alexa 647 conjugated anti-mouse CD326 antibody (Invitrogen, #17-5791-80), before a second Z-stack was acquired with the same imaging conditions as the label-free image acquisition. In each organoid, the centers of all nuclei were manually annotated based on the Hoechst signal, and the centers of all nuclei were automatically predicted using the LabelFreeTracker algorithm by an independent human annotator. This last annotator also manually annotated all cell centers based on the predicted membrane signal.

Semi-automated cell tracking

We used the position detection network (see "Predicting nucleus center positions") to generate a set of positions. Our next step was to link these positions over time. As a first step, we estimated the chance $P(L|d)$ which is the chance of two cell positions in subsequent time points being of the same cell (i.e. having a link L), given the distance d between both positions. This function is expected to start at a high chance for d=0, and then drop off towards zero for increasing d. To estimate this function, we used the tracking data of one organoid with a nuclear marker, that was tracked previously [143]. For every position, we recorded the distance to the nearest position in the previous time point, as well as the distance to any position that is at most twice as far. We also recorded whether that position represented the same cell, which allowed us to estimate the chance $P(L|d)$. We noticed that the center positions of the predicted nuclei were less accurate than the center positions of fluorescent nuclei. This resulted in larger apparent cell movements in between time points, which made the function $P(L|d)$ underestimate the chance of two nucleus positions being of the same cell. To correct for this, we simulated errors in the nucleus center positions of our previously tracked organoid. We added (rand()-rand()) 1.6 μm to the x and to the y coordinate of each position, with rand() a function that returns a uniformly distributed random number from 0 to 1. For the z coordinate, we choose a random integer from 1 to 6 (inclusive); if the number was 5, we added 2 μm (corresponding to one z layer) to the z coordinate, and if the number was 6, we subtracted 2 μm.

Having obtained a representation for $P(L|d)$, we used this as input for the track creation algorithm of Haubold [103]. This algorithm presents an approximate solution of the problem of linking cell detections over time. It builds on the shortest path min-cost flow solving algorithm but adapts the residual graph such that divisions become possible. Although the algorithm cannot guarantee an optimal solution, a good performance is nonetheless achieved within polynomial time. Besides the linking probabilities described in the previous paragraph, the algorithm additionally expects probabilities of a cell to divide at a given time point as input. We provided those with a single baseline division probability. As a result, the solver could only detect a few divisions (< 5 divisions per organoid). Using Organoid-Tracker [143], we manually corrected these tracks for five lineages, thereby adding the missing cell divisions.

Comparison of cell linking performance

Cell linking performance was compared against manual tracking based on a fluorescent nuclear marker. The same set of testing organoids was used as for validating nucleus

and membrane prediction performance. We manually tracked part of each organoid. We then performed automatic tracking as described in the previous section, and then used the links comparison feature of OrganoidTracker [143] to calculate the recall, precision and F_1 score. The comparison was done by matching manually annotated nucleus centers to automatically detected nucleus centers close by, up to a distance of 5 μm, and then checking whether the links of the position match. Areas where no manual center annotations were created (i.e. where automatically detected center positions could not be matched to any manual annotation close by) were excluded from the performance evaluation.

Reconstruction of cell shape in organoids

Here, we used a time-lapse movie of the H2B-mCherry / Lgr5-GFP organoids, where the Lgr5-GFP channel was not imaged. A membrane signal was predicted for each time point, as well as nucleus center points, both based on the transmitted light image of the confocal microscope. This signal was first used to reconstruct a mask of the entire organoid: the predicted membrane signal was thresholded at 10% of the maximum signal, followed by closing any holes in the mask and eroding the final mask by four pixels. Next, we reconstructed the masks of single-cells using a 3D watershed algorithm (Mahotas [46]) with the predicted nucleus center points as seeds, and the predicted membrane signal as the watershed landscape. The measured volume over time was noisy for most cells; to correct for this a six-hour moving average window was applied.

Software packages

The panels follow the standard boxplot settings of the software library Matplotlib version 3.6.0 [116]. Neural networks were implemented in Tensorflow 2.5.1 [1]. The 3D watershed algorithm was provided by the Mahotas software library [46] .

5.5 Supplementary Figures

5
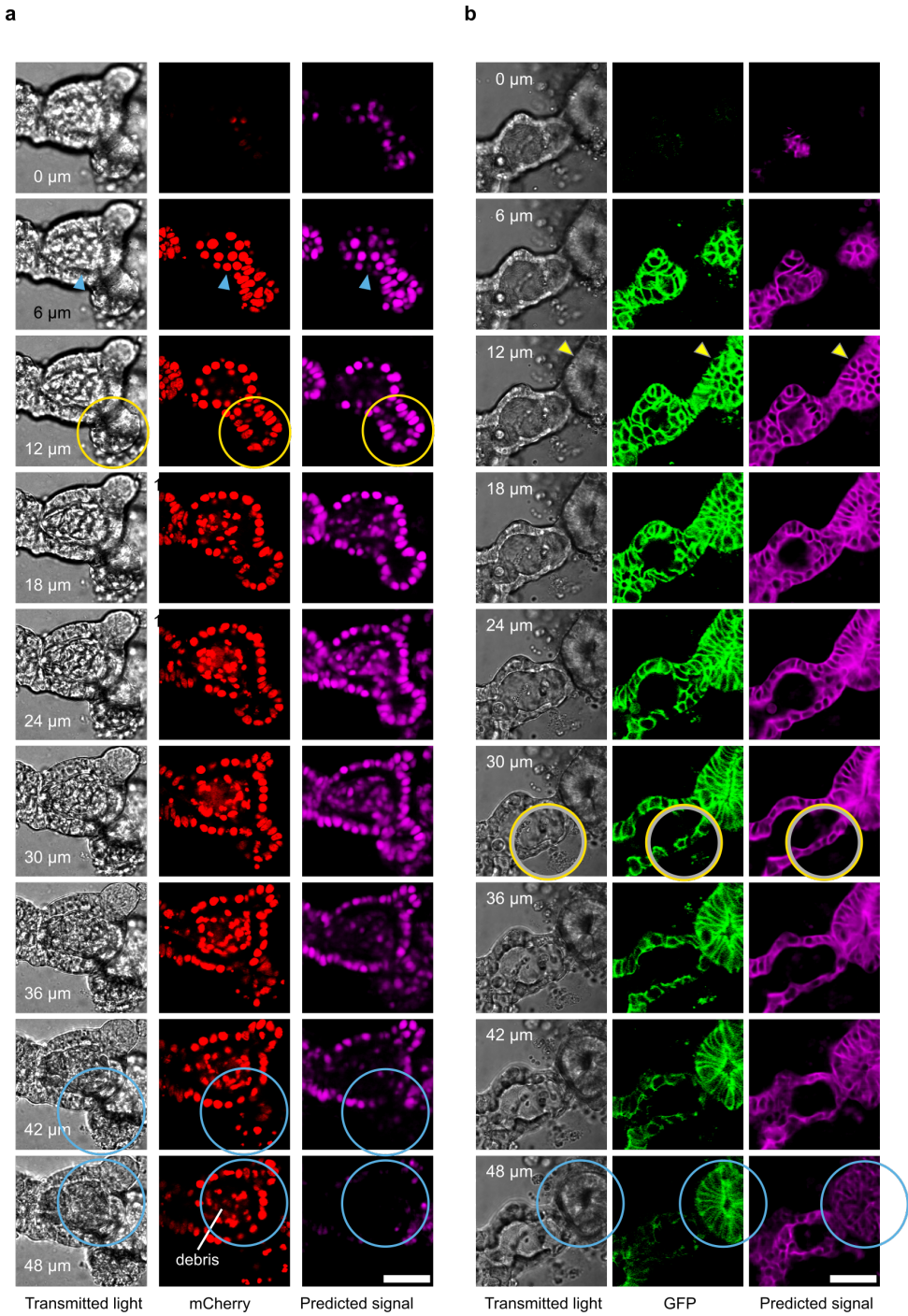
Figure 5.5: Organoids with a hard-to-interpret transmitted light signal at different depths.

Figure 5.5: (continued) (a) Transmitted light (grey), measured control (red) and nuclear predictions (purple). (b) Transmitted light (grey), measured control (green) and cell membrane predictions (purple). Indicated are example areas where LabelFreeTracker method works well (yellow arrows & circles), or even better than fluorescence (yellow + gray), and where the method starts failing (blue arrows & circles). For the latter one then often sees the fluorescence imaging failing as well. Scale bars indicate 20 μm.
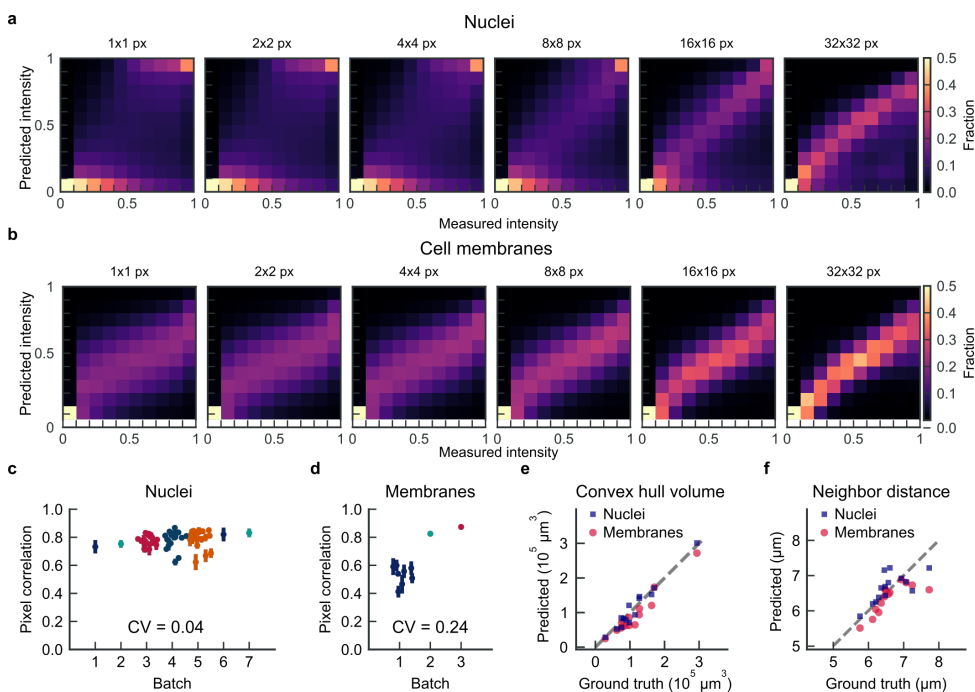
Figure 5.6: Verification of LabelFreeTracker. (a, b) Predicted versus measured fluorescence intensity for pixel areas of various sizes (327 and 136 stacks for nuclei and membranes, respectively, each from N = 3 organoids). (c, d) Batch-to-batch variability for LabelFreeTracker. Pixel correlations were determined by computing the Pearson correlation coefficient for individual pixels between nuclear fluorescence and prediction (N = 64 organoids), and membrane fluorescence and prediction (N = 10 organoids) at each time point. Every dot indicates the mean ± s.t.d. for one organoid. CV in panels c and d is the Coefficient of Variation (standard deviation over mean) between the average pixel correlation per batch. (e) Convex hull cell volume around predicted nucleus centers (from nucleus center prediction network) or predicted cell centers (from manual annotation based on predicted membrane images) versus manual locations after subsequent Hoechst staining (N = 14 organoids; R^2 = 95% for nucleus centers, R^2 = 95% for cell centers). (f) Idem, but for center-to-center nucleus distances (R^2 = 47% for nucleus centers, R^2 = 64% for cell centers).
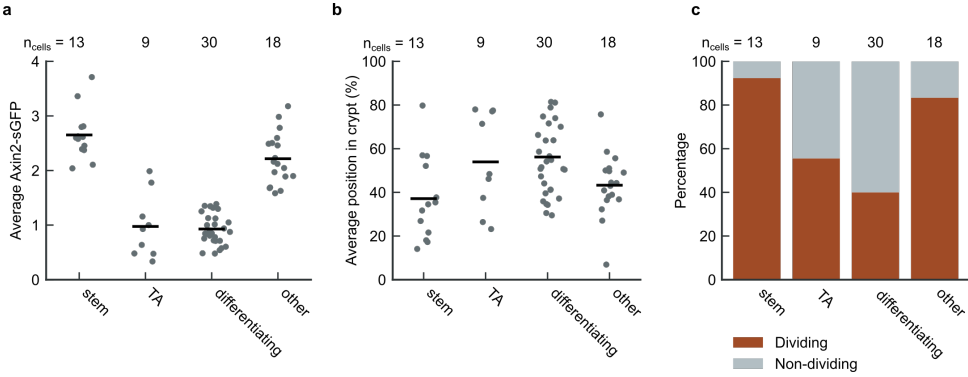
Figure 5.7: Classification of cells in the crypt. We analyzed crypt cells that could be tracked after the movie start or after a division, and until a next division or until the movie end. Crypt cells that did not divide for longer than 25 hours were not included, as they likely represent non-dividing Paneth cells, or tracking errors. We then classified cells using their Axin2/SGFP2 signal. Cells with a stable high Axin2/SGFP2 signal (mean > 2, final value between 85% and 115% of first value) are here denoted as stem cells. Cells with a decreasing Axin2/SGFP2 signal (final value less than 85% of first value) are here denoted as TA cells. Cells with a low Axin2/SGFP2 signal (mean < 1.5) are denoted as differentiating cells. The remaining cells are classified as "other cells", which tend to be cells that show an increase in Axin2/SGFP2. (a) Average Axin2/SGFP2 levels of cells. (b) Average position of cells in the crypt. 0% is defined as the crypt bottom, 100% is defined as the neck between the crypt and the villus, which was manually annotated at each time point. (c) The fraction of cells that are part of a proliferative lineage at the end of the movie, showing the proliferative character of cells in each category.
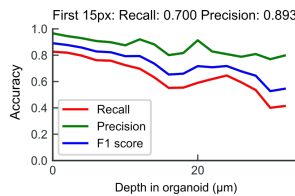
Figure 5.8: Linking accuracy. Recall, precision and F1 score for the linking of cells across timepoints. Overall recall is 0.695, overall precision is 0.892. Details of comparison are in section 5.4.
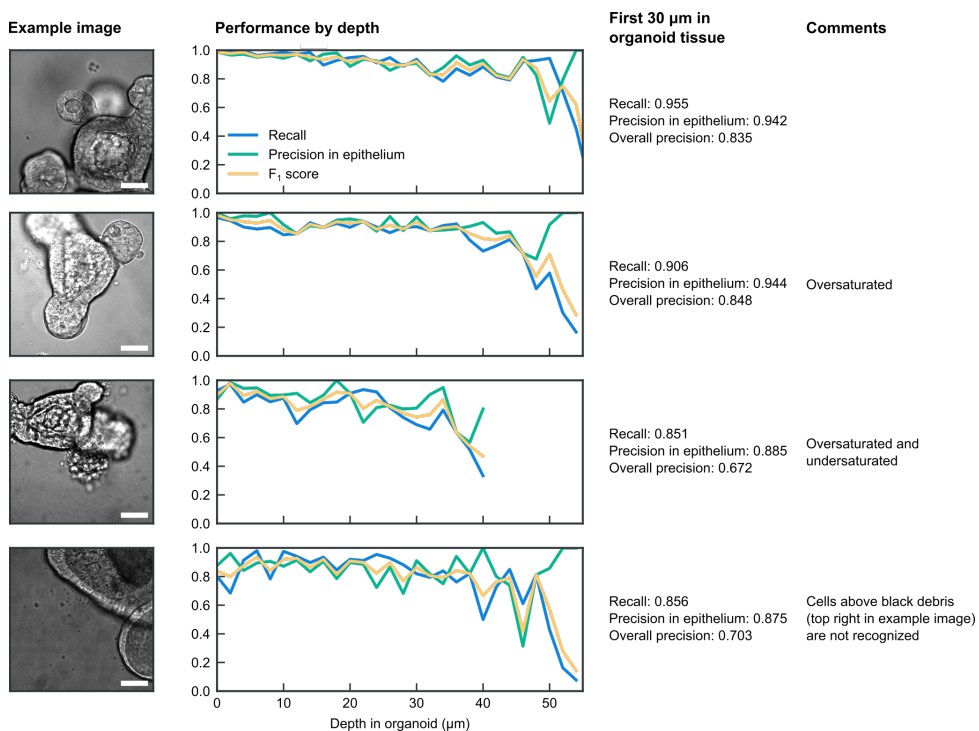
Figure 5.9: Requirements for training and application of LabelFreeTracker. Shown are the performances of position detection (recall, precision and F1 score) at different depths for different example organoids. Using and training LabelFreeTracker requires that the bright-field images are neither over- or undersaturated; cells located directly below dark debris cannot be recognized. Scale bars indicate 30 μm.

6

QUANTITATIVE IMAGING OF DYNAMIC PROCESSES IN INTESTINAL ORGANOIDS

"The truth is a bully we all pretend to like."

Gregory David Roberts (Shantaram)

Organoids are powerful models for studying tissue dynamics across multiple cellular generations and offer key insights into organ homeostasis, cellular differentiation, and disease. Here, we present protocols for long-term imaging and quantitative analysis of intestinal organoids at the cellular level. Our workflow consists of sample preparation, experimental manipulations (e.g. drug treatments, laser ablations, and fluorescence recovery after photobleaching), long-term live imaging (120 h), in situ fixation and permeabilization, multiplexed antibody staining, and single-cell tracking with lineage reconstruction. We outline strategies for optimizing organoid health, imaging conditions and experimental interventions to ensure efficient downstream analysis. Additionally, we describe how this workflow enables real-time quantification of gene expression using fluorescent reporters, as well as inferring cell type changes by combining multiplexed antibody staining with single-cell tracking data. These protocols are broadly applicable to studying dynamic cellular processes in both 2D and 3D organoids, spanning timescales from minutes to several days. By integrating live imaging with post-hoc analysis, this protocol provides a comprehensive approach for studying cellular behavior, lineage trees, expression dynamics, and cell-cell interactions in organoid systems. The full experimental protocol takes approximately 2 weeks and can be used with standard confocal microscopy.

6.1 Introduction

Development of the protocol

Live imaging is an established technique for understanding dynamics in tissues and cells. Intestinal organoids are in vitro models for the intestinal epithelium that mimic the in vivo intestine in cell type composition, and 3D crypt-villus compartmentalisation [235]. An important advantage of intestinal organoids is that they are accessible for live imaging, which makes them uniquely suited to study dynamic processes in the intestinal epithelium [20]. Obtaining meaningful information from live imaging experiments with single-cell resolution and over multiple days is, however, still technically challenging in organoid cultures. Live imaging induces stresses in the cells that are absent in cell culture incubators, such as phototoxicity and concentration of growth factors due to evaporation of the medium [245]. Furthermore, organoids typically consist of hundreds of densely packed cells, making manual tracking analyses highly labour-intensive and thus prone to selection biases. We therefore developed and optimized approaches for studying single-cell dynamics on timescales of multiple days [19, 62, 104, 115, 142, 143, 150, 195, 291].

Here, we describe protocols for long-term live imaging of organoids with detailed guidance on experimental perturbations, in situ fixation and permeabilization, and multiplexed antibody staining and re-imaging. Subsequently, we discuss how our custom-built Organoid-Tracker software [19, 143] can be used for single-cell tracking analysis and provide examples for different types of downstream data analysis, such as dynamic cell type inference and fluorescence intensity measurement.

Overview of the procedure

In its complete form the experimental protocol consists of six steps (Fig. 6.1): sample preparation (steps 1-14), pharmacological treatments (steps 15-17), long-term live imaging of intestinal organoids (up to five days; steps 18-22), photobleaching and laser ablations (steps 23-25), in situ fixation and permeabilization (steps 26-33), immunostaining (steps 34-56), and tracking and data analysis (e.g. using manual or AI-assisted single-cell tracking, lineage-tree reconstruction, and real-time fluorescence quantification; steps 57-82).

Advantages and limitations

Organoid systems combined with genetic modification [6, 239], 3D imaging and data analysis make it possible to quantify dynamic processes in complex tissue structures, which are central to a host of normal and pathological organ functions. Live imaging yields rich information about spatio-temporal dynamics that is hard or impossible to get from "omics" approaches such as transcriptomics and proteomics. Another advantage is that it serves as a platform for combining diverse interventions and imaging modalities, ranging from laser ablation to drug treatments and multiplexed immunostaining. Hence, it opens up the dynamic cell biology toolbox to cellular processes within the tissue context.

Live imaging, antibody staining, and cell tracking is inherently limited by a relatively low throughput, which is dependent on the imaging setup and desired temporal resolution. The approach presented here is typically limited to simultaneously following ~20 organoids
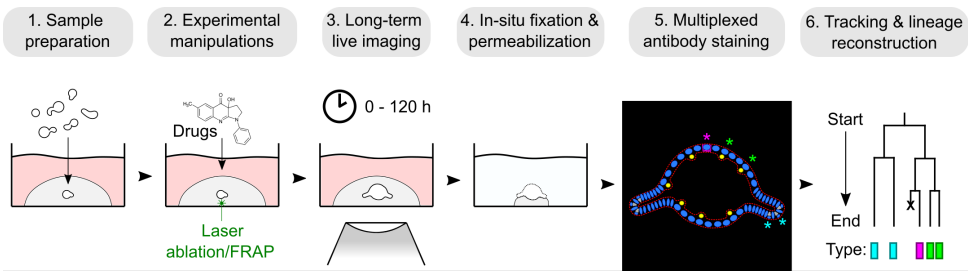
Figure 6.1: Overview of the protocol. The full protocol discussed here consists of 6 steps, being (1) sample preparation, (2) experimental manipulations (e.g. drug treatments, photobleaching, laser ablation), (3) long-term live imaging for up to five days, (4) in situ fixation & permeabilization, (5) antibody staining (multiplexed if necessary) and (6) single cell tracking and reconstruction of lineage trees. Asterisks in (5) indicate different cell types, and the cross at the lineage end in (6) represents a cell that dies prior to fixation. The tracking data can also be used to perform quantitative analysis on the motility, spatial organization and intensity of fluorescent reporters at the single cell level using our custom-built OrganoidTracker software.

(order 1000 cells in total), which represents only a fraction of the organoids in typical culturing wells. Furthermore, the data analysis is labor-intensive and time-consuming, especially when tracking is done manually. This limitation is increasingly mitigated by AI-based methods developed within the field [59, 143, 195]. Still, only a subset of organoids is used for detailed analysis, and the selection of this subset may introduce biases in the analyzed dataset. These biases include survivorship bias (overrepresentation of organoids that survive the imaging process), compositional bias (overrepresentation of organoids containing specific cell types or domains) and trackability bias (overrepresentation of organoids that show minimal morphological changes and cell motility). In Table 6.1, we provide an overview of these biases and accompanying mitigation strategies. In cases where organoids were manually chosen for analysis it is good practice to explicitly state what selection/exclusion criteria were used for the selection of the tracked organoids (e.g. "For single cell tracking, we selected organoids that survived throughout the imaging window, contained at least n cells of cell types X, Y, Z." or equivalent).

Applications

First, the described protocols are useful for obtaining information about single-cell dynamics in time, using genetically encoded transcriptional reporters for read-outs such as cell type [62, 104], cell signalling [142] or metabolism [195]. For example, we used transcriptional reporters for goblet cells (MUC2-mNeonGreen) and Paneth cells (DEFA5-DsRed) to show that Paneth cells arise from MUC2+ progenitor cells [104], while quantification of metabolic sensors revealed cell type changes in colorectal cancer organoids in response to lactate-induced histone acetylation [195]. Second, single-cell dynamics can be directly connected to the measured cell lineage, for instance, by linking induction and maintenance of stem cell fate [195] or the multiple differentiated cell types [291] between mother and daughter cells, sisters or cousins. We used such analysis to establish that both the proliferative state [115] and differentiation [291] of mouse intestinal stem cells is likely determined within their mother cell. Third, they allow following single-cell dynamics as function of cell position in space, or in relation to their cell neighbours. For example, such analysis revealed that the switch from the tuft-1 to tuft-2 subtype coincides with the migration these tuft cells from the crypt to the villus domain of the organoid [62]. Similarly, using a Wnt-signalling reporter [187] (Axin2/SGFP2), we examined how loss of contact with WNT-producing Paneth cells drives loss of stem cell fate and subsequent differentiation [142]. Finally, the ability to follow cells in time can potentially be used to quantify a much broader range of dynamic processes, provided that the key phenotype is detectable using fluorescent reporters or other methods. For instance, we recently followed Myosin-II dynamics in time to show that intestinal cells are engaged in a tensile tug-of-war, with loss of tensile strength being the trigger for extrusion from the epithelium [150]. In another type of example, we used AI-based reconstruction of 3D cell shapes from bright-field images to quantify how cell volume evolves during differentiation [141].

Combining time-lapse microscopy with endpoint analysis by immuno-staining offers additional possibilities when fluorescent reporters are difficult to incorporate or the number of markers is too large. Serra et al. used this combination to show that the initial symmetry breaking of mouse small intestinal organoids coincides with the differentiation of the first Paneth cell [242]. Using endpoint antibody staining of marker for stem cell fate and all differentiated intestinal cell types, we recently showed that cell fate decisions in mouse small intestinal organoids occur early – prior to upward migration towards the villus and the final cell division [291]. While the protocol presented here is optimized for combining time-lapse microscopy with multiplexed antibody staining, it can in principle also be combined with single-molecule Fluorescent In Situ Hybridization (smFISH). Combining end-point smFISH with time-lapse imaging-based reconstruction of cell lineages was previously used to infer cell-state transition dynamics in 2D embryonic stem cell culture [110]. Potentially, the protocol can also be used with other types of endpoint analysis, such as deterministic ("single-organoid") scRNA-sequencing [34, 137], intact-tissue sequencing [279] and in situ proteomics [221, 289].

Alternative methods

The protocol presented here is developed for standard confocal microscopy. One may alternatively use light-sheet microscopy [59, 151, 169, 178, 258], which allows faster imaging at

Table 6.1: Biases that may affect results in live imaging experiments of organoids.

Bias	Explanation	Implications	Mitigation strategies
Survivorship bias	Organoids being followed with live imaging may die or show signs of deterioration even with negligible phototoxicity.	Datasets is biased towards organoids that survive the imaging process, even if those form a small minority of the actual organoid population. Conclusions drawn from the tracking of these organoids are then not representative for the whole organoid population.	When comparing different experimental conditions (e.g. drug treatments), complement the imaging dataset with statistics on what fraction of organoids survives the treatment. These statistics can be obtained by imaging the organoid cultures at low-resolution and at randomly selected locations.
Compositional bias	Organoids may show high heterogeneity in composition. For example, the abundance of especially the rare cell types may vary greatly between organoids.	Dataset is biased towards organoids that contain specific cell types or either have abnormally large crypt or villus domains. Since rare cell types may have beneficial effects on other cells in the organoid, the organoid composition may be correlated to organoid survival.	Characterise heterogeneity between organoids and test main hypotheses also in an unbiased sample. For quantification of cell type abundances, complement the tracking dataset with statistics on the cell population level. These can be obtained using fluorescence activated cell sorting (FACS), western blotting, sequencing, mass-spectrometry, enzyme-linked immunosorbent assays (ELISA), or quantitative PCR (qPCR).
Trackability bias	Organoids may exhibit large-scale morphological changes or high levels of cell motility, which makes single cell tracking more challenging and labour-intensive.	Tracking dataset is biased towards organoids that show minimal morphological changes (e.g. inflation-collapse cycles) and limited cell motility.	Use semi-automated tracking algorithms.

low levels of phototoxicity. Furthermore, it can image deeper into the sample, and thus image organoids and developing embryos in their entirety (in toto). However, sample preparation is generally more involved than standard confocal microscopy, and datasets are much larger. New light-sheet imaging platforms reduce these demands, for instance using single objectives to support workflows like those for confocal microscopes. The presented protocols can therefore be readily adapted for these imaging systems.

Alternatives to cell tracking are for instance EdU/BrdU labelling for migration and proliferation dynamics [11, 149], and in vivo lineage tracing by induction of a heritable genetic marker [57, 187, 248]. Additionally, computational methods exist to infer cell type trajectories from single-cell RNA sequencing data [61, 230]. The main advantage of these inference methods is that they are more compatible with in vivo studies and are often less labour-intensive. However, they do not directly follow dynamic processes, as performing multiple observations of the same specimen at different points in time is highly challenging or impossible. Instead, the dynamics are inferred indirectly from single-snapshot data, thereby relying on the assumptions of the underlying model used for inference. In addition, they may miss key events because the number of timepoints is very low, and are limited in the ability to be combined with other imaging modalities.

EXPERIMENTAL DESIGN

While the protocol presented here is specifically tailored to mouse small intestinal organoids, it can be easily adapted to other organoid models. When designing an experiment, consider (i) which fluorescent reporters to use for tracking, (ii) whether to use 3D or 2D organoids, (iii) whether to start from single cells or from small organoids, (iv) which controls to include (especially in the case of drug treatments, photobleaching or laser ablations), (v) which antibodies to use after fixation and (vi) whether to perform tracking manually (this paper) or in (semi-)automated manner [19].

For single cell tracking over multiple generations it is highly recommended to integrate a bright fluorescent nuclear marker (e.g. H2B-mCherry, H2B-iRFP) or membrane marker (e.g. membranous tdTomato, E-cadherin-mNeonGreen), which can be added using lentiviral transduction, stable transfection or CRISPR-based genome editing (Fig. 6.2a). For short term tracking experiments (< 24 h) it is also possible to use nuclear dyes (e.g. Hoechst) or membrane markers (e.g. Cell mask, or conjugated EpCAM antibody), although these dyes may be actively exported from or degraded by the cells and may have adverse effects on cell health (Fig. 6.2b). A third option is to use in silico labelling, which is the prediction of nuclear and membrane from brightfield images. Neural networks for in silico labelling are available for both 2D cell monolayers [42, 49, 204] and 3D organoid cultures [141]. For measuring dynamics of protein expression, other fluorescent reporter proteins can be tagged endogenously using established methods for genetic modification of organoids such as CRISPaint [239] and CRISPR-HOT [6].

The second consideration is whether to perform tracking in 3D gel-embedded organoids [235] or in 2D ("open-lumen") organoids [209, 216, 257, 282]. 3D organoids have the advantage that the organoid remains at the same position in space, and preserve the 3D
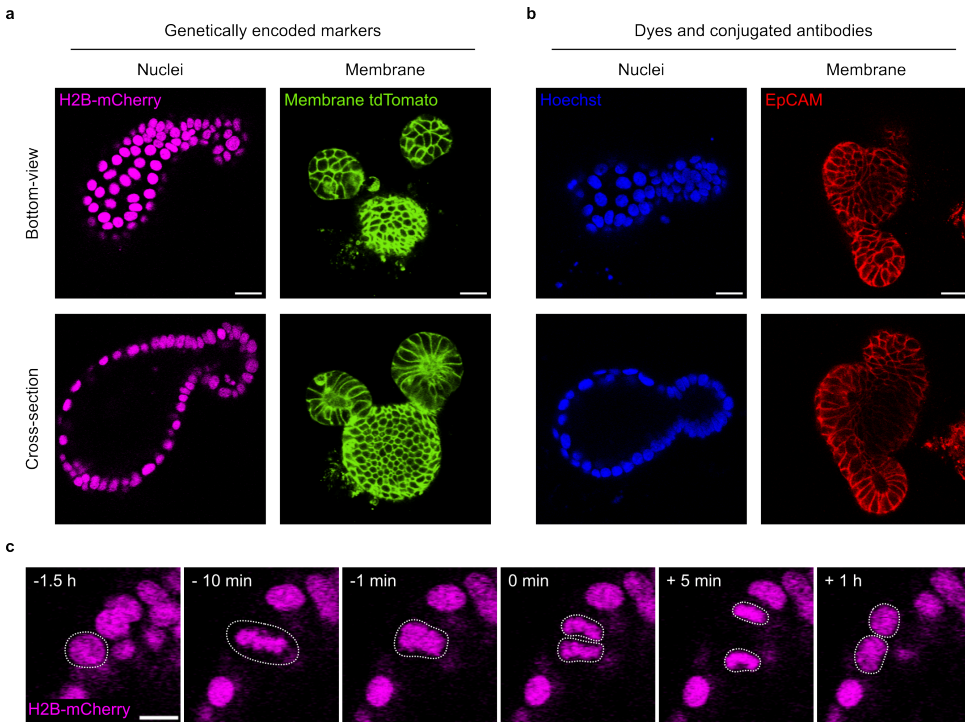
Figure 6.2: Experimental design. (a, b) Different types of (a) genetically encoded markers and (b) dyes (Hoechst) or conjugated antibodies (EpCAM) that can be used for live imaging and tracking. Scale bars: 20 μm. (c) Cell division process in mouse small intestinal organoids marked by H2B-mCherry. Dotted lines show outline of the dividing nucleus. Scale bar: 10 μm.

organization more faithfully. Although organoids may grow and shrink, cells are much less likely to move out of the imaging window than in 2D. Additionally, cells can modulate their luminal environment (e.g. pH and ion concentrations) in 3D organoids but not in 2D. While protocols exist for injecting microbes into the lumen 3D organoids [216], this only remains possible with low throughput. If direct access to the lumen is necessary, it is advised to use 2D organoids. 2D organoids require appropriate coating of the imaging slide, for example using BME2 [216], polyacrylamide [208], or invasin [282].

A third consideration is whether to start growing the organoids from single cells, or from dissociated crypts generated by mechanically breaking larger organoids. Starting from single cells is preferable where the research question focuses on the initial stages of the development of organoids in itself [242], or in cases where it is essential that all cells derive from a single starting cell. However, generating fully developed organoids from single cells may take 1-2 weeks, and may therefore require embedding them in a new gel.

A fourth consideration is which culture media and controls to include. In the case of drug treatments, a negative control with the drug's vehicle (BSA/DMSO/ethanol) is essential. It

is good practice to also include a negative control without vehicle, so that adverse effects from the vehicle can be excluded. For imaging experiments where individual organoids are manipulated using laser-ablation or photobleaching, it is advised to also image a few organoids where no manipulation is done in the same organoid. Typically, the number of organoids in the imaging well will exceed the number of organoids selected for time-lapse imaging. Finally, it is recommended to exclude a few organoids from imaging to control for phototoxicity.

A fifth consideration is whether to use in situ fixation and (multiplexed) antibody staining. If so, it can save time to choose the secondary antibodies such that the number of rounds of imaging is minimized while avoiding spectral overlap between the fluorescent antibodies.

6.2 Materials

Reagents

Organoid culturing and sample preparation

- Endotoxin-free water (ThermoFisher; cat. #J65589-K2).

- PBS (Phosphate-buffered saline; ThermoFisher; cat. #14190136).

- Advanced DMEM/F12 (ThermoFisher; cat. #12634010).

- GlutaMAX Supplement 100× (ThermoFisher; cat. #35050061).

- HEPES 100× (1M; ThermoFisher; cat. #15630080).

- Penicillin-streptomycin 100× (Fisher Scientific; cat. #11548876).

- Mouse recombinant EGF (ThermoFisher; cat. #315-09-500UG).

- Mouse recombinant Noggin (ThermoFisher; cat. # 250-38-100UG).

- Human recombinant R-spondin (ThermoFisher; cat. #120-38-5UG).

- NAC (N-Acetyl-L-cysteine; Merck; cat. #A9165-5G).

- N2 supplement (ThermoFisher; cat. #17502048).

- B27 supplement (ThermoFisher; cat. #17504044).

- BME2 (Cultrex Reduced Growth Factor Basement Membrane Extract, Type 2, Path-clear; biotechne; cat. #3533-010-02).

- DMSO (dimethyl sulfoxide; Merck; cat. #D2650).

- TrypLE Express Enzyme 1× (ThermoFisher; cat. #12605010).

- Y-27632 dihydrochloride (Enzo; cat. #ALX-270-333-M005).

- Hoechst 34580 (ThermoFisher; cat. #H21486).

- CD24 APC-conjugated antibody (ThermoFisher; cat. #17-0242-80).

- IWP-2 (Stemcell Technologies; cat. #72122).

- CHIR99021 (Merck; cat. #SML1046).

- Valproic acid (VPA; Enzo Life Sciences; cat. #ALX-550-304-G005).

- DAPT (Enzo Life Sciences; cat. #ALX-270-416).

- Mouse recombinant interleukin-13 (Enzo; cat. #ENZ-PRT184)

- Mouse recombinant interleukin-4 (Enzo; cat. #ICT-6520)

- PD0325901 (MEK/ERK-inhibitor; Merck; cat. #PZ0162)

in situ fixation and multiplexed antibody staining

- Formaldehyde solution about 37% (Sigma-Aldrich; cat. #104003, stabilized with ~10% methanol). CAUTION Formaldehyde is a fixative and needs to be handled with protective clothing, gloves, and face protection.

- Triton X-100 (Sigma-Aldrich; cat. #X100). CAUTION Harmful substance, handle with protective gloves and face protection. Very toxic to aquatic life.

- TBS (Tris-buffered saline pH 7.4; ThermoFisher; cat. #J60764.K2).

- Immunofluorescence blocking buffer (Cell Signaling Technology; cat. #12411).

- L-glycine (Merck; cat. #219517).

- Urea (Merck; cat. #51456).

- Guanidium chloride (Merck; cat. #G3272). CAUTION Harmful substance, handle with protective clothing, skin protection, eye/face protection and inside a fume hood.

- TCEP-HCl (tris(2-carboxyethyl)phosphine hydrochloride; Merck; cat. #75259). CAUTION Harmful substance, handle with protective clothing, gloves and face protection inside a fume hood.

- Antibodies of choice. For cell type specific antibodies that we have verified, see Table 6.3.

- DAPI (4',6-diamidino-2-phenylindole; ThermoFisher; cat. #62248).

Equipment

Culturing and sample preparation

- Flow cabinet (Kojair Biowizard Silver SL-130 Blue Series Class II).

- 0.2 μm sterile nylon filter (Whatman Puradisc; Cytiva; cat. #6786-0402).

- Vacuum pump (Integra Vacusafe).

- Glass Pasteur pipettes (150 mm; ISO 7712).

Table 6.3: Antibodies validated for cell type annotation in mouse small intestinal organoids. Note that not all the cell types in this table are mutually exclusive (e.g. secretory cells include goblet, Paneth, enteroendocrine and tuft cells). Abbreviations: AF, Alexa-Fluor; CF, Cyanine-based Fluorescent dye. *Goblet cells are differentiated (KRT20$^+$) and secretory (WGA$^+$), so can also be identified by positive staining for these two markers [291].

Cell type	Primary antibody
Proliferative cells	rabbit anti-Ki67 (BD Biosciences; cat. #556003)
Differentiated cells	mouse anti-cytokeratin 20 (KRT20) (Agilent Dako; cat. #M701901-2)
Epithelial cells	mouse anti-E-cadherin (Santa Cruz; cat. #sc-59778)
	Alexa Fluor® 488–conjugated mouse anti-CD326 (Ep-CAM) (BioLegend; cat. #118210)
Secretory cells	Wheat germ agglutinin (WGA) conjugated to CF405S (Avantor VWR; cat. #29027)
Stem cells	rabbit anti-OLFM4 (Cell Signaling Technology; cat. #39141T)
Enterocytes	rabbit anti-Aldolase B (Abcam; cat. #ab75751)
Paneth cells	rabbit anti-Lysozyme (Agilent Dako; cat. #Dako #A009915)
Goblet cells*	rabbit anti-mucin 2 (MUC2) (Abcam #ab272692)
Enteroendocrine cells	mouse anti-chromogranin A (CHGA) (Santa Cruz; cat. #sc-393941)
Tuft cells	rabbit anti-doublecortin-like kinase 1 (DCLK1) (Cell signaling/Bioke; cat. #62257)
Microfold (M) cells	mouse anti-glycoprotein 2 (GP2) (MBL Life Sciences; cat. #D278-3)

6

- Glass Pasteur pipettes with cotton plug (Volac art. #D810/PP; 150 mm; ISO 7712).

- 100 − 1000 μL pipette tips.

- 10 − 100 μL wide-opening pipette tips (ART XLG Pipet Tips; cat. #2160G).

- Accu-jet pro pipette controller (Brand 26302; cat. #10551433).

- 5 mL tubes (Eppendorf; cat. #0030119487).

- Imaging plate (CellVis 4 Chambered Coverglass System; #C4-1.5H-N).

- Top of a benchtop cooler (ThermoFisher; cat. #5115-0032), pre-cooled at 4 °C.

- Icebox, or a cold block for holding tubes (e.g. Benchmark Scientific DryChill; cat. #DC0650) pre-cooled between -4 °C to -20 °C.

- Water bath set at 37 °C (VWB2 12 L cat. #462 - 0557).

- Centrifuge (Eppendorf Centrifuge 5702; cat. #5702000010).

- Incubator (Panasonic MCO-170AICUVH-PE) set to 37 °C and 5% CO2.

Microscopes
- Benchtop brightfield/epifluorescence microscope (Carl Zeiss Axio Vert.A1).

- Confocal microscope including an incubation chamber with CO2 and temperature control. This protocol has been routinely performed using both a Nikon A1R MP confocal microscope outfitted with a 1.30 NA 40× magnification oil immersion objective, and with a Leica TCS SP8 confocal microscope outfitted with a 1.10 NA 40× magnification water immersion objective.

- MaiTai DeepSee.

Software
- NIS (for Nikon).

- LASX (for Leica).

- FIJI software [237].

- OrganoidTracker[143].

- Python packages: numpy, seaborn, lifelines [56], matplotlib [116], scipy [274].

Reagent setup

Preparing organoid culturing media
Culturing of mouse intestinal organoids requires wash medium and growth medium. Wash medium consists of 1× HEPES, 1× GlutaMAX and 1× Penicillin-streptomycin in Advanced DMEM/F12. ENR growth medium contains murine recombinant EGF (50 ng/mL), murine recombinant Noggin (100 ng/mL), human recombinant R-spondin (500 ng/mL), N-acetylcysteine (1 mM), N2 supplement (1×) and B27 supplement (1×) in wash medium. Mouse small intestinal organoids cultured in this medium will contain stem cells, transit-amplifying cells, enterocytes, goblet cells, Paneth cells, enteroendocrine cells and tuft cells [235]. If, in addition to these cell types, also microfold (M) cells are desired, also add 200 ng/mL RankL [57].

It is also possible to enrich the organoid culture for specific cell types or lineages by adding additional components. For example, activation of Wnt-signalling (e.g. using CHIR99021) increases the proportion of Lgr5+ stem cells and inhibits differentiation, whereas inhibition of Wnt-signalling (e.g. using IWP-2) induces differentiation [288]. Inhibition of Notch-signalling (e.g. using DAPT) biases commitment to the secretory lineage, whereas activation of Notch (e.g. using valproic acid; VPA) biases towards commitment to the absorptive lineage. Organoids can furthermore be enriched for enteroendocrine cells specifically using a combination of Wnt-, Notch- and MEK/ERK-inhibitors [17]. Tuft cell numbers can be increased by adding IL-4 and IL-13 [112, 275]). For a complete overview of the solvents, stock concentrations and working concentrations of medium components, see Table 6.5.

Preparing solutions for fixation, permeabilization and multiplexed antibody staining
Prepare formaldehyde solution by diluting formaldehyde (37% v/v stock) in PBS to a final concentration of 4% (v/v). Prepare permeabilization solution by diluting Triton-X-100 to a concentration of 0.2% (v/v) in PBS. For antibody stripping, prepare an elution buffer

Table 6.5: Overview of media components.

Component	Solvent	Stock concentration	Final concentration
HEPES	-	100×	1×
GlutaMAX	-	100×	1×
Pennicillin-streptomycin	-	100×	1×
EGF	PBS	50 µg/mL	50 ng/mL
Noggin	PBS	100 µg/mL	100 ng/mL
R-spondin	Wash medium	500 µg/mL	500 ng/mL
N-acetylcysteine	PBS (filter twice with 0.2 µm sterile nylon filter)	500 mM	1 mM
N2 supplement	-	100×	1×
B27 supplement	-	100×	1×
RankL	Water with 0.1% BSA	200 µg/mL	200 ng/mL
CHIR99021	DMSO	10 mM	5 µM
IWP-2	DMSO	2 mM	2 µM
Valproic acid	Water	1 M	1 mM
DAPT	DMSO	10 mM	10 µM
IL-4	PBS with 0.1% BSA	50 µg/mL	50 ng/mL
IL-13	PBS with 0.1% BSA	50 µg/mL	50 ng/mL
PD0325901	DMSO	10 mM	1 µM

containing 0.5 M L-glycine, 5 M urea, 5 M guanidinium chloride, 70 mM TCEP-HCL in water (pH 2.5). CAUTION these buffers contain toxic components and should be handled with appropriate protection and inside a fume hood.

Equipment setup
Optimization of imaging conditions for long-term live imaging with lineage tree reconstruction

For long-term time-lapse imaging, imaging settings must be set to minimize phototoxicity and photobleaching, while still providing sufficient spatiotemporal resolution and signal to noise ratio. Additionally, the time required for acquiring a Z-stack of one organoid typically sets an upper limit to the number of organoids that can be imaged in one experiment. The fastest cell movement is typically the movement of cell nuclei associated with the mitosis of dividing cells, which in mouse intestinal organoids takes approximately 1.5 hours (Fig. 6.2c). Daughter cells can be reliably linked to the mother cell if the time interval between image acquisitions of the same organoid is set to 12 minutes [115, 143, 291]. XY resolution is sufficient when using a 40X oil or water objective, but higher magnification may be necessary for imaging specific intracellular processes. As a guideline for Z-resolution, it is recommended for nuclei to be imaged in at least two adjacent Z-slices. This amounts to a Z-resolution of 2 µm for mouse small intestinal organoids.

Installation of OrganoidTracker software

This step only needs to be performed once for every computer on which one wishes to perform cell tracking and/or analysis. Install Anaconda or Miniconda on your computer. The software can be downloaded at `https://www.anaconda.com/download`. After the installation is completed, search for the "Anaconda Prompt" on your PC and open it. A command prompt should appear. The command prompt can be closed. Download OrganoidTracker [19, 143] from `https://github.com/jvzonlab/OrganoidTracker/archive/refs/heads/spoelstra-et-al-nature-protocols.zip`. Extract the resulting ZIP file to a location on your computer of your choice. Take note of the location where you extracted the files to.

It is also possible to clone `https://github.com/jvzonlab/OrganoidTracker.git` and switch to the "spoelstra-et-al-nature-protocols" branch. Follow the instructions at in the installation manual to install OrganoidTracker. The installation involves using Anaconda or Miniconda to create a so-called Conda environment, in which the OrganoidTracker code can run. Essentially, the installation instructions explain how to run the command "conda env create -f environment-exact-win64.yml" in the folder where you installed OrganoidTracker. Then, as instructed on the same page, start OrganoidTracker by running the command "python organoid_tracker.py" (from the Conda environment you just created). The OrganoidTracker software should now start.

6.3 Procedure

Sample preparation (TIMING 2 h hands-on time, at least 1 day before start of imaging)

1. Pre-cool the wide pipette tips, cold block for tubes and imaging plate at -20 °C.

2. Pre-cool the flat cold block at 4 °C.

3. Pre-warm growth medium at 37 °C. In case organoids will be grown from single cells (see step 13), pre-warm TrypLE at 37 °C.

4. Aspirate medium from culturing plate.

5. Add 1 mL cold wash medium to the well and pipette up and down until the BME2 gel containing the organoids is dissociated from the bottom of the culturing well.

6. Transfer the mixture to a 5 mL tube.

7. Add another 1 mL of cold wash medium to the 5 mL tube.

8. Twist the tip of a Pasteur pipette with cotton plug in a Bunsen burner for 2-3 seconds to narrow the opening to approximately one third of the inner diameter (Fig. 6.3a).

9. Insert the narrowed-tip Pasteur pipette into the pipette controller and pre-wet the Pasteur pipette with cold wash medium. This pre-wetting serves to reduce the fraction of organoids that stick to the glass, ensures that the pipette is cooled down sufficiently and shows how fast liquid goes into the pipette (note that this speed is variable due to variation in tip diameter).

10. Pipette the organoids up and down at least three times with the pre-wetted narrowed Pasteur pipette tip to break the organoids (Fig. 6.3b & Table 6.7).

11. Add another 2 mL of wash medium and spin down the dissociated organoids for 5 minutes at 100 g.

12. Aspirate the supernatant using the vacuum pump.

13. Organoids for live imaging can be grown either from dissociated crypts (option A) or from single cells (option B).

 A. Growing 3D organoids from dissociated crypts.

  i. Add 4 mL of wash medium to the pellet, mix the suspension by inverting the tube 5× and spin down again for 5 min at 100 g.

  ii. Aspirate the supernatant using the vacuum pump.

 B. Growing 3D organoids from single cells.

  i. Add 500 μL TrypLE and resuspend the dissociated organoids 10× with a 1 mL pipette tip.

  ii. Incubate the suspension in a water bath set to 37 °C for 6 – 12 minutes. Longer incubation times will increase the fraction of single cells compared to larger clumps of cells but will also result in cell death.

  iii. Transfer the tube back to a cold block and mix the suspension again by pipetting 10× up and down with a 1 mL pipette tip to dissociate cell clumps.

  iv. Add 3.5 mL of cold wash medium.

  v. Centrifuge the mixture for 5 minutes at 150 g.

  vi. Aspirate the supernatant.

14. Organoids can either be grown in 3D cultures (option A) or as 2D organoids (option B) depending on whether access to the lumen is needed for the experiment.

 A. Growing 3D organoids for long-term live imaging.

  i. Add 40 μL of BME2 using a wide opening pipette tip pre-cooled at -20 °C and use this pipette tip to mix the gel and the pelleted dissociated crypts into a homogeneous mixture. CRITICAL Keep the BME2 on ice or in a cold block that is between -20 °C and -4 °C, to prevent it from solidifying.

  ii. Place an imaging plate (pre-cooled at -20 °C) on top of a flat cold block that is pre-cooled to a temperature between -4 °C and 4 °C. CRITICAL do not pre-cool the cold block at a temperature below -4 °C, as this causes the organoid-BME2 mixture to freeze.

  iii. Add the organoid-BME2 mixture either as a thin layer or in tiny ~5 μL drops to the bottom of the imaging plate (Fig. 6.3c). While both options work for mouse small intestinal organoids, we recommend using the latter option for organoids that grow into cystic organoids with dimensions similar to the height of the gel (e.g. human intestinal organoids [104, 278], lung organoids [229]).

      iv. Let organoids settle down on the imaging plate on the cold block at 4 °C for 10 minutes (Fig. 6.3d). Place the sample at 4 °C to ensure that the gel remains liquid and to allow the organoids or single cells to sediment to the bottom (Table 6.7).

      v. Place the imaging plate in the incubator set at 37 °C and 5% CO2 for 15 minutes to solidify the gel.

      vi. Add growth medium pre-warmed at 37 °C. For mouse intestinal organoids from dissociated crypts, growth medium can be standard ENR medium. When growing organoids from single cells, add Rho-kinase inhibitor (1× Y-27632). CRITICAL Avoid direct flow on top of the gel, as this can partially dislodge the gel from the glass surface. Instead, add the warm medium dropwise, slowly to the side of the imaging well.

      vii. Let organoids recover in the incubator for at least 12 hours before moving to the next step.

    B. Growing 2D organoids for long-term live imaging.

      i. Add pre-warmed growth medium (37 °C) directly to the pellet.

      ii. Resuspend the cells by pipetting up and down into a homogeneous suspension.

      iii. Add the suspension consisting of single cells or dissociated organoids in growth medium to the coated culturing well.

      iv. Let cells adhere for at least 12 hours.

      v. Aspirate the medium to remove dead and unadhered cells from the imaging plate and add new medium.

(Optional) Drug treatments (TIMING 30 minutes hands-on time)

In case long-term live imaging is to be performed in multiple different media, it is recommended to add drugs after the organoids have recovered from the seeding for at least 12 hours (in case of 3D organoids), or after cells have adhered to the coating and unadhered cells have been removed (in case of 2D organoids).

15. Prepare the different cell culture media to be tested, including the controls with vehicles of added drugs.

16. Pre-warm all different media to 37 °C.

17. Aspirate medium from the wells in the imaging plate and add the media to the respective wells.

Live imaging (TIMING up to five days, 1.5 hours + 30 minutes on subsequent days)

18. Set the temperature and CO2 level of the incubating chamber at the microscope to 37 °C and 5% CO2. If humidity in the imaging chamber can be controlled automatically, set it to >90%.
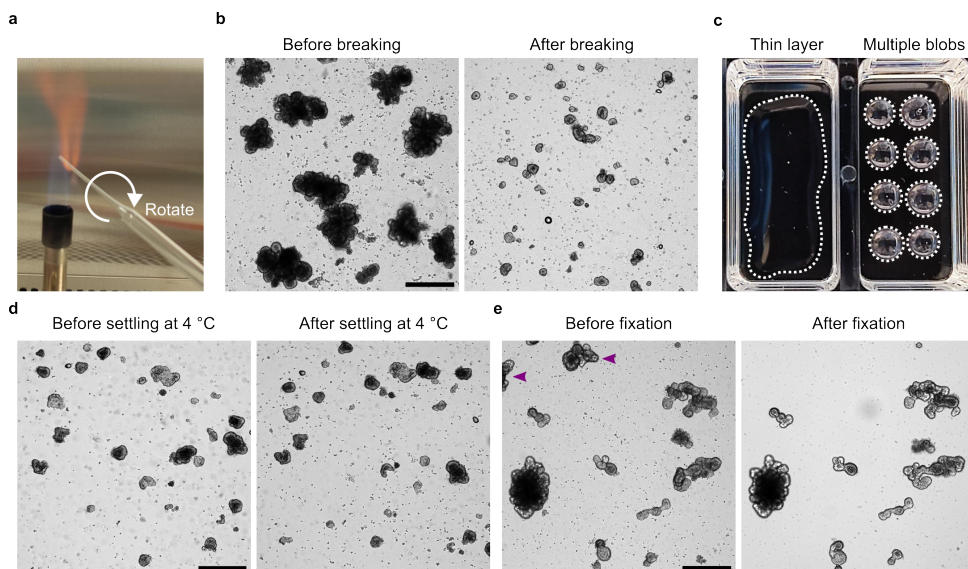
Figure 6.3: Sample preparation and in situ fixation. (a) Narrowing Pasteur pipette using a flame. (b) Organoids before (left) and after (right) breaking using a flame-narrowed Pasteur pipette. (c) Plating of gel-embedded organoids as a thin layer (left) or in multiple blobs (right) in a 4-well imaging plate. (d) Organoids before and after letting them settle at 4 °C. Because the gel is initially liquid, the organoids still move. (e) Organoids before and after fixation. Purple arrowheads indicate organoids lost from the imaging plate due to the in situ fixation protocol. All scale bars indicate 100 μm.

19. Transfer the sample to the microscope. CRITICAL when transporting the sample to the microscope, ensure that cells are not outside a 37 °C / 5% CO2 condition for longer than 10 minutes.

20. Find organoids and save their exact position. CRITICAL if the experimental design includes in situ fixation and multiplexed antibody staining at the endpoint, the positions should be stored so that the exact same organoids can be imaged later. Small shifts in the sample due to differences in the positioning of the sample holder or incubation chamber may already make it difficult to retrieve organoids after fixation (Table 6.7).

21. Load or set the appropriate imaging settings (laser power, gain, offset, frame- and/or line-averaging number, etc.) and acquisition settings (time interval between subsequent acquisitions, Z-step size, time-lapse duration).

22. Due to organoid growth some cells of interest may move out of view during the time-lapse. To avoid this, check the time-lapse at least once per day and adjust the imaging positions if necessary. To do this, pause the acquisition, adjust the position and resume the acquisitions within 30 minutes.

(Optional) Laser microsurgery and photobleaching (TIMING 1 hour hands-on time)

23. Image the organoids at least once prior to the laser-perturbation to establish a control condition. Laser-perturbations may not be compatible with the settings for long-term live imaging and may therefore require switching to more phototoxic imaging settings. To control for phototoxicity in these different settings, it is therefore recommended to keep some organoids without any perturbation as a negative control.

24. Select a region of interest (ROI) and apply the laser-perturbation.

25. Start the time-lapse for the desired duration.

(Optional) in situ fixation and permeabilization (TIMING 1 hour hands-on, 2 days total)

After completing the image acquisition, organoids can be fixed and permeabilized so that they can be stained with antibodies. The protocol below contains multiple PAUSE POINTS where the imaging plate can be left for multiple days at 4 °C. When storing imaging plates for multiple days, prevent the sample from drying out by wrapping parafilm around the imaging plate, and increase the humidity of the container by adding wet paper towel.

26. Bring the imaging plate to a fume hood. CRITICAL To ensure that organoids remain as they were at the last time-point of the acquisition, bring the cells to the fume hood within 10 minutes.

27. Aspirate the medium.

28. Add 4% formaldehyde dissolved in PBS and let this incubate at room temperature for 10 minutes inside the fume hood at room temperature.

29. Remove the formaldehyde from the imaging plate and discard according to the safety regulations.

30. Add PBS to the bottom of the imaging well and pipette up and down until most of the gel on the top and sides of organoids has disappeared, which should occur within 3 rounds of pipetting. Because the gel above and around the organoid is easier dissolved and washed off than the gel between the organoid and the glass slide, organoids remain in the same place (Fig. 6.3e). Still, a substantial number of organoids will be washed off in this step (Table 6.7).

31. Add new 4% formaldehyde to the well and incubate for 20 minutes at room temperature.

32. Remove the formaldehyde and wash the bottom of the well 3 consecutive times with PBS.

33. Add permeabilization solution (0.2% v/v triton in PBS) and leave organoids to permeabilize for at least 2 hours.

PAUSE POINT: organoids can be left in permeabilization solution for up to 4 days at 4 °C and can be stored for up to a month in PBS at 4 °C after permeabilization.

(Optional) Antibody staining (TIMING 3 hours hands-on time, 1-2 days incubation)

34. Rinse the bottom of imaging well containing the fixed and permeabilized organoids twice with PBS. CRITICAL to avoid losing organoids in this step, pipette gently and from the side of the well. Gel around the organoids should be removed thoroughly in step 29, but after the fixation is complete the remaining gel is typically too brittle to remove with pipetting.

35. Add immunofluorescence blocking buffer to the well and leave this on for 1 hour at room temperature.

36. Dilute the primary antibodies of choice in immunofluorescence blocking buffer (Table 6.7).

37. Remove the immunofluorescence blocking buffer from the imaging well and add the solution of primary antibody solution to the well.

38. Incubate the imaging plate at 4 °C overnight.

PAUSE POINT organoids can be left for at least four days in primary antibody solution.

39. Remove the primary antibody solution and rinse the bottom of the plate 3× with PBS.

40. Prepare the secondary antibody solution by diluting the appropriate secondary antibodies in TBS buffer.

41. Remove the PBS from the imaging well and add the secondary antibody solution for 1 hour at room temperature. CRITICAL to avoid photobleaching of secondary antibodies conjugated to a fluorophore, keep the sample away from light as much as possible.

42. Remove the secondary antibody solution and rinse the bottom of the imaging well 3× with PBS.

43. Add the desired counterstains for the nucleus (e.g. DAPI), carbohydrates (e.g. fluorescently conjugated WGA). Dilute these counterstains in TBS to the appropriate concentration and add the counterstain solution to the sample as per the manufacturer's instructions.

44. Wash 3× with PBS and leave the well in PBS after the third round of washing to prevent organoids from drying out.

PAUSE POINT although signal will decrease slightly over time, stained samples can typically be stored for up to a month, if kept away from light, at 4 °C in PBS.

45. Place the imaging plate in the sample holder at the microscope in exactly the same position as during the live imaging.

46. Load the positions of the organoids into the imaging software.
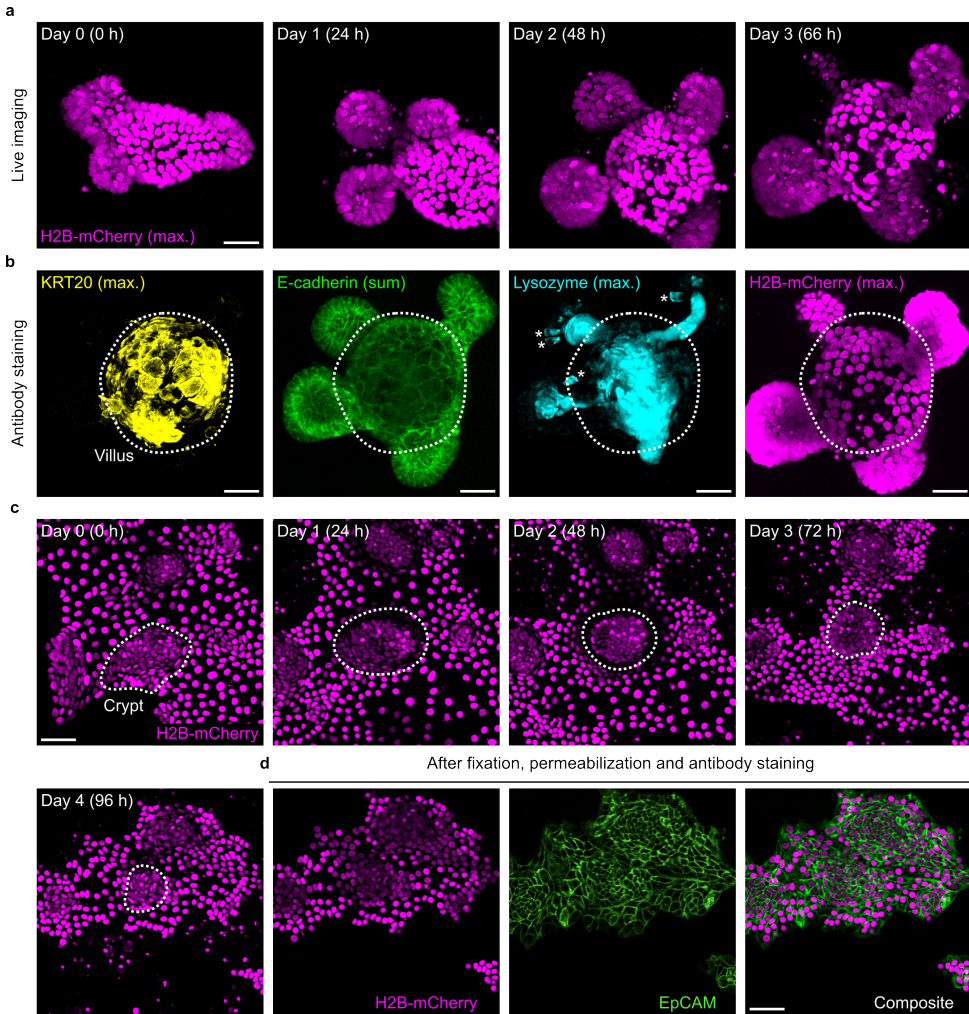
Figure 6.4: Long-term live imaging of 3D and 2D organoids with in situ fixation and antibody staining.
(a) Time-lapse images for a 3D organoid combined with (b) antibody staining for KRT20, E-cadherin and Lysozyme, and H2B-mCherry signal after fixation. Dotted white outline indicates villus region. Asterisks indicate Paneth cells. Antibody staining images are either sum or maximum projection as indicated. Organoid from ref. [291]. Scale bars: 30 μm. (c) Four-day time-lapse of 2D organoid with (d) in situ fixation, permeabilization and antibody staining for EpCAM. Scale bars: 50 μm.

47. Verify that the organoids used for time-lapse imaging are the same as those stained. Note that individual organoids may be washed away and that slight shifts in the imaging plate relative to the objective may require some searching (Table 6.7).

48. Adjust the positions for imaging such that organoids are imaged in a similar way as during live imaging. A close match between the last timepoint of the time-lapse and the fixed organoid helps mapping individual fixed cells to cells at the last timepoint (Fig. 6.4).

49. Adjust the microscope settings for imaging of the fluorescent antibodies. CRITICAL ensure that the right filters are used and keep an eye out for bleed-through between neighbouring channels (Table 6.7)..

(Optional) Antibody stripping for multiplexed antibody staining (TIMING 3 hours)

In case another round of antibody staining is warranted, antibodies can be stripped with elution buffer [242] and another round of antibody staining can be performed.

50. Remove the PBS solution from the imaging plate.

51. Add elution buffer to the well. CAUTION Elution buffer contains hazardous components and must be handled with appropriate protection and in a fume hood.

52. Tape the imaging plate to a shaker and incubate at room temperature for 15 minutes while shaking.

53. Remove the elution buffer from the imaging plate.

54. Repeat steps 51-53 six times.

55. Wash the well 3× with PBS, then add immunofluorescence blocking buffer and leave the imaging plate for 1 hour at room temperature.

56. Perform another round of antibody staining and imaging following steps 36-49.

Manual single cell tracking and lineage tree reconstruction

Cell tracking can be performed either manually or in a (semi-)automated manner. Here, we discuss basic manual cell tracking applications using our custom OrganoidTracker software. For details on how to train and use neural networks for (semi-)automated cell tracking, we refer to refs. [19, 143] and the OrganoidTracker GitHub page (`https://github.com/jvzonlab/OrganoidTracker`).

57. Start OrganoidTracker as instructed in the installation instructions in the Equipment Setup section.

58. Load the time-lapse images into the OrganoidTracker [143] software. This can be done using "File > Load Images…" button, or the appropriate button on the toolbar. OrganoidTracker allows direct loading of .tif, .lif, .nd2, .czi and .ims imaging files (Fig. 6.5a). In the case where each time point is saved to its own TIF file, load the TIF file of the first time point (Table 6.7).

59. Set the appropriate spatiotemporal resolution in μm/pixel using "Edit > Set image resolution".

60. To start manual tracking click "Edit" menu and click "Manually change data… [C]". This opens the default manual tracking environment.

61. One can move through time using the Left and Right arrow keys. Alternatively, the "Navigate" menu can be used to jump to a time point of your choice. Using the F and L keys on the keyboard, one can move the first and last time point of the time-lapse, respectively. Ensure that the time-lapse consists of the expected number of time points.

62. If at certain timepoints the organoids show large displacements, for example because the imaging window was adjusted between two timepoints, adjust the offset (Fig. 6.5b). This can be done using "Edit > Edit image offsets… [O]", which opens a menu where the organoid after displacement can be aligned to the previous timepoint using the Q (up in Z), E (down in Z), W (up in Y), A (left), S (down in Y), D (right) keys. The W, A, S, D keys by default move in steps of 10 pixels, hold the Alt key to move in steps of 1 pixel.

63. Positions can now be annotated using either the "Enter" or "Insert" button on the keyboard. By default, OrganoidTracker displays positions in previous, current and future timepoints as blue circles, green squares and red circles (Fig. 6.5c).

64. Once a position is annotated, it will automatically be selected. To track cells, go to the next time point (Right arrow key on the keyboard) and insert another annotation. This annotation will then be linked to the previous one. A full cell track is constructed by repeating this step.

65. One can also link two existing annotations by selecting them both and then pressing "Enter" or "Insert". Similarly, links or position annotations can be deleted using the "Backspace" or "Delete" keys.

66. Further editing functionality can be found in the "Edit" menu. Furthermore, in the status area at the bottom of the window, context-related hints are displayed on how to use the editor.

67. The user can exit the editor again using the Escape key (or "View > Exit this view", or the Home button on the toolbar). This will bring the user back to the main screen of OrganoidTracker.

68. Save the tracking data as .aut file. This file can be loaded back into OrganoidTracker or used for analysis.

6
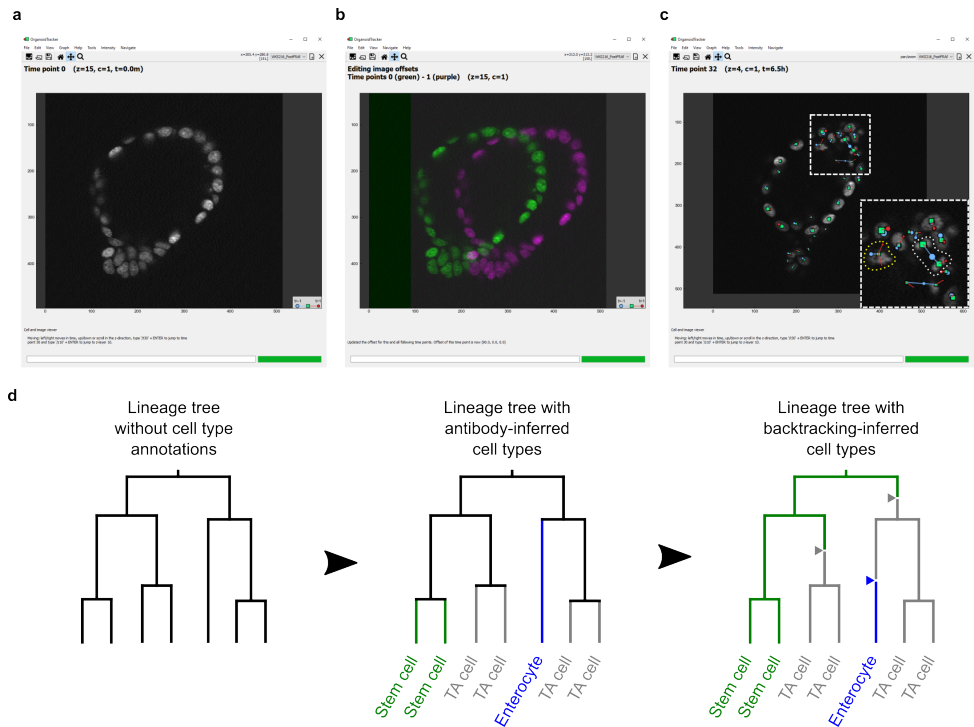
Figure 6.5: Tracking and cell type inference using OrganoidTracker. (a) OrganoidTracker software after loading a time-lapse microscopy dataset. (b) Correcting for abrupt movements during imaging by changing the image offset. Organoid at the current time point in green and at the next timepoint in magenta (c) Manual tracking in OrganoidTracker. Blue circles, green squares and red circles indicate position of a cell in the previous, current and next timepoint, respectively. Blue lines indicate movement of positions from the previous to present timepoint, and red lines indicate movement of positions from present to future timepoint. Yellow and white dotted lines in inset indicate cell divisions in the next and current timepoint, respectively. (d) Automatic cell type inference from in a hypothetical lineage tree based on cell types assigned at the endpoint. Arrowheads in the lineage tree on the right are placed in the middle of the cell track to indicate a transition somewhere along that track.

LINEAGE TREE PLOTTING

OrganoidTracker has built-in functionality to plot lineage trees.

69. Load images and tracking data into OrganoidTracker and use the menu option "Graph > Interactive lineage tree".

70. In the resulting popup window, several filtering options are available in the menu bar, for example to plot only lineages with at least one division.

71. Using the Diskette icon in the toolbar, lineages can be saved as an image, PDF or SVG.

72. If one double-clicks a lineage, OrganoidTracker jumps to that lineage in the tracking data. If the editor is open ("Edit > Manually change data… [C]" from the main

screen), the lineage will be selected automatically. From the "Edit" menu, one can give the lineage a color of choice, which is useful to highlight certain lineages.

Intensity measurement

OrganoidTracker can be used to measure fluorescent intensities from the images [195].

73. Load images and tracking data into OrganoidTracker. Measure fluorescence intensities using "Intensity > Record intensities". Choose the appropriate method of measurement (e.g. circle, sphere, Voronoi model) and set all parameters in the menu "Parameters" (image channel, name of the measurement, etc.; Table 6.7).

74. Start intensity measurement using "Edit > Record intensities…"

75. Once recording is finished, press Escape to go back to the main screen.

76. In the "Intensity" menu, options are available to normalize the intensities, do background correction, plot the intensities in space. It is also possible to plot the intensities over time, either as an average for the organoid, or for individual, selected cells. Finally, it is possible from that menu to create a lineage tree that is coloured by the measured intensities.

Cell type annotations

77. Load the time lapse images and tracking data into OrganoidTracker. Press "C" or use the menu option "Edit > Manually change data" to open the tracking editor. Go to the last time point of the time lapse by pressing "L" or using "Navigate > Last time point".

78. Load the corresponding immunostaining images in an image viewer of your choice (ImageJ, Napari, etc.) to determine how each cell in the live image should be annotated.

79. For any cell that you want to annotate as a certain cell type: first, select the existing position annotation (still in the last time point of the live imaging) by clicking on it, or insert a new annotation using the Insert or Enter key. Then, use "Edit > Set type of track", and click the appropriate type (Table 6.7).

80. Once done with the annotations, use "Edit > Guess parent cell types…", which will infer the cell type of parent cells, using the approach outlined in ref. [291]. For example, if a cell is annotated as a stem cell, the parent cell will also be assigned as a stem cell, and if two sister cells are enterocytes, the parent is identified as an enterocyte (Fig. 6.5d).

81. It is possible to change cell types of cells by selecting them, and using "Edit > Set type of track" to select a different cell type.

82. To visualize the lineage trees coloured by the annotated cell types, exit the tracking editor by pressing Escape or the home button on the toolbar. Then, use "Graph > Interactive lineage tree…". In the popup window, use "View > Toggle showing cell types".

Custom analysis

OrganoidTracker has a few built-in graphs, available through the "Graph" and "Intensity" menus. Instruction on how to write custom Python code that creates graphs based on OrganoidTracker data are included in the GitHub. Alternatively, one can parse the generated .aut files themselves using a programming language of choice.

Timing

- Sample preparation (steps 1-14): 2 hours hands-on time, at least 1 day before start of imaging.

- Drug treatments (steps 15-17): 30 minutes hands-on time.

- Live imaging (steps 18-22): up to five days, 1.5 hours to set up + 30 minutes on subsequent days.

- Laser-manipulations (steps 23-25): 1 hour hands-on time.

- Fixation and permeabilization (steps 26-33): 1 hour hands-on, 2 days total.

- Antibody staining (steps 34-49): 3 hours hands-on time, 1-2 days incubation.

- Antibody stripping (steps 50-56): 3 hours.

6

6.4 TROUBLESHOOTING

Suboptimal conditions during live imaging typically result in organoids dying or showing signs of severely diminished health (Fig. 6.6). An overview of commonly encountered problems and potential solutions is provided in Table 6.7.
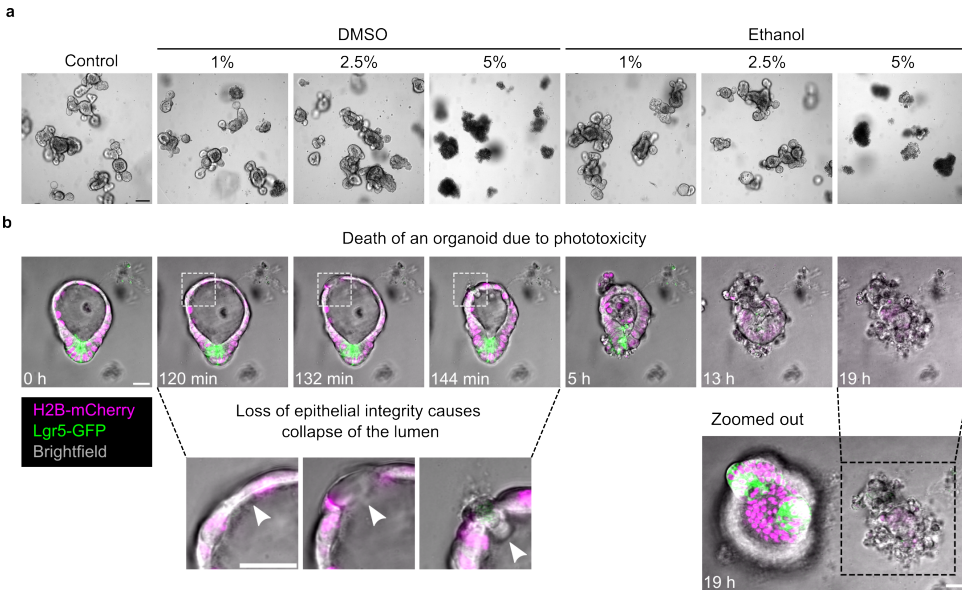
Figure 6.6: Compromised organoid health due to DMSO, ethanol and phototoxicity. (a) Organoids cultured in ENR medium with different concentrations of the DMSO and ethanol, which are commonly used solvents for compounds. Scale bar: 100 µm. (b) Organoid succumbing to phototoxicity. In case of excessive phototoxicity, organoids typically collapse due to loss of epithelial continuity and basal cell extrusion. Adverse effect due to photodamage can be distinguished from other problems by the fact that organoids that were not imaged do not show any signs of impaired health. Also, note that the collapse and death of the organoids can take longer than the duration of time-lapse imaging. Therefore, it is important to ensure that imaging settings do not impair organoid health. Scale bars: 20 µm.

Table 6.7: Troubleshooting commonly encountered problems.

Step(s)	Problem	Possible reason	Solution
10	Organoids don't dissociate during the breaking process.	The Pasteur pipette is not narrow enough.	First try pipetting up and down for a few more rounds. If this does not break the organoids to sufficiently small size, prepare a new Pasteur pipette with a narrower tip.
15-25	Organoids in negative control of drug treatments die or show signs of severely diminished health independent of imaging.	Overdose of vehicle of added compounds. For both DMSO and ethanol, the limit of toxicity is between 1% and 5% v/v (Fig. 6.5a).	Check that the vehicle for added compounds (e.g. DMSO, ethanol, BSA) itself does not affect organoid health. If this is the case, dissolve the compound at higher molarity.
15-25	Organoids selected for imaging die or show signs of severely diminished health during imaging.	Phototoxicity (Fig. 6.5b).	Check health of organoids not selected for imaging. If these are healthy, lower the laser power, imaging frequency or averaging.
18-22	Substantial amount of medium evaporates during imaging.	Humidity in the incubation chamber is not high enough.	Add water to all the empty wells to increase humidity in the imaging chamber. Also, lower the airflow through the incubation chamber.

30	Organoids are washed away during fixation.	Organoids did not sink to the glass during sample preparation. Gel is too brittle.	Let organoids sink to the glass longer during sample preparation (step 14iv). Add more wash medium to the gel during sample preparation (e.g. 50% BME2 in wash medium). Alternatively, prolong the first formaldehyde step in the fixation protocol.
47	Position of organoids cannot be retrieved after in situ fixation.	Imaging plate is in a different position with respect to the optical path compared to live imaging.	Use the exact same sample holder for live- and fixed-cell imaging. Ensure that the imaging plate is put into the exact same sample holder, and that the sample holder is placed back at the exact same position with respect to the optical path as during live imaging. If the sample and sample holder do not fit tightly on the stage and can still move with respect to the optical path, establish a convention for mounting the sample and sample holder on the microscope and stick to that during both live and fixed sample imaging.
36	Antibody staining does not work.	Antibody is prevented from reaching its target by inadequate permeabilization or excess gel around the organoid.	Test the antibody in isolation in a 2D culture or in dislodged and collagenase-treated solution.

58	Images do not load (correctly) in OrganoidTracker.	Unsupported image format. Especially for TIF files, there is a lot of internal variation in the file format, and TIF files beyond 4 GB are not supported.	The most conservative option is to convert the files to one 3D TIF file per channel per time point, which can be done using the BioFormats Exporter in Fiji. This will avoid file size and compatibility problems.
73	Intensity menu is not available.	The CellPhenTracker plugin [195] has not been installed.	See the Equipment Setup section for how to install this plugin, or re-install OrganoidTracker from the branch specifically made for this protocol.
79	No options appear for the cell types.	The intestinal cell type plugin has not been installed.	See the Equipment Setup section for how to install the correct edition of OrganoidTracker, or re-install OrganoidTracker from the branch specifically made for this protocol.

6.5 Anticipated results

Tracking of single cells in organoids yields a wealth of information that can be directly extracted from the tracking data, including proliferation rates, cell-cell contact interfaces and cellular movement [115, 229]. Combining live imaging with (multiplexed) antibody staining or pharmacological perturbations broadens the scope of the protocol presented here. Below, we discuss two types of more advanced data analysis, namely lineage tree reconstruction and quantification of reporter expression in a typical FRAP-experiment.

Lineage tree reconstruction and dynamic cell type inference

In combination with (multiplexed) antibody labelling, it is also possible to make inferences about where cell-type transitions occurred in the lineage trees [291]. This requires the assumption of rules that govern the inferences made about cells in previous timepoint, depending on antibody labelling of those cells and cells in the same lineage tree at the

endpoint. As previously described, these rules may take the following form for mouse intestinal organoids [291]: All cells present at the end are given a unique cell type based on antibody labelling. If two sister cells are of the same type, the mother cell is assigned that type as well. If one of the two sisters is a stem cell, the mother is marked a stem cell as well. If one of the two sisters is a TA cell and the other is neither a TA cell nor a stem cell, the mother is marked as TA cell. Together, with the inferred cell types generally displaying the expected proliferative state and position along the crypt-villus axis, these rules are sufficient to assign any cell in a lineage tree a unique cell fate (Fig. 6.5d). Note, however, that these rules assume that there is no dedifferentiation from any cell type into stem cells and that only stem and TA cells can divide to give rise to other TA cells. While this matches the consensus model of differentiation in the mouse intestine, these assumptions may be breached under the influence of certain compounds or regenerative contexts.

QUANTITATIVE ANALYSIS OF PROTEIN EXPRESSION DYNAMICS USING RECOVERY CURVES

Live imaging of fluorescence-recovery after photobleaching (FRAP) can yield information about protein expression dynamics [142]. Here, we only consider cases where cells are either bleached homogeneously across their volume or not bleached at all. If cells are only partially bleached (e.g. half the cell), other analyses are needed. Interpretation of recovery curves requires that fluorescence intensities of both bleached and control cells are measured and that all control cells show similar qualitative behaviour and small variability in their fluorescence intensity dynamics. In cases where the control cells display highly non-linear dynamics, or naturally fall into multiple categories, more complicated analysis are warranted. It also requires an underlying model for the expression dynamics of the reporter protein. The general assumption is that the fluorescent reporter protein is produced at constant rate $\alpha \geq 0$, degraded with rate $\delta \geq 0$, and photobleached due to imaging at rate $\beta \geq 0$ (Fig. 6.7a). Note that δ represents the intrinsic degradation of the fluorophore by the cell independent of imaging, while β reflects the photobleaching induced externally by live imaging. For quantitative analysis, it is practical to normalize the fluorescence intensities by the intensity just before photobleaching was performed for each individual cell. We refer to the normalized intensity as $f(t) = F(t)/F(0)$ where $F(0)$ is the raw intensity just after the photobleaching is performed. The differential equation for f(t) that describes the fluorescence over time is then

$$\frac{df}{dt} = \alpha - (\beta + \delta)f(t) \tag{6.1}$$

Typically, the fluorescence intensity of photobleached cells then falls into three categories: If degradation and photobleaching are negligible on the timescale of the FRAP experiment ($\beta + \delta \to 0$), the normalized intensity increases linearly for both control and bleached cells (Fig. 6.7b, blue lines). If production of the fluorescent protein has stopped completely before the photobleaching ($\alpha = 0$), both bleached and control cells show exponential decay with rate $\beta + \delta$ (Fig. 6.7b, green lines). If production and degradation are in equilibrium ($\alpha > 0, \beta > 0, \delta > 0$), the control cells will somewhat decrease in intensity due to photobleaching associated with imaging, and bleached cells will increase in intensity (Fig. 6.7b, orange lines).
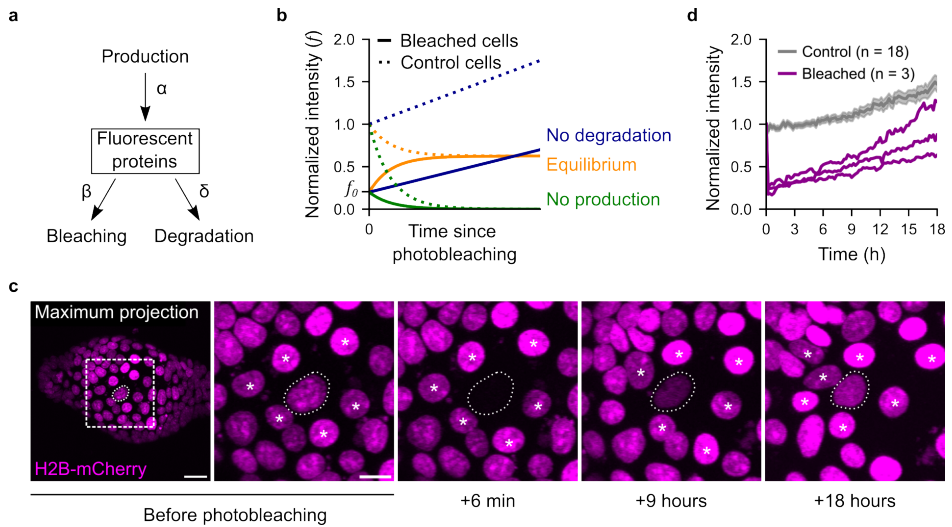
Figure 6.7: Analysing protein expression dynamics using Fluorescence-Recovery After Photobleaching (FRAP). (a) Basic model for expression dynamics of a fluorescent protein with constant rates of production (α), degradation (δ) and photobleaching (β). (b) Three limiting cases for FRAP-curves. The limiting cases correspond to negligible degradation and bleaching rates on the experiment timescale ($\beta + \delta \approx 0$; blue), negligible protein expression ($\alpha \approx 0$; green) and equilibrium between protein production and degradation (positive α, β and δ; orange). (c, d) Example of a FRAP-experiment. (c) Micrographs of an organoid in which one cell is photobleached. Scale bars: 20 μm (maximum projection) and 10 μm (zoom). (d) Fluorescence intensity values of the fluorescence recovery of bleached cells (magenta) and their immediate (non-bleached) neighbours (grey; mean ± S.E.M.). Intensities were measured using a circle of radius 3 μm inside the nucleus. Values were normalized by dividing by the intensity before photobleaching.

To demonstrate this analysis, we performed a FRAP-experiment in which we bleached the nucleus of single cells in the villus of H2B-mCherry reporter organoids and followed their recovery over the course of 18 hours (Fig. 6.7c). Control cells showed little variation and approximately linear increase in fluorescence intensity (Fig. 6.7d). Note that this corresponds to approximately constant production of H2B-mCherry fusion protein and limited degradation.

ACKNOWLEDGEMENTS

7

Conclusion and Outlook

"The light at the end of the tunnel...
...is just the light of an oncoming train."

Robert Lowell

The intestinal epithelium serves as a critical barrier that simultaneously facilitates nutrient absorption while protecting the lamina propria from the hostile content of the lumen. This barrier function relies on a complex interplay of processes that are still not well understood. It is increasingly recognized that studying the dynamics of the intestinal epithelium yields new insight into its function. The work presented in this thesis fits within a more general trend that emphasizes that dynamics are essential for understanding function. This chapter serves to place the work presented in this thesis into the broader context of understanding epithelial barrier regulation. First, we discuss open questions surrounding three key intestinal barrier functions of the intestinal epithelium, being the preservation of epithelial homeostasis, maintenance of mucus layer, and facilitating trans-epithelial communication. Second, we discuss how recent advances in organoid models, single-cell "omics" techniques, and AI-assisted quantitative microscopy should now be integrated to understand the intestinal barrier in space and time. Together, this provides a conclusion of this thesis and an outlook for future research.

7

Achieving homeostasis by balancing cell division, death and differentiation

For proper barrier function the intestinal epithelium must be in homeostasis, which for our purposes, we divide into physical homeostasis and compositional homeostasis. Physical homeostasis means that the intestinal epithelium can physically separate the lumen from the underlying lamina propria. Compositional homeostasis means that the relative abundances of different cell types are balanced such that all functions of the intestinal epithelium can be adequately performed. Both types of homeostasis are not yet fully understood, but the work presented in this thesis and by others has led to new insights.

Physical homeostasis

To achieve physical homeostasis, the intestinal epithelium must strike the right balance between proliferation and extrusion in space and time. Until now, physical homeostasis was believed to result from a positive correlation between cell extrusion rates and cell density [111, 209]. Indeed, in many model systems it has been shown that tissue crowding triggers cell extrusion [68, 156, 171], but recent work challenges this model in the mammalian intestine. In **Chapter 2**, we have demonstrated that the intestinal epithelium is under tension even at the villus tip and that cells that cannot exert sufficient tension on their neighbors extrude from the epithelium. In addition, evidence has emerged that proliferation rates increase with epithelial stretch [10, 181, 249].

Together, these findings suggest that cells extrude when they pose a threat to the epithelial integrity, which decreases density and increases tension, which in turn increases proliferation rates to keep homeostatic cell numbers. Future work could be aimed at unravelling the molecular pathways behind the coupling between mechanical stretch, proliferation and differentiation. A promising approach to achieving this is the combination of mechanical stretch, combined with single-cell omics approaches. In pioneering work, application of cyclic stretch to 2D intestinal organoids was recently shown to increase abundances of stem cells and proliferative cells, which depended on calcium influx due to activation of mechanosensitive PIEZO-channels [10].

Compositional homeostasis

To achieve compositional homeostasis, the epithelium must ensure proper rates of differentiation, as well as balanced commitment to the different cell fates. How compositional homeostasis is achieved is still a major question and requires detailed understanding of how differentiation starts and how cell fates are specified. It is established that the Wnt signaling pathway is essential for stem cells to retain their stemness [14, 88, 187]. Wnt signaling is activated by Wnt-ligands secreted by Paneth cells and the mesenchyme at the crypt bottom [233], giving rise to a decreasing Wnt gradient along the crypt axis [71]. These facts alone already suggested that loss of Wnt-signaling initiates differentiation in stem cells, but the lack of dynamics failed to resolve the exact mechanism. In **Chapter 3** we have shown that the rate of differentiation is set by a timer that starts after a stem cell loses contact with its Wnt source [142]. This work leads us to view the onset of differentiation not simply as a point of no return after cells leave the stem cell zone, but instead as a highly dynamic process repeatedly reset and restarted depending on the local neighborhood of a cell. The

dynamic, non-linear nature of the onset of differentiation is also emerging from other work, including the discovery of retrograde motion of differentiating cells back to the stem cell niche [9], dedifferentiation [191], stem cell replacement [39, 168] and the proliferation of cell types that were originally assumed to be post-mitotic, including (human) tuft cells [114] and (murine) goblet cells [201] and Paneth cells [291].

In addition to regulating differentiation rates, the relative abundances of cell types have to be balanced. The current model for cell fate commitment states that either during or directly after the start of differentiation, cells commit to either the secretory or the absorptive lineage [23]. Secretory progenitors subsequently commit to either goblet, Paneth, enteroendocrine or tuft cell types, and absorptive progenitors to enterocytes, M cells or BEST4/CA7$^+$ cells depending on Notch-, Wnt- and EGF-signaling [78, 242, 270, 288]. More direct observations of the differentiation dynamics have led to important modifications to this two-step model for cell fate specification. Time-resolved lineage labelling [30], tracking-based lineage tree analysis [291] and cell fate mapping in vivo [11] have independently shown that cell fate specification of the secretory cell types already occurs almost directly upon stem cells committing to differentiation. Cell fate commitment was furthermore shown to depend directly on mechanical stretch in the epithelium via mechanosensitive ion channels [10, 105]. In **Chapter 4** of this thesis, we looked at the differentiation of BEST4/CA7$^+$ cells using a synchronous organoid model and show that goblet cells instruct commitment to the BEST4/CA7$^+$ cell fate in their direct neighbors. This observation uncovered that the duration of differentiation is different for each cell type and raises new questions about the temporal order of differentiation in the intestinal epithelium.

Complexity further increases when considering the context of inflammation. The appropriate relative abundances of the differentiated cells depend on the context and the content of the gut. For example, bacterial infections warrant an increase in BEST4/CA7$^+$ cells in order to initiate sufficient water efflux [278], which is achieved by the secretion of interferon-γ by the immune system. During infections with pathogens that use M cells (e.g. Salmonella), the enteric nervous system instructs M cell extrusion [154]. Finally, helminth infections trigger the hyperplasia of both tuft and goblet cells [112, 275], which helps with the removal of the parasitic worms [89]. Future work is needed to map different contexts to optimal cell type compositions, which will help identify how relative cell type abundances can be controlled pharmacologically to enhance or suppress functionalities.

ANTIMICROBIAL DEFENSE: THE MAINTENANCE OF THE MUCUS LAYER AND THE MICROBIOME

In addition to the intestinal epithelium itself, a second layer of defense is provided by the mucus layer. Three major insights have recently changed how the mucus layer is understood, each raising new questions for future research. As discussed in the **Introduction**, it has become clear that goblet cells are a highly heterogeneous cell type. In mouse small intestine, goblet cells have been classified into four subtypes, being proliferative, canonical, non-canonical and intercrypt goblet cells [201]. So far, the precise role and specification of each subtype is still not well understood. Future work could delineate what causes the specification of these goblet cell subtypes, and whether specific subtypes can be up- or

7

downregulated pharmacologically in diseases characterized by abnormal intestinal mucus.

Second, it was recently discovered that BEST4/CA7$^+$ cells play an important role in the maintenance, hydration and electrolyte homeostasis of the mucus layer [278]. In **Chapter 4**, we also showed that BEST4/CA7$^+$ cells enhance goblet cell survival, and in that way also play an essential role in the maintenance of the mucus layer. This finding shifts the paradigm that goblet cells autonomously regulate mucus layer, to one in which maintenance of the mucus layer is a collaborative effort by goblet and BEST4/CA7$^+$ cells. The mechanism by which BEST4/CA7$^+$ cells enhance goblet cell survival remains unclear. A promising next step would be to systematically knock-out combinations of BEST4/CA7$^+$ cell markers and track goblet cell survival. Such screening will show which BEST4/CA7$^+$ cell markers are essential/redundant for goblet cell survival and may yield new targets for drug development. This is especially interesting in the context of inflammatory bowel disease, where both BEST4/CA7$^+$ cells and colonic (BEST2$^+$) goblet cells are depleted.

Third, time-resolved investigation of the intestinal mucus layer has shown that the mucus layer is highly dynamic. For example, after cholinergic stimulation goblet cells in the crypts rapidly release their mucus, leading to the clearance of the crypt-lumen (both organoids and in vivo) [64]. This rapid mucus release is distinct from normal mucus secretion and involves intracellular mucus expansion and rupture of the apical membrane. Future work should be aimed at understanding the dynamics of the intestinal mucus layer and the interactions with the microbiome, the immune system and the enteric nervous system. Open-lumen organoids [208] or mini-guts in microfluidic chips [184], overlaid with beads or fluorescent bacteria, can be tracked over time to determine growth rates of the intestinal mucus layer under a variety of conditions. This approach can be further expanded by including components from the immune or enteric nervous system, in order to arrive at a holistic model for maintenance of the intestinal mucus barrier.

Transepithelial communication

The human small intestine contains highly specialized M cells which function to transcytose luminal antigens and bacteria to underlying immune follicles. M cells reside in the follicle-associated epithelium (FAE) overlaying Peyer's patches and often contain a basal cavity with a dendritic cell. M cells are so rare that they are typically not well represented in primary single-cell RNA sequencing data [37, 69, 70, 95], but they can be studied in human organoid models [277]. In addition to M cells, goblet cells have also been reported to fulfill a role in luminal antigen sampling. While several papers have studied the transcytosis of luminal antigens and bacteria in organoid models [74, 100, 220, 222, 226], the dynamics of the process itself has not been investigated. Resolving transcytosis in real time could reveal whether the transfer of bacteria through M cells is an active, directional process driven by the cytoskeleton, or whether bacteria are endocytosed apically and exocytosed randomly. Additionally, the downstream activation of dendritic cells and the immune system has not yet been explored, and should be studied using co-culture models of bacteria, epithelia and immune cells.

Integrating the tools we need to understand the dynamics of the intestinal barrier

Besides the questions that the chapters of this thesis, and similar recent literature raises, the toolkit to answer these questions keeps expanding. While classical 3D organoids are still sufficient and essential for addressing many questions about the intestinal epithelium, tissue engineering efforts have yielded scaffolds for organoids to grow in a manner similar to in vivo [86, 87, 161, 162, 184, 196]. As illustrated in **Chapter 2**, some of these scaffolds can be readily combined with long-term live imaging, which makes it possible to study intestinal epithelial cells in their natural spatial environment. Because the tracking of individual cells over long periods of time is highly challenging [245], new tools and protocols for quantitative microscopy are still necessary in the effort to understand dynamical processes in intestinal organoids.

One promising direction in the field is the application of artificial intelligence (AI) to the analysis of live imaging data—particularly for the automation of cell tracking [19, 59, 143, 169]. In **Chapter 5**, we introduced the LabelFreeTracker algorithm, developed for the in silico labelling of nuclei and membranes in three-dimensional (3D) intestinal organoids [141]. Remarkably, the neural networks underlying LabelFreeTracker not only automate a process that could be performed manually but also succeeded in accomplishing a task that even experienced human annotators found infeasible. While our implementation focused on in silico labelling of cell nuclei and boundaries, the method holds potential for extension to other intracellular structures. In two-dimensional (2D) tissues, it has already been demonstrated that additional subcellular components—such as mitochondria and nuclear envelopes—can be visualized through in silico labelling [204]. However, extending this capability to dense, 3D organoids remains a challenge for future research.

On the experimental side, a fundamental limitation of live imaging is the restricted number of observable parameters. Using imaging alone, it is typically possible to monitor cell positions, lineage trajectories, and at most four fluorescent reporters simultaneously. To gain deeper insights into the molecular composition of cells, we and others have developed methodologies that combine live-imaging datasets with in situ fixation and multiple rounds of antibody staining [59, 115, 142, 169, 195, 291]. In practice, however, these workflows are technically demanding and require considerable expertise to implement successfully. In **Chapter 6** we presented a detailed protocol for long-term live imaging of experimentally perturbed intestinal organoids, followed by in situ fixation and endpoint analysis. While this protocol specifically focuses on multiplexed antibody staining as the endpoint, we anticipate that a wide range of additional endpoint analyses will soon become technically feasible. These include single-molecule RNA fluorescent in situ hybridization (smFISH) [110], deterministic single-cell RNA sequencing [34], spatial transcriptomics [137], three-dimensional intact-tissue sequencing [279], and in situ proteomics [221, 289]. In conclusion, we advocate for the development of integrated experimental pipelines that combine long-term live cell tracking with a comprehensive palette of single-cell omics techniques, enabling a more complete characterization of cellular states and dynamics.

7

Bibliography

References

[1] Abadi, M., A. Agarwal, P. Barham, E. Brevdo, Z. Chen, C. Citro, G. S. Corrado, A. Davis, J. Dean, M. Devin, S. Ghemawat, I. Goodfellow, A. Harp, G. Irving, M. Isard, Y. Jia, R. Jozefowicz, L. Kaiser, M. Kudlur, J. Levenberg, D. Mane, R. Monga, S. Moore, D. Murray, C. Olah, M. Schuster, J. Shlens, B. Steiner, I. Sutskever, K. Talwar, P. Tucker, V. Vanhoucke, V. Vasudevan, F. Viegas, O. Vinyals, P. Warden, M. Wattenberg, M. Wicke, Y. Yu, and X. Zheng (2016, March). TensorFlow: Large-Scale Machine Learning on Heterogeneous Distributed Systems.

[2] Ai, X., D. Wang, J. Zhang, and J. Shen (2020, January). Hippo signaling promotes Ets21c-dependent apical cell extrusion in the *Drosophila* wing disc. *Development*, dev.190124.

[3] Ambort, D., M. E. V. Johansson, J. K. Gustafsson, H. E. Nilsson, A. Ermund, B. R. Johansson, P. J. B. Koeck, H. Hebert, and G. C. Hansson (2012, April). Calcium and pH-dependent packing and release of the gel-forming MUC2 mucin. *Proc. Natl. Acad. Sci. U.S.A. 109*(15), 5645–5650.

[4] An, Y., G. Xue, Y. Shaobo, D. Mingxi, X. Zhou, W. Yu, T. Ishibashi, L. Zhang, and Y. Yan (2017, January). Apical constriction is driven by a pulsatile apical myosin network in delaminating Drosophila neuroblasts. *Development*, dev.150763.

[5] Arkell, R. M., N. Fossat, and P. P. Tam (2013, August). Wnt signalling in mouse gastrulation and anterior development: New players in the pathway and signal output. *Current Opinion in Genetics & Development 23*(4), 454–460.

[6] Artegiani, B., D. Hendriks, J. Beumer, R. Kok, X. Zheng, I. Joore, S. Chuva de Sousa Lopes, J. van Zon, S. Tans, and H. Clevers (2020, March). Fast and efficient generation of knock-in human organoids using homology-independent CRISPR–Cas9 precision genome editing. *Nat Cell Biol 22*(3), 321–331.

[7] Atieh, Y., T. Wyatt, A. M. Zaske, and G. T. Eisenhoffer (2021, March). Pulsatile contractions promote apoptotic cell extrusion in epithelial tissues. *Current Biology 31*(6), 1129–1140.e4.

[8] Atwell, S., D. J. E. Waibel, S. S. Boushehri, S. Wiedenmann, C. Marr, and M. Meier (2023, July). Label-free imaging of 3D pluripotent stem cell differentiation dynamics on chip. *Cell Reports Methods 3*(7), 100523.

[9] Azkanaz, M., B. Corominas-Murtra, S. I. J. Ellenbroek, L. Bruens, A. T. Webb, D. Laskaris, K. C. Oost, S. J. A. Lafirenze, K. Annusver, H. A. Messal, S. Iqbal, D. J. Flanagan, D. J. Huels, F. Rojas-Rodríguez, M. Vizoso, M. Kasper, O. J. Sansom, H. J. Snippert, P. Liberali,

B. D. Simons, P. Katajisto, E. Hannezo, and J. van Rheenen (2022, July). Retrograde movements determine effective stem cell numbers in the intestine. *Nature 607*(7919), 548–554.

[10] Baghdadi, M. B., R. M. Houtekamer, L. Perrin, A. Rao-Bhatia, M. Whelen, L. Decker, M. Bergert, C. Pérez-Gonzàlez, R. Bouras, G. Gropplero, A. K. H. Loe, A. Afkhami-Poostchi, X. Chen, X. Huang, S. Descroix, J. L. Wrana, A. Diz-Muñoz, M. Gloerich, A. Ayyaz, D. Matic Vignjevic, and T.-H. Kim (2024, November). PIEZO-dependent mechanosensing is essential for intestinal stem cell fate decision and maintenance. *Science 386*(6725), eadj7615.

[11] Banjac, I., M. Maimets, I. H. Tsang, M. Dioli, S. L. Hansen, K. Krizic, R. B. Bressan, C. Lövkvist, and K. B. Jensen (2025, January). Fate mapping in mouse demonstrates early secretory differentiation directly from Lgr5+ intestinal stem cells. *Developmental Cell*, S1534580724007627.

[12] Baribault, H., J. Penner, R. V. Iozzo, and M. Wilson-Heiner (1994, December). Colorectal hyperplasia and inflammation in keratin 8-deficient FVB/N mice. *Genes Dev. 8*(24), 2964–2973.

[13] Barker, N. (2014, January). Adult intestinal stem cells: Critical drivers of epithelial homeostasis and regeneration. *Nat Rev Mol Cell Biol 15*(1), 19–33.

[14] Barker, N., J. H. van Es, J. Kuipers, P. Kujala, M. van den Born, M. Cozijnsen, A. Haegebarth, J. Korving, H. Begthel, P. J. Peters, and H. Clevers (2007, October). Identification of stem cells in small intestine and colon by marker gene Lgr5. *Nature 449*(7165), 1003–1007.

[15] Barrett, T., S. E. Wilhite, P. Ledoux, C. Evangelista, I. F. Kim, M. Tomashevsky, K. A. Marshall, K. H. Phillippy, P. M. Sherman, M. Holko, A. Yefanov, H. Lee, N. Zhang, C. L. Robertson, N. Serova, S. Davis, and A. Soboleva (2012, November). NCBI GEO: Archive for functional genomics data sets—update. *Nucleic Acids Research 41*(D1), D991–D995.

[16] Bartscherer, K. and M. Boutros (2008, October). Regulation of Wnt protein secretion and its role in gradient formation. *EMBO Reports 9*(10), 977–982.

[17] Basak, O., J. Beumer, K. Wiebrands, H. Seno, A. van Oudenaarden, and H. Clevers (2017, February). Induced Quiescence of Lgr5+ Stem Cells in Intestinal Organoids Enables Differentiation of Hormone-Producing Enteroendocrine Cells. *Cell Stem Cell 20*(2), 177–190.e4.

[18] Behrndt, M., G. Salbreux, P. Campinho, R. Hauschild, F. Oswald, J. Roensch, S. W. Grill, and C.-P. Heisenberg (2012, October). Forces Driving Epithelial Spreading in Zebrafish Gastrulation. *Science 338*(6104), 257–260.

[19] Betjes, M. A., S. J. Tans, and J. S. Van Zon (2024, October). Cell tracking with accurate error prediction.

[20] Betjes, M. A., X. Zheng, R. N. U. Kok, J. S. Van Zon, and S. J. Tans (2021, June). Cell Tracking for Organoids: Lessons From Developmental Biology. *Front. Cell Dev. Biol. 9*, 675013.

[21] Bettess, M. D., N. Dubois, M. J. Murphy, C. Dubey, C. Roger, S. Robine, and A. Trumpp (2005, September). C-Myc Is Required for the Formation of Intestinal Crypts but Dispensable for Homeostasis of the Adult Intestinal Epithelium. *Molecular and Cellular Biology 25*(17), 7868–7878.

[22] Beumer, J., B. Artegiani, Y. Post, F. Reimann, F. Gribble, T. N. Nguyen, H. Zeng, M. Van Den Born, J. H. Van Es, and H. Clevers (2018, August). Enteroendocrine cells switch hormone expression along the crypt-to-villus BMP signalling gradient. *Nat Cell Biol 20*(8), 909–916.

[23] Beumer, J. and H. Clevers (2021, January). Cell fate specification and differentiation in the adult mammalian intestine. *Nat Rev Mol Cell Biol 22*(1), 39–53.

[24] Beumer, J., H. Gehart, and H. Clevers (2020, October). Enteroendocrine Dynamics – New Tools Reveal Hormonal Plasticity in the Gut. *Endocrine Reviews 41*(5), bnaa018.

[25] Beumer, J., J. Puschhof, F. Y. Yengej, L. Zhao, A. Martinez-Silgado, M. Blotenburg, H. Begthel, C. Boot, A. van Oudenaarden, Y.-G. Chen, and H. Clevers (2022, March). BMP gradient along the intestinal villus axis controls zonated enterocyte and goblet cell states. *Cell Reports 38*(9), 110438.

[26] Birchenough, G. M. H., E. E. L. Nyström, M. E. V. Johansson, and G. C. Hansson (2016, June). A sentinel goblet cell guards the colonic crypt by triggering Nlrp6-dependent Muc2 secretion. *Science 352*(6293), 1535–1542.

[27] Blache, P., M. van de Wetering, I. Duluc, C. Domon, P. Berta, J.-N. Freund, H. Clevers, and P. Jay (2004). SOX9 Is an Intestine Crypt Transcription Factor, Is Regulated by the Wnt Pathway, and Represses the CDX2 and MUC2 Genes. *The Journal of Cell Biology 166*(1), 37–47.

[28] Bonnet, I., P. Marcq, F. Bosveld, L. Fetler, Y. Bellaïche, and F. Graner (2012, October). Mechanical state, material properties and continuous description of an epithelial tissue. *J. R. Soc. Interface. 9*(75), 2614–2623.

[29] Borten, M. A., S. S. Bajikar, N. Sasaki, H. Clevers, and K. A. Janes (2018, March). Automated brightfield morphometry of 3D organoid populations by OrganoSeg. *Sci Rep 8*(1), 5319.

[30] Böttcher, A., M. Büttner, S. Tritschler, M. Sterr, A. Aliluev, L. Oppenländer, I. Burtscher, S. Sass, M. Irmler, J. Beckers, C. Ziegenhain, W. Enard, A. C. Schamberger, F. M. Verhamme, O. Eickelberg, F. J. Theis, and H. Lickert (2021, January). Non-canonical Wnt/PCP signalling regulates intestinal stem cell lineage priming towards enteroendocrine and Paneth cell fates. *Nat Cell Biol 23*(1), 23–31.

[31] Brassard, J. A., M. Nikolaev, T. Hübscher, M. Hofer, and M. P. Lutolf (2021, January). Recapitulating macro-scale tissue self-organization through organoid bioprinting. *Nat. Mater. 20*(1), 22–29.

[32] Brunt, L. and S. Scholpp (2018, March). The function of endocytosis in Wnt signaling. *Cell. Mol. Life Sci. 75*(5), 785–795.

[33] Bryan, D. S., M. Stack, K. Krysztofiak, U. Cichoń, D. G. Thomas, A. Surcel, E. S. Schiffhauer, M. A. Beckett, N. N. Khodarev, L. Xue, E. C. Poli, A. T. Pearson, M. C. Posner, D. N. Robinson, R. S. Rock, and R. R. Weichselbaum (2020, September). 4-Hydroxyacetophenone modulates the actomyosin cytoskeleton to reduce metastasis. *Proc. Natl. Acad. Sci. U.S.A. 117*(36), 22423–22429.

[34] Bues, J., M. Biočanin, J. Pezoldt, R. Dainese, A. Chrisnandy, S. Rezakhani, W. Saelens, V. Gardeux, R. Gupta, R. Sarkis, J. Russeil, Y. Saeys, E. Amstad, M. Claassen, M. P. Lutolf, and B. Deplancke (2022, March). Deterministic scRNA-seq captures variation in intestinal crypt and organoid composition. *Nat Methods 19*(3), 323–330.

[35] Buissant Des Amorie, J. R., M. A. Betjes, J. H. Bernink, J. H. Hageman, V. E. Geurts, H. Begthel, D. Laskaris, M. C. Heinz, I. Jordens, T. Vinck, R. M. Houtekamer, I. Verlaan-Klink, S. R. Brunner, J. Van Rheenen, M. Gloerich, H. Clevers, S. J. Tans, J. S. Van Zon, and H. J. G. Snippert (2025, July). Intestinal tuft cell subtypes represent successive stages of maturation driven by crypt-villus signaling gradients. *Nat Commun 16*(1), 6765.

[36] Bullen, T. F., S. Forrest, F. Campbell, A. R. Dodson, M. J. Hershman, D. M. Pritchard, J. R. Turner, M. H. Montrose, and A. J. M. Watson (2006, October). Characterization of epithelial cell shedding from human small intestine. *Laboratory Investigation 86*(10), 1052–1063.

[37] Burclaff, J., R. J. Bliton, K. A. Breau, M. T. Ok, I. Gomez-Martinez, J. S. Ranek, A. P. Bhatt, J. E. Purvis, J. T. Woosley, and S. T. Magness (2022). A Proximal-to-Distal Survey of Healthy Adult Human Small Intestine and Colon Epithelium by Single-Cell Transcriptomics. *Cellular and Molecular Gastroenterology and Hepatology 13*(5), 1554–1589.

[38] Busslinger, G. A., B. L. Weusten, A. Bogte, H. Begthel, L. A. Brosens, and H. Clevers (2021, March). Human gastrointestinal epithelia of the esophagus, stomach, and duodenum resolved at single-cell resolution. *Cell Reports 34*(10), 108819.

[39] Capdevila, C., J. Miller, L. Cheng, A. Kornberg, J. J. George, H. Lee, T. Botella, C. S. Moon, J. W. Murray, S. Lam, R. I. Calderon, E. Malagola, G. Whelan, C.-S. Lin, A. Han, T. C. Wang, P. A. Sims, and K. S. Yan (2024, June). Time-resolved fate mapping identifies the intestinal upper crypt zone as an origin of Lgr5+ crypt base columnar cells. *Cell 187*(12), 3039–3055.e14.

[40] Chanet, S., C. J. Miller, E. D. Vaishnav, B. Ermentrout, L. A. Davidson, and A. C. Martin (2017, May). Actomyosin meshwork mechanosensing enables tissue shape to orient cell force. *Nat Commun 8*(1), 15014.

[41] Cheng, H. (1974, December). Origin, differentiation and renewal of the four main epithelial cell types in the mouse small intestine II. Mucous cells. *Am. J. Anat. 141*(4), 481–501.

[42] Christiansen, E. M., S. J. Yang, D. M. Ando, A. Javaherian, G. Skibinski, S. Lipnick, E. Mount, A. O'Neil, K. Shah, A. K. Lee, P. Goyal, W. Fedus, R. Poplin, A. Esteva, M. Berndl, L. L. Rubin, P. Nelson, and S. Finkbeiner (2018, April). In Silico Labeling: Predicting Fluorescent Labels in Unlabeled Images. *Cell 173*(3), 792–803.e19.

[43] Çiçek, Ö., A. Abdulkadir, S. S. Lienkamp, T. Brox, and O. Ronneberger (2016). 3D U-Net: Learning Dense Volumetric Segmentation from Sparse Annotation. In S. Ourselin, L. Joskowicz, M. R. Sabuncu, G. Unal, and W. Wells (Eds.), *Medical Image Computing and Computer-Assisted Intervention – MICCAI 2016*, Volume 9901, pp. 424–432. Cham: Springer International Publishing.

[44] Clevers, H. (2013, July). The Intestinal Crypt, A Prototype Stem Cell Compartment. *Cell 154*(2), 274–284.

[45] Clevers, H. (2016, June). Modeling Development and Disease with Organoids. *Cell 165*(7), 1586–1597.

[46] Coelho, L. P. (2013, July). Mahotas: Open source software for scriptable computer vision. *Journal of Open Research Software 1*(1), e3.

[47] Cohen, N., H. Massalha, S. Ben-Moshe, A. Egozi, M. Rozenberg, K. Bahar Halpern, and S. Itzkovitz (2021, October). Spatial gene expression maps of the intestinal lymphoid follicle and associated epithelium identify zonated expression programs. *PLoS Biol 19*(10), e3001214.

[48] Cornes, J. S. (1965, June). Number, size, and distribution of Peyer's patches in the human small intestine: Part I The development of Peyer's patches. *Gut 6*(3), 225–229.

[49] Cross-Zamirski, J. O., E. Mouchet, G. Williams, C.-B. Schönlieb, R. Turkki, and Y. Wang (2022, June). Label-free prediction of cell painting from brightfield images. *Sci Rep 12*(1), 10001.

[50] Cumming, T. and R. Levayer (2024, March). Toward a predictive understanding of epithelial cell death. *Seminars in Cell & Developmental Biology 156*, 44–57.

[51] Curran, S., C. Strandkvist, J. Bathmann, M. De Gennes, A. Kabla, G. Salbreux, and B. Baum (2017, November). Myosin II Controls Junction Fluctuations to Guide Epithelial Tissue Ordering. *Developmental Cell 43*(4), 480–492.e6.

[52] Darwich, A. S., U. Aslam, D. M. Ashcroft, and A. Rostami-Hodjegan (2014, December). Meta-Analysis of the Turnover of Intestinal Epithelia in Preclinical Animal Species and Humans. *Drug Metab Dispos 42*(12), 2016–2022.

[53] Das, B., K. Okamoto, J. Rabalais, P. A. Kozan, R. R. Marchelletta, M. D. McGeough, N. Durali, M. Go, K. E. Barrett, S. Das, and M. Sivagnanam (2019, November). Enteroids expressing a disease-associated mutant of EpCAM are a model for congenital tufting enteropathy. *American Journal of Physiology-Gastrointestinal and Liver Physiology 317*(5), G580–G591.

[54] Das, B., K. Okamoto, J. Rabalais, J. A. Young, K. E. Barrett, and M. Sivagnanam (2021). Aberrant Epithelial Differentiation Contributes to Pathogenesis in a Murine Model of Congenital Tufting Enteropathy. *Cellular and Molecular Gastroenterology and Hepatology 12*(4), 1353–1371.

[55] Das, B. and M. Sivagnanam (2020, December). Congenital Tufting Enteropathy: Biology, Pathogenesis and Mechanisms. *JCM 10*(1), 19.

[56] Davidson-Pilon, C. (2019, August). Lifelines: Survival analysis in Python. *JOSS 4*(40), 1317.

[57] de Lau, W., P. Kujala, K. Schneeberger, S. Middendorp, V. S. W. Li, N. Barker, A. Martens, F. Hofhuis, R. P. DeKoter, P. J. Peters, E. Nieuwenhuis, and H. Clevers (2012, September). Peyer's Patch M Cells Derived from Lgr5 $^+$ Stem Cells Require SpiB and Are Induced by RankL in Cultured "Miniguts". *Mol Cell Biol 32*(18), 3639–3647.

[58] De Lau, W., W. C. Peng, P. Gros, and H. Clevers (2014, February). The R-spondin/Lgr5/Rnf43 module: Regulator of Wnt signal strength. *Genes Dev. 28*(4), 305–316.

[59] De Medeiros, G., R. Ortiz, P. Strnad, A. Boni, F. Moos, N. Repina, L. Challet Meylan, F. Maurer, and P. Liberali (2022, August). Multiscale light-sheet organoid imaging framework. *Nat Commun 13*(1), 4864.

[60] Deben, C., E. C. De La Hoz, M. L. Compte, P. Van Schil, J. M. Hendriks, P. Lauwers, S. K. Yogeswaran, F. Lardon, P. Pauwels, S. Van Laere, A. Bogaerts, E. Smits, S. Vanlanduit, and A. Lin (2023, April). OrBITS: Label-free and time-lapse monitoring of patient derived organoids for advanced drug screening. *Cell Oncol. 46*(2), 299–314.

[61] Deconinck, L., R. Cannoodt, W. Saelens, B. Deplancke, and Y. Saeys (2021, September). Recent advances in trajectory inference from single-cell omics data. *Current Opinion in Systems Biology 27*, 100344.

[62] Des Amorie, J. R. B., M. A. Betjes, J. Bernink, J. H. Hageman, M. C. Heinz, I. Jordens, T. Vinck, R. M. Houtekamer, I. Verlaan-Klink, S. R. Brunner, D. Laskaris, J. Van Rheenen, M. Gloerich, H. Clevers, J. S. Van Zon, S. J. Tans, and H. J. Snippert (2024, November). Mature tuft cell phenotypes are sequentially expressed along the intestinal crypt-villus axis following cytokine-induced tuft cell hyperplasia.

[63] Diaz-Cuadros, M. and O. Pourquié (2023, November). The Clockwork Embryo: Mechanisms Regulating Developmental Rate. *Annu. Rev. Genet. 57*(1), 117–134.

[64] Dolan, B., A. Ermund, B. Martinez-Abad, M. E. V. Johansson, and G. C. Hansson (2022, September). Clearance of small intestinal crypts involves goblet cell mucus secretion by intracellular granule rupture and enterocyte ion transport. *Sci. Signal. 15*(752), eabl5848.

[65] Dos Reis, D. C., J. Jin, A. Santos, C. Muiler, E. Zagoren, M. Donnelley, D. Parsons, P. Cmielewski, N. Reyne, A. McCarron, Z. Smith, K. Sumigray, and N. A. Ameen (2025, January). CFTR High Expresser BEST4+ cells are pH-sensing neuropod cells: New implications for intestinal physiology and Cystic Fibrosis disease.

[66] Durand, A., B. Donahue, G. Peignon, F. Letourneur, N. Cagnard, C. Slomianny, C. Perret, N. F. Shroyer, and B. Romagnolo (2012, June). Functional intestinal stem cells after Paneth cell ablation induced by the loss of transcription factor Math1 (Atoh1). *Proc. Natl. Acad. Sci. U.S.A. 109*(23), 8965–8970.

[67] Duszyc, K., G. A. Gomez, A. K. Lagendijk, M.-K. Yau, B. N. Nanavati, B. L. Gliddon, T. E. Hall, S. Verma, B. M. Hogan, S. M. Pitson, D. P. Fairlie, R. G. Parton, and A. S. Yap (2021, March). Mechanotransduction activates RhoA in the neighbors of apoptotic epithelial cells to engage apical extrusion. *Current Biology 31*(6), 1326–1336.e5.

[68] Eisenhoffer, G. T., P. D. Loftus, M. Yoshigi, H. Otsuna, C.-B. Chien, P. A. Morcos, and J. Rosenblatt (2012, April). Crowding induces live cell extrusion to maintain homeostatic cell numbers in epithelia. *Nature 484*(7395), 546–549.

[69] Elmentaite, R., N. Kumasaka, K. Roberts, A. Fleming, E. Dann, H. W. King, V. Kleshchevnikov, M. Dabrowska, S. Pritchard, L. Bolt, S. F. Vieira, L. Mamanova, N. Huang, F. Perrone, I. Goh Kai'En, S. N. Lisgo, M. Katan, S. Leonard, T. R. W. Oliver, C. E. Hook, K. Nayak, L. S. Campos, C. Domínguez Conde, E. Stephenson, J. Engelbert, R. A. Botting, K. Polanski, S. van Dongen, M. Patel, M. D. Morgan, J. C. Marioni, O. A. Bayraktar, K. B. Meyer, X. He, R. A. Barker, H. H. Uhlig, K. T. Mahbubani, K. Saeb-Parsy, M. Zilbauer, M. R. Clatworthy, M. Haniffa, K. R. James, and S. A. Teichmann (2021, September). Cells of the human intestinal tract mapped across space and time. *Nature 597*(7875), 250–255.

[70] Elmentaite, R., A. D. Ross, K. Roberts, K. R. James, D. Ortmann, T. Gomes, K. Nayak, L. Tuck, S. Pritchard, O. A. Bayraktar, R. Heuschkel, L. Vallier, S. A. Teichmann, and M. Zilbauer (2020, December). Single-Cell Sequencing of Developing Human Gut Reveals Transcriptional Links to Childhood Crohn's Disease. *Developmental Cell 55*(6), 771–783.e5.

[71] Farin, H. F., I. Jordens, M. H. Mosa, O. Basak, J. Korving, D. V. F. Tauriello, K. de Punder, S. Angers, P. J. Peters, M. M. Maurice, and H. Clevers (2016, February). Visualization of a short-range Wnt gradient in the intestinal stem-cell niche. *Nature 530*(7590), 340–343.

[72] Farin, H. F., W. R. Karthaus, P. Kujala, M. Rakhshandehroo, G. Schwank, R. G. Vries, E. Kalkhoven, E. E. Nieuwenhuis, and H. Clevers (2014, June). Paneth cell extrusion and release of antimicrobial products is directly controlled by immune cell–derived IFN-gamma. *Journal of Experimental Medicine 211*(7), 1393–1405.

[73] Farin, H. F., J. H. Van Es, and H. Clevers (2012, December). Redundant Sources of Wnt Regulate Intestinal Stem Cells and Promote Formation of Paneth Cells. *Gastroenterology 143*(6), 1518–1529.e7.

[74] Fasciano, A. C., G. S. Dasanayake, M. K. Estes, N. C. Zachos, D. T. Breault, R. R. Isberg, S. Tan, and J. Mecsas (2021, January). Yersinia pseudotuberculosis YopE prevents uptake by M cells and instigates M cell extrusion in human ileal enteroid-derived monolayers. *Gut Microbes 13*(1), 1988390.

[75] Fawkner-Corbett, D., A. Antanaviciute, K. Parikh, M. Jagielowicz, A. S. Gerós, T. Gupta, N. Ashley, D. Khamis, D. Fowler, E. Morrissey, C. Cunningham, P. R. Johnson, H. Koohy, and A. Simmons (2021, February). Spatiotemporal analysis of human intestinal development at single-cell resolution. *Cell 184*(3), 810–826.e23.

[76] Fernández-Sánchez, M. E., S. Barbier, J. Whitehead, G. Béalle, A. Michel, H. Latorre-Ossa, C. Rey, L. Fouassier, A. Claperon, L. Brullé, E. Girard, N. Servant, T. Rio-Frio, H. Marie, S. Lesieur, C. Housset, J.-L. Gennisson, M. Tanter, C. Ménager, S. Fre, S. Robine, and E. Farge (2015). Mechanical induction of the tumorigenic β-catenin pathway by tumour growth pressure. *Nature 523*(7558), 92–95.

[77] Fevr, T., S. Robine, D. Louvard, and J. Huelsken (2007, November). Wnt/β-Catenin Is Essential for Intestinal Homeostasis and Maintenance of Intestinal Stem Cells. *Molecular and Cellular Biology 27*(21), 7551–7559.

[78] Fre, S., M. Huyghe, P. Mourikis, S. Robine, D. Louvard, and S. Artavanis-Tsakonas (2005, June). Notch signals control the fate of immature progenitor cells in the intestine. *Nature 435*(7044), 964–968.

[79] Fujii, M., M. Matano, K. Nanki, and T. Sato (2015, October). Efficient genetic engineering of human intestinal organoids using electroporation. *Nat Protoc 10*(10), 1474–1485.

[80] Fujii, M., M. Matano, K. Toshimitsu, A. Takano, Y. Mikami, S. Nishikori, S. Sugimoto, and T. Sato (2018, December). Human Intestinal Organoids Maintain Self-Renewal Capacity and Cellular Diversity in Niche-Inspired Culture Condition. *Cell Stem Cell 23*(6), 787–793.e6.

[81] Gehart, H., J. H. van Es, K. Hamer, J. Beumer, K. Kretzschmar, J. F. Dekkers, A. Rios, and H. Clevers (2019, February). Identification of Enteroendocrine Regulators by Real-Time Single-Cell Differentiation Mapping. *Cell 176*(5), 1158–1173.e16.

[82] Gerbe, F., B. Brulin, L. Makrini, C. Legraverend, and P. Jay (2009, December). DCAMKL-1 Expression Identifies Tuft Cells Rather Than Stem Cells in the Adult Mouse Intestinal Epithelium. *Gastroenterology 137*(6), 2179–2180.

[83] Gerbe, F., J. H. Van Es, L. Makrini, B. Brulin, G. Mellitzer, S. Robine, B. Romagnolo, N. F. Shroyer, J.-F. Bourgaux, C. Pignodel, H. Clevers, and P. Jay (2011, March). Distinct ATOH1 and Neurog3 requirements define tuft cells as a new secretory cell type in the intestinal epithelium. *Journal of Cell Biology 192*(5), 767–780.

[84] Gersemann, M., S. Becker, I. Kübler, M. Koslowski, G. Wang, K. R. Herrlinger, J. Griger, P. Fritz, K. Fellermann, M. Schwab, J. Wehkamp, and E. F. Stange (2009, January). Differences in goblet cell differentiation between Crohn's disease and ulcerative colitis. *Differentiation 77*(1), 84–94.

[85] Ghazavi, F., J. Huysentruyt, J. De Coninck, S. Kourula, S. Martens, B. Hassannia, T. Wartewig, T. Divert, R. Roelandt, B. Popper, A. Hiergeist, P. Tougaard, T. Vanden Berghe, M. Joossens, G. Berx, N. Takahashi, A. Wahida, and P. Vandenabeele (2022, February). Executioner caspases 3 and 7 are dispensable for intestinal epithelium turnover and homeostasis at steady state. *Proc. Natl. Acad. Sci. U.S.A. 119*(6), e2024508119.

[86] Gjorevski, N., M. Nikolaev, T. E. Brown, O. Mitrofanova, N. Brandenberg, F. W. DelRio, F. M. Yavitt, P. Liberali, K. S. Anseth, and M. P. Lutolf (2022, January). Tissue geometry drives deterministic organoid patterning. *Science 375*(6576), eaaw9021.

[87] Gjorevski, N., N. Sachs, A. Manfrin, S. Giger, M. E. Bragina, P. Ordóñez-Morán, H. Clevers, and M. P. Lutolf (2016, November). Designer matrices for intestinal stem cell and organoid culture. *Nature 539*(7630), 560–564.

[88] Gregorieff, A. and H. Clevers (2005, April). Wnt signaling in the intestinal epithelium: From endoderm to cancer. *Genes Dev. 19*(8), 877–890.

[89] Grencis, R. K. (2015, March). Immunity to Helminths: Resistance, Regulation, and Susceptibility to Gastrointestinal Nematodes. *Annu. Rev. Immunol. 33*(1), 201–225.

[90] Gu, Y., T. Forostyan, R. Sabbadini, and J. Rosenblatt (2011, May). Epithelial cell extrusion requires the sphingosine-1-phosphate receptor 2 pathway. *Journal of Cell Biology 193*(4), 667–676.

[91] Gudipaty, S. A., J. Lindblom, P. D. Loftus, M. J. Redd, K. Edes, C. F. Davey, V. Krishne-gowda, and J. Rosenblatt (2017, March). Mechanical stretch triggers rapid epithelial cell division through Piezo1. *Nature 543*(7643), 118–121.

[92] Günther, C., E. Martini, N. Wittkopf, K. Amann, B. Weigmann, H. Neumann, M. J. Waldner, S. M. Hedrick, S. Tenzer, M. F. Neurath, and C. Becker (2011, September). Caspase-8 regulates TNF-α-induced epithelial necroptosis and terminal ileitis. *Nature 477*(7364), 335–339.

[93] Gustafsson, J. K., A. Ermund, D. Ambort, M. E. Johansson, H. E. Nilsson, K. Thorell, H. Hebert, H. Sjövall, and G. C. Hansson (2012, July). Bicarbonate and functional CFTR channel are required for proper mucin secretion and link cystic fibrosis with its mucus phenotype. *Journal of Experimental Medicine 209*(7), 1263–1272.

[94] Gustafsson, J. K. and M. E. V. Johansson (2022, December). The role of goblet cells and mucus in intestinal homeostasis. *Nat Rev Gastroenterol Hepatol 19*(12), 785–803.

[95] Haber, A. L., M. Biton, N. Rogel, R. H. Herbst, K. Shekhar, C. Smillie, G. Burgin, T. M. Delorey, M. R. Howitt, Y. Katz, I. Tirosh, S. Beyaz, D. Dionne, M. Zhang, R. Raychowdhury, W. S. Garrett, O. Rozenblatt-Rosen, H. N. Shi, O. Yilmaz, R. J. Xavier, and A. Regev (2017, November). A single-cell survey of the small intestinal epithelium. *Nature 551*(7680), 333–339.

[96] Haja, A., J. M. Horcas-Nieto, B. M. Bakker, and L. Schomaker (2023). Towards automatization of organoid analysis: A deep learning approach to localize and quantify organoid images. *Computer Methods and Programs in Biomedicine Update 3*, 100101.

[97] Hänninen, U. A., R. Katainen, T. Tanskanen, R.-M. Plaketti, R. Laine, J. Hamberg, A. Ristimäki, E. Pukkala, M. Taipale, J.-P. Mecklin, L. M. Forsström, E. Pitkänen, K. Palin, N. Välimäki, N. Mäkinen, and L. A. Aaltonen (2018, March). Exome-wide somatic mutation characterization of small bowel adenocarcinoma. *PLoS Genet 14*(3), e1007200.

[98] Hansen, A. K., C. H. F. Hansen, L. Krych, and D. S. Nielsen (2014, December). Impact of the gut microbiota on rodent models of human disease. *WJG 20*(47), 17727–17736.

[99] Haramis, A.-P. G., H. Begthel, M. Van Den Born, J. Van Es, S. Jonkheer, G. J. A. Offerhaus, and H. Clevers (2004, March). De Novo Crypt Formation and Juvenile Polyposis on BMP Inhibition in Mouse Intestine. *Science 303*(5664), 1684–1686.

[100] Hase, K., K. Kawano, T. Nochi, G. S. Pontes, S. Fukuda, M. Ebisawa, K. Kadokura, T. Tobe, Y. Fujimura, S. Kawano, A. Yabashi, S. Waguri, G. Nakato, S. Kimura, T. Murakami, M. Iimura, K. Hamura, S.-I. Fukuoka, A. W. Lowe, K. Itoh, H. Kiyono, and H. Ohno (2009, November). Uptake through glycoprotein 2 of FimH+ bacteria by M cells initiates mucosal immune response. *Nature 462*(7270), 226–230.

[101] Hase, K., S. Kimura, H. Takatsu, M. Ohmae, S. Kawano, H. Kitamura, M. Ito, H. Watarai, C. C. Hazelett, C. Yeaman, and H. Ohno (2009, December). M-Sec promotes membrane nanotube formation by interacting with Ral and the exocyst complex. *Nat Cell Biol 11*(12), 1427–1432.

[102] Hase, K., S. Ohshima, K. Kawano, N. Hashimoto, K. Matsumoto, H. Saito, and H. Ohno (2005, January). Distinct Gene Expression Profiles Characterize Cellular Phenotypes of Follicle-Associated Epithelium and M Cells. *DNA Research 12*(2), 127–137.

[103] Haubold, C., J. Aleš, S. Wolf, and F. A. Hamprecht (2016). A Generalized Successive Shortest Paths Solver for Tracking Dividing Targets. In B. Leibe, J. Matas, N. Sebe, and M. Welling (Eds.), *Computer Vision – ECCV 2016*, Volume 9911, pp. 566–582. Cham: Springer International Publishing.

[104] He, G.-W., L. Lin, J. DeMartino, X. Zheng, N. Staliarova, T. Dayton, H. Begthel, W. J. Van De Wetering, E. Bodewes, J. Van Zon, S. Tans, C. Lopez-Iglesias, P. J. Peters, W. Wu, D. Kotlarz, C. Klein, T. Margaritis, F. Holstege, and H. Clevers (2022, September). Optimized human intestinal organoid model reveals interleukin-22-dependency of paneth cell formation. *Cell Stem Cell 29*(9), 1333–1345.e6.

[105] He, L., G. Si, J. Huang, A. D. T. Samuel, and N. Perrimon (2018, March). Mechanical regulation of stem-cell differentiation by the stretch-activated Piezo channel. *Nature 555*(7694), 103–106.

[106] Helander, H. F. and L. Fändriks (2014, June). Surface area of the digestive tract – revisited. *Scandinavian Journal of Gastroenterology 49*(6), 681–689.

[107] Hendriks, D., B. Artegiani, H. Hu, S. Chuva De Sousa Lopes, and H. Clevers (2021, January). Establishment of human fetal hepatocyte organoids and CRISPR–Cas9-based gene knockin and knockout in organoid cultures from human liver. *Nat Protoc 16*(1), 182–217.

[108] Herbert, S., L. Valon, L. Mancini, N. Dray, P. Caldarelli, J. Gros, E. Esposito, S. L. Shorte, L. Bally-Cuif, N. Aulner, R. Levayer, and J.-Y. Tinevez (2021, December). LocalZProjector and DeProj: A toolbox for local 2D projection and accurate morphometrics of large 3D microscopy images. *BMC Biol 19*(1), 136.

[109] Hoey, T., W.-C. Yen, F. Axelrod, J. Basi, L. Donigian, S. Dylla, M. Fitch-Bruhns, S. Lazetic, I.-K. Park, A. Sato, S. Satyal, X. Wang, M. F. Clarke, J. Lewicki, and A. Gurney

(2009, August). DLL4 Blockade Inhibits Tumor Growth and Reduces Tumor-Initiating Cell Frequency. *Cell Stem Cell 5*(2), 168–177.

[110] Hormoz, S., Z. S. Singer, J. M. Linton, Y. E. Antebi, B. I. Shraiman, and M. B. Elowitz (2016, November). Inferring Cell-State Transition Dynamics from Lineage Trees and Endpoint Single-Cell Measurements. *Cell Systems 3*(5), 419–433.e8.

[111] Houtekamer, R. M., M. C. Van Der Net, M. M. Maurice, and M. Gloerich (2022, July). Mechanical forces directing intestinal form and function. *Current Biology 32*(14), R791–R805.

[112] Howitt, M. R., S. Lavoie, M. Michaud, A. M. Blum, S. V. Tran, J. V. Weinstock, C. A. Gallini, K. Redding, R. F. Margolskee, L. C. Osborne, D. Artis, and W. S. Garrett (2016, March). Tuft cells, taste-chemosensory cells, orchestrate parasite type 2 immunity in the gut. *Science 351*(6279), 1329–1333.

[113] Hsieh, E.-H. and D. D. Lo (2012, June). Jagged1 and Notch1 help edit M cell patterning in Peyer's patch follicle epithelium. *Developmental & Comparative Immunology 37*(2), 306–312.

[114] Huang, L., J. H. Bernink, A. Giladi, D. Krueger, G. J. F. Van Son, M. H. Geurts, G. Busslinger, L. Lin, H. Begthel, M. Zandvliet, C. J. Buskens, W. A. Bemelman, C. López-Iglesias, P. J. Peters, and H. Clevers (2024, October). Tuft cells act as regenerative stem cells in the human intestine. *Nature 634*(8035), 929–935.

[115] Huelsz-Prince, G., R. N. U. Kok, Y. Goos, L. Bruens, X. Zheng, S. Ellenbroek, J. Van Rheenen, S. Tans, and J. S. van Zon (2022, November). Mother cells control daughter cell proliferation in intestinal organoids to minimize proliferation fluctuations. *eLife 11*, e80682.

[116] Hunter, J. D. (2007). Matplotlib: A 2D Graphics Environment. *Computing in Science & Engineering 9*(3), 90–95.

[117] Ireland, H., C. Houghton, L. Howard, and D. J. Winton (2005, August). Cellular inheritance of a Cre-activated reporter gene to determine paneth cell longevity in the murine small intestine. *Developmental Dynamics 233*(4), 1332–1336.

[118] Ito, G., R. Okamoto, T. Murano, H. Shimizu, S. Fujii, T. Nakata, T. Mizutani, S. Yui, J. Akiyama-Morio, Y. Nemoto, E. Okada, A. Araki, K. Ohtsuka, K. Tsuchiya, T. Nakamura, and M. Watanabe (2013, November). Lineage-Specific Expression of Bestrophin-2 and Bestrophin-4 in Human Intestinal Epithelial Cells. *PLoS ONE 8*(11), e79693.

[119] Izquierdo, E., T. Quinkler, and S. De Renzis (2018, June). Guided morphogenesis through optogenetic activation of Rho signalling during early Drosophila embryogenesis. *Nat Commun 9*(1), 2366.

[120] Jho, E.-h., T. Zhang, C. Domon, C.-K. Joo, J.-N. Freund, and F. Costantini (2002). Wnt/Beta-Catenin/Tcf Signaling Induces the Transcription of Axin2, a Negative Regulator of the Signaling Pathway. *MOL. CELL. BIOL. 22*.

[121] Jiang, X., O. Charlat, R. Zamponi, Y. Yang, and F. Cong (2015, May). Dishevelled Promotes Wnt Receptor Degradation through Recruitment of ZNRF3/RNF43 E3 Ubiquitin Ligases. *Molecular Cell 58*(3), 522–533.

[122] Johansson, M. E. V. (2012, July). Fast Renewal of the Distal Colonic Mucus Layers by the Surface Goblet Cells as Measured by In Vivo Labeling of Mucin Glycoproteins. *PLoS ONE 7*(7), e41009.

[123] Johansson, M. E. V., J. K. Gustafsson, J. Holmén-Larsson, K. S. Jabbar, L. Xia, H. Xu, F. K. Ghishan, F. A. Carvalho, A. T. Gewirtz, H. Sjövall, and G. C. Hansson (2014, February). Bacteria penetrate the normally impenetrable inner colon mucus layer in both murine colitis models and patients with ulcerative colitis. *Gut 63*(2), 281–291.

[124] Johansson, M. E. V., J. K. Gustafsson, K. E. Sjöberg, J. Petersson, L. Holm, H. Sjövall, and G. C. Hansson (2010, August). Bacteria Penetrate the Inner Mucus Layer before Inflammation in the Dextran Sulfate Colitis Model. *PLoS ONE 5*(8), e12238.

[125] Johansson, M. E. V. and G. C. Hansson (2016, October). Immunological aspects of intestinal mucus and mucins. *Nat Rev Immunol 16*(10), 639–649.

[126] Kabiri, Z., G. Greicius, B. Madan, S. Biechele, Z. Zhong, H. Zaribafzadeh, Edison, J. Aliyev, Y. Wu, R. Bunte, B. O. Williams, J. Rossant, and D. M. Virshup (2014, June). Stroma provides an intestinal stem cell niche in the absence of epithelial Wnts. *Development 141*(11), 2206–2215.

[127] Kanaya, T., K. Hase, D. Takahashi, S. Fukuda, K. Hoshino, I. Sasaki, H. Hemmi, K. A. Knoop, N. Kumar, M. Sato, T. Katsuno, O. Yokosuka, K. Toyooka, K. Nakai, A. Sakamoto, Y. Kitahara, T. Jinnohara, S. J. McSorley, T. Kaisho, I. R. Williams, and H. Ohno (2012, August). The Ets transcription factor Spi-B is essential for the differentiation of intestinal microfold cells. *Nat Immunol 13*(8), 729–736.

[128] Kanaya, T., S. Sakakibara, T. Jinnohara, M. Hachisuka, N. Tachibana, S. Hidano, T. Kobayashi, S. Kimura, T. Iwanaga, T. Nakagawa, T. Katsuno, N. Kato, T. Akiyama, T. Sato, I. R. Williams, and H. Ohno (2018, February). Development of intestinal M cells and follicle-associated epithelium is regulated by TRAF6-mediated NF-kappaB signaling. *Journal of Experimental Medicine 215*(2), 501–519.

[129] Kelsall, M. A. (1946, April). Number of Peyer's Patches in Mice Belonging to High and Low Mammary Tumor Strains. *Experimental Biology and Medicine 61*(4), 423–427.

[130] Keshara, R., Y. H. Kim, and A. Grapin-Botton (2022, October). Organoid Imaging: Seeing Development and Function. *Annu. Rev. Cell Dev. Biol. 38*(1), 447–466.

[131] Kiecker, C. and C. Niehrs (2001, November). A morphogen gradient of Wnt/β-catenin signalling regulates anteroposterior neural patterning in *Xenopus*. *Development 128*(21), 4189–4201.

[132] Kim, M., M. Ogawa, Y. Fujita, Y. Yoshikawa, T. Nagai, T. Koyama, S. Nagai, A. Lange, R. Fässler, and C. Sasakawa (2009, May). Bacteria hijack integrin-linked kinase to stabilize focal adhesions and block cell detachment. *Nature 459*(7246), 578–582.

[133] Kim, T.-H., S. Escudero, and R. A. Shivdasani (2012, March). Intact function of Lgr5 receptor-expressing intestinal stem cells in the absence of Paneth cells. *Proc. Natl. Acad. Sci. U.S.A. 109*(10), 3932–3937.

[134] Kimura, S., N. Kobayashi, Y. Nakamura, T. Kanaya, D. Takahashi, R. Fujiki, M. Mutoh, Y. Obata, T. Iwanaga, T. Nakagawa, N. Kato, S. Sato, T. Kaisho, H. Ohno, and K. Hase (2019, April). Sox8 is essential for M cell maturation to accelerate IgA response at the early stage after weaning in mice. *Journal of Experimental Medicine 216*(4), 831–846.

[135] Kimura, S., Y. Nakamura, N. Kobayashi, K. Shiroguchi, E. Kawakami, M. Mutoh, H. Takahashi-Iwanaga, T. Yamada, M. Hisamoto, M. Nakamura, N. Udagawa, S. Sato, T. Kaisho, T. Iwanaga, and K. Hase (2020, December). Osteoprotegerin-dependent M cell self-regulation balances gut infection and immunity. *Nat Commun 11*(1), 234.

[136] Kingma, D. P. and J. Ba (2017, January). Adam: A Method for Stochastic Optimization.

[137] Kishi, J. Y., N. Liu, E. R. West, K. Sheng, J. J. Jordanides, M. Serrata, C. L. Cepko, S. K. Saka, and P. Yin (2022, November). Light-Seq: Light-directed in situ barcoding of biomolecules in fixed cells and tissues for spatially indexed sequencing. *Nat Methods 19*(11), 1393–1402.

[138] Klein, J. P., B. Logan, M. Harhoff, and P. K. Andersen (2007, October). Analyzing survival curves at a fixed point in time. *Statistics in Medicine 26*(24), 4505–4519.

[139] Knoop, K. A., N. Kumar, B. R. Butler, S. K. Sakthivel, R. T. Taylor, T. Nochi, H. Akiba, H. Yagita, H. Kiyono, and I. R. Williams (2009, November). RANKL Is Necessary and Sufficient to Initiate Development of Antigen-Sampling M Cells in the Intestinal Epithelium. *J Immunol 183*(9), 5738–5747.

[140] Kobayashi, A., D. S. Donaldson, C. Erridge, T. Kanaya, I. R. Williams, H. Ohno, A. Mahajan, and N. A. Mabbott (2013, September). The functional maturation of M cells is dramatically reduced in the Peyer's patches of aged mice. *Mucosal Immunol 6*(5), 1027–1037.

[141] Kok, R. N., W. K. Spoelstra, M. A. Betjes, J. S. Van Zon, and S. J. Tans (2025, April). Label-free cell imaging and tracking in 3D organoids. *Cell Reports Physical Science 6*(102522).

[142] Kok, R. N., X. Zheng, T. Clement, W. K. Spoelstra, H. Clevers, R. Amerongen, S. J. Tans, and J. S. Van Zon. Loss of Paneth cell contact starts a Wnt differentiation timer in the intestinal crypt. *in preparation.*

[143] Kok, R. N. U., L. Hebert, G. Huelsz-Prince, Y. J. Goos, X. Zheng, K. Bozek, G. J. Stephens, S. J. Tans, and J. S. van Zon (2020, October). OrganoidTracker: Efficient cell tracking using machine learning and manual error correction. *PLoS ONE 15*(10), e0240802.

[144] Kok, R. N. U., S. J. Tans, and J. S. van Zon (2023). Minimizing cell number fluctuations in self-renewing tissues with a stem cell niche. *Physical Review E 108*(064403).

[145] Kondo, S. and T. Miura (2010, September). Reaction-Diffusion Model as a Framework for Understanding Biological Pattern Formation. *Science 329*(5999), 1616–1620.

[146] Kosinski, C., V. S. W. Li, A. S. Y. Chan, J. Zhang, C. Ho, W. Y. Tsui, T. L. Chan, R. C. Mifflin, D. W. Powell, S. T. Yuen, S. Y. Leung, and X. Chen (2007, September). Gene expression patterns of human colon tops and basal crypts and BMP antagonists as intestinal stem cell niche factors. *Proc. Natl. Acad. Sci. U.S.A. 104*(39), 15418–15423.

[147] Krens, S. F. and C.-P. Heisenberg (2011). Cell Sorting in Development. In *Current Topics in Developmental Biology*, Volume 95, pp. 189–213. Elsevier.

[148] Kretzschmar, K. and F. M. Watt (2012, January). Lineage Tracing. *Cell 148*(1-2), 33–45.

[149] Krndija, D., F. El Marjou, B. Guirao, S. Richon, O. Leroy, Y. Bellaiche, E. Hannezo, and D. Matic Vignjevic (2019, August). Active cell migration is critical for steady-state epithelial turnover in the gut. *Science 365*(6454), 705–710.

[150] Krueger, D., W. K. Spoelstra, D. J. Mastebroek, R. N. U. Kok, S. Wu, M. Nikolaev, M. Bannier-Hélaouët, N. Gjorevski, M. Lutolf, J. Van Es, J. Van Zon, S. J. Tans, and H. Clevers (2025, September). Epithelial tension controls intestinal cell extrusion. *Science 389*(6764), eadr8753.

[151] Krzic, U., S. Gunther, T. E. Saunders, S. J. Streichan, and L. Hufnagel (2012, July). Multiview light-sheet microscope for rapid in toto imaging. *Nat Methods 9*(7), 730–733.

[152] La Manno, G., R. Soldatov, A. Zeisel, E. Braun, H. Hochgerner, V. Petukhov, K. Lidschreiber, M. E. Kastriti, P. Lönnerberg, A. Furlan, J. Fan, L. E. Borm, Z. Liu, D. van Bruggen, J. Guo, X. He, R. Barker, E. Sundström, G. Castelo-Branco, P. Cramer, I. Adameyko, S. Linnarsson, and P. V. Kharchenko (2018, August). RNA velocity of single cells. *Nature 560*(7719), 494–498.

[153] Ladoux, B. and R.-M. Mège (2017, December). Mechanobiology of collective cell behaviours. *Nat Rev Mol Cell Biol 18*(12), 743–757.

[154] Lai, N. Y., M. A. Musser, F. A. Pinho-Ribeiro, P. Baral, A. Jacobson, P. Ma, D. E. Potts, Z. Chen, D. Paik, S. Soualhi, Y. Yan, A. Misra, K. Goldstein, V. N. Lagomarsino, A. Nordstrom, K. N. Sivanathan, A. Wallrapp, V. K. Kuchroo, R. Nowarski, M. N. Starnbach, H. Shi, N. K. Surana, D. An, C. Wu, J. R. Huh, M. Rao, and I. M. Chiu (2020, January). Gut-Innervating Nociceptor Neurons Regulate Peyer's Patch Microfold Cells and SFB Levels to Mediate Salmonella Host Defense. *Cell 180*(1), 33–49.e22.

[155] Lemke, S. B. and C. M. Nelson (2021, September). Dynamic changes in epithelial cell packing during tissue morphogenesis. *Current Biology 31*(18), R1098–R1110.

[156] Levayer, R., C. Dupont, and E. Moreno (2016, March). Tissue Crowding Induces Caspase-Dependent Competition for Space. *Current Biology 26*(5), 670–677.

[157] Levine, M. S. and A. J. Holland (2018, May). The impact of mitotic errors on cell proliferation and tumorigenesis. *Genes Dev. 32*(9-10), 620–638.

[158] Li, H., X. Wang, Y. Wang, M. Zhang, F. Hong, H. Wang, A. Cui, J. Zhao, W. Ji, and Y.-G. Chen (2022). Cross-species single-cell transcriptomic analysis reveals divergence of cell composition and functions in mammalian ileum epithelium.pdf.

[159] Lin, L., J. DeMartino, D. Wang, G. J. F. Van Son, R. Van Der Linden, H. Begthel, J. Korving, A. Andersson-Rolf, S. Van Den Brink, C. Lopez-Iglesias, W. J. Van De Wetering, A. Balwierz, T. Margaritis, M. Van De Wetering, P. J. Peters, J. Drost, J. H. Van Es, and H. Clevers (2023, October). Unbiased transcription factor CRISPR screen identifies ZNF800 as master repressor of enteroendocrine differentiation. *Science 382*(6669), 451–458.

[160] Liu, J., N. M. Walker, A. Ootani, A. M. Strubberg, and L. L. Clarke (2015, March). Defective goblet cell exocytosis contributes to murine cystic fibrosis–associated intestinal disease. *J. Clin. Invest. 125*(3), 1056–1068.

[161] Lorenzo-Martín, L. F., N. Broguiere, J. Langer, L. Tillard, M. Nikolaev, G. Coukos, K. Homicsko, and M. P. Lutolf (2024, July). Patient-derived mini-colons enable long-term modeling of tumor–microenvironment complexity. *Nat Biotechnol*.

[162] Lorenzo-Martín, L. F., T. Hübscher, A. D. Bowler, N. Broguiere, J. Langer, L. Tillard, M. Nikolaev, F. Radtke, and M. P. Lutolf (2024, April). Spatiotemporally resolved colorectal oncogenesis in mini-colons ex vivo. *Nature*.

[163] Lustig, B., B. Jerchow, M. Sachs, S. Weiler, T. Pietsch, U. Karsten, M. Van De Wetering, H. Clevers, P. M. Schlag, W. Birchmeier, and J. Behrens (2002, February). Negative Feedback Loop of Wnt Signaling through Upregulation of Conductin/Axin2 in Colorectal and Liver Tumors. *Molecular and Cellular Biology 22*(4), 1184–1193.

[164] Ma, Y., J. Yue, Y. Zhang, C. Shi, M. Odenwald, W. G. Liang, Q. Wei, A. Goel, X. Gou, J. Zhang, S.-Y. Chen, W.-J. Tang, J. R. Turner, F. Yang, H. Liang, H. Qin, and X. Wu (2017, May). ACF7 regulates inflammatory colitis and intestinal wound response by orchestrating tight junction dynamics. *Nat Commun 8*(1), 15375.

[165] Maghzal, N., H. A. Kayali, N. Rohani, A. V. Kajava, and F. Fagotto (2013, November). EpCAM Controls Actomyosin Contractility and Cell Adhesion by Direct Inhibition of PKC. *Developmental Cell 27*(3), 263–277.

[166] Magney, J. E., S. L. Erlandsen, M. L. Bjerknes, and H. Cheng (1986, September). Scanning electron microscopy of isolated epithelium of the murine gastrointestinal tract: Morphology of the basal surface and evidence for paracrinelike cells. *Am. J. Anat. 177*(1), 43–53.

[167] Maître, J.-L., H. Turlier, R. Illukkumbura, B. Eismann, R. Niwayama, F. Nédélec, and T. Hiiragi (2016, August). Asymmetric division of contractile domains couples cell positioning and fate specification. *Nature 536*(7616), 344–348.

[168] Malagola, E., A. Vasciaveo, Y. Ochiai, W. Kim, B. Zheng, L. Zanella, A. L. Wang, M. Middelhoff, H. Nienhüser, L. Deng, F. Wu, Q. T. Waterbury, B. Belin, J. LaBella, L. B. Zamechek, M. H. Wong, L. Li, C. Guha, C.-W. Cheng, K. S. Yan, A. Califano, and T. C.

Wang (2024, June). Isthmus progenitor cells contribute to homeostatic cellular turnover and support regeneration following intestinal injury. *Cell 187*(12), 3056–3071.e17.

[169] Malin-Mayor, C., P. Hirsch, L. Guignard, K. McDole, Y. Wan, W. C. Lemon, D. Kainmueller, P. J. Keller, S. Preibisch, and J. Funke (2023, January). Automated reconstruction of whole-embryo cell lineages by learning from sparse annotations. *Nat Biotechnol 41*(1), 44–49.

[170] Malonga, T., N. Vialaneix, and M. Beaumont (2024, May). BEST4+ cells in the intestinal epithelium. *American Journal of Physiology-Cell Physiology 326*(5), C1345–C1352.

[171] Marinari, E., A. Mehonic, S. Curran, J. Gale, T. Duke, and B. Baum (2012, April). Live-cell delamination counterbalances epithelial growth to limit tissue overcrowding. *Nature 484*(7395), 542–545.

[172] Marshall, T. W., I. E. Lloyd, J. M. Delalande, I. Näthke, and J. Rosenblatt (2011, November). The tumor suppressor adenomatous polyposis coli controls the direction in which a cell extrudes from an epithelium. *MBoC 22*(21), 3962–3970.

[173] Martin, A. C., M. Kaschube, and E. F. Wieschaus (2009, January). Pulsed contractions of an actin–myosin network drive apical constriction. *Nature 457*(7228), 495–499.

[174] Martínez-Sánchez, L. D. C., P. A. Ngo, R. Pradhan, L.-S. Becker, D. Boehringer, D. Soteriou, M. Kubankova, C. Schweitzer, T. Koch, V. Thonn, L. Erkert, I. Stolzer, C. Günther, C. Becker, B. Weigmann, M. Klewer, C. Daniel, K. Amann, S. Tenzer, R. Atreya, M. Bergo, C. Brakebusch, A. J. M. Watson, J. Guck, B. Fabry, I. Atreya, M. F. Neurath, and R. López-Posadas (2023, February). Epithelial RAC1-dependent cytoskeleton dynamics controls cell mechanics, cell shedding and barrier integrity in intestinal inflammation. *Gut 72*(2), 275–294.

[175] Massimino, L., L. A. Lamparelli, Y. Houshyar, S. D'Alessio, L. Peyrin-Biroulet, S. Vetrano, S. Danese, and F. Ungaro (2021, August). The Inflammatory Bowel Disease Transcriptome and Metatranscriptome Meta-Analysis (IBD TaMMA) framework. *Nat Comput Sci 1*(8), 511–515.

[176] Matsushita, T., H. Hayashi, S. Kunishima, M. Hayashi, M. Ikejiri, K. Takeshita, Y. Yuzawa, T. Adachi, K. Hirashima, M. Sone, K. Yamamoto, A. Takagi, A. Katsumi, K. Kawai, T. Nezu, M. Takahashi, T. Nakashima, T. Naoe, T. Kojima, and H. Saito (2004, December). Targeted disruption of mouse ortholog of the human MYH9 responsible for macrothrombocytopenia with different organ involvement: Hematological, nephrological, and otological studies of heterozygous KO mice. *Biochemical and Biophysical Research Communications 325*(4), 1163–1171.

[177] Matthews, J. M., B. Schuster, S. S. Kashaf, P. Liu, R. Ben-Yishay, D. Ishay-Ronen, E. Izumchenko, L. Shen, C. R. Weber, M. Bielski, S. S. Kupfer, M. Bilgic, A. Rzhetsky, and S. Tay (2022, November). OrganoID: A versatile deep learning platform for tracking and analysis of single-organoid dynamics. *PLoS Comput Biol 18*(11), e1010584.

[178] McDole, K., L. Guignard, F. Amat, A. Berger, G. Malandain, L. A. Royer, S. C. Turaga, K. Branson, and P. J. Keller (2018, October). In Toto Imaging and Reconstruction of Post-Implantation Mouse Development at the Single-Cell Level. *Cell 175*(3), 859–876.e33.

[179] Mehta, S., S. Hingole, and V. Chaudhary (2021, August). The Emerging Mechanisms of Wnt Secretion and Signaling in Development. *Front. Cell Dev. Biol. 9*, 714746.

[180] Meijer, W. H. and K. F. Sonnen (2024, December). From signalling oscillations to somite formation. *Current Opinion in Systems Biology 39*, 100520.

[181] Meng, F., C. Shen, L. Yang, C. Ni, J. Huang, K. Lin, Z. Cao, S. Xu, W. Cui, X. Wang, B. Zhou, C. Xiong, J. Wang, and B. Zhao (2022, November). Mechanical stretching boosts expansion and regeneration of intestinal organoids through fueling stem cell self-renewal. *Cell Regen 11*(1), 39.

[182] Messal, H. A., S. Alt, R. M. M. Ferreira, C. Gribben, V. M.-Y. Wang, C. G. Cotoi, G. Salbreux, and A. Behrens (2019, February). Tissue curvature and apicobasal mechanical tension imbalance instruct cancer morphogenesis. *Nature 566*(7742), 126–130.

[183] Michel, M. and C. Dahmann (2020, March). Tissue mechanical properties modulate cell extrusion in the *Drosophila* abdominal epidermis. *Development 147*(5), dev179606.

[184] Mitrofanova, O., M. Nikolaev, Q. Xu, N. Broguiere, I. Cubela, J. G. Camp, M. Bscheider, and M. P. Lutolf (2024, August). Bioengineered human colon organoids with in vivo-like cellular complexity and function. *Cell Stem Cell 31*(8), 1175–1186.e7.

[185] Montes-Olivas, S., D. Legge, A. Lund, A. G. Fletcher, A. C. Williams, L. Marucci, and M. Homer (2023, August). In-silico and in-vitro morphometric analysis of intestinal organoids. *PLoS Comput Biol 19*(8), e1011386.

[186] Moor, A. E., Y. Harnik, S. Ben-Moshe, E. E. Massasa, M. Rozenberg, R. Eilam, K. Bahar Halpern, and S. Itzkovitz (2018, November). Spatial Reconstruction of Single Enterocytes Uncovers Broad Zonation along the Intestinal Villus Axis. *Cell 175*(4), 1156–1167.e15.

[187] Moosdijk, A. A. A., Y. B. C. Grift, S. M. A. Man, A. L. Zeeman, and R. Amerongen (2020, September). A novel *Axin2* knock-in mouse model for visualization and lineage tracing of WNT / CTNNB1 responsive cells. *genesis 58*(9).

[188] Mueller, J. L., M. D. McGeough, C. A. Peña, and M. Sivagnanam (2014, February). Functional consequences of *EpCam* mutation in mice and men. *American Journal of Physiology-Gastrointestinal and Liver Physiology 306*(4), G278–G288.

[189] Muenzner, P., M. Rohde, S. Kneitz, and C. R. Hauck (2005, August). CEACAM engagement by human pathogens enhances cell adhesion and counteracts bacteria-induced detachment of epithelial cells. *The Journal of Cell Biology 170*(5), 825–836.

[190] Muñoz, J., D. E. Stange, A. G. Schepers, M. Van De Wetering, B.-K. Koo, S. Itzkovitz, R. Volckmann, K. S. Kung, J. Koster, S. Radulescu, K. Myant, R. Versteeg, O. J. Sansom, J. H. Van Es, N. Barker, A. Van Oudenaarden, S. Mohammed, A. J. R. Heck, and H. Clevers

(2012, July). The Lgr5 intestinal stem cell signature: Robust expression of proposed quiescent '+4' cell markers: Transcriptomic and proteomic signature of Lgr5 $^+$ stem cells. *The EMBO Journal 31*(14), 3079–3091.

[191] Murata, K., U. Jadhav, S. Madha, J. Van Es, J. Dean, A. Cavazza, K. Wucherpfennig, F. Michor, H. Clevers, and R. A. Shivdasani (2020, March). Ascl2-Dependent Cell Dedifferentiation Drives Regeneration of Ablated Intestinal Stem Cells. *Cell Stem Cell 26*(3), 377–390.e6.

[192] Nagashima, K., S. Sawa, T. Nitta, M. Tsutsumi, T. Okamura, J. M. Penninger, T. Nakashima, and H. Takayanagi (2017, June). Identification of subepithelial mesenchymal cells that induce IgA and diversify gut microbiota. *Nat Immunol 18*(6), 675–682.

[193] Nakata, T., H. Shimizu, S. Nagata, G. Ito, S. Fujii, K. Suzuki, A. Kawamoto, F. Ishibashi, R. Kuno, S. Anzai, T. Murano, T. Mizutani, S. Oshima, K. Tsuchiya, T. Nakamura, K. Hozumi, M. Watanabe, and R. Okamoto (2017, February). Data showing proliferation and differentiation of intestinal epithelial cells under targeted depletion of Notch ligands in mouse intestine. *Data in Brief 10*, 551–556.

[194] Naydenov, N. G., A. Feygin, D. Wang, J. F. Kuemmerle, G. Harris, M. A. Conti, R. S. Adelstein, and A. I. Ivanov (2016, April). Nonmuscle Myosin IIA Regulates Intestinal Epithelial Barrier in vivo and Plays a Protective Role During Experimental Colitis. *Sci Rep 6*(1), 24161.

[195] Nguyen, N. T. B., S. Gevers, R. N. U. Kok, L. M. Burgering, H. Neikes, N. Akkerman, M. A. Betjes, M. C. Ludikhuize, C. Gulersonmez, E. C. A. Stigter, Y. Vercoulen, J. Drost, H. C. Clevers, M. Vermeulen, J. S. van Zon, S. J. Tans, B. M. T. Burgering, and R. Colman (2025). Lactate controls cancer stemness and plasticity through epigenetic regulation. *Cell Metabolism 37*, 1–17.

[196] Nikolaev, M., O. Mitrofanova, N. Broguiere, S. Geraldo, D. Dutta, Y. Tabata, B. Elci, N. Brandenberg, I. Kolotuev, N. Gjorevski, H. Clevers, and M. P. Lutolf (2020, September). Homeostatic mini-intestines through scaffold-guided organoid morphogenesis. *Nature 585*(7826), 574–578.

[197] Noah, T. K. and N. F. Shroyer (2013, February). Notch in the Intestine: Regulation of Homeostasis and Pathogenesis. *Annu. Rev. Physiol. 75*(1), 263–288.

[198] Nordström, U., T. M. Jessell, and T. Edlund (2002, June). Progressive induction of caudal neural character by graded Wnt signaling. *Nat Neurosci 5*(6), 525–532.

[199] Nusse, R. and H. Clevers (2017, June). Wnt/β-Catenin Signaling, Disease, and Emerging Therapeutic Modalities. *Cell 169*(6), 985–999.

[200] Nyga, A., S. Ganguli, H. K. Matthews, and B. Baum (2023, January). The role of RAS oncogenes in controlling epithelial mechanics. *Trends in Cell Biology 33*(1), 60–69.

[201] Nyström, E. E. L., B. Martinez-Abad, L. Arike, G. M. H. Birchenough, E. B. Nonnecke, P. A. Castillo, F. Svensson, C. L. Bevins, G. C. Hansson, and M. E. V. Johansson (2021,

April). An intercrypt subpopulation of goblet cells is essential for colonic mucus barrier function. *Science 372*(6539), eabb1590.

[202] Obata, Y., S. Kimura, G. Nakato, K. Iizuka, Y. Miyagawa, Y. Nakamura, Y. Furusawa, M. Sugiyama, K. Suzuki, M. Ebisawa, Y. Fujimura, H. Yoshida, T. Iwanaga, K. Hase, and H. Ohno (2014, December). Epithelial–stromal interaction via Notch signaling is essential for the full maturation of gut-associated lymphoid tissues. *EMBO Reports 15*(12), 1297–1304.

[203] Ouchi, T., S. Morimura, L. E. Dow, H. Miyoshi, and M. C. Udey (2021, January). Ep-CAM (CD326) Regulates Intestinal Epithelial Integrity and Stem Cells via Rho-Associated Kinase. *Cells 10*(2), 256.

[204] Ounkomol, C., S. Seshamani, M. M. Maleckar, F. Collman, and G. R. Johnson (2018, November). Label-free prediction of three-dimensional fluorescence images from transmitted-light microscopy. *Nat Methods 15*(11), 917–920.

[205] Parikh, K., A. Antanaviciute, D. Fawkner-Corbett, M. Jagielowicz, A. Aulicino, C. Lagerholm, S. Davis, J. Kinchen, H. H. Chen, N. K. Alham, N. Ashley, E. Johnson, P. Hublitz, L. Bao, J. Lukomska, R. S. Andev, E. Björklund, B. M. Kessler, R. Fischer, R. Goldin, H. Koohy, and A. Simmons (2019, March). Colonic epithelial cell diversity in health and inflammatory bowel disease. *Nature 567*(7746), 49–55.

[206] Patil, G. and J. S. Van Zon (2024, April). Timers, variability, and body-wide coordination: C. elegans as a model system for whole-animal developmental timing. *Current Opinion in Genetics & Development 85*, 102172.

[207] Pellegrinet, L., V. Rodilla, Z. Liu, S. Chen, U. Koch, L. Espinosa, K. H. Kaestner, R. Kopan, J. Lewis, and F. Radtke (2011). Dll1- and Dll4-Mediated Notch Signaling Are Required for Homeostasis of Intestinal Stem Cells. *Gastroenterology 140*, 1230–1240.

[208] Pérez-González, C., G. Ceada, F. Greco, M. Matejčić, M. Gómez-González, N. Castro, A. Menendez, S. Kale, D. Krndija, A. G. Clark, V. R. Gannavarapu, A. Álvarez-Varela, P. Roca-Cusachs, E. Batlle, D. M. Vignjevic, M. Arroyo, and X. Trepat (2021, July). Mechanical compartmentalization of the intestinal organoid enables crypt folding and collective cell migration. *Nat Cell Biol 23*(7), 745–757.

[209] Pérez-González, C., G. Ceada, M. Matejčić, and X. Trepat (2022, February). Digesting the mechanobiology of the intestinal epithelium. *Current Opinion in Genetics & Development 72*, 82–90.

[210] Pleguezuelos-Manzano, C., J. Puschhof, S. Van Den Brink, V. Geurts, J. Beumer, and H. Clevers (2020, September). Establishment and Culture of Human Intestinal Organoids Derived from Adult Stem Cells. *CP in Immunology 130*(1), e106.

[211] Popkova, A., O. J. Stone, L. Chen, X. Qin, C. Liu, J. Liu, K. Belguise, D. J. Montell, K. M. Hahn, M. Rauzi, and X. Wang (2020, April). A Cdc42-mediated supracellular network drives polarized forces and Drosophila egg chamber extension. *Nat Commun 11*(1), 1921.

[212] Prados, A., L. Onder, H.-W. Cheng, U. Mörbe, M. Lütge, C. Gil-Cruz, C. Perez-Shibayama, V. Koliaraki, B. Ludewig, and G. Kollias (2021, April). Fibroblastic reticular cell lineage convergence in Peyer's patches governs intestinal immunity. *Nat Immunol 22*(4), 510–519.

[213] Pritchard, D. M., C. S. Potten, S. J. Korsmeyer, S. Roberts, and J. A. Hickman (1999, December). Damage-induced apoptosis in intestinal epithelia from bcl-2-null and bax-null mice: Investigations of the mechanistic determinants of epithelial apoptosis in vivo. *Oncogene 18*(51), 7287–7293.

[214] Pritchard, D. M., C. Print, L. O'Reilly, J. M. Adams, C. S. Potten, and J. A. Hickman (2000, August). Bcl-w is an important determinant of damage-induced apoptosis in epithelia of small and large intestine. *Oncogene 19*(34), 3955–3959.

[215] Priya, R., S. Allanki, A. Gentile, S. Mansingh, V. Uribe, H.-M. Maischein, and D. Y. R. Stainier (2020, December). Tension heterogeneity directs form and fate to pattern the myocardial wall. *Nature 588*(7836), 130–134.

[216] Puschhof, J., C. Pleguezuelos-Manzano, A. Martinez-Silgado, N. Akkerman, A. Saftien, C. Boot, A. de Waal, J. Beumer, D. Dutta, I. Heo, and H. Clevers (2021, October). Intestinal organoid cocultures with microbes. *Nat Protoc 16*(10), 4633–4649.

[217] Randriamanantsoa, S., A. Papargyriou, H. C. Maurer, K. Peschke, M. Schuster, G. Zecchin, K. Steiger, R. Öllinger, D. Saur, C. Scheel, R. Rad, E. Hannezo, M. Reichert, and A. R. Bausch (2022, September). Spatiotemporal dynamics of self-organized branching in pancreas-derived organoids. *Nat Commun 13*(1), 5219.

[218] Rauzi, M., P. Verant, T. Lecuit, and P.-F. Lenne (2008, December). Nature and anisotropy of cortical forces orienting Drosophila tissue morphogenesis. *Nat Cell Biol 10*(12), 1401–1410.

[219] Rensing, L., U. Meyer-Grahle, and P. Ruoff (2001, January). BIOLOGICAL TIMING AND THE CLOCK METAPHOR: OSCILLATORY AND HOURGLASS MECHANISMS. *Chronobiology International 18*(3), 329–369.

[220] Rey, C., Y.-Y. Chang, P. Latour-Lambert, H. Varet, C. Proux, R. Legendre, J.-Y. Coppée, and J. Enninga (2020, April). Transcytosis subversion by M cell-to-enterocyte spread promotes Shigella flexneri and Listeria monocytogenes intracellular bacterial dissemination. *PLoS Pathog 16*(4), e1008446.

[221] Rhee, H.-W., P. Zou, N. D. Udeshi, J. D. Martell, V. K. Mootha, S. A. Carr, and A. Y. Ting (2013, March). Proteomic Mapping of Mitochondria in Living Cells via Spatially Restricted Enzymatic Tagging. *Science 339*(6125), 1328–1331.

[222] Rios, D., M. B. Wood, J. Li, B. Chassaing, A. T. Gewirtz, and I. R. Williams (2016, July). Antigen sampling by intestinal M cells is the principal pathway initiating mucosal IgA production to commensal enteric bacteria. *Mucosal Immunol 9*(4), 907–916.

[223] Ritsma, L., E. J. A. Steller, S. I. J. Ellenbroek, O. Kranenburg, I. H. M. Borel Rinkes, and J. van Rheenen (2013, March). Surgical implantation of an abdominal imaging window for intravital microscopy. *Nat Protoc 8*(3), 583–594.

[224] Rogers, K. W. and A. F. Schier (2011, November). Morphogen Gradients: From Generation to Interpretation. *Annu. Rev. Cell Dev. Biol. 27*(1), 377–407.

[225] Ronneberger, O., P. Fischer, and T. Brox (2015). U-Net: Convolutional Networks for Biomedical Image Segmentation. In N. Navab, J. Hornegger, W. M. Wells, and A. F. Frangi (Eds.), *Medical Image Computing and Computer-Assisted Intervention – MICCAI 2015*, Volume 9351, pp. 234–241. Cham: Springer International Publishing.

[226] Rouch, J. D., A. Scott, N. Y. Lei, R. S. Solorzano-Vargas, J. Wang, E. M. Hanson, M. Kobayashi, M. Lewis, M. G. Stelzner, J. C. Y. Dunn, L. Eckmann, and M. G. Martín (2016, January). Development of Functional Microfold (M) Cells from Intestinal Stem Cells in Primary Human Enteroids. *PLoS ONE 11*(1), e0148216.

[227] Royston, P. and M. K. Parmar (2013, December). Restricted mean survival time: An alternative to the hazard ratio for the design and analysis of randomized trials with a time-to-event outcome. *BMC Med Res Methodol 13*(1), 152.

[228] Rueden, C. T., J. Schindelin, M. C. Hiner, B. E. DeZonia, A. E. Walter, E. T. Arena, and K. W. Eliceiri (2017, December). ImageJ2: ImageJ for the next generation of scientific image data. *BMC Bioinformatics 18*(1), 529.

[229] Sachs, N., A. Papaspyropoulos, D. D. Zomer-van Ommen, I. Heo, L. Böttinger, D. Klay, F. Weeber, G. Huelsz-Prince, N. Iakobachvili, G. D. Amatngalim, J. De Ligt, A. Van Hoeck, N. Proost, M. C. Viveen, A. Lyubimova, L. Teeven, S. Derakhshan, J. Korving, H. Begthel, J. F. Dekkers, K. Kumawat, E. Ramos, M. F. Van Oosterhout, G. J. Offerhaus, D. J. Wiener, E. P. Olimpio, K. K. Dijkstra, E. F. Smit, M. Van Der Linden, S. Jaksani, M. Van De Ven, J. Jonkers, A. C. Rios, E. E. Voest, C. H. Van Moorsel, C. K. Van Der Ent, E. Cuppen, A. Van Oudenaarden, F. E. Coenjaerts, L. Meyaard, L. J. Bont, P. J. Peters, S. J. Tans, J. S. Van Zon, S. F. Boj, R. G. Vries, J. M. Beekman, and H. Clevers (2019, February). Long-term expanding human airway organoids for disease modeling. *The EMBO Journal 38*(4), e100300.

[230] Saelens, W., R. Cannoodt, H. Todorov, and Y. Saeys (2019, May). A comparison of single-cell trajectory inference methods. *Nat Biotechnol 37*(5), 547–554.

[231] Sanman, L. E., I. W. Chen, J. M. Bieber, V. Steri, C. Trentesaux, B. Hann, O. D. Klein, L. F. Wu, and S. J. Altschuler (2021, February). Transit-Amplifying Cells Coordinate Changes in Intestinal Epithelial Cell-Type Composition. *Developmental Cell 56*(3), 356–365.e9.

[232] Sasaki, N., N. Sachs, K. Wiebrands, S. I. J. Ellenbroek, A. Fumagalli, A. Lyubimova, H. Begthel, M. Van Den Born, J. H. Van Es, W. R. Karthaus, V. S. W. Li, C. López-Iglesias, P. J. Peters, J. Van Rheenen, A. Van Oudenaarden, and H. Clevers (2016, September). Reg4+ deep crypt secretory cells function as epithelial niche for Lgr5+ stem cells in colon. *Proc. Natl. Acad. Sci. U.S.A. 113*(37).

[233] Sato, T., D. E. Stange, M. Ferrante, R. G. Vries, J. H. van Es, S. van den Brink, W. J. van Houdt, A. Pronk, J. van Gorp, P. D. Siersema, and H. Clevers (2011, November). Long-term Expansion of Epithelial Organoids From Human Colon, Adenoma, Adenocarcinoma, and Barrett's Epithelium. *Gastroenterology 141*(5), 1762–1772.

[234] Sato, T., J. H. van Es, H. J. Snippert, D. E. Stange, R. G. Vries, M. van den Born, N. Barker, N. F. Shroyer, M. van de Wetering, and H. Clevers (2011, January). Paneth cells constitute the niche for Lgr5 stem cells in intestinal crypts. *Nature 469*(7330), 415–418.

[235] Sato, T., R. G. Vries, H. J. Snippert, M. van de Wetering, N. Barker, D. E. Stange, J. H. van Es, A. Abo, P. Kujala, P. J. Peters, and H. Clevers (2009, May). Single Lgr5 stem cells build crypt-villus structures in vitro without a mesenchymal niche. *Nature 459*(7244), 262–265.

[236] Schepers, A. G., R. Vries, M. van den Born, M. van de Wetering, and H. Clevers (2011, March). Lgr5 intestinal stem cells have high telomerase activity and randomly segregate their chromosomes: Lgr5 adult intestinal stem cell characteristics. *The EMBO Journal 30*(6), 1104–1109.

[237] Schindelin, J., I. Arganda-Carreras, E. Frise, V. Kaynig, M. Longair, T. Pietzsch, S. Preibisch, C. Rueden, S. Saalfeld, B. Schmid, J.-Y. Tinevez, D. J. White, V. Hartenstein, K. Eliceiri, P. Tomancak, and A. Cardona (2012, July). Fiji: An open-source platform for biological-image analysis. *Nat Methods 9*(7), 676–682.

[238] Schliffka, M. F., A. F. Tortorelli, Ö. Özgüç, L. De Plater, O. Polzer, D. Pelzer, and J.-L. Maître (2021, April). Multiscale analysis of single and double maternal-zygotic Myh9 and Myh10 mutants during mouse preimplantation development. *eLife 10*, e68536.

[239] Schmid-Burgk, J. L., K. Höning, T. S. Ebert, and V. Hornung (2016, November). CRISPaint allows modular base-specific gene tagging using a ligase-4-dependent mechanism. *Nat Commun 7*(1), 12338.

[240] Schuijers, J., J. P. Junker, M. Mokry, P. Hatzis, B.-K. Koo, V. Sasselli, L. G. van der Flier, E. Cuppen, A. van Oudenaarden, and H. Clevers (2015, February). Ascl2 Acts as an R-spondin/Wnt-Responsive Switch to Control Stemness in Intestinal Crypts. *Cell Stem Cell 16*(2), 158–170.

[241] Seidlitz, T., S. R. Merker, A. Rothe, F. Zakrzewski, C. Von Neubeck, K. Grützmann, U. Sommer, C. Schweitzer, S. Schölch, H. Uhlemann, A.-M. Gaebler, K. Werner, M. Krause, G. B. Baretton, T. Welsch, B.-K. Koo, D. E. Aust, B. Klink, J. Weitz, and D. E. Stange (2019, February). Human gastric cancer modelling using organoids. *Gut 68*(2), 207–217.

[242] Serra, D., U. Mayr, A. Boni, I. Lukonin, M. Rempfler, L. Challet Meylan, M. B. Stadler, P. Strnad, P. Papasaikas, D. Vischi, A. Waldt, G. Roma, and P. Liberali (2019, May). Self-organization and symmetry breaking in intestinal organoid development. *Nature 569*(7754), 66–72.

[243] Sivagnanam, M., J. L. Mueller, H. Lee, Z. Chen, S. F. Nelson, D. Turner, S. H. Zlotkin, P. B. Pencharz, B.-Y. Ngan, O. Libiger, N. J. Schork, J. E. Lavine, S. Taylor, R. O. Newbury, R. D. Kolodner, and H. M. Hoffman (2008, August). Identification of EpCAM as the Gene for Congenital Tufting Enteropathy. *Gastroenterology 135*(2), 429–437.

[244] Sjöqvist, M. and E. R. Andersson (2019, March). Do as I say, Not(ch) as I do: Lateral control of cell fate. *Developmental Biology 447*(1), 58–70.

[245] Skylaki, S., O. Hilsenbeck, and T. Schroeder (2016, November). Challenges in long-term imaging and quantification of single-cell dynamics. *Nat Biotechnol 34*(11), 1137–1144.

[246] Slattum, G., Y. Gu, R. Sabbadini, and J. Rosenblatt (2014, January). Autophagy in Oncogenic K-Ras Promotes Basal Extrusion of Epithelial Cells by Degrading S1P. *Current Biology 24*(1), 19–28.

[247] Smillie, C. S., M. Biton, J. Ordovas-Montanes, K. M. Sullivan, G. Burgin, D. B. Graham, R. H. Herbst, N. Rogel, M. Slyper, J. Waldman, M. Sud, E. Andrews, G. Velonias, A. L. Haber, K. Jagadeesh, S. Vickovic, J. Yao, C. Stevens, D. Dionne, L. T. Nguyen, A.-C. Villani, M. Hofree, E. A. Creasey, H. Huang, O. Rozenblatt-Rosen, J. J. Garber, H. Khalili, A. N. Desch, M. J. Daly, A. N. Ananthakrishnan, A. K. Shalek, R. J. Xavier, and A. Regev (2019, July). Intra- and Inter-cellular Rewiring of the Human Colon during Ulcerative Colitis. *Cell 178*(3), 714–730.e22.

[248] Snippert, H. J., L. G. van der Flier, T. Sato, J. H. van Es, M. van den Born, C. Kroon-Veenboer, N. Barker, A. M. Klein, J. van Rheenen, B. D. Simons, and H. Clevers (2010, October). Intestinal Crypt Homeostasis Results from Neutral Competition between Symmetrically Dividing Lgr5 Stem Cells. *Cell 143*(1), 134–144.

[249] Spencer, A. U., X. Sun, M. El-Sawaf, E. Q. Haxhija, D. Brei, J. Luntz, H. Yang, and D. H. Teitelbaum (2006, August). Enterogenesis in a clinically feasible model of mechanical small-bowel lengthening. *Surgery 140*(2), 212–220.

[250] Spit, M., B.-K. Koo, and M. M. Maurice (2018, September). Tales from the crypt: Intestinal niche signals in tissue renewal, plasticity and cancer. *Open Biol. 8*(9), 180120.

[251] Sugawara, K., Ç. Çevrim, and M. Averof (2022, January). Tracking cell lineages in 3D by incremental deep learning. *eLife 11*, e69380.

[252] Sui, L., S. Alt, M. Weigert, N. Dye, S. Eaton, F. Jug, E. W. Myers, F. Jülicher, G. Salbreux, and C. Dahmann (2018, November). Differential lateral and basal tension drive folding of Drosophila wing discs through two distinct mechanisms. *Nat Commun 9*(1), 4620.

[253] Sutherland, A. and A. Lesko (2020, February). Pulsed actomyosin contractions in morphogenesis. *F1000Res 9*, 142.

[254] Teo, J. L., G. A. Gomez, S. Weeratunga, E. M. Davies, I. Noordstra, S. Budnar, H. Katsuno-Kambe, M. J. McGrath, S. Verma, V. Tomatis, B. R. Acharya, L. Balasubramaniam, R. M. Templin, K.-A. McMahon, Y. S. Lee, R. J. Ju, S. J. Stehbens, B. Ladoux,

C. A. Mitchell, B. M. Collins, R. G. Parton, and A. S. Yap (2020, July). Caveolae Control Contractile Tension for Epithelia to Eliminate Tumor Cells. *Developmental Cell 54*(1), 75–91.e7.

[255] Terahara, K., M. Yoshida, O. Igarashi, T. Nochi, G. S. Pontes, K. Hase, H. Ohno, S. Kurokawa, M. Mejima, N. Takayama, Y. Yuki, A. W. Lowe, and H. Kiyono (2008, June). Comprehensive Gene Expression Profiling of Peyer's Patch M Cells, Villous M-Like Cells, and Intestinal Epithelial Cells. *J Immunol 180*(12), 7840–7846.

[256] Thompson, E. M., Y. E. Price, and N. A. Wright (1990, April). Kinetics of enteroendocrine cells with implications for their origin: A study of the cholecystokinin and gastrin subpopulations combining tritiated thymidine labelling with immunocytochemistry in the mouse. *Gut 31*(4), 406–411.

[257] Thorne, C. A., I. W. Chen, L. E. Sanman, M. H. Cobb, L. F. Wu, and S. J. Altschuler (2018). Enteroid Monolayers Reveal an Autonomous WNT and BMP Circuit Controlling Intestinal Epithelial Growth and Organization. *Developmental Cell 44*, 624–633.

[258] Tomer, R., K. Khairy, F. Amat, and P. J. Keller (2012, July). Quantitative high-speed imaging of entire developing embryos with simultaneous multiview light-sheet microscopy. *Nat Methods 9*(7), 755–763.

[259] Tóth, B., S. Ben-Moshe, A. Gavish, N. Barkai, and S. Itzkovitz (2017, January). Early commitment and robust differentiation in colonic crypts. *Molecular Systems Biology 13*(1), 902.

[260] Tsubouchi, S. and C. P. Leblond (1979, December). Migration and turnover of entero-endocrine and caveolated cells in the epithelium of the descending colon, as shown by radioautography after continuous infusion of ^{3} H-thymidine into mice. *Am. J. Anat. 156*(4), 431–451.

[261] Tveriakhina, L., K. Schuster-Gossler, S. M. Jarrett, M. B. Andrawes, M. Rohrbach, S. C. Blacklow, and A. Gossler (2018, October). The ectodomains determine ligand function in vivo and selectivity of DLL1 and DLL4 toward NOTCH1 and NOTCH2 in vitro. *eLife 7*, e40045.

[262] Ulicna, K., G. Vallardi, G. Charras, and A. R. Lowe (2021, October). Automated Deep Lineage Tree Analysis Using a Bayesian Single Cell Tracking Approach. *Front. Comput. Sci. 3*, 734559.

[263] Valon, L., A. Marín-Llauradó, T. Wyatt, G. Charras, and X. Trepat (2017, February). Optogenetic control of cellular forces and mechanotransduction. *Nat Commun 8*(1), 14396.

[264] van Bodegraven, A. A., C. R. Curley, K. A. Hunt, A. J. Monsuur, R. K. Linskens, C. M. Onnie, J. B. A. Crusius, V. Annese, A. Latiano, M. S. Silverberg, A. Bitton, S. A. Fisher, A. H. Steinhart, A. Forbes, J. Sanderson, N. J. Prescott, D. P. Strachan, R. J. Playford, C. G. Mathew, C. Wijmenga, M. J. Daly, J. D. Rioux, and D. A. van Heel (2006, December). Genetic Variation in Myosin IXB Is Associated With Ulcerative Colitis. *Gastroenterology 131*(6), 1768–1774.

[265] van de Wetering, M., H. E. Francies, J. M. Francis, G. Bounova, F. Iorio, A. Pronk, W. van Houdt, J. van Gorp, A. Taylor-Weiner, L. Kester, A. McLaren-Douglas, J. Blokker, S. Jaksani, S. Bartfeld, R. Volckman, P. van Sluis, V. S. Li, S. Seepo, C. Sekhar Pedamallu, K. Cibulskis, S. L. Carter, A. McKenna, M. S. Lawrence, L. Lichtenstein, C. Stewart, J. Koster, R. Versteeg, A. van Oudenaarden, J. Saez-Rodriguez, R. G. Vries, G. Getz, L. Wessels, M. R. Stratton, U. McDermott, M. Meyerson, M. J. Garnett, and H. Clevers (2015, May). Prospective Derivation of a Living Organoid Biobank of Colorectal Cancer Patients. *Cell 161*(4), 933–945.

[266] Van Der Flier, L. G., A. Haegebarth, D. E. Stange, M. Van De Wetering, and H. Clevers (2009, July). OLFM4 Is a Robust Marker for Stem Cells in Human Intestine and Marks a Subset of Colorectal Cancer Cells. *Gastroenterology 137*(1), 15–17.

[267] Van Der Flier, L. G., J. Sabates–Bellver, I. Oving, A. Haegebarth, M. De Palo, M. Anti, M. E. Van Gijn, S. Suijkerbuijk, M. Van De Wetering, G. Marra, and H. Clevers (2007, February). The Intestinal Wnt/TCF Signature. *Gastroenterology 132*(2), 628–632.

[268] Van Der Sluis, M., B. A. De Koning, A. C. De Bruijn, A. Velcich, J. P. Meijerink, J. B. Van Goudoever, H. A. Büller, J. Dekker, I. Van Seuningen, I. B. Renes, and A. W. Einerhand (2006, July). Muc2-Deficient Mice Spontaneously Develop Colitis, Indicating That MUC2 Is Critical for Colonic Protection. *Gastroenterology 131*(1), 117–129.

[269] Van Es, J. H., T. Sato, M. Van De Wetering, A. Lyubimova, A. N. Yee Nee, A. Gregorieff, N. Sasaki, L. Zeinstra, M. Van Den Born, J. Korving, A. C. M. Martens, N. Barker, A. Van Oudenaarden, and H. Clevers (2012, October). Dll1+ secretory progenitor cells revert to stem cells upon crypt damage. *Nat Cell Biol 14*(10), 1099–1104.

[270] Van Es, J. H., M. E. Van Gijn, O. Riccio, M. Van Den Born, M. Vooijs, H. Begthel, M. Cozijnsen, S. Robine, D. J. Winton, F. Radtke, and H. Clevers (2005, June). Notch/γ-secretase inhibition turns proliferative cells in intestinal crypts and adenomas into goblet cells. *Nature 435*(7044), 959–963.

[271] Van Es, J. H., K. Wiebrands, C. López-Iglesias, M. Van De Wetering, L. Zeinstra, M. Van Den Born, J. Korving, N. Sasaki, P. J. Peters, A. Van Oudenaarden, and H. Clevers (2019, December). Enteroendocrine and tuft cells support Lgr5 stem cells on Paneth cell depletion. *Proc. Natl. Acad. Sci. U.S.A. 116*(52), 26599–26605.

[272] Verdugo, P. (1991). Mucin Exocytosis. *Am Rev Respir Dis 144*, S33–S37.

[273] Verhagen, M. P., R. Joosten, M. Schmitt, N. Välimäki, A. Sacchetti, K. Rajamäki, J. Choi, P. Procopio, S. Silva, B. Van Der Steen, T. P. P. Van Den Bosch, D. Seinstra, A. C. De Vries, M. Doukas, L. H. Augenlicht, L. A. Aaltonen, and R. Fodde (2024, July). Non-stem cell lineages as an alternative origin of intestinal tumorigenesis in the context of inflammation. *Nat Genet 56*(7), 1456–1467.

[274] Virtanen, P., R. Gommers, T. E. Oliphant, M. Haberland, T. Reddy, D. Cournapeau, E. Burovski, P. Peterson, W. Weckesser, J. Bright, S. J. van der Walt, M. Brett, J. Wilson, K. J. Millman, N. Mayorov, A. R. J. Nelson, E. Jones, R. Kern, E. Larson, C. J. Carey, İ. Polat, Y. Feng, E. W. Moore, J. VanderPlas, D. Laxalde, J. Perktold, R. Cimrman,

I. Henriksen, E. A. Quintero, C. R. Harris, A. M. Archibald, A. H. Ribeiro, F. Pedregosa, P. van Mulbregt, SciPy 1.0 Contributors, A. Vijaykumar, A. P. Bardelli, A. Rothberg, A. Hilboll, A. Kloeckner, A. Scopatz, A. Lee, A. Rokem, C. N. Woods, C. Fulton, C. Masson, C. Häggström, C. Fitzgerald, D. A. Nicholson, D. R. Hagen, D. V. Pasechnik, E. Olivetti, E. Martin, E. Wieser, F. Silva, F. Lenders, F. Wilhelm, G. Young, G. A. Price, G.-L. Ingold, G. E. Allen, G. R. Lee, H. Audren, I. Probst, J. P. Dietrich, J. Silterra, J. T. Webber, J. Slavič, J. Nothman, J. Buchner, J. Kulick, J. L. Schönberger, J. V. de Miranda Cardoso, J. Reimer, J. Harrington, J. L. C. Rodríguez, J. Nunez-Iglesias, J. Kuczynski, K. Tritz, M. Thoma, M. Newville, M. Kümmerer, M. Bolingbroke, M. Tartre, M. Pak, N. J. Smith, N. Nowaczyk, N. Shebanov, O. Pavlyk, P. A. Brodtkorb, P. Lee, R. T. McGibbon, R. Feldbauer, S. Lewis, S. Tygier, S. Sievert, S. Vigna, S. Peterson, S. More, T. Pudlik, T. Oshima, T. J. Pingel, T. P. Robitaille, T. Spura, T. R. Jones, T. Cera, T. Leslie, T. Zito, T. Krauss, U. Upadhyay, Y. O. Halchenko, and Y. Vázquez-Baeza (2020, March). SciPy 1.0: Fundamental algorithms for scientific computing in Python. *Nat Methods 17*(3), 261–272.

[275] Von Moltke, J., M. Ji, H.-E. Liang, and R. M. Locksley (2016, January). Tuft-cell-derived IL-25 regulates an intestinal ILC2–epithelial response circuit. *Nature 529*(7585), 221–225.

[276] Wakisaka, Y., S. Sugimoto, M. Oda, S. Pastuhov, M. Fujii, and T. Sato (2025). Understanding the Differentiation Pathway to BEST4+ Cells in Human Colonic Epithelium. *Gastroenterology 169*(1), 154–157.e5.

[277] Wang, D., S. Lim, Y. Teranishi-Ikawa, A. Mizoroki, W. K. Spoelstra, T. Dayton, J. S. van, S. J. Tans, P. J. Peters, J. H. van Es, and H. Clevers. Human intestinal microfold (M) cells resemble dendritic cells and present gluten antigen. *In revision at Nature.*

[278] Wang, D., W. K. Spoelstra, L. Lin, N. Akkerman, D. Krueger, T. Dayton, J. S. Van Zon, S. J. Tans, J. H. Van Es, and H. Clevers (2025, April). Interferon-responsive intestinal BEST4/CA7+ cells are targets of bacterial diarrheal toxins. *Cell Stem Cell 32*, 598–612.

[279] Wang, X., W. E. Allen, M. A. Wright, E. L. Sylwestrak, N. Samusik, S. Vesuna, K. Evans, C. Liu, C. Ramakrishnan, J. Liu, G. P. Nolan, F.-A. Bava, and K. Deisseroth (2018, July). Three-dimensional intact-tissue sequencing of single-cell transcriptional states. *Science 361*(6400), eaat5691.

[280] Westfall, A. K., S. S. Gopalan, J. C. Kay, T. S. Tippetts, M. B. Cervantes, K. Lackey, S. M. Chowdhury, M. W. Pellegrino, and T. A. Castoe (2024, October). Single-cell resolution of intestinal regeneration in pythons without crypts illuminates conserved vertebrate regenerative mechanisms. *Proc. Natl. Acad. Sci. U.S.A. 121*(43), e2405463121.

[281] Wiese, K. E., R. Nusse, and R. Van Amerongen (2018, June). Wnt signalling: Conquering complexity. *Development 145*(12), dev165902.

[282] Wijnakker, J. J., G. J. Van Son, D. Krueger, W. J. Van De Wetering, C. Lopez-Iglesias, R. Schreurs, F. Van Rijt, S. Lim, L. Lin, P. J. Peters, R. R. Isberg, C. Y. Janda, W. De Lau, and H. Clevers (2025, January). Integrin-activating *Yersinia* protein Invasin sustains long-term expansion of primary epithelial cells as 2D organoid sheets. *Proc. Natl. Acad. Sci. U.S.A. 122*(1), e2420595121.

[283] Williams, J. M., C. A. Duckworth, A. J. M. Watson, M. R. Frey, J. C. Miguel, M. D. Burkitt, R. Sutton, K. R. Hughes, L. J. Hall, J. H. Caamaño, B. J. Campbell, and D. M. Pritchard (2013, January). A mouse model of pathological small intestinal epithelial cell apoptosis and shedding induced by systemic administration of lipopolysaccharide. *Disease Models & Mechanisms*, dmm.013284.

[284] Willms, R. J., L. O. Jones, J. C. Hocking, and E. Foley (2022, February). A cell atlas of microbe-responsive processes in the zebrafish intestine. *Cell Reports 38*(5), 110311.

[285] Wu, X. S., X.-Y. He, J. J. Ipsaro, Y.-H. Huang, J. B. Preall, D. Ng, Y. T. Shue, J. Sage, M. Egeblad, L. Joshua-Tor, and C. R. Vakoc (2022, July). OCA-T1 and OCA-T2 are coactivators of POU2F3 in the tuft cell lineage. *Nature 607*(7917), 169–175.

[286] Xue, Y., A. W. Browne, W. C. Tang, J. Delgado, B. T. McLelland, G. Nistor, J. T. Chen, K. Chew, N. Lee, H. S. Keirstead, and M. J. Seiler (2021, December). Retinal Organoids Long-Term Functional Characterization Using Two-Photon Fluorescence Lifetime and Hyperspectral Microscopy. *Front. Cell. Neurosci. 15*, 796903.

[287] Yang, Q. and P. Liberali (2021, October). Collective behaviours in organoids. *Current Opinion in Cell Biology 72*, 81–90.

[288] Yin, X., H. F. Farin, J. H. van Es, H. Clevers, R. Langer, and J. M. Karp (2014, January). Niche-independent high-purity cultures of Lgr5+ intestinal stem cells and their progeny. *Nat Methods 11*(1), 106–112.

[289] Zhang, Y. (2025). In situ lysosomal proteomics enabled by bioorthogonal photocatalytic proximity labelling. *Nature Catalysis 8*, 162–177.

[290] Zhang, Y., M. A. Conti, D. Malide, F. Dong, A. Wang, Y. A. Shmist, C. Liu, P. Zerfas, M. P. Daniels, C.-C. Chan, E. Kozin, B. Kachar, M. J. Kelley, J. B. Kopp, and R. S. Adelstein (2012, January). Mouse models of MYH9-related disease: Mutations in nonmuscle myosin II-A. *Blood 119*(1), 238–250.

[291] Zheng, X., M. A. Betjes, P. Ender, Y. J. Goos, G. Huelsz-Prince, H. Clevers, J. S. Van Zon, and S. J. Tans (2023, August). Organoid cell fate dynamics in space and time. *Sci. Adv. 9*(33), eadd6480.

[292] Zhou, B., W. Lin, Y. Long, Y. Yang, H. Zhang, K. Wu, and Q. Chu (2022, March). Notch signaling pathway: Architecture, disease, and therapeutics. *Sig Transduct Target Ther 7*(1).

[293] Zulueta-Coarasa, T. and J. Rosenblatt (2022, February). The role of tissue maturity and mechanical state in controlling cell extrusion. *Current Opinion in Genetics & Development 72*, 1–7.

Acknowledgments

In addition to whatever I think we may have learned about the biophysics and quantitative developmental biology of the intestinal epithelium, I have learned that true scientific success is not measured by the quality or quantity of publications, honours and awards, and research grants, but by the extent to which you help your colleagues succeed in doing science along the way. I can say that I have truly made many friends during my PhD research, which makes me view this thesis as a successful enterprise. In this chapter I want to thank and acknowledge all those who have made this thesis possible, or at least more fun to write.

First and foremost, I want to thank my direct supervisors **Sander** and **Jeroen**. The circumstances in which I joined AMOLF under your shared supervision in late 2021 were unusual. I am grateful for this opportunity, and for all the lessons that I have learned from you in the years that followed. **Sander**, your incredible work ethic, attention for fine details, drive to push scientific projects to completion and investment in the yearly group retreat made working in your lab a fantastic experience. **Jeroen**, your sharp comments on detailed experiments, joy in science and your personal investment in my academic growth made it a pleasure to work in your lab. Our off-topic discussions at coffee and lunch were highlights of many days. I hope you both will continue the work at the interface between biophysics and quantitative developmental biology together. I am certain that many more discoveries in this relatively uncharted territory will follow. I also want to thank both of you for encouraging and supporting me to present my work at international conferences in Ein Gedi, Dresden, Lindau, Heidelberg, Lisbon (twice) and San Diego. Thank you **Pieter Rein**, for your input into my projects in the Organoid Meetings; it was very helpful to get the perspective of theoreticians in my experimental projects. I also want to thank the other committee members, **Marileen Dogterom**, **Martijn Gloerich**, **Gunnar Hansson**, **Xavier Trepat** and **Marvin Tanenbaum**, for taking the time to critically reflect on this thesis.

I am deeply grateful to **Daniel Krueger** and **Daisong Wang**, two exceptional postdocs from the Clevers group at the Hubrecht Institute. Thank you both for the fruitful and motivating collaborations that resulted in multiple chapters of this thesis. **Daniel**, you managed to introduce me into the field of mechanobiology, the most complicated field I have ever considered myself to be part of. When I think of our meetings and look back on our extrusion project, I am still amazed at what we were able to distil from what at first seemed impossible data. **Daisong**, your outstanding work on rare intestinal cell types is truly inspiring. I am thankful that you supported and encouraged me to further investigate BEST4/CA7$^+$ cell biology. I also want to thank **Hans Clevers** for supervision and invaluable input into most of my research projects.

Next, I want to thank the group of people at AMOLF with whom I've had the pleasure to work on the biophysics of intestinal organoids. **Rutger**, your welcoming attitude, unlimited patience, and willingness to involve me in your projects were extremely useful and enjoyable. It would not have been possible for me to complete this thesis without your technical support and help with OrganoidTracker software. **Pascal**, I can still see us sitting at the little flower-decorated table in front of the AMOLF reception on the 1st of October 2021, as we were waiting to be picked up and introduced. I greatly enjoyed sharing an office (and initially, even a desk) with you, and our discussions on basically all topics ranging from the liveability of Almere to geopolitical trends. **Max**, thank you for your critical, constructive and motivating feedback on my data during group meetings. Your knowledge, analytical thinking, and curiosity are truly contagious. **Michael**, thank you for our almost daily walks across the Science Park. These walks were a perfect way to relax and blow off steam. I have fond memories of our discussions regarding your multilayer 3D vertex model and your views on General Relativity, which almost always ended with you shaking your head and (probably correctly) saying "I don't want to get into it, it's too complicated". **Xuan**, thank you for introducing me to the world of long-term live-cell imaging of intestinal organoids and tracking. Your experimental work paved the way for me to pursue the projects in this thesis. **Yvonne**, **Aarzo**, **Corinna**, **Marko**, **Sebastian** and **Hinco** thank you for your support and dedication to the organoid research, your technical expertise and hard work were essential to keep the lab (and my experiments) going. Thank you **Kim**, for being a fantastic MSc student and working so hard on the differentiation of M cells in organoids. **Susi**, **Jasper** and **Heidi**, I wish our overlap would have been longer. You are terrific additions to the organoid team at AMOLF, and I wish you all the best for the remainder of your projects.

I also want to thank colleagues, past and present, for providing the highly enjoyable working environment. **Nebojsa**, I love that we could not have a conversation for longer than 10 minutes without bursting into roaring laughter. And also thank you and **Jasper** for being my paranymphs. **Dhawal**, your rallying cries on the football pitch are still ringing in my ears. It was fantastic how you organized parties, the football team and all kinds of social gatherings. **Jack**, thanks for organizing the pubquizzes with me, they remain the most highly valued PowerPoint slides of my PhD. **Kathi**, thanks for all the fun (instant-noodle) dinners at AMOLF where we discussed career options, life goals and so much more. **Burak**, thanks for all lunchtime talks and your philosophical insights. **Evan**, despite working in the same building for 3 years, I still feel like more than half of our conversations took place abroad, while being utterly doorhandled (even if only you know what that means). **Marija**, thank you for always being such a cheerful office mate. And **Rutger** and **Burak**, thanks for giving me a taste of the PhD defense ceremony as your paranymph. In addition to those mentioned above, I thank **Rachel**, **Cátia**, **Bibi**, **Vanda**, **Luca**, **Timo**, **Gouri**, **Ananya**, **Yifei**, **Christopher**, **Anna**, and the rest of the Biomeeting and Organoid Meeting audience for being great colleagues, input on my projects and making AMOLF and BN a truly great place to come to work to every day. **Christos**, thank you for being such a great friend and all your support and insights along the way. **Jeroen (Jacques)**, **Lukas** and **Jurriaan**, thank you for being such great students. It warms my heart that you are doing so well in your academic careers. And thanks **Jeroen (Jacques)**, for joining me for that midnight

polar bear plunge in the stormy, mid-winter Atlantic Ocean. That was unforgettable.

Willem Kasper Spoelstra
Amsterdam, October 2025

Curriculum Vitæ

Willem Kasper Spoelstra

1995/10/21	Born in Voorburg, Netherlands
2007/09 - 2013/06	Graduated from Hofstad Lyceum, Den Haag, Netherlands
2013/09 - 2016/08	Bachelor of Science Nanobiology, TU Delft & Erasmus Medical Center, Netherlands (with Honours)
2016/11 - 2017/02	Research internship, Harvard Medical School & Massachusetts General Hospital, Boston MA, USA
2016/09 - 2019/08	Master Nanobiology, TU Delft & Erasmus Medical Center, Netherlands (*cum laude*)
2019/09 - 2021/09	PhD student, TU Delft, Netherlands
2021/10 - ongoing	PhD student, AMOLF, Netherlands

List of Publications

Related to this thesis

📄 Daniel Krueger*, **Willem Kasper Spoelstra***, Dirk Jan Mastebroek, Rutger Kok, Shanie Wu, Mike Nikolaev, Marie Bannier-Hélaouët, Nikolche Gjorevski, Matthias Lutolf, Johan van Es, Jeroen van Zon, Sander Tans, Hans Clevers. Epithelial tension controls intestinal cell extrusion. *Science* **389** (6764), eadr8753 (2025). – **Chapter 2**

📄 Rutger N.U. Kok*, Xuan Zheng*, **Willem Kasper Spoelstra**, Tinka Clement, Yorick B. C. van de Grift, Hans Clevers, Renée van Amerongen, Sander Tans, Jeroen S. van Zon. Loss of Paneth cell contact starts a WNT differentiation timer in intestinal crypts. Under revision at *Nature Communications* – **Chapter 3**

📄 **Willem Kasper Spoelstra***, Daisong Wang*, Johan van Es, Hans Clevers, Jeroen S. van Zon, Sander J. Tans. BEST4/CA7$^+$ and goblet cells are interdependent regulators of intestinal mucus homeostasis. Under review at *Nature Cell Biology* – **Chapter 4**

📄 Rutger N.U. Kok, **Willem Kasper Spoelstra**, Max A. Betjes, Jeroen S. van Zon, Sander J. Tans. Label-free cell imaging and tracking in 3D organoids. *Cell Reports Physical Science* **6** (4), 102522, (2025). – **Chapter 5**

📄 **Willem Kasper Spoelstra**, Xuan Zheng, Rutger Kok, Guizela Huelsz-Prince, Max Betjes, Pascal Ender, Yvonne Goos, Kim Annabel Kuentzelmann, Daniel Krueger, Daisong Wang, Hans Clevers, Sander J. Tans, Jeroen S. van Zon. Quantitative imaging of dynamic processes in intestinal organoids. Under revision at *Nature Protocols*. – **Chapter 6**

Daisong Wang, **Willem Kasper Spoelstra**, Lin Lin, Ninouk Akkerman, Daniel Krueger, Talya Dayton, Jeroen S van Zon, Sander J Tans, Johan H van Es, Hans Clevers. Interferon-responsive intestinal BEST4/CA7$^+$ cells are targets of bacterial diarrheal toxins. *Cell Stem Cell* **32** (4), 598-612 (2025).

Daisong Wang*, Sangho Lim*, Willine J. van de Wetering, Carmen Lopez-Iglesias, Yuu Okura, Yuri Teranishi-Ikawa, Akihiko Mizoroki, **Willem Kasper Spoelstra**, Talya Dayton, Gijs J. F. van Son, Apollo Pronk, Niels Smakman, Gieneke B.C. Gonera-de Jong, Sebo Withoff, Iris H. Jonkers, Jeroen S. van Zon, Sander J. Tans, Peter J. Peters, Johan H. van Es and Hans Clevers. Human intestinal microfold cells resemble dendritic cells and present gluten antigen. Accepted at *Nature*.

📄 Included in this thesis.
* Equal contribution

OTHER

Willem Kasper Spoelstra, Jeroen M. Jacques, Rodrigo Gonzalez-Linares, Franklin L. Nobrega, Anna C. Haagsma, Marileen Dogterom, Dimphna H. Meijer, Timon Idema, Stan J.J. Brouns, Louis Reese. CRISPR-based DNA and RNA detection with liquid-liquid phase separation. *Biophysical Journal* **120** (7), 1198-1209, (2021).

Willem Kasper Spoelstra, Eli O Van Der Sluis, Marileen Dogterom, Louis Reese. Nonspherical coacervate shapes in an enzyme-driven active system. *Langmuir* **36** (8), 1956-1964, (2020).

Siddharth Deshpande, Frank Brandenburg, Anson Lau, Mart GF Last, **Willem Kasper Spoelstra**, Louis Reese, Sreekar Wunnava, Marileen Dogterom, Cees Dekker. Spatiotemporal control of coacervate formation within liposomes. *Nature Communications* **10**, (2019).

Willem Kasper Spoelstra*, Siddharth Deshpande*, Cees Dekker. Tailoring the appearance: what will synthetic cells look like? *Current Opinion in Biotechnology* **51**, 47-56, (2018).

Siddharth Deshpande, **Willem Kasper Spoelstra**, Marleen Van Doorn, Jacob Kerssemakers, Cees Dekker. Mechanical division of cell-sized liposomes. *ACS Nano* **12** (3), 2560-2568, (2018).

PATENTS

Willem Kasper Spoelstra, Louis Reese. Secure Communication using CRISPR-Cas. (2019).

Louis Reese, **Willem Kasper Spoelstra**, Stan J.J. Brouns. Coacervate-based detection of a compound of interest (2017).